Tectonic Stresses and Injection-Induced Fault Slip Assessment

by

Ali Yaghoubi

A thesis

presented to the University of Waterloo

in fulfillment of the

thesis requirement for the degree of

Doctor of Philosophy

in

Earth Science

Waterloo, Ontario, Canada, 2022

Examining Committee Membership

The following served on the Examining Committee for this thesis. The decision of the Examining Committee is by majority vote.

External Examiner	Dr. Mirko van der Baan Professor, Dept. of Physics University of Alberta
Supervisor(s)	Dr. Maurice B. Dusseault Professor, Dept. of Earth and Environmental Sciences, University of Waterloo
	Dr. Yuri Leonenko Associate Professor, Dept. of Earth and Environmental Sciences, University of Waterloo
Internal Member	Dr. Tony Endres Associate Professor, Dept. of Earth and Environmental Sciences, University of Waterloo
Internal-external Member	Dr. Robert Gracie Associate Professor, Dept. of Civil and Environmental Eng, University of Waterloo
Other Member(s)	Dr. Colby Steelman Lecturer, Dept. of Earth and Environmental Sciences, University of Waterloo

Author's Declaration

I hereby declare that I am the sole author of this thesis. This is a true copy of the thesis, including any required final revisions, as accepted by my examiners.

I understand that my thesis may be made electronically available to the public.

Abstract

Understanding the Earth's stress state at depth is fundamental to a wide variety of subsurface projects, ranging from seismology projects to studies on underground energy storage or extraction. The primary objectives of this dissertation are first to constrain the state of stress by combining drilling-induced wellbore failures and earthquake focal mechanisms, and second to use a probabilistic approach for stresses, pore pressures and rock properties to assess injection-induced fault slip in unconventional and geothermal resources.

Knowledge of the state of stress in an area helps us understand the seismic hazard and crustal-scale seismicity pattern issues (>10 km); the energy development (3-6 km) issues from hydrocarbon to geothermal resources; the reservoir scale issues (0.1-1 km) of induced seismicity arising from energy extraction; and borehole scale engineering issues (up to 100 m) related to casing shear and borehole stability. As part of this dissertation, I measure the orientation and constrain the magnitude of present-day stresses in the Dezful Embayment within Iran's Zagros Fold and Thrust Belt (ZFTB), Alberta's Fox Creek area, the Montney Formation in Alberta and British Columbia, and Alberta's Grande Prairie area. The ZFTB in southwest Iran is one of the world's most seismically active areas. The Dezful Embayment (DE) within the ZFTB is also one of the richest hydrocarbon regions in the world, hosting many onshore hydrocarbon fields. Western Canada is also home to some of the largest oil and gas reserves in the world, including unconventional resources such as the Montney and Duvernay Formations. The injection-induced earthquakes in western Canada have some of the largest magnitudes reported worldwide, such as those near Fort St. John in British Columbia and Fox Creek in Alberta. Considering the economic importance of the region and the seismic activity in these areas, it is important that we gain a better understanding of the state of stress in ZFTB and Western Canada. It is noteworthy that tectonic stresses have not been studied on such a large scale in these regions.

To understand the state of stress in each region, two datasets were used. The first included petrophysical data from drilled wells, and the second contained natural and injection-induced earthquake focal mechanisms. Formal stress inversion analysis of the tectonic earthquake focal mechanisms in ZFTB demonstrates that there is currently a compressional stress state in the basement below the sediments. The seismologically determined S_{Hmax} direction is NE-SW, nearly perpendicular to the strike of most faults in the region. However, borehole geomechanics analysis in the ZFTB region using rock strength and drilling evidence leads to the counterintuitive result that the shallow state of stress is a normal/strike-slip regime. Based on Coulomb faulting theory, these results indicate that a reverse fault regime with a maximum horizontal principal direction of SW-NE is unfavorable for slip along the N-S strike-slip basement Kazerun Fault System. In Alberta and British Columbia, a similar approach but using injection-induced earthquakes indicates that strike-slip faulting with NE-SW S_{Hmax} directions dominates the region. It has been observed that relative stress magnitudes are primarily related to pore pressure variation in Alberta and British Columbia. In the compartmentalized

Montney Formation of western Alberta and northeastern British Columbia, these characteristics are evident.

Stress measurements will always contain some level of uncertainty due to either inadequate data or inherent uncertainties. These uncertainties impact any project in which the stress plays a central role at different scales. Therefore, probabilistic methods are necessary to quantify the impact of these uncertainties on each project. The uncertainty invariably associated with the state of stress measurements affects the analysis of subsurface events such as seismicity induced by hydraulic fracture (HF) stimulation. HF for energy extraction from underground conventional, unconventional, and geothermal resources is typically accompanied by anthropogenic seismicity. Increasing pore pressure by injecting fluid into naturally fractured media leads to slip/shearing of faults and fractures, resulting in detectable earthquakes. The magnitude and rate of such human-made earthquakes are directly related to stress orientations and magnitudes. This uncertainty in the stress state, plus a variety of uncontrollable subsurface parameters including the original pore pressure, size, and density of pre-existing faults/fractures, fault/fracture orientation, and frictional strength make up the most important factors affecting the probabilistic assessment of fault/fracture slip. In HF treatments, accounting for parametric uncertainty by using appropriate statistical probability distributions leads to better decision-making/risk management for user-controlled parameters such as injection pressure.

Historically quiet areas in Alberta and eastern British Columbia have experienced noticeably higher seismicity rates over the last decade. Shale gas and shale oil production from the unconventional plays in the Western Canada Sedimentary Basin has grown with the use of multi-stage HF (Hydraulic Fracture stimulation) technology. Supported by high oil prices and new HF technology availability, development started in 2005 and accelerated significantly in 2011; accordingly, the seismicity rate has increased. The anthropogenic seismicity for this area includes some of the largest M_W values reported globally, including events near Fort St. John of M_W 4.6 on August 17, 2015, and M_W 4.2 on November 30, 2018. Most of these occur during HF treatments and are spatially and temporally restricted to the region around the wells at a scale of 1-2 km, rather than being regional at a scale of more than two kilometers.

As part of this dissertation, the probability assessment of fault/fracture slip due to fluid injection has been used and implemented in three different case studies. These include Alberta's Fox Creek area, the Montney Formation of western Alberta and northeastern British Columbia, and Alberta's Grande Prairie area. In each case study, geomechanics parameters are expressed as probability distributions using different datasets from borehole petrophysical data to injection-induced focal mechanisms. Monte Carlo simulations are applied to assess the potential slip tendency of local faults. The cumulative distribution function of critical pore pressure to cause slip on each known fault is developed by using analyses of the Mohr-Coulomb shear parameters and local tectonic stress state. Injection-induced seismicity in the region is a formation-related phenomenon governed by the in-situ

formation conditions and pre-existing fault patterns. A map is developed that can be used to predict which area of the Montney Formation is at greater risk of earthquakes caused by fracking. Probabilistic maps of fault stability can provide a basis for future fluid injection projects, such as wastewater disposal, hydraulic fracture stimulation, CO_2 storage, and geothermal energy extraction.

Acknowledgements

My time at Waterloo has been filled with a number of rewarding experiences, and I am grateful to those who have contributed to my academic and personal growth. First and foremost, I would like to express my gratitude to Maurice Dusseault and Yuri Leonenko for allowing me to pursue my academic interests, and for their scientific knowledge and insight. I am grateful to have both of you available to me whenever I require assistance. I would like to thank Catherine Hickson for having allowed me to participate in the Alberta No. 1 geothermal project. In appreciation of Alireza Dehghani Sanij's scientific discourse and his wise advice, I would like to thank him. I am grateful for Bijan Mahbaz's support as a brother; I appreciate your constant availability to me whenever I need you. I would also like to thank the members of my committee for their guidance, suggestions, and comments.

I would like to acknowledge geoLOGIC systems ltd. for their contribution of the geoSCOUT™ data and software. Several part of my Ph.D. program research would not have been possible without geoSCOUT™ data. As well, I would like to thank MITACS as well as Terrapin Geothermics for providing me with the opportunity to benefit from the support provided by Alberta's No.1 geothermal project.

It would not have been as enjoyable for me to complete my Ph.D. program during the Coronavirus pandemic without the assistance of a few individuals. I would like to thank Alireza Dehgan Sanji, Bijan and his wife Roja, Farid Fallhai, Max Salman, Mehdi Mahmoudi, Mohammad Roostaie, and Mohammad Rouhi, Reza Valiollahi, and Rouzbeh Rahami.

I would like to express my gratitude and appreciation to my parents, sisters, brother, niece, and nephews for their love and emotional support over my life. Love to all of you.

Table of Contents

List of Figures xi
List of Tables xvi
CHAPTER 1 1
Introduction 1
1.1 Overview and motivation 2
1.1 Thesis outline 4
CHAPTER 2 7
Methodology and Background 7
2.1 Stress Field and Faulting Systems 7
2.1.1 Constraining the Stress Orientation 8
2.1.2 Constraining Stress Magnitude 11
2.2 Probabilistic Assessment of Fault Slip 12
2.3 Summary 16
CHAPTER 3 17
Seismicity and the State of Stress in the Dezful Embayment, Zagros Fold and Thrust Belt 17
3.1 Introduction 18
3.2 Regional Tectonic Setting 19
3.3 Dezful Embayment Stratigraphy 21
3.4 Data Collection 21
3.5 Constraining the state of stress from borehole data 22
3.5.1 Methodology 22
3.5.2 Stress Orientation 23
3.5.3 Stress Magnitude 27
3.6 State of the Stress from Earthquake Focal Mechanisms 31
3.6.1 Methodology 32
3.6.2 Stress Orientation 32
3.6.3 Relative Stress Magnitudes and Style of Faulting 33
3.7 Seismicity and State of Stress 33
3.8 Discussion 40
3.9 Conclusions 41
CHAPTER 4 42
Stress Variation around the Balarud Lineament in the Zagros Fold and Thrust Belt and its Implication for Reservoir Geomechanics 42
4.1 Introduction 43
4.2 Regional Tectonic Setting 44
4.3 Stress Orientation around Balarud Lineament 46

4.4 Balarud Fault Plane Identification 48
4.5 Stress Reorientation 50
4.6 Wellbore Stability in the Northern DE's Hydrocarbon Fields 54
4.7 Conclusion: 57
CHAPTER 5 58
Probabilistic Injection-Induced Fault Slip Assessment in Fox Creek Alberta 58
5.1 Introduction 58
5.2 Seismicity in Fox Creek 59
5.3 State of Stress in Fox Creek 62
5.4 Faults in Fox Creek 63
5.5 Probabilistic Fault Slip Assessment 64
5.6 Conclusions 68
CHAPTER 6 69
Injection-Induced Fault Slip Assessment in Montney Formation in Western Canada 69
6.1 Introduction 70
6.2 State of Stress in the Montney Formation 74
6.3 Pre-existing Faults in the Region 81
6.4 Assessment of Fault-Slip Potential 82
6.5 Discussion 84
6.6 Conclusions 87
CHAPTER 7 89
Injection- Induced Seismicity assessment at the Alberta No. 1 Geothermal Project site 89
7.1 Introduction 90
7.2 Geology Setting 92
7.3 Seismicity in the Region 95
7.4 Pre-existing Faults in Grande Prairie 96
7.5 State of Stress around Grande Prairie 97
7.6 Assessment of Fault-Slip Potential 102
7.7 Discussion 106
7.8 Conclusion 108
CHAPTER 8 109
Conclusions and Recommendations: 109
8.1 Publications 109
8.1.1 Refereed Publications: 109
8.1.2 Conference Publications 109
8.2 Conclusions 110
8.3 Recommendations 112

Bibliography 114
Appendices 125
Appendix A 125
Appendix B 139

List of Figures

Figure 2-1: a) Stress tensor components in three dimensions in an arbitrary cartesian coordinate system where Sxx, Syy, and Szz are normal stresses, and Sxy, Sxz, Syx, Syz, Szx, and Szy are shear stresses. b) In the principal coordinate system, all shear stresses disappear, and only normal components of the stress tensor remain. Stress tensors at depth can be defined in terms of three magnitudes, S_1, S_2, and S_2, as well as their orientations. 8

Figure 2-2: a) Variation of circumferential effective stress around a vertical borehole when S_{Hmax} azimuth is 45°. b) An ultrasonic image log with caliper log and borehole shape measurements of a vertical well in the Dezful Embayment demonstrates borehole breakout failure. (c) An ultrasonic image log showing axial drilling-induced tensile fractures in a Dezful Embayment vertical well section (note that the azimuthal positioning of the images are different). 10

Figure 2-3: Color-coded stress polygons according to Aφvalues in normal faulting (NF), in strike-slip faulting (SS) and in reverse faulting (RF). 12

Figure 2-4: An example of three-dimensional Mohr diagram with two representative fault planes. When the ratio of shear to normal effective stress acting on the fault surface exceeds the failure criterion line ($\tau\mu\sigma n \geq 1$), the fault is deemed frictionally unstable or critically stressed. An illustration of how a frictionally stable fault may become critically stressed as a result of fluid injection is shown by the blue arrows. As indicated by the green error bar, there are uncertainties associated with three principal stress magnitudes that affect the stability of faults and fractures. Furthermore, as is usual practice in these assessments, poroelastic effects within the surrounding rock mass are not considered. 13

Figure 2-5: The minimum stress gradient in the Watt Mountain Formation derived from DFIT. The red curve represents the fit od a Gaussian distribution with mean of 20.9 MPa and standard deviation of 1.9 MPa. 15

Figure 2-6: A graphical representation of the likelihood of fault slip, $P\ \tau - \mu\sigma n \leq 0$. The distribution of shear and normal stresses acting on an example fault after n number of realizations. The shaded area is the probability of fault slip. 16

Figure 3-1: Topographic, structural and seismicity map of Zagros Fold and Thrust Belt along with locations of hydrocarbon fields (green oval shapes). Colored circles are IRCS-recorded earthquake centroid depths between 2010 and 2020. Details of each earthquake are provided Yaghoubi (2020). The bottom left histogram shows the depth (km) distribution of earthquakes. Red triangles denote the location of the 25 wells investigated in this study. A-A′ and B-B′ are cross-sections of the seismicity and topography shown in Figure 3-5. Fault traces (the solid black lines) are inferred and compiled from (Berberian, 1995) and (Talebian and Jackson, 2004). The white lines show the main structural subdivisions of the ZFTB. Major Active Faults are the HZF, High Zagros Fault; KZ, Kazerun Fault System; MFF, Mountain Front Fault; MRF, Main Recent Fault; MZRF, Main Zagros Reverse Fault; ZFF, Zagros Foredeep Fault; BL, Balarud Fault. 20

Figure 3-2: Examples of a) borehole breakout in the E-W direction in vertical well CK-8 in the Cheshmeh-khush oil field (3460 m) and b) tensile induced fracture in NE-SW direction in vertical well KH-5 in the Khesht oil field (2880 m), and c) one in the N-S direct in vertical well P-2 in the Paydar oil field (3210 m). Note that for c) the image started from the west (W) side of the borehole to better show two axial induced fractures at θ=0° and θ=180°. 24

Figure 3-3:UBI log of borehole breakouts in vertical well P-7 in the Paydar Field at a depth between 3925-4130 m; b) and c) rose diagram and histogram showing that the frequency of observed borehole breakout azimuth in well P-7 (S_{hmin} direction) is 100°±5.7°. 25

Figure 3-4: a) Example of stress concentration around a vertical borehole and the location of borehole breakout and tensile induced fracture and their relation to principal stress orientations; b) range of possible stress magnitudes (stress polygon) for horizontal principal stress at a depth of 3.5 km where Pp = 35 MPa, and S_v = 87.5 MPa; c) and d) rock strength required to initiate a breakout in normal and reverse faulting regimes in the

Sarvak and Asmari formations of the Dezful Embayment, assuming that the stresses at the limit are constrained by a friction coefficient where μ = 0.6, Pp = 10 MPa/km, and S_v = 25 MPa/km. The color bar for each case shows the rock strength needed to prevent borehole breakout in vertical boreholes. The Mohr-Coulomb failure criterion and Kirsch equations were used in these calculations. 30

Figure 3-5: Cross-sections of Dezful Embayment displaying topography and seismicity in A-A' and B-B' sections shown in Figure 3-1. The color scale represents earthquake magnitudes. The high seismicity density in the area is restricted to below 5 km. The inset is an upper view of the cross-section profile (red dash line) and its nearby seismicity shown in Figure 3-1. Details of each earthquake are provided in Yaghoubi (2020)..... 31

Figure 3-6: a) Map view of the value of 108 interpreted focal mechanisms in the Dezful Embayment. Colors show the stress regimes, with Aϕ values ranging from 0 to 1.0 for normal faulting, 1.0 to 2.0 for strike-slip faulting, 2.0 to 3.0 for reverse faulting. Red and black lines indicate the orientation of S_{Hmax} for individual focal earthquakes (P-Axis) and formal stress inversion respectively. Blue inward arrows show the S_{Hmax} direction derived from borehole breakouts and induced tensile fractures of A quality (Table 3.1). b) interpreted focal mechanism in southern Dezful Embayment (inset 2); c) histogram of Aϕ value from the inversion of 108 focal mechanisms using Simpson (1997) approach. Light blue arrow is GPS velocity vectors relative to central Iran derived from Walpersdorf *et al.* (2006). The greatest concentration of earthquakes is around the Balarud fault in the northern part of the embayment (inset 1)..... 36

Figure 3-7: a) 3D Mohr's circle showing representative reverse focal mechanism and resolved shear and normal stresses for each nodal plane. The color inside the beach ball represents $A\varphi = 2.16$ and is based on the color bar shown in Figure 3-6. b) Lower hemisphere stereonet plot of the preferred nodal plane for 92 focal mechanisms in the Dezful Embayment where the state of stress is a thrust-faulting regime. Colors show the ratio of shear to effective normal stresses (required μ) needed for shear failure on a fault plane..... 36

Figure 3-8: a) Earthquake focal mechanisms in the vicinity of the N-S Kazerun transverse active fault. The state of stress changes from strike-slip faulting around the fault to a reverse faulting regime on either side, whereas the seismologically (red line) determined azimuth S_{Hmax} (P-Axis) is stable and uniform around the area. b) 3D Mohr's circle showing a representative strike-slip focal mechanism and resolved shear and normal stresses for each nodal plane. The red line on the focal beach-ball indicates the actual fault plane. c) Lower hemisphere stereonet plot illustrates the slip-tendency (ratio of resolved shear to normal stress) for strike-slip faulting regime nearby Kazerun Fault System and actual nodal plane for 12 fault plane solutions mapped in (a)..... 38

Figure 3-9: Large-scale faults examined in slip tendency analysis, in terms of $\tau\sigma n$ for the normal state of stress in the sedimentary cover of Dezful Embayment. Black circles represent earthquakes at a depth above 6 km with M_W=>4 in the area since 2010. The lower left inset illustrates 3D Mohr diagram frictional slip stability assigned for the slip tendency analysis..... 39

Figure 4-1: Stress Map of Dezful Embayment in ZFTB as determined from drilling-induced wellbore failures and earthquake focal mechanisms. The red lines with a dot in the center are seismologically determined S_{Hmax} (P-Axis) orientations. The heavy black arrows also indicate the orientation of S_{Hmax} derived from formal stress inversion (Yaghoubi *et al.*, 2021). The blue inward arrows are S_{Hmax} orientations (quality ranking A) obtained from borehole breakout and drilling-induced tensile fractures in vertical wells. Solid black lines represent fault traces inferred and compiled from Berberian (1995) and Talebian and Jackson (2004), where KF represents the Kazerun Fault. 45

Figure 4-2: Topographic, structural and seismicity map of Balarud Lineament along with hydrocarbon fields. Each circle denotes a seismic event that occurred in the area between 2010 and 2020 (Iranian Seismological Centre catalog). Fault traces, the black lines in the background, are compiled from Berberian (1995) and Talebian & Jackson (2004). Major active faults are the HZF, High Zagros Fault; MFF, Mountain Front Fault; BL, Balarud Lineament. 46

Figure 4-3: Map view of the value of Twenty-five interpreted focal mechanisms in the vicinity of BL. Colors show the stress regimes with Aφ ranging from 0.0 to 1.0 for normal faulting, 1.0 to 2.0 for strike-slip faulting, 2.0 to 3.0 for reverse faulting. Red and black lines indicate the orientation of S_{Hmax} for individual focal

earthquakes and formal stress inversion respectively. Blue inward arrows show the S_{Hmax} direction derived from borehole breakouts and induced tensile fractures of A quality. 49

Figure 4-4: 3D Mohr's circle showing representative reverse focal plane mechanism and resolved shear and normal stresses for preferred (red circle point) and auxiliary planes (black circle point). 50

Figure 4-5: Strike and dip of the preferred (a) and the conjugate (b) nodal planes for 22 earthquake plane mechanisms. Both the preferred and conjugate nodal planes have almost the same strike (~300° or 120°); however, the preferred dip angle (34.1°±10.8°) is less the conjugate one (60°±10.3°). 51

Figure 4-6: Schematic illustration of stress rotation due to local uniaxial stress: a) reference coordinate system in which the S_{Hmax} is the direction of X, b) local coordinate system where X' is aligned with the fault strike, and c) the resultant state of stress. The assumption is one principal stress that is assumed to be vertical (modified from Sonder (1990)) 52

Figure 4-7: S_{Hmax} rotation as a function of the angle between local uniaxial stresses and regional maximum horizontal stresses around the Balarud Lineament. Colors represent the ratio of regional horizontal stress to the magnitude of local uniaxial stress (equation 4). The red and blue boxes indicate the possible stress variations (θ and Υ) due to the Balarud Lineament at seismogenic depths and the sedimentary cover, respectively. The inset is stress rotation (blue axes) from the reference stress (red axes) nearby the Balarud Lineament at shallow depths. 54

Figure 4-8: Required mud pressure to prevent borehole breakout in in arbitrarily oriented wells at depth of 4018m (Sarvak Formation), where Sv=S_{Hmax}=105 MPa, S_{hmin}=70 MPa, Pp=41MPa, and UCS=120 MPa. 56

Figure 5-1: Cumulative number of earthquakes with Mw>2.5 around Fox Creek, Alberta, showing a rapid increase since 2012 60

Figure 5-2: a) Cumulative fluid injection along with 115 induced earthquakes by magnitude through time in one multistage well in Fox Creek. b) Histogram showing the depth distribution of the local seismicity induced by 12.04×10^4 m3 fluid injection 61

Figure 5-3: Gutenberg-Richter frequency-magnitude distribution of 1087 earthquakes recorded during multistage HF in Fox Creek 61

Figure 5-4: a) Seismicity around Fox Creek, Alberta. White circles represent earthquakes recorded in the area. The eleven interpreted focal mechanisms are compiled from Schultz et al. (2017), b) 3D Mohr's circle showing representative strike-slip earthquake focal (M_w=3, 2015-08-19) (Pp=60 MPa and μ=0.65). 65

Figure 5-5: a) Relation between fault patch size and M_w (Moment magnitude). The straight lines give the relations for fault with two constant stress drops 0.1 and 10 MPa. Colors show the amount of fault slip corresponding to M_w and fault size. The black points represent eleven focal earthquakes displayed in Figure 5-4a. The color bar is a log10 base scale. 66

Figure 5-6: Lower hemisphere stereonet plot illustrates the deterministic approach to the slip-tendency (critical injection pressure) 66

Figure 5-7: Statistical Mohr-Coulomb variables used in Monte Carlo simulation. 67

Figure 5-8: a) 3D Mohr's circle showing reactivated fault (red points) and stable faults (black points) b) injection pressure required to cause slip for one fault segment and c) Cumulative probability function of the injection pressure required to cause slip. Each curve represents one fault segment 68

Figure 6-1: Cumulative number of earthquakes with Mw >3 within areas 52°N to 60°N and 114°W to 126°W in Western Canada, indicating a rapid increase in the last decade. 71

Figure 6-2: a) Approximately 8.2×10^5 m^3 of fluid have been injected in 16 wells in the Kiskatinaw area, resulting in 617 earthquakes, including event M_W 4.6 on August 17, 2015. b) Map showing the distribution of local seismicity (colored circles) and the locations of the 16 wells (green triangles). Color bars indicate the magnitude of the earthquake. 72

Figure 6-3: Seismicity, fault traces, HF wells in the Montney Formation. The dashed line defines the Montney Formation area. The colored circles are seismicity reported by Visser *et al.* (2017) and Visser *et al.* (2020). Not all these earthquakes are within the Montney Formation; the colored circles outside of the area of the Montney Formation are natural tectonic earthquakes. The earthquakes around Fox Creek have resulted from HF in the Duvernay Formation and wastewater disposal near Musreau Lake (event M_L 3.94) (Li *et al.*, 2021). Grey thick lines are the main faults in the studied area. Black dots show wells drilled into the Montney Formation. Geographical locations of seismic stations are indicated by yellow triangles (Schultz and Stern, 2015). The focal mechanism events represent some major earthquakes recorded in the area. 75

Figure 6-4: Spatial pore pressure gradient values in the Montney Formation. Extremely low Pp (5 MPa/km) are observed around Peace River and Grande Prairie where less seismicity has been recorded. Pore pressure gradients are highest (15 MPa/km) in the areas around Fort St. John and Dawson Creek. The western parts of the formation have relatively higher pore pressure values and gradients than the eastern parts. Gray lines indicate faults crossing one another in the Montney play. The white dashes show the zoning of the Montney Formation based on pore pressure gradients at various locations. Each zone is represented by a mean pore pressure value (Pp) and a standard deviation (Std)..... 76

Figure 6-5: Map of S_{hmin} gradients in the Montney Formation. The data have been extracted from geoLOGIC™ systems. The black arrows, extracted from World Stress Map datasets (Heidbach *et al.*, 2018), represent the maximum horizontal principal stress (S_{Hmax}) orientation (inset rose diagram). Beachballs present large-magnitude injection-induced focal mechanisms recorded in the studied area. 80

Figure 6-6: The Mohr-Coulomb shear failure criterion (the diagonal line), Mohr's circles representing and a representative strike-slip earthquake focal mechanism (M_w=4.6, 2018-11-30). The red line on the focal beach ball indicates the actual fault plane..... 82

Figure 6-7: The cumulative probability function of the required injection pressure to cause slip on faults located in stress area 4. The histogram presents the pore pressure distribution in the stress area 4. Each curve represents the cumulative probability function of slip on each fault segment. The difference between current injection pressure and mean Pp distribution is 2 MPa. The depth of injection is assumed to be 2.5 km..... 84

Figure 6-8: Fault map color-coded to highlight the probability of slip in the Montney Formation. Black points represent wells that were hydraulically stimulated. The red circles are seismicity reported by Visser *et al.* (2017) and Visser *et al.* (2020)..... 85

Figure 6-9: a) The Mohr-Coulomb shear failure criterion (the diagonal line) and 3D Mohr's circle, depicting the reverse focal mechanism and resolved normal and shear stresses for each nodal plane. (b) Lower hemisphere stereonet plot for the case that state of stress is reverse faulting regime. Colors show the ratio of shear to effective normal stresses (required μ) needed for shear failure on a fault plane. In a reverse faulting regime, faults dipping from 15° to 60° and striking northwest to southeast are critically stressed. 87

Figure 7-1: The location of Alberta No. 1 geothermal project (red box). Black circles represent earthquakes reported in the area. The blue arrows, extracted from World Stress Map datasets (Heidbach *et al.*, 2018), represent the maximum horizontal principal stress (S_{Hmax}) orientation. Grey thick lines are the main faults in the studied area. The green triangles represent the locations of seismic stations. Details of the seismic stations are provided in Stern *et al.* (2011) Table 1. The strike-slip focal mechanism events represent major induced earthquakes recorded in the area..... 92

Figure 7-2: Stratigraphic column and table of formations in the Alberta No. 1 geothermal project in Grande Prairie in Northwest Alberta (modified from Alberta Geological Survey (2019). The vector version of this figure can be found in the supplementary information or online at https://ags.aer.ca/publication/alberta-table-formations..... 94

Figure 7-3: Top of the (a) Leduc and (b) Granite Wash Formations as seen in drilled wells in the region. Black lines are the main faults in the studied area. Seismic stations are indicated by black triangles..... 95

Figure 7-4: A top view of 706 HF wells drilled in the Grande Prairie area. The majority of these wells were drilled into the Montney and Duverney formations. The area in this figure is represented by a red square in Figure 1 98

Figure 7-5: 706 HF wells in the Grande Prairie region have been injected around 9×10^6 m^3, yet no major injection-induced seismicity has been reported in the area. 98

Figure 7-6: Pore pressure (Pp) gradient in the Leduc Formation from drilled wells in a) WCSB and b) around Grande Prairie. Pp gradient frequency in c) WCSB and d) around Grande Prairie are shown in the histogram. Each point represents the location of the well and the color display represents the Pp gradient. High pore pressure was observed around Fox Creek. Black triangles indicate seismic stations. 100

Figure 7-7: Pore pressure gradient for the Granite Wash Formation from drilled wells in a) WCSB and b) around Grande Prairie. Pp gradient frequency in c) WCSB and d) around Grande Prairie are shown in the histogram. Each point represents the location of the well and the color display Pp gradient. Black triangles indicate seismic stations. 101

Figure 7-8: The minimum stress gradient in Muskeg and Watt Mountain formations derived from DFIT..... 101

Figure 7-9: A stereonet plot illustrating the slip-tendency (ratio of resolved shear stress to normal stress) around Grande Prairie in the strike-slip faulting regime. 103

Figure 7-10: Statistics used in Monte Carlo simulations of fault slip around Grande Prairie. It is assumed that pore pressure and principal stress magnitudes in both target formations follow the Gaussian distribution 104

Figure 7-11: a) 3D Mohr diagram presenting principal stress magnitudes acting on known faults located in the Grande Prairie area. b) The cumulative probability function of the required injection pressure to cause slip on each fault segment patch. Note that the injection depth is assumed to be 4 km. 105

Figure 7-12: Map of faults in the Grande Prairie region colored according to the probability of slip. The red circles represent seismicity reported by Visser et al. (2017) and Visser et al. (2020). Fox Creek earthquakes were caused by HF in the Duvernay Formation, where the Pp gradient is 18 MPa/km. 106

Figure 7-13: Required injection pressures for fault reactivation in the Grande Prairie region. Faults are color-coded according to the critical pore pressure that would cause them to slip. 107

List of Tables

Table 3-1: S_{Hmax} orientations derived from both borehole breakout (BO) and drilling induced fracture (DIF) in the different fields of the Dezful Embayment (S.D, standard deviation). S_{Hmax} orientations are ranked from A to D according to the World Stress Map (WSM) quality ranking system. 25

Table 3-2: Summary of the leak-off test results reported for the Dezful Embayment. 27

Table 3-3: Stress inversion results at different locations in the Dezful Embayment. 33

Table 4-1: Stress inversion results around the Balarud Lineament and the rest of the DE. 48

Table 4-2: Detailed information on sidetracks of well PY-7. 56

Table 6-1: $S_{hmin.}$ S_v and S_{Hmax} and fault properties statistical measures are used in Monte Carlo Simulation for each stress area. The number of earthquakes reported by Visser et al. (2017 and 2020) represents the number of occurrences in each stress area. 81

CHAPTER 1

Introduction

Knowledge of the earth's current state of stress at depth is a key component of a wide range of subsurface projects at various scales, from seismology subjects (Hauksson, 1994; Levandowski et al., 2018) to reservoir geomechanics studies (Dusseault, 2011; Zoback, 2007). Among the applications of understanding tectonic stress variation at depth is the optimization and execution of underground fluid injection projects (Barton et al., 1988; Dusseault, 1977; Moeck et al., 2009; Rutqvist, 2012; Valley and Evans, 2019). This is of particular importance since the injection (and withdrawal) of fluids within the subsurface can result in earthquakes. (Frohlich et al., 2014; Hojka et al., 1993; McClure and Horne, 2011; McGarr, 2014; McGarr et al., 2002; Weingarten et al., 2015; Yu et al., 2021a; Zoback and Harjes, 1997). There have been a number of large injection-induced earthquakes in various parts of the world that have been caused by fluid injection projects such as wastewater disposal, geothermal energy development, carbon dioxide sequestration, and hydrocarbon extraction (Atkinson et al., 2016; Atkinson et al., 2020; Bao and Eaton, 2016; Dusseault, 1977; Frohlich et al., 2014; Ghofrani and Atkinson, 2020; Johann et al., 2018; Kaven et al., 2014; Mukuhira et al., 2013; Ries et al., 2020; Schultz et al., 2017; Zang et al., 2014). In British Columbia and Alberta, there have been several recent injection-induced earthquakes that have caused considerable concern among the public, including those near Fort St. John and Fox Creek (Atkinson et al., 2016; Atkinson et al., 2020; Bao and Eaton, 2016; Eaton and Schultz, 2018; Ghofrani and Atkinson, 2020). Induced seismicity is therefore of concern to the technical management of projects that involve fluid perturbations within the subsurface of the western Canadian region, as well as other regions in the world.

There have been a number of studies conducted to determine what mechanisms are responsible for wide spread injection-induced seismicity in western Canada and what parameters control it (Enlighten Geoscience Ltd., 2021; Hayes et al., 2020; Konstantinovskaya et al., 2021; Peña Castro et al., 2020; Schultz et al., 2017; Wozniakowska and Eaton, 2020; Zhang et al., 2019). The magnitude and rate of anthropogenic earthquakes are influenced by two sets of field parameters: extrinsic parameters that can be controlled, such as fluid injection pressure (Walsh III and Zoback, 2016), rate (Weingarten et al., 2015), viscosity (Cornelio et al., 2020), volume (McGarr, 2014), and type (Ries et al., 2020); and,

the intrinsic uncontrollable subsurface parameters, including stress state (Hennings et al., 2019) and pore pressure (Eaton and Schultz, 2018), size and density of pre-existing faults/fractures (Yaghoubi, 2019), fault/fracture orientation (Yaghoubi, 2019) and frictional strength, steady-state coefficient of friction (Kohli and Zoback, 2013) and rock's permeability and compressibility (Chang and Yoon, 2022). However, wide inherent uncertainty affects the value of each uncontrollable parameter. In HF treatments, accounting for parametric uncertainty by using appropriate probability distributions (Morris et al., 2021; Walsh III and Zoback, 2016) leads to better decision-making for user-controlled parameters such as injection pressure. Probabilistic fault slip assessment is a useful quantitative approach to improve understanding of seismic hazards in the Western Canada Sedimentary Basin region. This is of importance because of the recent large-scale injection-induced earthquakes, and because no studies on such a scale have been presented for this region. Induced seismicity studies have been performed in Fox Creek, Alberta (Shen et al., 2019b), north-central Oklahoma (Walsh III and Zoback, 2016), the Fort Worth Basin (Hennings et al., 2019), and the Delaware Basin in Texas (Morris et al., 2021). This dissertation aims to determine the state of stress at depth and apply the results to the assessment of injection-induced seismicity.

1.1 Overview and motivation

There are two main objectives in this thesis, which are addressed in five central chapters. This dissertation has as its primary objective to determine the tectonic state of stress using drilling-induced wellbore failures and earthquake focal mechanisms. As an important secondary objective, this dissertation also aims to use stress and pressure data to perform a probabilistic analysis of injection-induced fault slip in unconventional and geothermal resource development. Several studies have been conducted at various locations in order to achieve the main objectives of this thesis, including:

The tectonic state of stress in:

- The Dezful Embayment, Zagros Fold and Thrust Belt (ZFTB) of Iran (Chapters 3 and 4),
- Duvernay Formation in Fox Creek, Alberta (Chapter 5),
- Montney Formation in Western Canada (Chapter 6),
- The Alberta No. 1 Geothermal Project site (Chapter 7).

Injection-induced fault slip assessment in:

- Duvernay Formation in Fox Creek, Alberta (Chapter 5),
- Montney Formation in Western Canada (Chapter 6),
- The Alberta No. 1 Geothermal Project site (Chapter 7).

In this dissertation, the Dezful Embayment in the ZFTB, as well as some formations and locations in Western Canadian Sedimentary Basin (WCSB), were selected as case studies due to their economic importance and seismic activity. The ZFTB region of southwest Iran is one of the world's most seismically active areas, registering more than 5000 earthquakes of $M_W \geq 3$ between January 1, 2010, and January 1, 2020. The Dezful Embayment is also one of the world's richest hydrocarbon regions, containing about 9% of global hydrocarbon resources. Similarly, western Canada contains some of the world's largest reserves of natural gas and petroleum, including the resources found in the Duverney and Montney Formations' shale gas strata. The Alberta's No. 1 geothermal project, the province's first proposed conventional geothermal electrical energy project, is also located in this region. Additionally, some of the induced earthquakes reported in Alberta and British Columbia during oil and gas operations (hydraulic stimulation, waterflooding, depletion), such as those near Fort St. John in British Columbia and Fox Creek in Alberta, have registered M_W values among the highest reported worldwide.

Even though the ZFTB and Western Canada are quite different regions, the geomechanical analyses applied to them are governed by similar principles. Defining the stress state for the area of interest is an important component of a comprehensive geomechanical model. To achieve this, it is necessary to constrain both the magnitude and orientation of each of the three principal stresses, as well as the formation pore pressure. To assess the state of stress in the region, two datasets are employed: one contains petrophysical data obtained from oil and gas wells, and the other contains focal mechanisms of natural or anthropogenic earthquakes. Identifying pre-existing faults is a second component of a complete geomechanical model; this involves determining the fault orientation, dip and frictional strength. Finally, Coulomb faulting theory (the Mohr-Coulomb slip criterion) is then used to calculate the fault slip probability within the stress field. In different regions, this process has been conducted to address the following motivational questions:

- What is the relationship between seismicity and the tectonic stress field in the ZFTB?
- Why does the S_{Hmax} direction derived from borehole data at depths of 3-4 kilometers differ from the seismologically determined one at the basement depth in the ZFTB area? How do such stress deflections in sedimentary cover affect reservoir geomechanics projects?
- Why do strike-slip earthquakes occur along the N-S Kazerun Fault System within ZFTB, a tectonic setting for a thrust/reverse faulting regime?
- What are the key parameters associated with injection-induced seismicity in western Canada?
- What is the likelihood of fault slip as a result of fluid injection into the Montney Formation?

- Is it possible to identify problematic active faults prior to fluid injection projects such as hydraulic fracturing stimulation or geothermal energy extraction projects?

The next section presents an outline of each chapter of this thesis as well as a general response to each of the questions raised above.

1.1 Thesis outline

This dissertation consists of seven chapters. In addition to this Introduction and *Chapter 2*, which provides a background on the methodology, five other chapters discuss the methodologies and results generated in pursuing the dissertation's objectives. *Chapters 3* and *4* discuss the stress state in the Dezful Embayment, *Chapters 5* and *6* address stimulation-induced earthquakes in western Canada, and *Chapter 7* involves the assessment of fault slip potential due to fluid injection in the Alberta No 1 geothermal project site.

Chapter 3 focuses on determining the orientation and constraining the magnitude of present-day stresses in the Dezful Embayment in Iran's ZFTB. The area, one of the richest hydrocarbon regions in the world, is also one of Earth's most seismologically active areas. To accomplish this objective, I used petrophysical data at depths of 3 to 4 km in oil and gas boreholes, as well as deeper earthquake focal mechanisms located along blind active basement faults at depths of 5 to 20 km. I address the influence of tectonic stress variations at different depths on seismicity patterns in the study area. The stress state situation in the field was used to identify the optimally oriented fault planes and constrain the value of the fault friction coefficient. By using the field stress state, I identified the optimally oriented fault planes and the fault friction coefficient, and I explained why the N-S Kazerun Fault System has an unfavorable orientation for slip in a reverse fault regime with an average SW-NE S_{Hmax} orientation.

Chapter 4 examines horizontal stress variations near the deep-seated Balarud Lineament in the northern part of the ZFTB. Throughout this chapter, I discuss why sedimentary rock strata and basement rock exhibit entirely different types of stress orientations around the Balarud Fault Zone. In the basement, from earthquake data, I observed constant regional S_{Hmax} orientation in the NE-SW direction in the northern ZFTB. However, tensile-induced fractures and borehole breakouts in shallower oil and gas wells indicate that the dominant S_{Hmax} orientation near the Balarud Lineament is N-S. There are several significant parameters that can be used to measure the deviation of local stress orientation. These include the magnitude of local stresses compared to regional stresses, along with the angle between local structures and regional stress orientations. The consistent stress direction in the basement indicates a high differential horizontal stress magnitude, whereas the principal stress orientation rotates counterclockwise in the sedimentary cover where the state of stress is extensional. Finally, I examine the impact of the second-order stress pattern around the Lineament on wellbore placement and completion.

In *Chapters 5* and *6*, I develop and employ a probabilistic approach for assessing the slip tendency of faults crossing the Duvernay Formation near Fox Creek, Alberta, as well as the compartmentalized Montney Formation of western Alberta and northeastern British Columbia. There has been a significant increase in seismic activity in the previously quiescent Fox Creek, Alberta, and Fort St John, British Columbia, areas in recent years. More than 200 $M_W > 2.5$ earthquakes around Fox Creek are associated with hydraulic stimulation operations; the largest events include ones of M_W 4.1 on January 12, 2016, and M_W 3.9 on June 13, 2016. Both case studies include an assessment and discussion of the current stress state as an input to the probabilistic assessment of fault slip. To calculate the associated seismic risk due to fluid injection, the uncertainties associated with the stress tensor, the fault/fracture orientation, and the faults' frictional strength (Mohr-Coulomb parameters) must be incorporated in the evaluation process.

In *Chapter 6*, a probabilistic approach is used to assess the slip tendency of known faults crossing the compartmentalized Montney Formation of western Alberta and northeastern British Columbia. I first divide the Montney Formation into four different stress areas based on pore pressure deviations from hydrostatic. In each stress area, geomechanics parameters are expressed as probability distributions using multivariate datasets from borehole petrophysical data and injection-induced focal mechanisms. A Monte Carlo simulation approach is applied to assess the potential slip tendency of local faults. I display the cumulative distribution function of critical pore pressure needed to cause slip on each fault by using analyses of the Mohr-Coulomb shear parameters and local tectonic stress state. The results provide useful input for seismic hazard assessment and risk mitigation for local faults affected by high-rate fluid injection. I present a map that can be used to predict which area of western Canada is most at risk of earthquakes caused by aggressive hydraulic stimulation.

In *Chapter 7*, I assess the possibility of injection-induced earthquakes arising during geothermal energy extraction in the central parts of the Western Canada Sedimentary Basin. Alberta No.1 is a potential geothermal project located in the Municipal District of Greenview, south of Grande Prairie, Alberta, Canada, that targets carbonates, conglomerates, and sandstone formations. The project owners are concerned about anthropogenic seismicity from oil, gas, and well field fluid injection. An analysis of the geomechanical properties of the Leduc and Granite Wash formations, two potential injection/production zones for geothermal energy, has been conducted based on borehole geophysics and injection-induced earthquake focal mechanisms. Geomechanical analysis results with associated uncertainties are used to assess the potential for injection-induced seismicity. A Monte Carlo probability analysis is employed to estimate the likelihood of slippage of the known faults close to the Alberta No.1 Geothermal Project site.

In summary, *Chapters 3 to 7* contain novel results related to determination and interpretation of stress state in the earth and the potential for induced seismicity arising from human activity related to

well stimulation and geothermal energy development. These novel results are of practical value to engineers and geoscientists planning projects.

CHAPTER 2

Methodology and Background

2.1 Stress Field and Faulting Systems

Stress is defined as "force per unit area", and at a point in the rock mass it can be represented by a second-order tensor known as the stress tensor. The stress tensor is a 3×3 matrix consisting of nine components (six independent ones) that define the complete state of stress at a particular depth (Figure 2-1 a). There are two types of stress tensor components: normal stress components (S_{xx}, S_{yy}, and S_{zz}), which represent stresses acting perpendicular to the specified cartesian coordinate (*x*-*y*-*z*) plane (the diagonal components of stress matrix), and shear stress components (S_{xy}, S_{xz}, S_{yx}, S_{yz}, S_{zx}, and S_{zy}) which represent resolved (shear) stresses acting parallel to the specified cartesian coordinate plane (the off-diagonal components of the stress matrix) (Figure 2-1a). Using tensor transformations, a stress tensor at a point in one coordinate system (x, y, z) can be evaluated in any other coordinate system (x′, y′, z′) if the three angular rotations are specified. At a point, the unique orientation of coordinates in which planes perpendicular to the system are free of shear stresses is referred to as the principal coordinate system. Therefore, the stress field can also be described by three principal (normal) stresses σ_1, σ_2, and σ_3 in the principal coordinate system (Figure 2-1b), which is defined by three orientation components (direction cosines). This approach is by far the most common method of reporting earth stresses: three principal directions and three principal stresses (compression positive).

Because the surface of the Earth is a free surface (no shear stress, no normal stress), stresses are usually specified as horizontal and vertical components in the Earth's upper crust. Interpretation of earthquake focal mechanisms as well as other stress indicators generally confirm that one of the principal stresses in the Earth's upper crust (at depths to 15-20 km) is vertical or close to vertical (Heidbach *et al.*, 2016a; Zoback, 1992). Considering this, a full stress tensor at a particular depth can be specified by defining three principal stresses: vertical stress, S_v; maximum horizontal stress, S_{Hmax}; and minimum horizontal stress, S_{hmin}. In addition, the orientation of the maximum or minimum

horizontal stress must be specified. The assumption that the vertical stress is a principal stress reduces the independent components of the stress tensor from six to four.

Field stress orientation is typically displayed as a maximum horizontal principal stress orientation (S_{Hmax}). Following geophysics symbology, I use "S" to mean total stress, which at a point is the sum of the effective stress σ and the pore fluid pressure, viz.: $S_v = \sigma_v + P_p$; $S_{Hmax} = \sigma_{Hmax} + P_p$; $S_{hmin} = \sigma_{hmin} + P_p$.

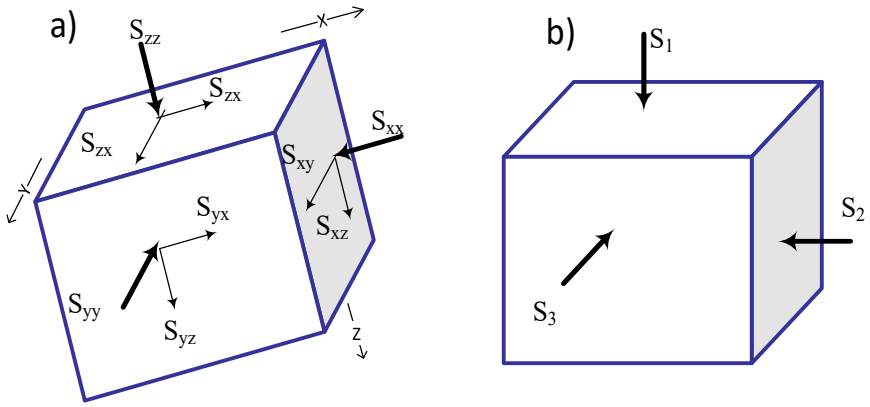

$$\begin{bmatrix} S_{xx} & S_{xy} & S_{xz} \\ S_{yz} & S_{yy} & S_{yz} \\ S_{zx} & S_{zy} & S_{zz} \end{bmatrix} \qquad \begin{bmatrix} S_1 & 0 & 0 \\ 0 & S_2 & 0 \\ 0 & 0 & S_3 \end{bmatrix}$$

Figure 2-1: a) Stress tensor components in three dimensions in an arbitrary cartesian coordinate system where S_{xx}, S_{yy}, and S_{zz} are normal stresses, and S_{xy}, S_{xz}, S_{yx}, S_{yz}, S_{zx}, and S_{zy} are shear stresses. b) In the principal coordinate system, all shear stresses disappear, and only normal components of the stress tensor remain. Stress tensors at depth can be defined in terms of three magnitudes, S_1, S_2, and S_2, as well as their orientations.

Anderson (1951) identified three general classifications of faulting regimes according to the magnitude and orientation of the three principal stresses:

1) Normal faulting regimes where $S_V > S_{Hmax} > S_{hmin}$
2) Strike slip faulting regimes where $S_{Hmax} > S_V > S_{hmin}$
3) Reverse faulting regimes where $S_{Hmax} > S_{hmin} > S_V$

The vertical stress (S_v) corresponds to the maximum principal stress (S_1) in normal faulting regimes, to the intermediate principal stress (S_2) in strike-slip faulting regimes, and to the minimum principal stress (S_3) in reverse faulting regimes.

2.1.1 Constraining the Stress Orientation

Full stress tensor at depth can be defined by defining both the magnitude and orientation of the three principal stresses: vertical stress, S_v, maximum horizontal stress, S_{Hmax}, and minimum horizontal

stress, S_{hmin}, as well as the orientation of maximum or minimum horizontal stress. Various indicators can be used to estimate or measure the horizontal principal stress orientation in the brittle crust (Heidbach *et al.*, 2016a), including:

- Borehole breakout and drilling-induced tensile fractures,
- Earthquake focal mechanisms,
- Borehole direct measurement tests including hydraulic fracture orientation, overcoring and borehole slotter, and
- Young geologic data including fault-slip analysis and volcanic vent alignments.

Throughout this dissertation, I used two available datasets to study the orientation of principal stresses in the different case studies' locations, including borehole breakout and tensile-induced fractures as well as earthquake focal mechanisms. The following is an outline of the background for these two indicators.

There are well-established techniques for determining stress orientation from borehole geometry and borehole geophysics datasets (Heidbach *et al.*, 2016b; Heidbach *et al.*, 2010; Plumb and Cox, 1987; Zoback, 2007). Drilling causes stress concentrations around the borehole wall. Kirsch's solution can be used to calculate the local stress concentrations resulting from drilling a circular hole in a homogenous infinite rock mass (Jaeger *et al.*, 2009). The stresses concentration at a vertical wellbore wall can be described as the circumferential stress ($\sigma_{\theta\theta}$), the radial stress (σ_{rr}), and the stress parallel to the wellbore wall (σ_{zz}) (Jaeger *et al.*, 2009).

$$\sigma_{\theta\theta} = S_{Hmax} + S_{hmin} - 2(S_{Hmax} - S_{hmin})\cos 2\theta - 2P_p - \Delta P \geq rock\ stength$$

$$\sigma_{zz} = S_V - 2\nu(S_{Hmax} - S_{hmin})\cos 2\theta - P_p \geq rock\ stength$$

$$\sigma_{rr} = \Delta P \qquad (2.1)$$

where S_v, S_{Hmax}, S_{hmin} are the vertical, maximum, and minimum horizontal stress magnitudes respectively; ν is the static Poisson's ratio; Pp is pore pressure, ΔP is the difference between mud pressure and pore pressure and θ indicates the angle around the wellbore from the azimuth of S_{Hmax}. In the context of Mohr-Coulomb theory and considering the Kirsch equation for a circular opening, compressive failure leading to borehole breakouts in a vertical well occur when the circumferential effective stress ($\sigma_{\theta\theta}$) or the vertical effective stress (σ_{zz}) exceeds the rock strength. Drilling-induced tensile fractures form when the circumferential effective stress ($\sigma_{\theta\theta}$) or the vertical effective stress (σ_{zz}) goes into tension. In a vertical wellbore, observation of breakouts and tensile-induced fractures proves to be an effective approach for determining the minimum and maximum horizontal principal stress orientation respectively (Barton *et al.*, 1988; Haimson and Herrick, 1989; Mastin, 1988; Nelson *et al.*, 2005; Peska and Zoback, 1995).

Figure 2.2a illustrates an example of induced circumferential effective stress caused by drilling a vertical borehole. It also displays the locations of borehole breakouts and tensile-induced fractures in relation to the minimum and maximum principal stress orientations. A borehole image log and a borehole caliper log are commonly used tools for identifying borehole shapes and detecting breakouts. To detect tensile-induced fractures, however, a detailed interpretation of the image log is required. Figures 2.2b and 2.2c illustrate borehole breakout and tensile-induced fractures that were detected in two vertical wells within the ZFTB's Dezful Embayment.

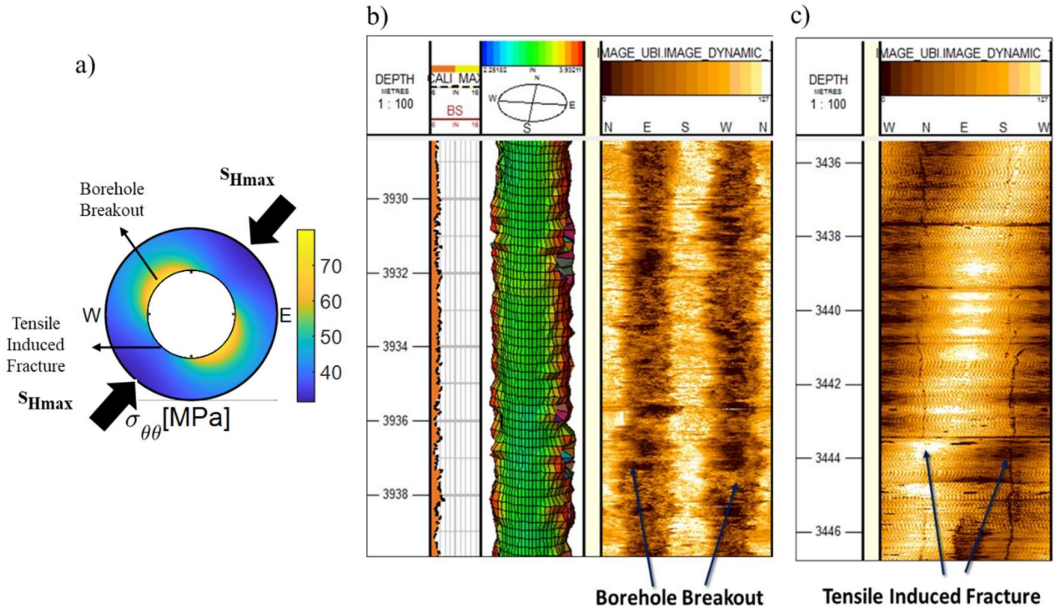

Figure 2-2: a) Variation of circumferential effective stress around a vertical borehole when S_{Hmax} azimuth is 45°. b) An ultrasonic image log with caliper log and borehole shape measurements of a vertical well in the Dezful Embayment demonstrates borehole breakout failure. (c) An ultrasonic image log showing axial drilling-induced tensile fractures in a Dezful Embayment vertical well section (note that the azimuthal positioning of the images are different).

Earthquake focal mechanisms also provide valuable information on maximum principal stress magnitudes. Assuming that S_v is one of the principal stresses, an appropriate stress regime for each earthquake focal mechanism can be assigned based on WSM criteria (Table 3, Zoback (1992)). The S_{Hmax} orientation can be determined from a single earthquake focal mechanism solution (FMS) and the formal stress inversion (FMF) of that focal mechanism. Whereas single focal mechanisms are only approximate indicators of S_{Hmax} orientation, the inversion of sets of earthquake focal mechanisms determines a best-fitting stress field and provides a more accurate estimation of principal stress orientations (Gephart and Forsyth, 1984; Michael, 1984). In this dissertation, I also conduct a formal inversion of moment tensors using MSATSI MATLAB™ code, which iteratively inverts for the stress field based on the SATSI algorithm (Hardebeck and Michael, 2006; Lund and Townend, 2007; Martínez-Garzón *et al.*, 2014).

2.1.2 Constraining Stress Magnitude

Having discussed the background of principal stress orientations, the following section discusses the three principal stress magnitudes: S_v, S_{Hmax} and S_{hmin}.

Vertical stress can be calculated (estimated) by integrating the rock density from geophysical logs from the surface to the depth of interest.

$$S_V = \int_{z=0}^{Z} \rho(z) \times g \times z \, dz, \tag{2.2}$$

where ρ is rock density, g is gravitational acceleration, and z is the depth. S_v is obtained from the typical density logs that are abundant for most drilled wells. Because of density log availability, less uncertainty is associated with the vertical stress component in stress tensors.

There are reliable methods for determining S_{hmin}'s magnitude directly, as long as vertical stress is not the minimum component of the stress tensor ($S_v > S_{hmin}$). The Leak-Off Test (Gaarenstroom, 1993), Diagnostic Fracture Injection Test (DFIT) or mini-frac (Nicholson *et al.*, 2019) and Pressure While Drilling (PWD) (Ward and Andreassen, 1997) are different methods to provide direct estimates of S_{hmin} during deep well drilling. Throughout this dissertation, only direct S_{hmin} measurements obtained through DFIT for the western Canadian cast studies have been accessed. Since direct measurements of S_{hmin} stress are not available for the Dezful Embayment region, borehole well log data were analyzed at depths 3-4 to estimate the current state of stress.

The magnitude of maximum horizontal principal stress is the most difficult parameter to quantify in a strike-slip (or thrust) stress state tensor. However, its range can be constrained by utilizing the observations of wellbore failures along with considering that the stress magnitudes are in equilibrium or close-to-equilibrium with the frictional strength of proximal pre-existing faults (Brace and Kohlstedt, 1980). Assuming that the crust is in a state of frictional failure equilibrium, The ratio of the maximum (S_1-P_P) to minimum (S_3-P_P) effective stress on an optimally oriented cohesionless fault is limited by the frictional strength:

$$(S_1 - P_p)/\,(S_3 - P_p) = \left[\sqrt{1+\mu^2} + \mu\right]^2 \tag{2.3}$$

where P_P is pore pressure and μ is the coefficient of sliding friction on a pre-existing fault (Jaeger *et al.*, 2009). Using equation 2.3, Figure 2-3 illustrates possible stress magnitudes within different stress regimes at a depth of 1 km. It has been found in laboratory studies and in-situ experiments that the magnitude of the coefficient of friction falls within the range of 0.6 to 1 (Byerlee, 1978). In this study, I have used the observation of borehole failure, information on rock strength, and the frictional strength of faults to constrain the state of stress at shallow depths in the sedimentary cover in the Dezful Embayment.

Earthquake focal mechanisms also provide valuable information on the relative stress magnitudes and maximum principal stress magnitudes. One of the parameters that can be derived from the

inversion of the focal mechanism is Angelier's shape parameter $\varphi = \frac{S_2 - S_3}{S_1 - S_3}$, in which S is the principal stress magnitude and $S_1 > S_2 > S_3$ (Angelier, 1979). Simpson (1997) generalized the parameter φ values to provide a quantitative measure with which to determine the relative stress magnitudes in each stress regime by expressing the equation as $A_\varphi = (n + 0.5) + (-1)^n(\varphi - 0.5)$ with n = 0, 1, 2, for normal, strike-slip and reverse faulting respectively. The Anderson fault parameter A_φ ranges continuously from 0 to 1 for normal, 1 to 2 for strike-slip, and 2 to 3 for reverse faults (Hurd and Zoback, 2012b; Yaghoubi *et al.*, 2021; Yang and Hauksson, 2013). A color-coded representation of A_φ within stress polygons is shown in figure 2-3. Using the natural and injection-induced earthquake focal mechanisms recorded in ZFTB and WCSB respectively, I constrain the maximum principal stress magnitudes.

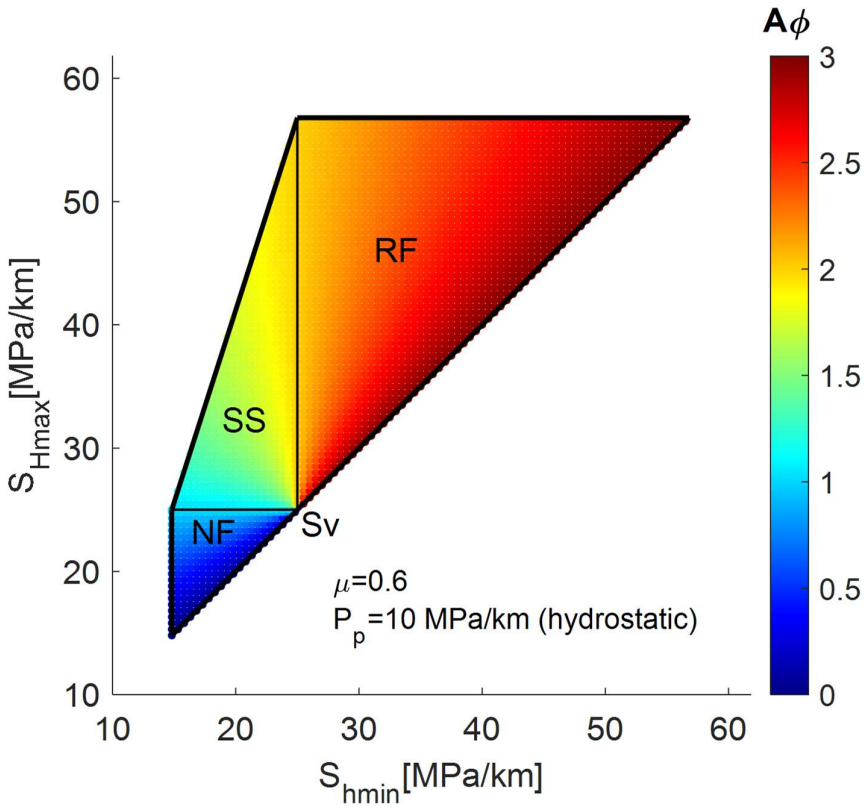

Figure 2-3: Color-coded stress polygons according to A_φ values in normal faulting (NF), in strike-slip faulting (SS) and in reverse faulting (RF).

2.2 Probabilistic Assessment of Fault Slip

The likelihood of fault slip in the current state of stress can be characterized after building a comprehensive geomechanical model. According to Coulomb faulting theory, fault or fracture slip depends on the relative stress magnitude, the angle between the principal stress directions and the

fault plane, and the coefficient of friction μ (Morris *et al.*, 1996). The slip tendency in a pre-existing cohesionless fault can be defined in terms of the Mohr-Coulomb failure criterion:

$$\tau = \mathrm{c} + \mu\sigma_n \qquad (2.4)$$

where σ_n and τ are the effective normal stress and shear stress across the slip surface, and c is the fault's cohesion. In this dissertation, I assume that the fault is a cohesionless fault (i.e., c = 0), which implies that earthquakes occur when $\tau/\sigma_n = \mu$. Therefore, the fault slip analysis in this dissertation has been conducted in a more conservative manner.

Fault plane slippage is more likely to occur when the resolved shear stress, τ, equals, or is very close to, the frictional resistance of the fault surface; the fault is then called "critically stressed". A critically stressed fault is more likely to be hydraulically conductive and permeable (Barton *et al.*, 1995; Zoback, 2007). Even those faults that are frictionally stable in the current stress state may become critically stressed as a result of fluid injection. Three-dimensional Mohr diagrams provide a graphical representation of principal stresses as well as shear and normal stresses acting on fault planes (Figure 2-4). A dot in the space between the three semicircles represents a fault with a specific orientation and dip.

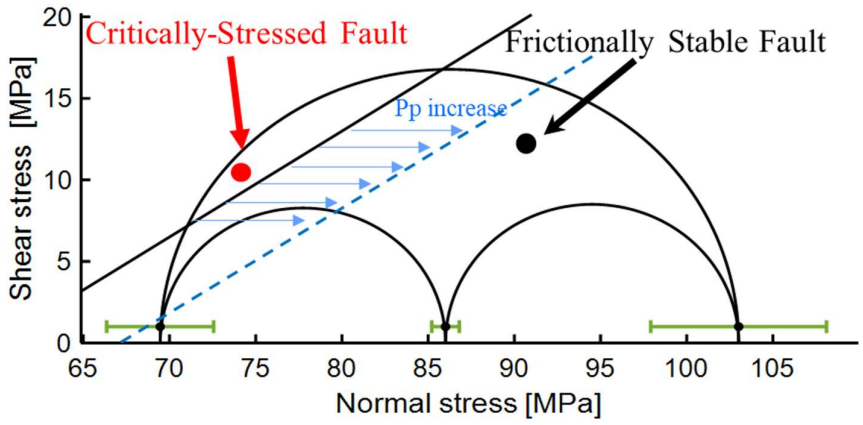

Figure 2-4: An example of three-dimensional Mohr diagram with two representative fault planes. When the ratio of shear to normal effective stress acting on the fault surface exceeds the failure criterion line ($\tau/\mu\sigma_n \geq 1$), the fault is deemed frictionally unstable or critically stressed. An illustration of how a frictionally stable fault may become critically stressed as a result of fluid injection is shown by the blue arrows. As indicated by the green error bar, there are uncertainties associated with three principal stress magnitudes that affect the stability of faults and fractures. Furthermore, as is usual practice in these assessments, poroelastic effects within the surrounding rock mass are not considered.

The deterministic fault slip tendency is expressed as the ratio of effective normal stress to shear stress on a potential sliding surface ($\tau/\sigma_n \geq \mu$). The deterministic approach thus considers just one single analysis as finite and therefore underestimates potential risks. The slip tendency in a probabilistic analysis, however, considers inherent uncertainties for each input variable, including stress magnitudes and orientations, fault dip directions, angles, and frictional strengths. Green error

bars in Figure 2-4 indicate the uncertainty associated with the estimated magnitude of the stress in a case study. Since fault slip tendency is directly related to the magnitude of principal stresses, any change in any one of these stresses will directly affect the outcome. Probabilistic slip tendency analysis is, therefore, more comprehensive and more suitable for evaluating slip probability in multiple scenarios. An appropriate probability distribution should be assigned for each of the input parameters in the model. The probability of failure then can be defined as

$$P_f = P[\,\tau - \mu\sigma_n \leq 0] \quad (2.5)$$

When there are quantifiable random factors present in a problem, *Monte Carlo simulations* can be used to estimate the probabilities of different outcomes based on that data. In this study, for each fault patch mapped in different location of western Canada, a Monte Carlo simulation using MATLAB™ has been applied to evaluate the slip tendency of faults in multiple scenarios. Each input variable effective in the Mohr-Coulomb shear failure can be defined as a random sample using the moment method with a specific mean and variance. The Monte Carlo simulation used in this study consists of five steps:

1) Select a random sample from the underlying statistical distribution of each variable. this has been done. The Randn MATLAB™ function was used to select a random sample from the variable distribution. As a first step, the function generates random numbers between 0 and 1. These random numbers are then transformed into random variables based on their respective distributions (Pandey, 2020). It has also been used MATLAB™ functions to carry out the transformation in accordance with the distribution.For example, the norminv MATLAB™ function can be used if the random variable follows a Gaussian distribution. In this context, the term variables refer to all variables that influence the Mohr-Coulomb failure criterion, such as stress magnitude and orientation, fault orientation and dip angles, pore pressure, etc. For each input variable, statistic parameters have been estimated based on direct measurements for the mean and standard deviation of parameters. The selection of the probability distribution is of fundamental importance since it directly impacts the calculation outcomes. In this study, stress tensor parameters are assumed to be statistically characterized by a Gaussian distribution defined by a mean and a standard deviation. For example, different studies in western Canada indicated that vertical stresses ranging from 24 to 26 MPa/km at the depth 2-3 km (Bell and Gough, 1979; Bell and Grasby, 2012; Bell *et al.*, 1990; Enlighten Geoscience Ltd., 2021; Haug and Bell, 2016a). I therefore assume that the vertical stress in the region follows a Gaussian distribution with a mean of 25 MPa/km and a standard deviation of 0.3. There are, however, some variables with a higher level of uncertainty. A study of 28 DFIT tests in the Watt Mountain Formation (Chapter 7), for example, indicates a S_{hmin} gradient ranging between 16 and 25 MPa/km. Figure 2-5 illustrates the histogram of 28 S_{hmin} gradient measurements within the Watt Mountain Formation. The mean and standard

deviation of these measurements are calculated as 20.9 and 1.9 MPa/km, respectively. As result, the blue curve in Figure 2-5 represents the corresponding Gaussian distribution of S_{hmin} gradients within the Watt Mountain Formation. The same methodology has been applied to each random variable that is effective in the fault stability analysis.

2) Evaluate fault slip stability deterministically using equation 2.4 and calculate shear and normal stress acting on each fault.

3) Store and count the results.

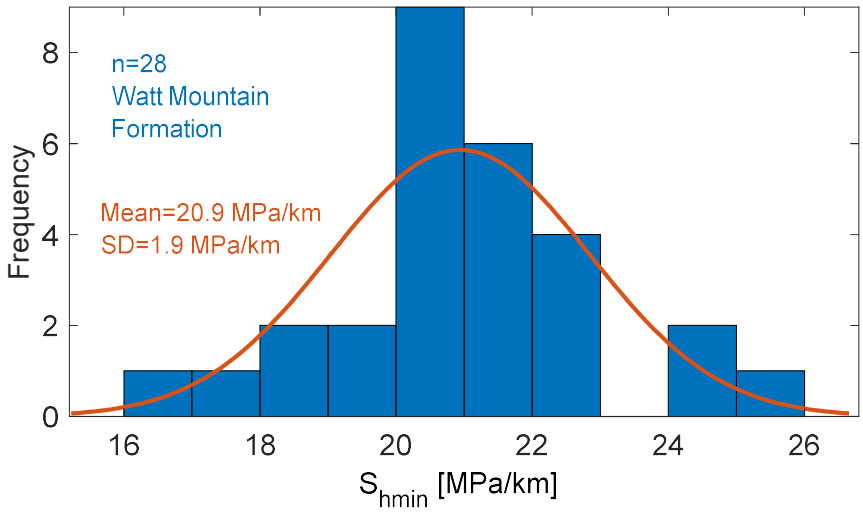

Figure 2-5: The minimum stress gradient in the Watt Mountain Formation derived from DFIT. The red curve represents the fit od a Gaussian distribution with mean of 20.9 MPa and standard deviation of 1.9 MPa.

4) Repeat steps 1 to 3 for n realizations (for the Monterey Formation project, for example, the number of realizations is set to 5000).

5) Calculate the cumulative probability of slip for each fault segment mapped. By following the previous steps, n number of τ and $\mu\sigma_n$ can be calculated for each fault segment. The uncertainty in τ and $\mu\sigma_n$, as an example, is illustrated in Figure 2-6 by probability distributions. Since $\tau > \mu\sigma_n$ is defined as the fault slip condition, $P[\tau - \mu\sigma_n \leq 0]$ is the probability of slip; therefore, the shaded area between τ and $\mu\sigma_n$ is a representation of the probability of fault slip.

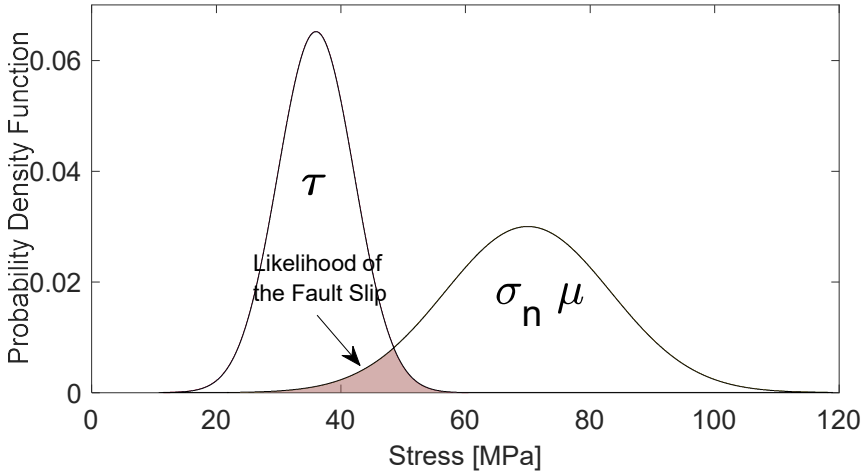

Figure 2-6: A graphical representation of the likelihood of fault slip, $P[\tau - \mu\sigma_n \leq 0]$. The distribution of shear and normal stresses acting on an example fault after n number of realizations. The shaded area is the probability of fault slip.

2.3 Summary

This chapter provides an overview of the background mythology of the thesis. A basic understanding of stress tensors is presented, followed by a description of how borehole and focal mechanism datasets can be utilized to determine the orientation and magnitude of subsurface stress. In addition, this chapter discusses the theoretical background of deterministic and probabilistic fault stability analyses within the context of the Mohr-Coulomb faulting theory. The final section of this chapter presents a Monte Carlo simulation process for assessing the likelihood of fault slip caused by fluid injection.

CHAPTER 3

Seismicity and the State of Stress in the Dezful Embayment, Zagros Fold and Thrust Belt[1]

Abstract

This study focuses on determining the orientation and constraining the magnitude of present-day stresses in the Dezful Embayment in Iran's Zagros Fold and Thrust Belt. Two datasets are used: the first includes petrophysical data from 25 wells (3 to 4 km deep), and the second contains 108 earthquake focal mechanisms, mostly occurring in blind active basement faults (5 to 20 km deep). Formal stress inversion analysis of the focal mechanisms demonstrates that there is currently a compressional stress state ($A_\varphi = 2.0 - 2.2$) in the basement. The seismologically determined S_{Hmax} direction is 37° ± 10°, nearly perpendicular to the strike of most faults in the region. However, borehole geomechanics analysis using rock strength and drilling evidence leads to the counterintuitive result that the shallow state of stress is a normal/strike-slip regime. These results are consistent with the low seismicity level in the sedimentary cover in the Dezful Embayment, and may be evidence of stress decoupling due to the existence of salt layers. The stress state situation in the field was used to identify the optimally oriented fault planes and the fault friction coefficient. This finding also aligns with the prediction Coulomb faulting theory in that the N-S strike-slip basement Kazerun Fault System has an unfavorable orientation for slip in a reverse fault regime with an average SW-NE S_{Hmax} orientation. These results are useful for determining the origin of seismic activity in the basin and better assessing fault-associated seismic hazards in the area.

[1] This chapter was published as Yaghoubi, A., Mahbaz, S., Dusseault, M.B. and Leonenko, Y., 2021. Seismicity and the State of Stress in the Dezful Embayment, Zagros Fold and Thrust Belt. Geosciences, 11(6): 254.

3.1 Introduction

The Zagros fold-and-thrust belt (ZFTB), southwest Iran, is one of the most seismically active areas in the world (Berberian, 1995; Talebian and Jackson, 2004), with more than 5000 earthquakes of $M_w \geq 3$ recorded between January 1, 2010, and January 1, 2020 (Iranian Seismological Centre catalog). The Dezful Embayment (DE) within the ZFTB is also one of the richest hydrocarbon regions in the world, hosting many onshore hydrocarbon fields and containing about 9% of global hydrocarbon (Bordenave and Hegre, 2010). Improving our knowledge of its state of stress is important in view of the area's enormous economic value and seismic activity.

In the Dezful Embayment area, most seismicity occurs around the Balarud Fault (BL), Kazerun Fault (KZ) System, and the Mountain Front Fault (MFF), and is restricted to depths below 5 km and to the area with a surface elevation of fewer than 1500 m above sea level (Figure 3-1). However, the major oil and gas fields of the Dezful Embayment region are located at low elevation; therefore, combining both earthquake datasets and borehole well logs leads to better coverage of the various scales.

Numerous studies have focused on determining stress states in the ZFTB by using earthquake focal mechanism data, where most seismicity happens on blind faults at basement level or beneath the sedimentary cover at depths of 5-20 km (Allen *et al.*, 2013; Berberian, 1995; Jackson and Fitch, 1981; Lacombe *et al.*, 2006; Nissen *et al.*, 2011; Talebian and Jackson, 2002; Talebian and Jackson, 2004; Tatar *et al.*, 2004). Berberian (1995) stated that active thrust basement fault systems are covered by quiescent sedimentary layers in the ZFTB. A micro-earthquake study (Yamini-Fard *et al.*, 2006) carried out around the Kazerun Fault System also revealed that the shallower sedimentary cover deforms by strike-slip faulting, but that a reverse faulting regime exists at greater depths (>7km). However, very few studies have integrated drilled wellbore datasets for shallower depths (<5 km) to help delineate the area's current state of stress (Haghi *et al.*, 2018; Yaghoubi and Zeinali, 2009). The study by Yaghoubi and Zeinali (2009) of the Cheshmeh-khosh field and by Haghi *et al.* (2018) of the Mansouri field indicated that normal/strike-slip faulting predominates in the sedimentary cover to a depth of 5 km.

The presence of several continuous highly ductile layers (the Hormuz Salt, and the evaporitic Dashtak and Gachsaran Formations) in the ZFTB leads the upper sedimentary cover to be decoupled from the basement (Mouthereau *et al.*, 2007). The state of stress in the Dezful Embayment might be a classic case of decoupling, where the stress regimes are changed at various depths because of the existence of highly ductile layers. These ductile zones shield the shallower sediments from the compressional strains in the basement rock arising from the collision between the Arabian and Eurasian plates that have generated the Zagros (Bahroudi and Koyi, 2003; Berberian, 1995; Sepehr and Cosgrove, 2004; Walpersdorf *et al.*, 2006).

This study determines the orientation and constrains the magnitude of the area's present-day stresses and tectonic regimes based on the geophysical wellbore log datasets of 25 wells as well as 108 earthquake focal plane mechanisms. The database includes the style of faulting derived from earthquake focal mechanism and analyses of borehole breakouts and tensile induced fractures. Evidence of stress-induced borehole instability and geophysical data from various wells, as well as seismicity datasets are used to estimate the state of stress in the Dezful Embayment.

First, I used borehole failures, drilling evidence, and rock strength information to constrain the stress state to a depth of around 4 km. Second, I determined the style of fault movement using focal mechanism events at depths of more than 5 km. Finally, the seismicity pattern in the region and strike-slip earthquake events around the N-S Kazerun Fault System are used to verify and confirm that the state of stress in the Dezful Embayment changes with depth.

3.2 Regional Tectonic Setting

The Zagros fold-and-thrust belt (ZFTB) results from the active collision of the Arabian and Eurasian plates. Extending for almost 1400 km and 100-200 km wide, with an approximately N125°-160° trend, the Belt stretches from eastern Turkey to the northern area of the Strait of Hormuz in the Persian Gulf. The ongoing collision started during the Miocene era as the Arabian plate pushed against the central Iranian one (Berberian, 1995). This compressional tectonic activity has led to significant crustal shortening across the fold belt, and resulted in the faulting and folding, thrusting, and reactivation of large-scale strike-slip faulting of the sedimentary cover sequence. Among the major faults are the Izeh-Hendijan Fault (IZHF), the Kharg-Mish Fault (KMF), and the Kazerun Fault (KZ) System (Figure 3-1).

The deep-seated strike-slip Balarud Fault (BL) from the northwest and the Kazerun Fault System from the southeast divide the ZFTB into various geological zones, each with a different structural style and stratigraphy. These zones include two regional embayments: the Kirkuk Embayment to the northwest and the Dezful Embayment to the southeast. There are also folded belts: from NW to SE, the in the Lorestan area, Izeh zone, and Fars (Central Zagros) arch (Sepehr and Cosgrove, 2007). An earlier study by Sherkati and Letouzey (2004) showed that the Dezful Embayment has subsided approximately 5000 m, compared to the Izeh zone across the Mountain Front Fault.

Extending over 60,000 km^2, the Dezful Embayment is a discrete structural lowland bounded by the Balarud Fault (BL) and the Mountain Front Fault (MFF) to the north and northeast, the Kazerun Fault (KF) System to the east and southeast, and the Zagros Foredeep Fault (ZFF) to the south and southeast. Most seismicity in the area occurs around the Balarud Fault, Kazerun Fault, and the Mountain Front Fault. Each colored dot in Figure 3-1 indicates the epicenter of an earthquake recorded by the Iranian Seismological Centre after 2010. I display that earthquakes have a recorded

waveform only for the sake of accuracy (Yaghoubi, 2020). This embayment is one of the most prolific oil regions in the world (Bordenave and Burwood, 1995) and hosts more than 40 onshore hydrocarbon fields. Most of the hydrocarbon fields (oval green shapes in Figure 3- 1) are elongated along the regional strike of the whaleback folds, NW-SE, orthogonal to the shortening direction (SW-NE). The majority of oil and gas hydrocarbon fields in the Dezful Embayment are found in two regional carbonate zones, the Asmari and the Sarvak Formations.

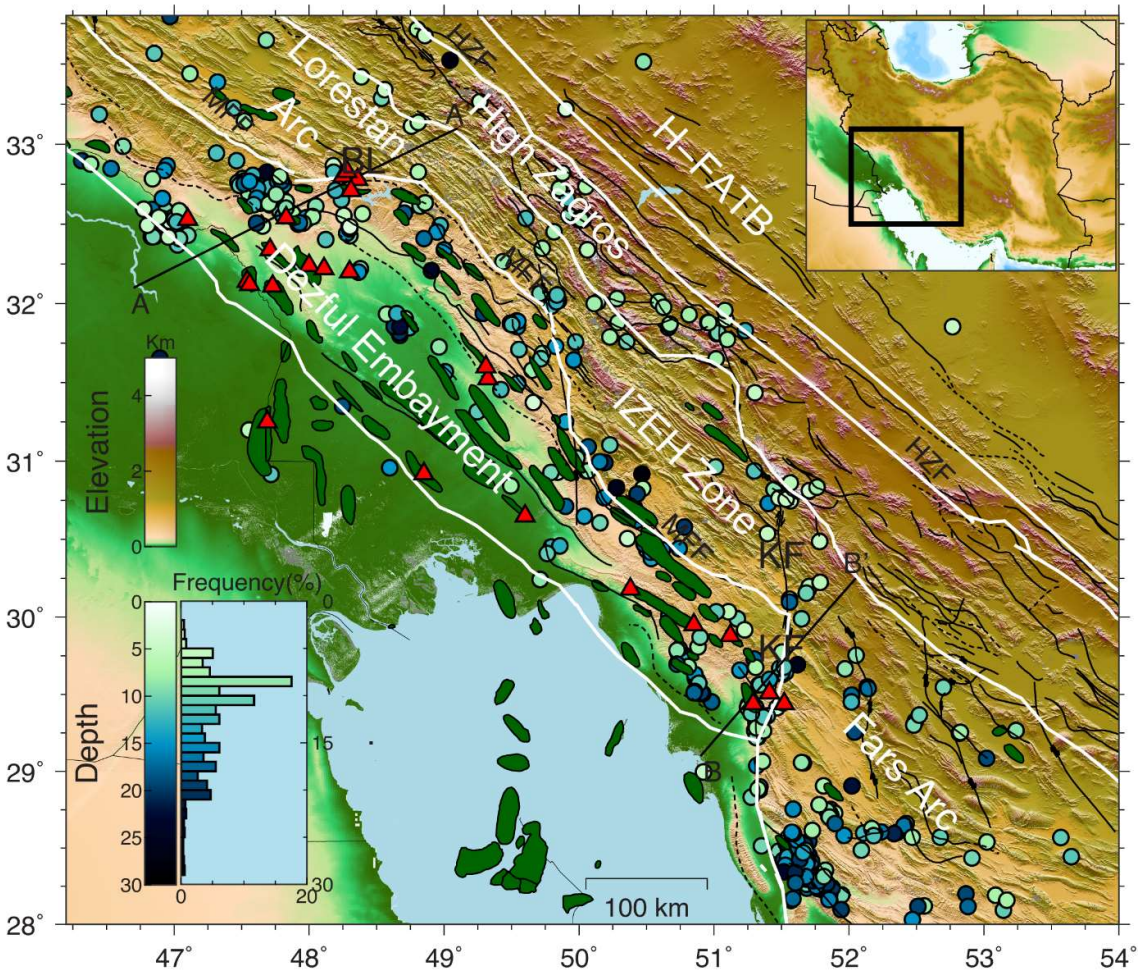

Figure 3-1: Topographic, structural and seismicity map of Zagros Fold and Thrust Belt along with locations of hydrocarbon fields (green oval shapes). Colored circles are IRCS-recorded earthquake centroid depths between 2010 and 2020. Details of each earthquake are provided Yaghoubi (2020). The bottom left histogram shows the depth (km) distribution of earthquakes. Red triangles denote the location of the 25 wells investigated in this study. A-A′ and B-B′ are cross-sections of the seismicity and topography shown in Figure 3-5. Fault traces (the solid black lines) are inferred and compiled from (Berberian, 1995) and (Talebian and Jackson, 2004). The white lines show the main structural subdivisions of the ZFTB. Major Active Faults are the HZF, High Zagros Fault; KZ, Kazerun Fault System; MFF, Mountain Front Fault; MRF, Main Recent Fault; MZRF, Main Zagros Reverse Fault; ZFF, Zagros Foredeep Fault; BL, Balarud Fault.

3.3 Dezful Embayment Stratigraphy

The present-day stratigraphic disposition of the Zagros Mountains and the Dezful Embayment is well established and is the result of a long geological history (Alavi, 1994; Alavi, 2007; Bahroudi and Koyi, 2003; Jahani *et al.*, 2007; Pirouz, 2018; Sherkati and Letouzey, 2004).

More than 10 km of Palaeozoic sedimentary successions have been deposited over the infra-Cambrian Hormuz in the ZFTB. The significant difference in the stratigraphy between the Dezful Embayment and Fars geological province is that the sedimentary cover of Fars province has been deposited on top of the infra-Cambrian Hormuz Salt layer, whereas this layer is much thinner or absent in the north Zagros (Jahani *et al.*, 2007). The main detachment levels in the Dezful Embayment are located in the evaporite-rich Triassic Dashtak and Miocene Gachsaran Formations (the yellow formations in Figure A1 of the supplementary materials).

The Gachsaran Formation (lower Fars) varies in thickness from several hundred to 2000 m and includes thick beds of evaporates (anhydrite, gypsum, and salt) with some marl, limestone, dolomite, and shale zones (Bahroudi and Koyi, 2004). The Gachsaran Formation is a regional seal and is the caprock for the Asmari Formation reservoirs. The Asmari Formation is composed of sandstone in its lower part and carbonates in the upper part (Figure A1), but at the northern edge of the basin, its uppermost part is conglomeratic, with clasts derived from the Asmari itself. The Upper Cretaceous Sarvak Formation, the second-most important reservoir unit in the Dezful Embayment, is part of the carbonate series of the Sarvak and Ilam Formations and overlain by the Gurpi Formation. Motiei (1994) pointed out that the Sarvak Formation consists of three limestone units, together reaching a maximum thickness of 821 m in the Dezful Embayment. The high hydrocarbon productivity of these reservoirs, particularly the Asmari, results mostly from the fracture systems created by the compressive folding characteristic of the Zagros area (Bordenave and Hegre, 2010).

3.4 Data Collection

Logging data and drilling reports of twenty-five wells of the Dezful Embayment have been analyzed. For all these wells, resistivity and acoustic image logs are available and provide a circumferential picture of the borehole walls. This information has enabled the identification of structures in the borehole wall, due to the differences in acoustic, resistivity reflectivity, and the rugosity of the borehole wall. To analyze the stress state, borehole breakouts and drilling-induced tensile fractures (according to WSM) have been examined. Details of each well, including the depth of their image logs, are provided in Table 3.1. Red triangles in Figure 3-1 denote the locations of the examined wells, which were drilled in 15 different hydrocarbon fields at various locations in the Dezful Embayment.

A total of 108 individual well-constrained focal mechanisms have been extracted and compiled from previous publications and sources (Adams *et al.*, 2009; Baker *et al.*, 1993; Jackson and Fitch, 1981; Jackson and McKenzie, 1984; Maggi *et al.*, 2000; McKenzie, 1972; Ni and Barazangi, 1986; Nissen *et al.*, 2011; Peyret *et al.*, 2008; Priestley *et al.*, 1994; Talebian and Jackson, 2004) and the Iranian Seismological Centre. Details of each focal mechanism and its references are provided in the supplementary materials. I have selected only those focal mechanisms that rank A in their references. Of the 108 focal mechanisms, 73 are compiled from the Iranian Seismological Centre (Hosseini *et al.*, 2019) using broad-wave forms modeling. The selected focal mechanisms range in depth from 4 to 20 km, with an average depth of 10 km. A number of the focal mechanisms belong to the Lorestan Arc and Fars Arc to evaluate the state stress variation on the border of structural subdivisions. Of all earthquakes considered in this focal mechanism study, 86 are thrust faulting at various locations, and 22 events are strike-slip which mostly occur around the NS striking Kazerun Fault System.

3.5 Constraining the state of stress from borehole data

3.5.1 Methodology

Since most of the ZFTB's earthquakes have been recorded below a depth of 4 km, datasets obtained from boreholes fill a critical gap in understanding the state of stress at shallower depths in the sedimentary cover. There are well-established techniques for determining stress orientation from borehole geometry and borehole geophysics datasets (Plumb and Cox, 1987). Drilling causes stress concentrations around the borehole wall. The local stress concentrations due to drilling a circular hole in an infinite homogenous rock mass can be calculated from the Kirsch solution (Jaeger *et al.*, 2009). In a vertical wellbore, observation of compressive features (breakouts) and tensile features (induced axial fractures) proves to be an effective approach for determining the minimum and maximum horizontal principal stress orientation respectively (Schmitt *et al.*, 2012).

In the context of the Mohr-Coulomb theory and considering the Kirsch equation, compressive failure, borehole breakout, in a vertical well occur when the circumferential effective stress ($\sigma_{\theta\theta}$) or the vertical effective stress (σ_{zz}) exceeds the rock strength.

$$\sigma_{\theta\theta} = S_{Hmax} + S_{hmin} - 2(S_{Hmax} - S_{hmin})\cos 2\theta - 2P_p - \Delta P \geq rock\ stength$$

$$\sigma_{zz} = S_V - 2\nu(S_{Hmax} - S_{hmin})\cos 2\theta - P_p \geq rock\ stength$$

$$\sigma_{rr} = \Delta P \qquad (3.1)$$

where S_v, S_{Hmax}, S_{hmin} are the vertical, maximum, and minimum horizontal stress magnitudes respectively; ν is the static Poisson's ratio; Pp is pore pressure, and ΔP is the difference between mud pressure and pore pressure. Drilling-induced tensile fracture form when the circumferential effective

stress ($\sigma_{\theta\theta}$) or the vertical effective stress (σ_{zz}) goes into tension. Note that the above equation is a simple presentation of induced stress around a vertical borehole wall due to drilling. Please see Schmitt *et al.* (2012) for more information on the stress state surrounding arbitrarily inclined boreholes.

The Leak-Off Test (Gaarenstroom, 1993), Hydraulic Fracturing Test, and Pressure While Drilling (PWD) (Ward and Andreassen, 1997) are different direct in-situ stress measurements taken during well drilling. Since no direct S_{hmin} measurement was available for this study, the state of stress had to be constrained from the borehole well-log data for the lower depth of the Dezful Embayment. An alternate approach used to constrain the in-situ stress magnitude in the absence of direct stress measurement is to utilize the observations of wellbore failures (equation 3.1) along with considering that the stress magnitudes are in equilibrium with the frictional strength of pre-existing faults (Brace and Kohlstedt, 1980). The ratio of the maximum (S_1-P_P) to minimum (S_3-P_P) effective stress on an optimally oriented cohesionless fault is limited by frictional strength:

$$(S_1 - P_p)/\,(S_3 - P_p) = \left[\sqrt{1+\mu^2} + \mu\right]^2 \qquad (3.2)$$

where P_P is pore pressure and μ is the coefficient of frictional sliding on a pre-existing fault (Jaeger *et al.*, 2009). It has been found in laboratory studies and in-situ experiments that the magnitude of the coefficient of friction falls within the range of 0.6 to 1 (Byerlee, 1978). In this study, I have used the observation of borehole failure (equation 1), information on rock strength, and the frictional strength of crust (equation 2) to constrain the state of stress at shallow depths in the sedimentary cover in the Dezful Embayment.

3.5.2 Stress Orientation

Detailed analysis was done on the image logs of 25 wells. Figure 3-2 illustrates examples of a) borehole breakouts, and b) and c) tensile induced fractures detected in different hydrocarbon fields located in the Dezful Embayment. Figure 3-3 shows the depth, frequency, and orientations of borehole breakouts in well P-7 of the Paydar field. Statistical analysis indicates that the S_{hmin} direction (borehole breakout azimuth) in P-7 is 100.7°±5.7°. This result is approximately the same as that for the borehole breakout azimuth analysis for P-6, drilled about 4 km away (101.7°±12.1°). The same analysis was performed for different wells in the Paydar, Agha-Jari, Khaviz, Abe-Teymor, Lali, Marun, Dalpari, Cheshmeh-khosh, and Mansori fields. The S_{Hmax} orientations resulting from breakouts, plus the tensile-induced fractures in each well, are ranked A to D according to the World Stress Map quality ranking system (Heidbach *et al.*, 2016b). Table 3.1 presents the result of this analysis of borehole breakouts and tensile-induced fractures observed in the vertical wells at different fields in the Dezful Embayment.

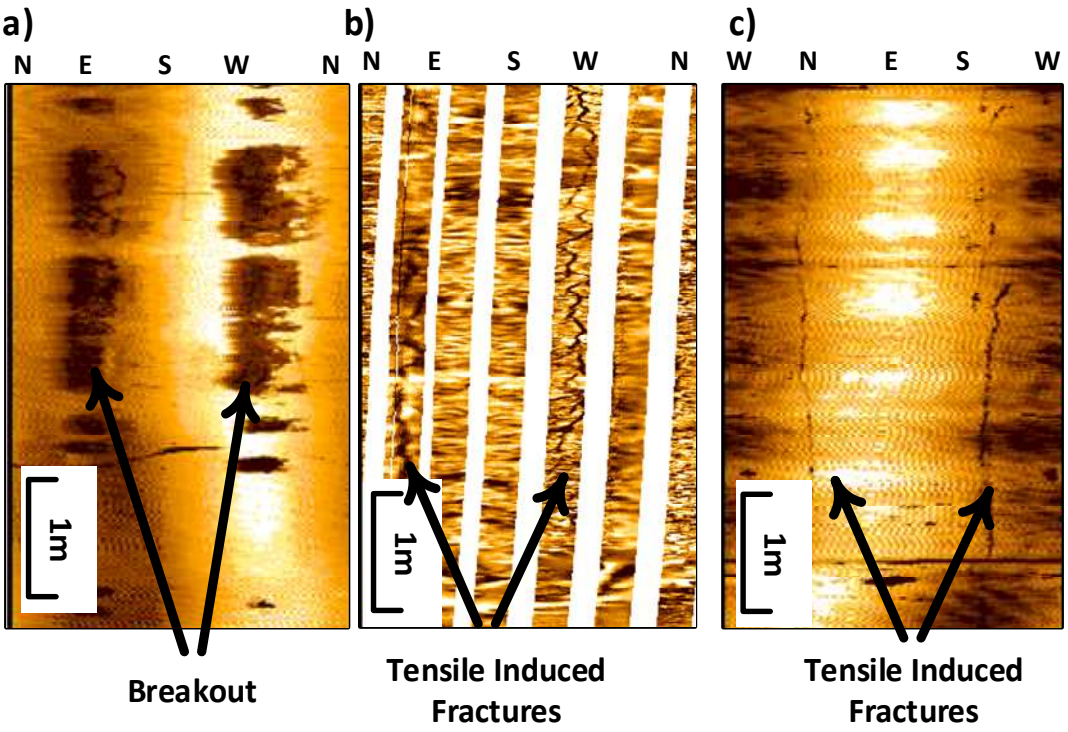

Figure 3-2: Examples of a) borehole breakout in the E-W direction in vertical well CK-8 in the Cheshmeh-khush oil field (3460 m) and b) tensile induced fracture in NE-SW direction in vertical well KH-5 in the Khesht oil field (2880 m), and c) one in the N-S direct in vertical well P-2 in the Paydar oil field (3210 m). Note that for c) the image started from the west (W) side of the borehole to better show two axial induced fractures at θ=0° and θ=180°.

Of all wells, wells CK-9, LL-29, and the wells drilled in the Balarud field show significant variations and anomalies in breakout azimuths (D quality) and tensile-induced fractures as a function of depth, due to stress perturbations associated with geological structures and faults. Figure A3 (supplementary materials) shows how breakout azimuths on the ultrasonic image logs for wells CK-9 and LL-29 change abruptly at different depths, resume at slightly greater depths, and gradually change in the vicinity of the fault. Seismic interpretation (3D) of the Cheshmeh-khosh field revealed two sets of faults with a NW-SE and WNW-ESE trend in the field, one of them close to well CK-9 (internal communication with NIOC). Talebi *et al.* (2018) and Hosseini *et al.* (2015) also observed that the stress orientations in the Lali field varied from well to well and were too complex to interpret due to an east-west trending strike-slip fault in the Asmari Formation. The Balarud Field is also a fault-bend fold, where stress orientations are significantly affected and perturbed by their geological setting. The stress orientations in the different part of the Balarud Field are highly variable.

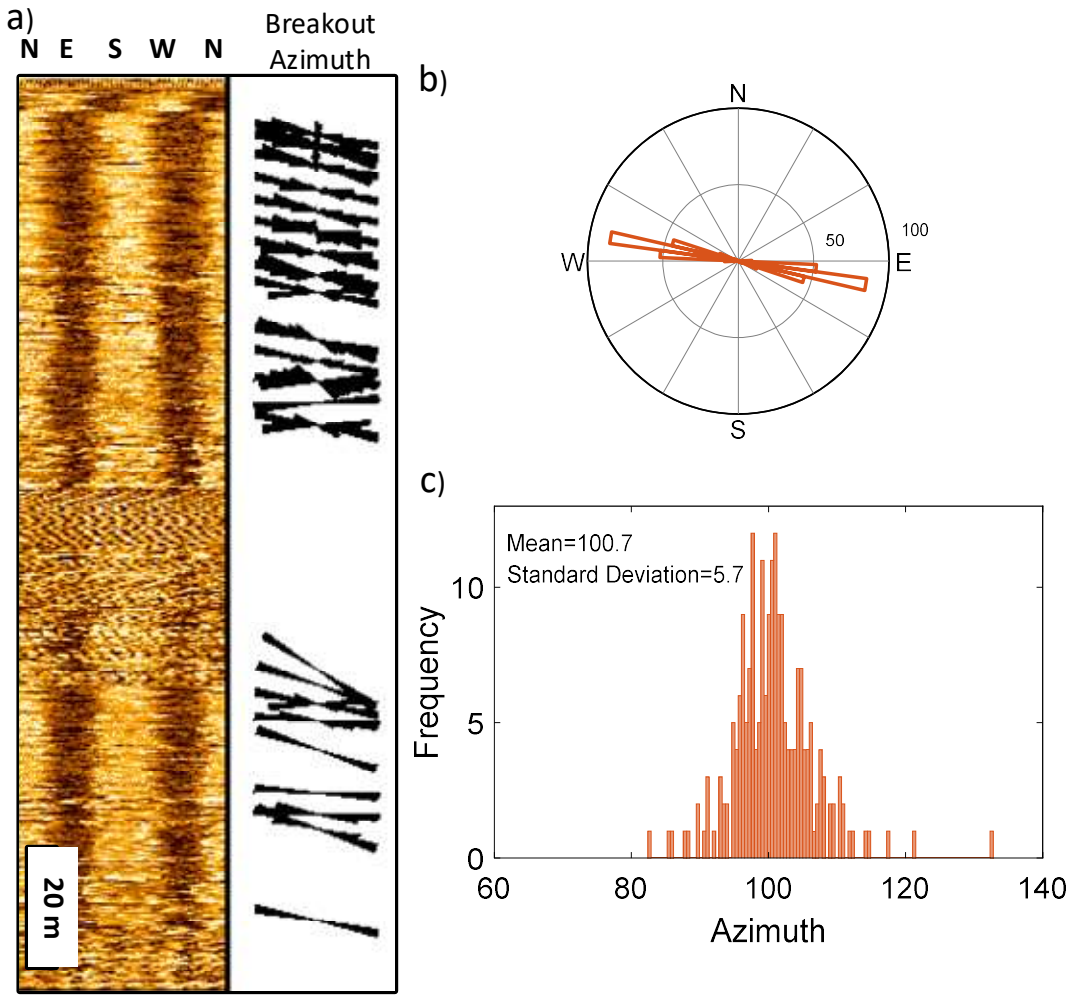

Figure 3-3:UBI log of borehole breakouts in vertical well P-7 in the Paydar Field at a depth between 3925-4130 m; b) and c) rose diagram and histogram showing that the frequency of observed borehole breakout azimuth in well P-7 (S_{hmin} direction) is 100°±5.7°.

Table 3-1: S_{Hmax} orientations derived from both borehole breakout (BO) and drilling induced fracture (DIF) in the different fields of the Dezful Embayment (S.D, standard deviation). S_{Hmax} orientations are ranked from A to D according to the World Stress Map (WSM) quality ranking system.

Field	Well Name abbreviation	Latitude	Longitude	S_{Hmax} Azimuth (deg)	Type	No	Total length (m)	Depth (m)	Orientation (deg.)	S.D.	WSM (quality)
Aghajari	AJ-215	30.69	43.86	32	BO	5	110	2475	122	7.3	C
Balarud	BL-2	32.8	48.25	147.6	BO	6	140	2243	57.6	2.1	B
	BL-2	32.8	48.25	152.5	DIF	6	464	2174	152.5	11.1	B
	BL-3	32.78	48.36	175	BO	1	---	1616	85	----	D
	BL-3	32.78	48.36	174.9	DIF	10	269	1805	174.9	20	B
	BL-4	32.83	48.28	42.9	BO	19	503	1846	132.92	19.9	B

Field	Well Name abbreviation	Latitude	Longitude	S_{Hmax} Azimuth (deg)	Type	No	Total length (m)	Depth (m)	Orientation (deg.)	S.D.	WSM (quality)
	BL-4	32.83	48.28	109.9	DIF	3	18	1705	109.9	18.6	D
	BL-6	32.71	48.31	169.08	DIF	24	623	1934	169.08	12.9	A
Bibi-Hakimih	BH-177	29.95	50.85	87.2	BO	51	210	1972	177.2	11.6	A
	BH-179	30.18	50.38	90.3	BO	109	520	2121	180.3	10.8	A
Chahar Bisheh	CB-4	29.88	51.12	52	BO	149	295	1953	142.0	9.9	A
Cheshmeh-khosh	CK-8	32.24	48.00	176	BO	25	238	3548	86.00	4.2	A
	CK-9	32.34	47.71	75	BO	43	221	4172	165.00	26.0	C
	CK-22	32.20	48.30	182.6	BO	10	106	3522	92.6	6.9	A
Dalpari	DP-08	32.54	47.83	157.3	BO	30	150	2340	67.3	32.1	D
Dehloran	DH-23	32.53	47.1	31.4	BO	52	415	4164	121.4	7.14	A
Khesht	KH-2	29.51	51.41	138	BO	28	402	2810	48.0	9.8	A
	KH-2	29.51	51.41	142.75	DIF	4	191	2845	322.75	8.7	C
	KH-5	29.44	51.29	124.05	BO	36	197	2994	34.05	8.7	A
	KH-5	29.44	51.52	119.4	DIF	19	215	2984	299.4	17.8	B
Lali	LL-22	32.25	134.2	44.2	BO	35	230	2278	44.2	11.2	A
	LL-29	32.22	48.11	135	BO	158	466	2547	46.10	43.3	E
Mansouri	MI-99	30.92	48.85	72.02	BO	22	179	3259	162.02	5.02	A
Maroun	MN446	31.524	49.324	75.7	BO	167	125	4293	165.70	5.3	A
Naft_Sefied	NS-47	31.60	49.31	72.75	BO	29	270	1625	162.75	9.78	A
Paydar	P-2	32.11	47.73	1.3	BO	89	681	3304	91.30	6.8	A
	P-2	32.11	47.73	179.2	DIF	99	576	3294	179.2	20.3	A
	P-6	32.14	47.54	10.7	BO	213	310	4045	100.7	5.7	A
	P-7	32.12	47.56	9.8	BO	135	230	4035	99.8	6.2	A
Ramshir	RR-19	30.65	49.6	59.65	BO	32	248	3061	149.65	6.70	A
	RR-19	30.65	49.6	70.8	DIF	3	48	2818	70.8	3.9	D
Yaran	YRRN-2	31.25	47.69	43.6	BO	11	140	3980	133.60	7.5	A

3.5.3 Stress Magnitude

From the surface to a 7 km depth, three abnormally pressured formations are present in the Dezful Embayment: the Miocene evaporitic Gachsaran Formation (Lower Fars), the Triassic Dashtak Formation, and the Lower Cretaceous carbonate Fahliyan Formation. Almost all wells drilled in the Embayment experience difficulties in penetrating the Gachsaran Formation, sometimes leading to blowouts (Nabaei *et al.*, 2011). The pressure gradient in the Gachsaran Formation ranges from 15.5 to 22.1 MPa/km in several oil fields located in the Dezful Embayment, such as the Masjid-i-Sulaiman, Lali, Haft-Kel, Naft Safid, AghaJari, Pazanan, Gachsaran, and Naft Shahar. The Dashtak Formation in the Embayment is located at a greater depth. The pressure variation along the Triassic Dashtak Formation is equivalent to that of the Gachsaran formation due to both having evaporitic rock composites; however, the former is the caprock in the Fars region hydrocarbon fields. Drilling experience in the Fars region shows that high mud weights are needed to drill into the Dashtak Formation (Salehi *et al.*, 2012). The lower Fahliyan Formation, which mainly consists of limestone, is another location of slight overpressure in the ZFTB, mostly in the Abadan Plain (Atashbari, 2016; Soleimani *et al.*, 2017). Apart from these three strata, other formations such as Asmari and Sarvak is close to hydrostatic. Since the Gachsaran and Dashtak Formations are severely overpressured, running the petrophysical well tools and performing formation evaluation tests are challenging. Therefore, there is not much information available on the rock physics and geomechanics properties of these two specific formations. Figure A2 of the supplementary materials shows variations of mud weight and direct pore pressures with depth, drawn from direct observations of several wells in the Dezful Embayment.

Few Hydraulic fracturing tests and extended leak-off tests have been reported for the ZFTB area. Table 3.2 provides a summary of the leak-off tests and Hydraulic fracture tests reported for the Gachsaran and Ahvaz oil fields in the Dezful Embayment. Since no direct S_{hmin} measurement was available for this study, the stress state was taken from well log data at the shallow depth (<5 km) of the Dezful Embayment.

Table 3-2: Summary of the leak-off test results reported for the Dezful Embayment.

Field	Latitude	Longitude	Depth (m)	S_{hmin} Magnitude (MPa)	S_{hmin} Gradient (MPa/km)	Reference
Gachsaran	30.32	50.48	2410	35.1	14.5	Amiri *et al.* (2019)
			2578	37.7	14.6	
Ahvaz	31.19	48.4	3450	52.44	15.2	Haghi *et al.* (2018)
			3513	53.4	15.2	

Sufficient rock mechanics studies are available for the Sarvak and Asmari Formations to use in establishing the relation between static and dynamic elastic moduli and rock mechanics properties. The study carried out by Najibi *et al.* (2015) shows that the uniaxial compressive rock strength (UCS) of limestone in the Sarvak and Asmari Formations varies considerably between 30 to 180 MPa, with the most-frequent value being 80 MPa. The same results have been reported by other studies (Asadi *et al.*, 2013; Asef and Farrokhrouz, 2010; Farrokhrouz *et al.*, 2014; Haghnejad *et al.*, 2014; Koleini, 2012; Mazidi Saber Mehrabi *et al.*, 2012; Najibi and Asef, 2014; Najibi *et al.*, 2015). Note that the Asmari and Sarvak Formations, as described above, also contain sandstone and shale of lower strength than the carbonate parts.

In the absence of direct stress measurement, observations of drilling-induced wellbore failure in a vertical borehole along with the information on rock strength can estimate the range of possible horizontal stresses acting around a drilled well at any given depth. To elaborate on this, Figure 3-4a illustrates an example of the rock strength (UCS) required to prevent breakout in a vertical borehole for a case $S_v = 100$ MPa, $S_{min} = 100$ MPa, $S_{Hmax} = 120$ MPa, and $P_p = 40$ MPa, which is equivalent to a strike-slip/reverse faulting stress state at depth of 4 km. The Mohr-Coulomb failure criterion and Kirsch formulation (equation (3.2)) (Jaeger *et al.*, 2009) were used in these calculations. For this example, the rock strength required to prevent borehole breakout is around 180 MPa. Thus, for such a state of stress, compressive failure would not be expected if the rock is stronger than 180 MPa and wide breakout failure (wash-out) would also result in lower rock strength than 80 MPa. When the rock strength is known, the presence and absence of breakouts provide a lower and upper bound on the horizontal stress difference acting around the borehole, respectively.

Figure 3-4b shows the range of possible magnitude (stress polygon) for the horizontal principal stresses for a depth of 3.5 km where pore pressure is 35 MPa and vertical stress is 87.5 MPa. It is assumed that the crust is in a state of frictional failure equilibrium and the coefficient of friction (μ) is 0.6 (equation 3.2). The color inside of the stress polygon represents the rock strength required to prevent breakout formation for different stress regimes. For each possible stress state case, the analysis same as a present for Figure 3-4a has been performed to know the rock strength under which borehole breakout might have occurred. For instance, Dark blue, in Figure 3-4b indicates the possible state of stress at which compressive failure will occur if the rock strength is less than 120 MPa.

Assuming that stress magnitudes at each depth are consistent with Coulomb frictional-failure theory for a coefficient of friction (equation 3.2), Figure 3-4c and Figure 3-4d illustrate two possible states of stress, extensional (normal/strike-slip) and compressional (reverse/strike-slip) in the sedimentary cover of the Dezful Embayment. Figure 3-4c and Figure 3-4d present an analysis similar to that of Figure 3-4.b (stress polygon) but at various depths (see Figure 9 of Moos and Zoback (1990)). In each case, Sv is assumed to be principal stress and is equal to the weight of the overburden rocks ($\rho \approx 2.5$ g/cm3). A depth between 2000 to 4500 m has been chosen since the reservoir

formations, the Asmari and Sarvak in the Dezful Embayment, are generally located at such depths, and most of the relevant conventional petrophysics and image logs are usually available. In Figure 3-4c, S_{hmin} changes from the value limited by a friction coefficient $\mu = 0.6$ to $S_v=S_{Hmax}$ (the horizontal dashed line inside of the stress polygon in Figure 3-4b). The same idea applies for Figure 3-4d; but S_{Hmax} changes from S_v to the value limited by a friction coefficient $\mu = 0.6$ (the vertical dashed line inside of the stress polygon in Figure 3-4b). The color shows the rock strength needed to prevent breakouts occurs for a given value of horizontal principal stress for each possible case. As stress magnitudes increase with depth, the compressive rock strength needed to prevent failure increases at any state of stress.

In a compressional stress system in the studied region (Figure 3-4d), the minimum rock strength needed to prevent borehole failure at a depth of 2 km, for example, should be around 180 MPa except when the three principal stresses are close together ($S_v \approx S_{hmax} \approx S_{hmin}$). Whereas in an extensional environment at such depth, the minimum required compressive rock strength to make a vertical hole stable is around 90 MPa. Figure 3-3, the UBI log of well P-7 in the Payder Field, can be used here as a related example. First, the presence of breakouts shown in Figure 3-3 at depths between 3925-4130 m indicates that horizontal principal stresses are not equal ($S_{hmax} \neq S_{hmin}$). Second, if the state of stress were reverse faulting regime, the minimum rock stress needed to prevent borehole breakout at these depths should be around 180 MPa (like the case presented in Figure 3-4a). Hence, considering the average UCS value of 80 MPa in the Sarvak and Asmari Formations, one would expect to observe continuous wide breakouts at all azimuths (wash-out) around any borehole drilled in the Dezful Embayment. In other words, for a compressional state of stress at a depth of 4 km when rock strength is around 80 MPa, major borehole instability (such as wash-out) is expected to occur. Note that the Asmari and Sarvak Formations in the shale and sandstone section has a lower rock strength than carbonate. Observations of borehole breakout with respect to average rock strength in the Sarvak and Asmari Formation support that the state of stress is not in a compressional stress system.

The normal/strike-slip faulting regime in the shallow sedimentary cover of the Dezful Embayment also aligns with drilling experience such instability problem as well as mud weight in vertical and deviated boreholes. Many oil and gas wells have been drilled vertically into the Sarvak and Asmari Formations in the studied area, with no instability problems or borehole breakout. Directional and horizontal wells, however, do experience instability, and normally need more mud weight for safe drilling. Note that Table 1.2 presents just those wells that breakouts and tensile-induced fractures have been observed. Directional wells drilled in the direction of minimum principal stress (borehole breakout azimuth) are much more stable, as less horizontal stress difference is acting around the borehole wall. For example, well P-7 in the Paydar Field is side-tracked in two azimuths of 212° and 292°: ST-1, the first side-track at azimuth 212°, was drilled 212 meters in 20 days with a mud weight of 70 pcf, and ST-2 was drilled 717 meters in 15 days at azimuth 292° with a mud weight

of 63 pcf. Both side-tracks were drilled in the Sarvak Formation at a depth of 4020 m TVD (see Table A2 for more information). This drilling experience example supports the counterintuitive fact that the state of stress in the sedimentary cover of the Dezful Embayment is a normal/strike-slip regime.

These results are similar to those reported by Yaghoubi and Zeinali (2009) for the Cheshmeh-khosh field, Haghi *et al.* (2018) for the Ahvaz field in the southern part of the Dezful Embayment, and others (Amiri *et al.*, 2019; Taghipour *et al.*, 2019). Their results show that normal/strike-slip faulting predominates in the sedimentary cover to a depth of 5 km. Haghi *et al.* (2018) performed borehole geomechanics modelling of the Sarvak Formation in the southern part of the Dezful Embayment and determined through extended leak-off tests that the S_{hmin} gradient varies from 15.2 MPa/km (0.67 psi/ft) to 17.4 MPa/km (0.77 psi/ft). The normal/strike-slip faulting regime in the shallow sedimentary cover of the Dezful Embayment is also consistent with little seismicity and fault slip. A micro-earthquake study by (Yamini-Fard *et al.*, 2006) revealed that the shallower sedimentary cover deforms by less-compressive states of stress, confirming the legitimacy of our results.

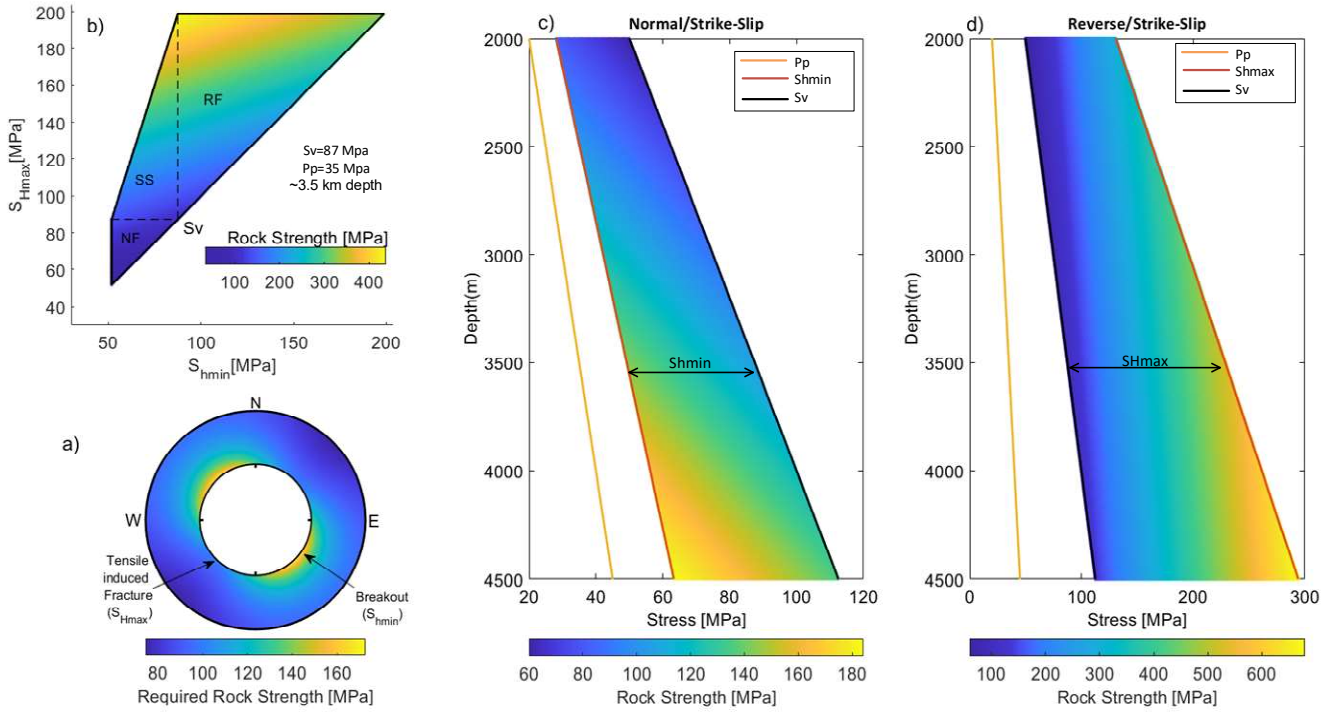

Figure 3-4: a) Example of stress concentration around a vertical borehole and the location of borehole breakout and tensile induced fracture and their relation to principal stress orientations; b) range of possible stress magnitudes (stress polygon) for horizontal principal stress at a depth of 3.5 km where Pp = 35 MPa, and S_v = 87.5 MPa; c) and d) rock strength required to initiate a breakout in normal and reverse faulting regimes in the Sarvak and Asmari formations of the Dezful Embayment, assuming that the stresses at the limit are constrained by a friction coefficient where μ = 0.6, Pp = 10 MPa/km, and S_v = 25 MPa/km. The color bar for each case shows the rock strength needed to prevent borehole breakout in vertical boreholes. The Mohr-Coulomb failure criterion and Kirsch equations were used in these calculations.

3.6 State of the Stress from Earthquake Focal Mechanisms

More than 5000 earthquakes of $M_w \geq 3$ have been recorded in the area since 2010 (Iranian Seismological Centre). Their magnitude and distribution increase from northwest to southeast, but they are scattered and rarely associated with co-seismic surface rupture (except in the case reported by Walker *et al.* (2005)). Most have occurred on active blind and hidden faults (Berberian, 1995) beneath sedimentary cover (Figure 3-1). There is always uncertainty associated with the depth of an earthquake. However, of the earthquakes observed in the ZFTB, most occurred relatively deeper underground (with an average depth of 12 km) and fewer occurred at shallow depths in the sedimentary cover (see the histogram in Figure 3-1). Talebian and Jackson (2004) stated that earthquakes in the ZFTB are only rarely associated with surface faulting. Many seismicity analyses in the ZFTB confirmed that the sedimentary cover is not highly seismically active even though it has been crisscrossed by many faults, as shown in Figure 3-1 (Hatzfeld *et al.*, 2010; Lacombe *et al.*, 2006; Molinaro *et al.*, 2005). Rarely have earthquakes with an M_w greater than 7 been recorded in the ZFTB.

Figure 3-5 displays two NE-SW cross-sections of the topography and earthquake hypocenters in the northern (A-A') and southern parts (B-B') of the Dezful Embayment. As illustrated in Figure 3-1 inset (histogram) and Figure 3-5, most earthquakes are located and nucleate at a depth greater than 5 km, and are confined between 10 and 15 km, below the sedimentary cover at the site of hidden faults. Seismic events are restricted to an elevation less than 1500 m in the area where most oil and gas fields are located (the embayment area).

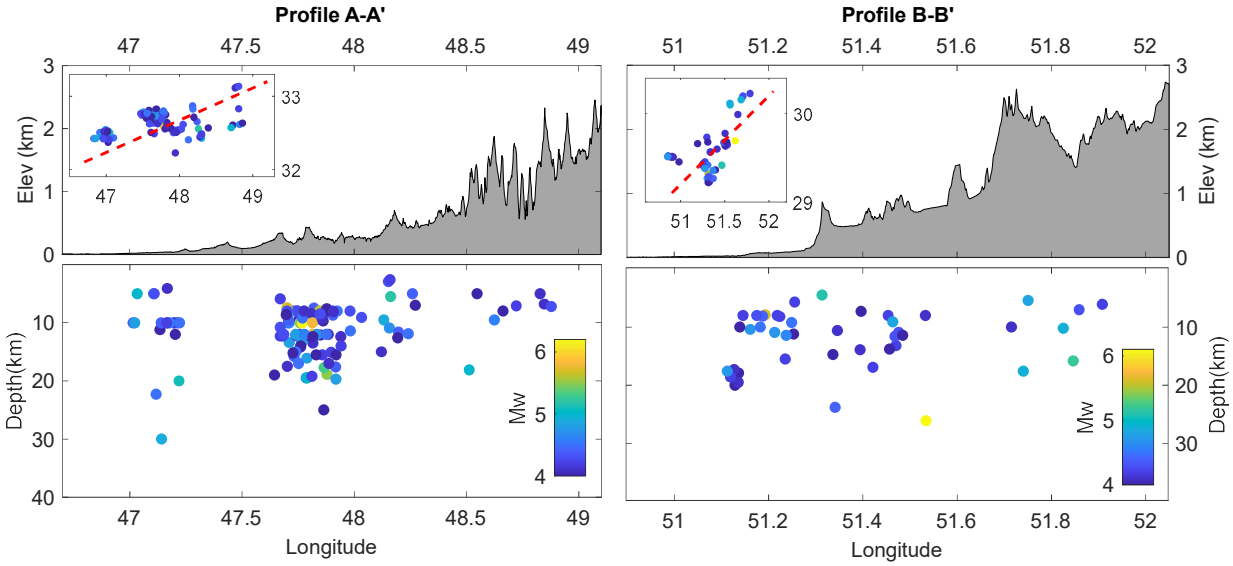

Figure 3-5: Cross-sections of Dezful Embayment displaying topography and seismicity in A-A' and B-B' sections shown in Figure 3-1. The color scale represents earthquake magnitudes. The high seismicity density in the area is restricted to below 5 km. The inset is an upper view of the cross-section profile (red dash line) and its nearby seismicity shown in Figure 3-1. Details of each earthquake are provided in Yaghoubi (2020).

3.6.1 Methodology

Earthquake focal mechanisms enable to constrain relative stress magnitudes. Assuming that S_v is one of the principal stresses, an appropriate stress regime for each earthquake focal mechanism can be assigned based on WSM criteria (Table 3, Zoback (1992)). The S_{Hmax} orientation can be determined from a single earthquake focal mechanism solution (FMS) and the formal stress inversion (FMF) of that focal mechanism. Whereas single focal mechanisms are only approximate indicators of S_{Hmax} orientation, the inversion of sets of earthquake focal mechanisms determines a best-fitting stress field and provides a more accurate estimation of principal stress orientations (Gephart and Forsyth, 1984; Michael, 1984). In this study, I also conduct a formal inversion of moment tensors using MSATSI MATLAB™ code, which iteratively inverts for the stress field based on the SATSI algorithm (Hardebeck and Michael, 2006; Lund and Townend, 2007; Martínez-Garzón *et al.*, 2014).

Assuming that the state of stress is in frictional failure equilibrium as one constraint on relative stress magnitudes (equation 2), Angelier (1984) introduced another constraint by quantity φ, defined by the equation

$$\varphi = S_2 - S_3/S_1 - S_3 \tag{3.3}$$

where S_1, S_2, and S_3 are the maximum, intermediate, and minimum principal stresses. Depending on the magnitude of the intermediate stress magnitude relative to the other two, Angelier's shape parameter φ must fall between zero and one. Simpson (1997) generalized the parameter φ values to provide a quantitative measure for each possible faulting regime as an equation:

$$A_\varphi = (n + 0.5) + (-1)^n(\varphi - 0.5) \tag{3.4}$$

where n=0, 1, 2, for normal faulting, strike-slip faulting, and reverse faulting, respectively. The fault parameter A_φ (the style of faulting) ranges continuously from 0 to 1 for normal, 1 to 2 for strike-slip, and 2 to 3 for reverse faults (Yang and Hauksson, 2013).

3.6.2 Stress Orientation

The S_{Hmax} orientation has been determined from 108 single earthquake focal mechanisms and the formal stress inversion of those focal mechanisms (Table A2 in the supporting material). I determine the S_{Hmax} orientation of every single focal mechanism based on the plunge of P, B, and T Axes (Table 3, Zoback (1992)). Besides, The total data cluster into three groups based on their location (latitude and longitude), so stress inversion is calculated for each group using the method presented in Martínez-Garzón *et al.* (2014) (see Figures A4 and A5 for more information). Table 3 contains the results of the formal stress inversion. The red lines crossing the beachballs in Figure 3-6 show the 108 S_{Hmax} orientations inferred from individual focal mechanisms (P-axis), while the inward-pointing black arrows (reverse faulting regime) and green arrows (strike-slip) represent the S_{Hmax} direction calculated from formal stress inversion in the Dezful Embayment.

Seismologically determined maximum horizontal stress (S_{Hmax}) orientations show more overall consistency and spatial uniformity than those obtained from the borehole wall examination (the blue inward arrows in Figure 3-6). The study suggests that the evaluated earthquakes are in both a thrust and a strike-slip faulting regime, with an average S_{Hmax} orientation of 37°±10°. However, stress orientation variations are seen in most of the investigated oil and gas fields, from relatively abrupt changes of stress orientation when drilling crosses a fault, to gradual lateral variations over scales of several hundred meters. The resultant spatial variation of stress orientations determined from boreholes in different locations of the study area shows general stress heterogeneity (discussed later).

Table 3-3: Stress inversion results at different locations in the Dezful Embayment.

Lat (°N)	Long (°W)	Number of Focal Mechanisms	S_1 Azimuth (°)	S_1 Plunge (°)	R= (1-φ)	Faulting Regime
48	33	68	205	3.8	0.70±0.2	R
52	29	31	223	5.7	0.78±0.25	R
51.6	29.8	23	221	4.3	0.84±0.15	S

3.6.3 Relative Stress Magnitudes and Style of Faulting

Using equation 4 (Simpson (1997)), the style of faulting regime for each focal mechanism is displayed by colours in Figure 3-6. The color inside of each focal beachball indicates the style of faulting based on A_φ values. Noticeably, the highest frequency value (Figure 3-6c) for $A_\varphi \cong 2.2$ suggests that S_{Hmax} is considerably greater than the vertical stress (S_3) and S_{hmin} (S_2) and S_{hmin}/S_V stress permutations. This compressional environment regime corresponds to a state in which both the reverse fault and strike-slip fault are potentially active. Of the 108 earthquake focal mechanisms considered, 22 earthquakes are strike-slip events at various locations, but most occurred around the NS striking Kazerun Fault System.

3.7 Seismicity and State of Stress

In this section, the relationship between seismicity and stress states in the Dezful Embayment are investigated. The seismicity pattern in the sedimentary cover and basement as well as strike-slip earthquake events around the N-S Kazerun Fault System are used to confirm that the state of stress in the Dezful Embayment changes with depth. I then determine that fewer earthquakes occur in the sedimentary cover because of less compressional stress state at relatively shallow depths.

The occurrence of fewer earthquakes in an area, such as in the sedimentary cover of the ZFTB, can generally be explained in two main ways. First, the state of stress in an area is not sufficient to exceed the rock's frictional strength to the point that a failure/earthquake is nucleated by the relative stress magnitudes. Second, there may be no critically stressed faults in the area with respect to in-situ

stress orientation (Snee and Zoback, 2016). Hence, the presence or absence of seismicity with respect to fault orientations in an area with a known stress orientation will provide information on the stress magnitudes. Since seismogenic fault properties, such as fault orientation and dip angle, in the studied area are unknown, this section first investigates which of two nodal planes for an earthquake focal mechanism is geometrically optimal for fault slip, and what the frictional likelihood is of a slip occurring along the preferred nodal plane. That helps us to understand and investigate the relationship between seismicity and the state of stress, particularly for the Kazerun Fault area.

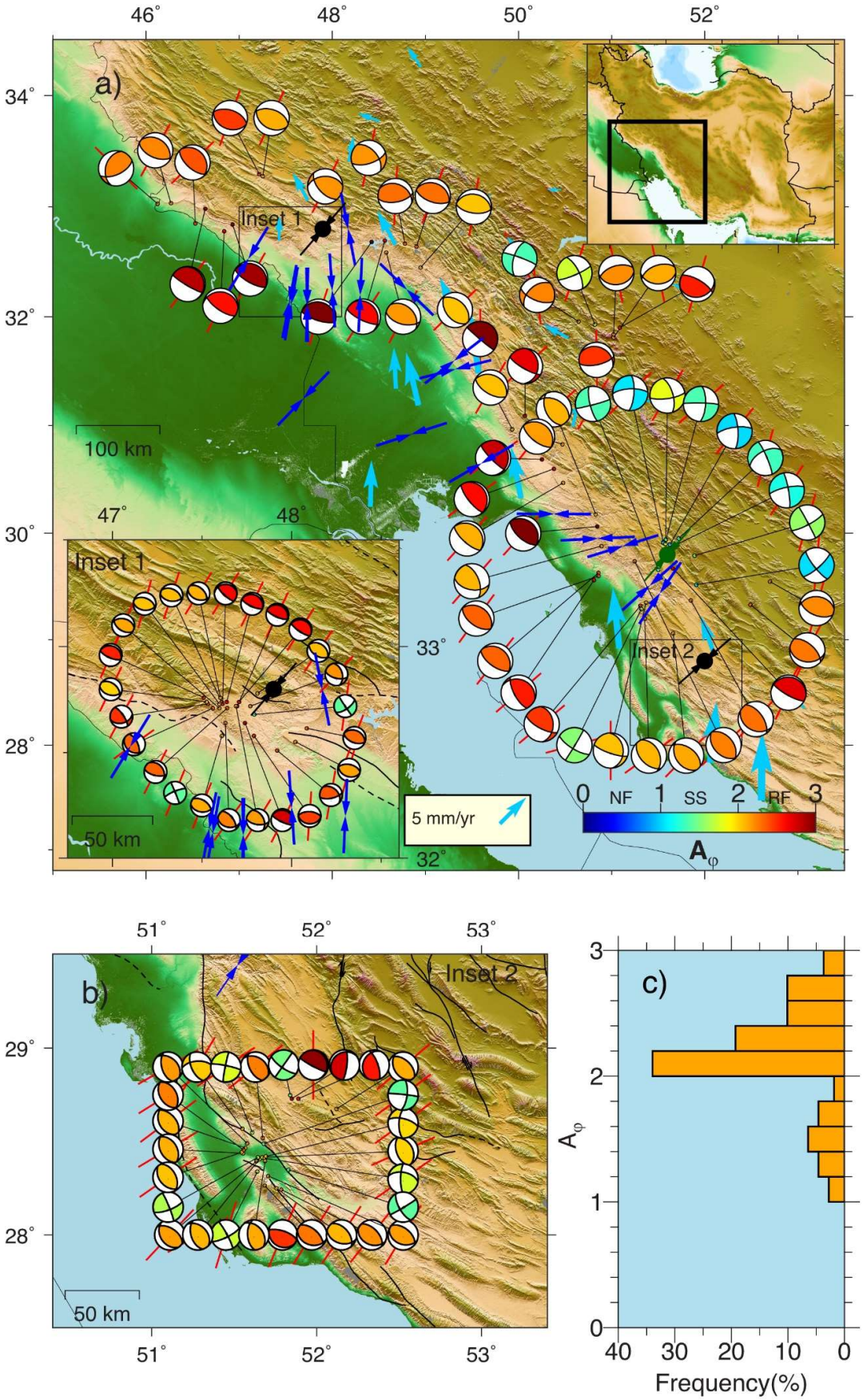
a)
b)
c)
Inset 1
Inset 2
100 km
50 km
5 mm/yr
0 NF 1 SS 2 RF 3
A_φ
Frequency(%)
46°
48°
50°
52°
34°
32°
30°
28°
47°
33°
51°
53°
29°
40 30 20 10 0
3
2
1
0

Figure 3-6: a) Map view of the value of 108 interpreted focal mechanisms in the Dezful Embayment. Colors show the stress regimes, with Aϕ values ranging from 0 to 1.0 for normal faulting, 1.0 to 2.0 for strike-slip faulting, 2.0 to 3.0 for reverse faulting. Red and black lines indicate the orientation of S_{Hmax} for individual focal earthquakes (P-Axis) and formal stress inversion respectively. Blue inward arrows show the S_{Hmax} direction derived from borehole breakouts and induced tensile fractures of A quality (Table 3.1). b) interpreted focal mechanism in southern Dezful Embayment (inset 2); c) histogram of Aϕ value from the inversion of 108 focal mechanisms using Simpson (1997) approach. Light blue arrow is GPS velocity vectors relative to central Iran derived from Walpersdorf *et al.* (2006). The greatest concentration of earthquakes is around the Balarud fault in the northern part of the embayment (inset 1).

Earthquakes in the Zagros area occur along blind/hidden faults for which neither geological mapping nor 3D seismic imaging can clearly determine the geometries (Berberian, 1995). However, existing faults can now be inferred from earthquake events. Using earthquake focal mechanisms that provide two nodal planes, I can deduce the possible fault plane. Figure 3-7a illustrates a normalized 3D Mohr diagram with a representative reverse focal event (M_w=4.2, 2015-08-14). The stress magnitude in the diagram is based on the A_φ value calculated for the event. The circle points in Figure 3-7a correspond to the normalized shear and normal stress acting on each nodal plane. As shown for this example, the plane fault striking NW-SE and dipping 25° NE is most likely to slip and is the preferred nodal plane. Figure 3-7b shows the slip-tendency in a case where the state of stress is the reverse faulting regime ($A_\varphi = 2.2$), with an average S_{Hmax} orientation of N37°E and hydrostatic pore pressure. A red circle on the Mohr diagram represents critically stressed fault poles, and black corresponds to fault poles with a lower likelihood of slip (τ/σ_n). Small-circles on the stereonet represent 92 preferentially-oriented nodal planes. The result shows that in the reverse fault regime, where S_{Hmax} is oriented NEE, faults striking NW-SE and dipping $30° - 50°$ either NE or SW are most likely to slip. According to the analysis, a friction coefficient of 0.5–0.6 can be inferred as an optimum friction angle for NW-SE oriented faults in the Zagros.

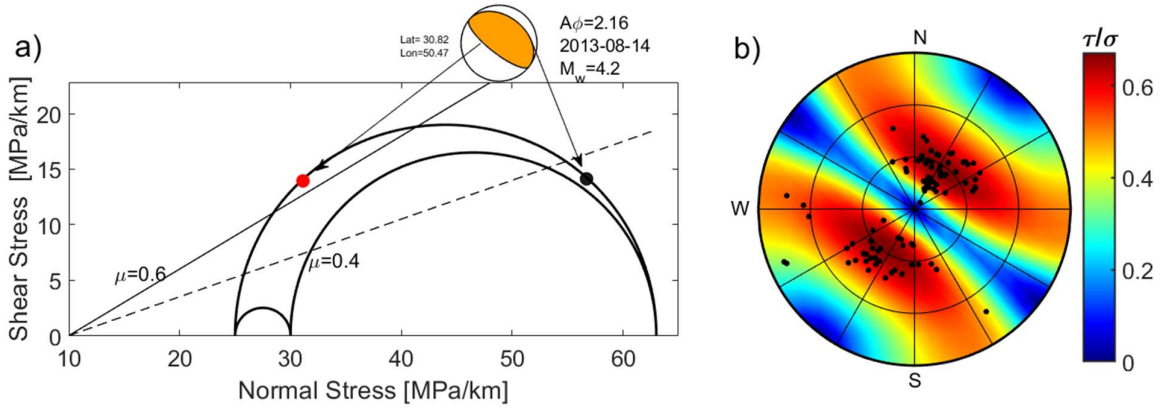

Figure 3-7: a) 3D Mohr's circle showing representative reverse focal mechanism and resolved shear and normal stresses for each nodal plane. The color inside the beach ball represents $A_\varphi = 2.16$ and is based on the color bar shown in Figure 3-6. b) Lower hemisphere stereonet plot of the preferred nodal plane for 92 focal mechanisms in the Dezful Embayment where the state of stress is a thrust-faulting regime. Colors show the ratio of shear to effective normal stresses (required μ) needed for shear failure on a fault plane.

Despite relatively uniform compressive stress orientations on both sides of the N-S Kazerun transverse active fault, the relative principal stress magnitudes inferred from earthquake focal mechanisms abruptly change from a reverse faulting regime to a pure strike-slip faulting regime near the fault segment (Figure 3-8). Previous studies (Baker *et al.*, 1993; Maggi *et al.*, 2000; Talebian and Jackson, 2004) have stated that the strike-slip earthquake associated with the old inherited basement Kazerun Fault System occurred at a depth of 4-10 km, with an average depth uncertainty ±3 km in the uppermost basement. In contrast, reverse-faulting focal mechanisms occurred at greater depths in the basement. In fact, the state of stress in the different sides of the Kazerun Fault System does not change laterally but rather vertically. The same results were reported after seven weeks' observations of micro-seismicity around the northern end of the near-vertical Kazerun Fault, in which slips at greater depths occurred in response to a pure reverse faulting regime (Yamini-Fard *et al.*, 2006). They reported that nearly all of the shallow-depth events resulted from a pure strike-slip regime.

These observations align with the frictional faulting theory that the N-S trending Kazerun Fault System is in an unfavorable orientation for a slip in a reverse fault regime with an average SW-NE S_{Hmax} orientation. Figure 3-8b presents an analysis similar to that of Figure 3-7b. As shown, the fault striking N-S and dipping more than 80° NE is most likely to slip and is the preferred nodal plane around the Kazerun Fault system. In Figure 3-8c, black circles on the stereonet plot represent the seismologically actual fault plane around the Kazerun Fault System, showing that the N-S strike fault has a higher slip likelihood. The same fault plane (N-S strike) in a reverse faulting regime (Figure 3-7b) is not in a geometric state permitting nucleation of an earthquake, except for a fault surface having a frictional strength within $\mu \approx 0.3$-0.4. Since the state of stress varies with depth, the slip tendency for a N-S strike Kazerun Fault increases when the state of stress changes to the strike-slip regime at the upper depths.

High heat flow in fault zones generally indicates a fault's frictional resistance to slip and implies that the fault is frictionally strong (Lachenbruch and Sass, 1980). Heat flow measured in different oil and gas wells in the Dezful Embayment reflects significantly higher temperatures in the vicinity of the Kazerun Fault System (66 mW/m^2) (Figure 3-4 Rudkiewicz *et al.* (2007)), whereas the central and northern embayment has a mean heat flux between 30-40 mW/m^2. No particular reason is stated for such a high thermal anomaly around the Kazerun line, but one can assume that it results from friction and that the fault is not weak. This supposition is consistent with the lack of reverse slip around the fault, as the frictional strength needs to be as low as 0.3-0.4 (Figure 3-7b) and demonstrates why most earthquakes around the Kazerun Fault System are a response to a strike-slip stress state. Note that the reverse slip observed in the northern Kazerun Fault System is small in magnitude (Yamini-Fard *et al.*, 2006).

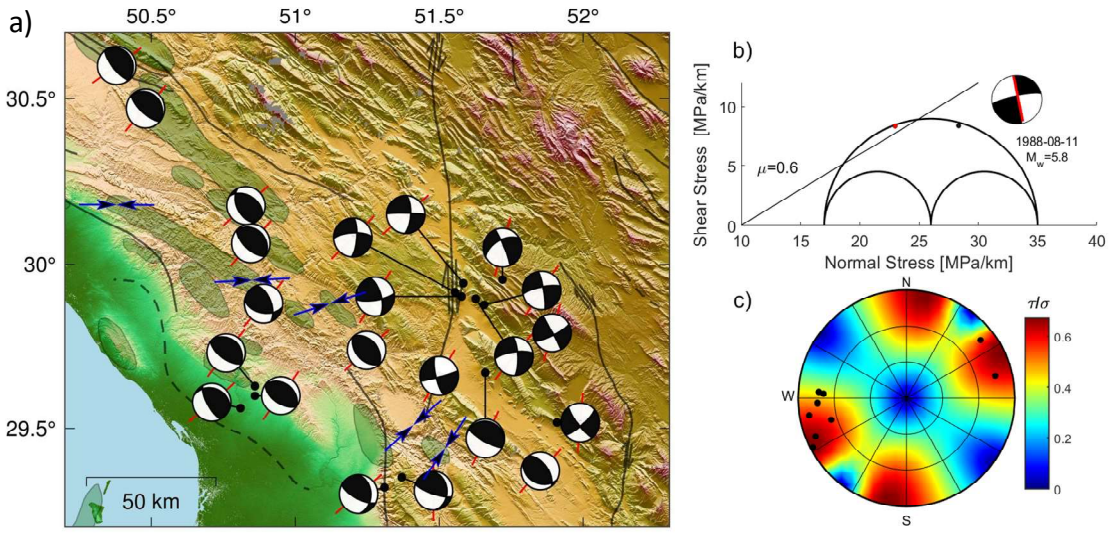

Figure 3-8: a) Earthquake focal mechanisms in the vicinity of the N-S Kazerun transverse active fault. The state of stress changes from strike-slip faulting around the fault to a reverse faulting regime on either side, whereas the seismologically (red line) determined azimuth S_{Hmax} (P-Axis) is stable and uniform around the area. b) 3D Mohr's circle showing a representative strike-slip focal mechanism and resolved shear and normal stresses for each nodal plane. The red line on the focal beach-ball indicates the actual fault plane. c) Lower hemisphere stereonet plot illustrates the slip-tendency (ratio of resolved shear to normal stress) for strike-slip faulting regime nearby Kazerun Fault System and actual nodal plane for 12 fault plane solutions mapped in (a).

Fewer earthquakes in an area can generally be explained by a state of stress in a faulted area that is not sufficient to exceed the rock's frictional strength. This phenomenon could explain the situation in the Dezful Embayment, as regional geophysics and geological studies have revealed its sedimentary cover to be crisscrossed by faults at both low and highly elevated areas. Similarly, many oil and gas boreholes have been drilled through local faults (Figure 3A); nevertheless, earthquakes at shallow depth in the sedimentary cover are rare.

Figure 3-9 shows a stability analysis of faults mapped in the Zagros area color-coded by the ratio of shear to effective normal stress (the required frictional coefficient) τ/σ_n; it is assumed that the state of stress is on the border of the strike-slip and normal faulting regimes ($S_{Hmax} \cong S_V > S_{hmin}$), as illustrated in the lower left inset in the 3D Mohr diagram. In a normal faulting regime with an average S_{Hmax} orientation of $N035°E$, the NW striking faults will have highly unfavourable orientations for slip. The locations of earthquakes since 2009 at a depth above 6 km are mapped as black circles in Figure 3-9. These earthquakes are scattered over the area, except for the August 2014, Murmuri Mw 6.2 event in the north of the Dezful Embayment.

Since most faults in the area strike NW-SE, almost perpendicular to the maximum horizontal stress orientation, they are critically stressed and associated with seismicity only in the reverse faulting regime (Figure 3-7). Consequently, the state of stress in the sedimentary cover cannot be as

strongly compressional as that in the basement; otherwise, more earthquakes would be expected in the area. In fact, the few earthquakes occurring at shallow depths compared to the number at greater depths in the area, plus the present NW-SE striking faults, strongly indicate that the state of stress in the sedimentary cover in all areas of the Dezful Embayment is a normal/strike-slip faulting regime. This fact confirms that the state of stress in the sedimentary cover is gradually changing from extensional to compressional from the sedimentary cover to the basement. The analysis has determined that earthquakes are concentrated within the basement and concludes that the state of stress at the near-surface deposits is not as compressional as that deeper in the basement.

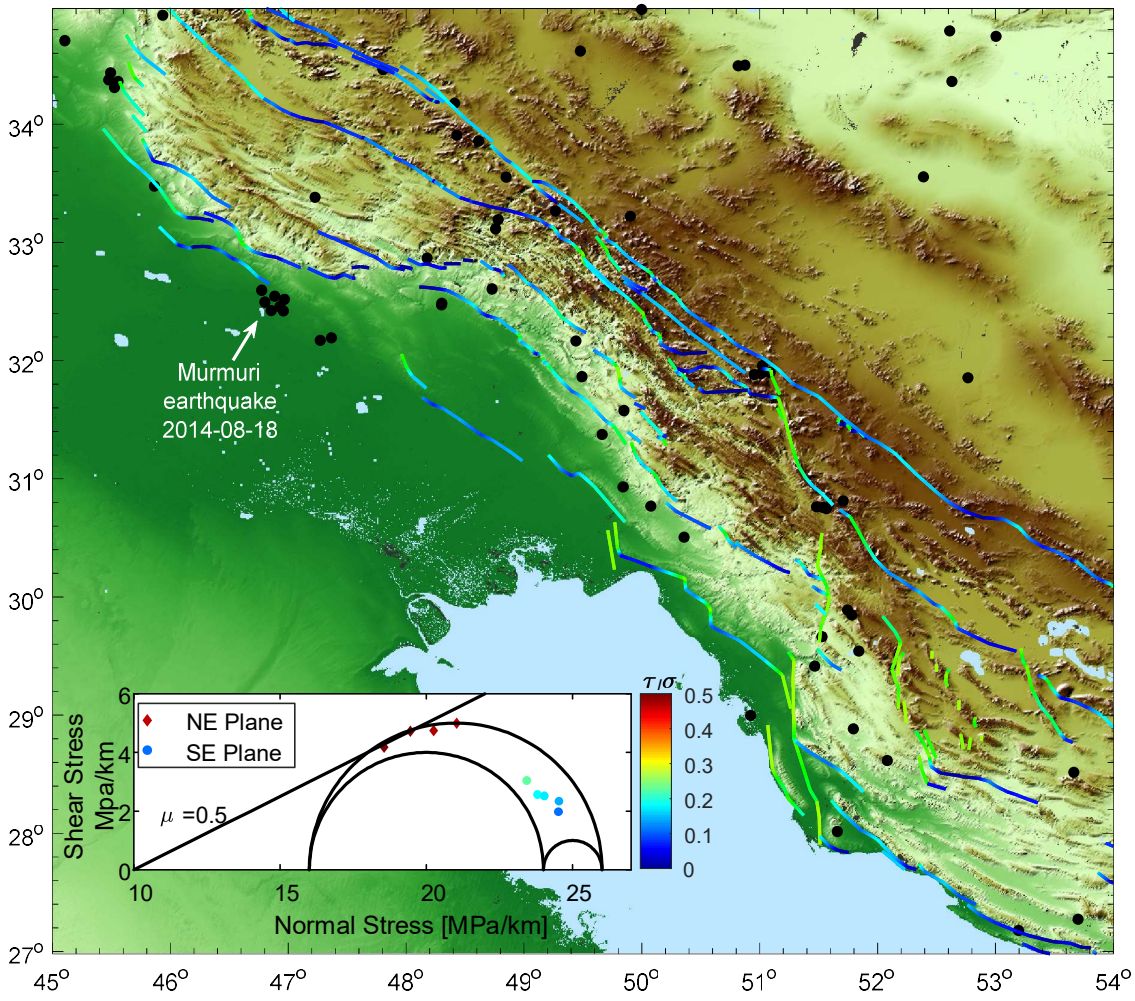

Figure 3-9: Large-scale faults examined in slip tendency analysis, in terms of τ/σ_n for the normal state of stress in the sedimentary cover of Dezful Embayment. Black circles represent earthquakes at a depth above 6 km with M_W=>4 in the area since 2010. The lower left inset illustrates 3D Mohr diagram frictional slip stability assigned for the slip tendency analysis.

3.8 Discussion

The stress orientation in the sedimentary rock strata and the basement shows two entirely distinct types. The stress orientations constrained from inversion of the focal mechanisms are consistently in the NE-SW direction in all areas of the ZFTB. However, lateral variations of stress orientations (blue arrow line in Figure 3-6) are seen in most of the investigated oil and gas fields in the area, from relatively abrupt changes of borehole breakouts to gradual variations over scales of several hundred meters.

Stress deflections or second-order stress patterns can be due to lateral density/strength contrasts, flexural stresses, or superimposed geological structures such as faults (Sonder, 1990). The magnitude of local stresses relative to regional stress along with the angle between local structures and the regional stress orientation are all significant parameters affecting the deviation of local stress orientation (Sonder, 1990; Zoback, 1992).

The regional horizontal stress difference (S_{Hmax}-S_{hmin}) is the determining factor (Sonder, 1990) for these anomalies in the folded and faulted sedimentary cover in the ZFTB. With this compressional state of the stress field at seismogenic depths (5-15 km) in the ZFTB, where S_{Hmax}-$S_{hmin} \approx$ 30 MP/km (see Figure 3-7), the local uniaxial stress is not sufficient to deflect stress orientation. However, in the sedimentary rock where the regional state of stress has been constrained to be on the border between normal and the strike-slip faulting regime ($S_{Hmax} \cong S_V > S_{hmin}$), a moderate local horizontal stress difference can cause stress deflection. Thus, variations in stress orientations are seen in most of the oil and gas fields examined in the Dezful Embayment.

Stress variation with depth can be explained by decoupling of the stress because of the existence of a ductile formation (Ahlers *et al.*, 2019; Cornet and Röckel, 2012; Roth and Fleckenstein, 2001). The ZFTB can be considered as a classic case for stress decoupling and a varying stress regime with depth in sedimentary basins due to several continuous highly ductile formations: the Precambrian Hormuz, Triassic Dashtak, and Miocene Gachsaran. These formations can shield the shallower sediments from the compressional strains in the basement rock arising from the collision between the Arabian and Eurasian plates (Bahroudi and Koyi, 2003; Molinaro *et al.*, 2005; Sepehr and Cosgrove, 2004; Walpersdorf *et al.*, 2006). These detachment horizons can also result in the decoupling of the basement and overburden deformation during crustal compression. Similar vertical variations in the state of a stress regime have been observed in the eastern part of the Paris Basin (Cornet and Röckel, 2012), the eastern North German Basin (NGB) (Ahlers *et al.*, 2019; Roth and Fleckenstein, 2001), and the Nile Delta (Tingay *et al.*, 2011).

3.9 Conclusions

The state of stress and the style of faulting for the Dezful Embayment in the ZFTB was investigated using data from boreholes drilled for hydrocarbon resources development and from earthquake focal mechanism records. The study supports the following findings:

1. Geomechanics study of 25 boreholes confirms that the stresses in the sedimentary cover is normal to strike-slip faulting. This finding is consistent with fault slip tendency analysis of the sedimentary cover, and the relatively few earthquakes at shallower depths, as well as the leak-off test results reported by other researchers.
2. The style of faulting and relative stress magnitudes and stress orientation in the area were investigated using Simpson's (1997) approach in 108 well-constrained earthquake focal mechanisms. This analysis shows that the Anderson fault parameter, A_{φ}, varies from 2 (strike-slip faulting) to 3 (reverse faulting) in the Dezful Embayment, with the highest frequency being between 2.0-2.2, suggesting that the style of faulting in the basement is compressional (a reverse to a strike-slip faulting regime) because the S_{hmin} and S_V magnitudes are close to one another but far less than the maximum horizontal stress value.
3. Studying both the sedimentary cover and the basement of the Dezful Embayment shows a change from the normal/strike-slip faulting stress regime in the former to a thrust–fault stress regime in the latter.
4. Critically stressed fault analysis using the Mohr-Coulomb failure criterion was applied to both the sedimentary cover and the basement in the Dezful Embayment. The analysis shows that the fault plane most likely to slip in the basement is 30°-50° dip angle fault aligned NW-SE. The local shallow depth faults, mostly lying NW-SE, are not critically stressed, and in fact, at the current state of stress, they are mechanically quiescent.

CHAPTER 4

Stress Variation around the Balarud Lineament in the Zagros Fold and Thrust Belt and its Implication for Reservoir Geomechanics

Abstract

This study investigates horizontal stress variation in the vicinity of the deep-seated Balarud Lineament in the northern part of Iran's Dezful Embayment in the Zagros Fold and Thrust Belt (ZFTB). The area, one of the richest hydrocarbon regions in the world, is also one of the most-seismologically active areas within the ZFTB. I use both petrophysical data from drilled oil and gas wells (3-4 km deep) and earthquake focal plane mechanisms (6 to 25 km deep) to constrain the orientation and relative magnitudes of the local and regional stresses. The stress orientations in the sedimentary rock strata and the basement are of two entirely distinct types. In the basement, I observed constant regional S_{Hmax} orientation in NE-SW in the northern ZFTB. The seismologically determined local S_{Hmax} direction from 25 focal mechanisms around the Balarud Lineament is 29.3°±8.5°. However, observations of borehole breakouts and tensile-induced fractures indicate that the dominant S_{Hmax} orientation is N-S near the Balarud Lineament. The consistent stress direction in the basement indicates a high differential horizontal stress magnitude, whereas the principal stress orientation rotates 35° counter-clockwise in the sedimentary cover where the state of stress is extensional. Since stress orientation is particularly valuable for optimum wellbore trajectory, hydraulic fracture outcomes, and induced seismicity assessment, I address the impact of the second-order stress pattern around the Lineament on wellbore placement and completion decisions.

4.1 Introduction

Anomalous relative stress magnitudes and orientations have been observed in the world's various uniform lithospheric stress fields. Stress deflection may be observed due to lateral density/strength contrasts, flexural stresses, or superimposed geological structures such as faults (Sonder, 1990) and salt diapirs (Dusseault *et al.*, 2004; Fredrich *et al.*, 2003). In the east-west-trending Transverse Ranges (California), the horizontal stress orientation is different by 25° from the reference stress state in the NW-SE San Andreas fault (Sonder, 1990). The regional NE-SW S_{Hmax} is reoriented to N-S in the area overlying the Peace River Arch in the Western Canadian Sedimentary Basin (Bell and McCallum, 1990). The same phenomenon is reported for the Amazon rift in central Brazil (Zoback and Richardson, 1996) and in the Swiss Alps and the northern Alpines foreland (Kastrup *et al.*, 2004). Stress deflections can also be caused by reservoir depletion (Yale *et al.*, 1994) and by earthquakes (Hardebeck and Hauksson, 2001). Hauksson (1994) observed a 15° (±10°) rotation of local stress axes due to the 1992 M_w 7.3 Landers's earthquake sequence. The scale at which second-order stress patterns occur depends on the degree of lateral density/strength contrasts and the size of geological structures and their orientation relative to regional stress fields (Sonder, 1990; Zoback, 1992).

The deep-seated Balarud Lineament is located on the northern side of the Dezful Embayment within the Zagros Fold and Thrust Belt (ZFTB). The Dezful Embayment, one of the richest hydrocarbon regions in the world, hosts many onshore hydrocarbon fields and contains about 9% of proven global hydrocarbon reserves (Bordenave and Hegre, 2010). Many oil and gas fields are located in the northern part of the Dezful Embayment close to the Balarud Lineament. The Balarud Lineament divides the northern part of the ZFTB into two different geological and structural settings: the Dezful Embayment and the Lorestan geological province. The left-lateral shear Balarud Lineament is also associated with much of the seismicity within the ZFTB, with more than 570 $M_w \geq 3$ earthquakes recorded from January 1, 2010 to Jan 1, 2020 (Iranian Seismological Centre Catalogue).

Stress orientation and relative stress magnitudes around the Balarud Lineament are key components of seismology and of reservoir geomechanics studies at various scales in this region. Most seismicity around the Balarud Lineament is restricted to below 6 km, and most hydrocarbon fields are located at depth around 3-4 km. Therefore, combining earthquake datasets with borehole well logs to better understand the tectonic stress state in the area permits addressing different seismology and reservoir geomechanics issues at various scales.

The ZFTB, a classic tectonic setting for a thrust/reverse faulting regime, has a regional NE-SW maximum compressive stress orientation. Most active faults in the ZFTB are located in the basement with a NW-SE strike which is the critically stressed fault strike in a thrust regime with an NE-SW S_{Hmax} direction. Most active faults in the ZFTB are located in the basement with a NW-SE strike, the

critically stressed faults orientation in a thrust regime with NE-SW S_{Hmax} orientation (Yaghoubi *et al.*, 2021) . However, superimposing a fault like the Balarud Lineament on this thrust fault tectonic setting causes stress reorientation and a second-order stress pattern in the region, like Transverse Ranges in the San Andreas fault (Sonder, 1990).

In Figure 4-1, I have mapped the S_{Hmax} orientations in the Dezful Embayment within ZFTB based on analyses of borehole breakouts and tensile-induced fractures (blue inward pointed arrows), and well-constrained seismic focal mechanisms (red lines). According to the interpretation of individual well-constrained focal mechanisms (red line with a dot in the centre) and the formal stress inversion of that focal mechanism (black inward arrow), horizontal stress orientation in the basement (5-20 km) was relatively uniform. However, high-resolution stress orientation (A-quality) obtained from wellbore failure (blue inward arrow) indicates that stress orientation is spatially heterogeneous in the Sedimentary Cover (3-4 deep) of Dezful Embayment. The S_{Hmax} orientation at shallow depths (3-4 deep) rotates to the north near the Balarud fault. In the southern part of the embayment, the regional NE-SW S_{Hmax} is also reoriented E-W in the vicinity of the N-S Kazerun Fault (KF). In this paper, I particularly focus on stress variation around the Balarud Lineament in the northwest part of ZFTB. Nevertheless, the same result can be extended to assess stress variations in different parts of the ZFTB.

In this study, I use both borehole data and earthquake focal mechanisms around the Balarud Lineament to constrain the stress orientations. I then compare the regional and local S_{Hmax} magnitude determined both seismologically and from borehole data collected. The ratio of the resolved shear to effective normal stresses is used to identify the deep-seated (blind) Balarud Lineament's plane (dip direction and angle). The local stress reorientation in the vicinity of the lineament is evaluated quantitatively with the procedure presented by Sonder (1990). The resultant stress reorientation around the shear zone is then discussed in terms of reservoir geomechanics applications: wellbore placement and completion decisions.

4.2 Regional Tectonic Setting

The Zagros Fold and Thrust Belt (ZFTB) results from the active collision of the Eurasian and Arabian plates. Starting in eastern Turkey, the ZFTB stretches nearly 1400 km, is 100 to 200 km wide, and follows a roughly N125°-160° trend. It finally ends in the Persian Gulf, in the northern region of the Strait of Hormuz. The ongoing collision started during the Miocene era as the Arabian plate pushed against the Eurasian plate. This compressional tectonic activity has led to significant crustal shortening across the fold belt, and resulted in the faulting and folding, thrusting, and reactivation of large-scale strike-slip faulting of the sedimentary cover sequence (Alavi, 2007) . The oblique lateral ramp Balarud Lineament, as characterized and defined by Sepehr and Cosgrove (2007), is one of the major blind tectonic lineaments bounding the northern Zagros. The lineament

divides the northwest ZFTB into different geological zones, each with a different structural style and stratigraphy. This fault zone divided the Lurestan and Dezful basins during the deposition of the Upper Cretaceous sediments (Sepehr and Cosgrove, 2007).

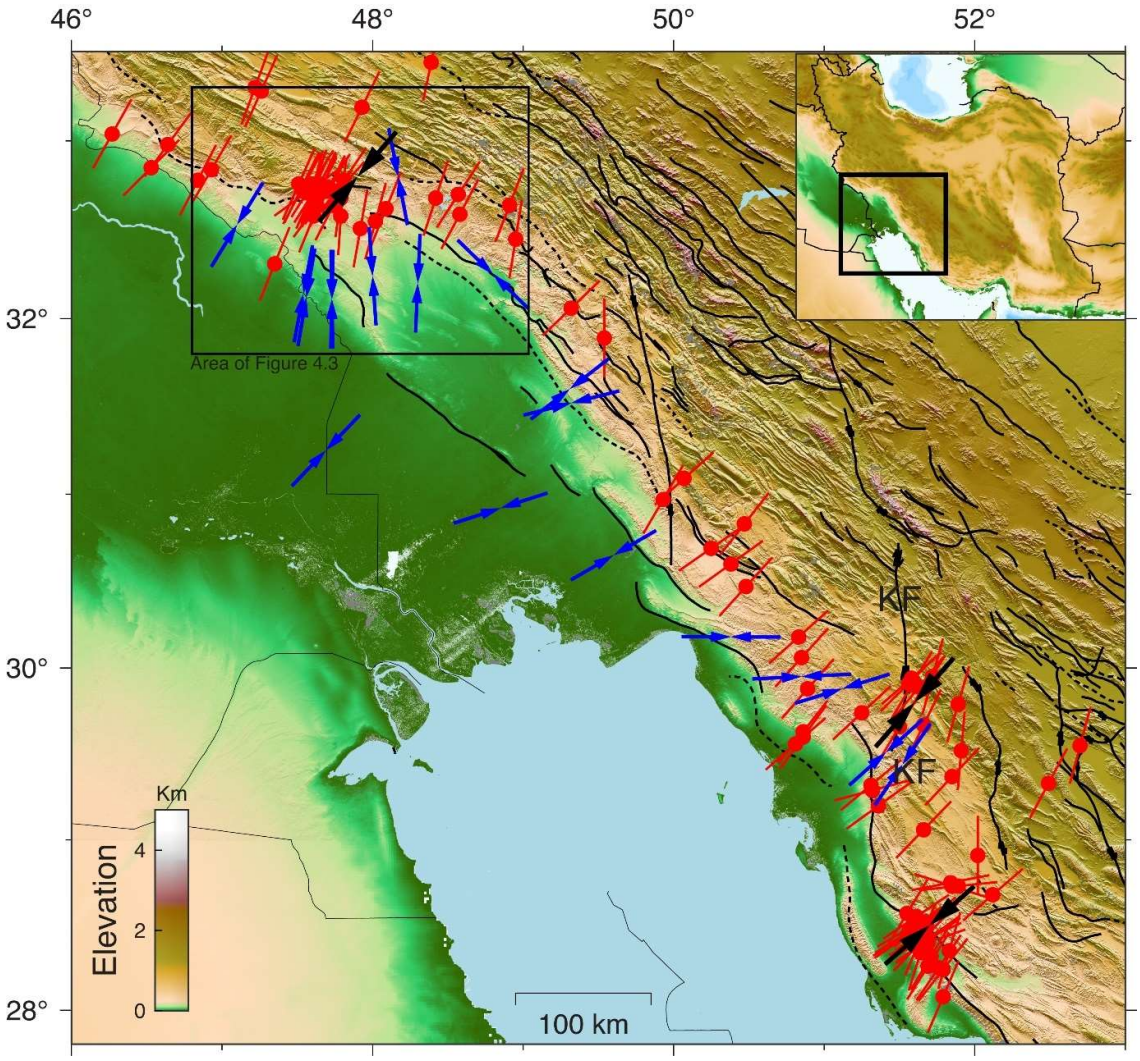

Figure 4-1: Stress Map of Dezful Embayment in ZFTB as determined from drilling-induced wellbore failures and earthquake focal mechanisms. The red lines with a dot in the center are seismologically determined S_{Hmax} (P-Axis) orientations. The heavy black arrows also indicate the orientation of S_{Hmax} derived from formal stress inversion (Yaghoubi *et al.*, 2021). The blue inward arrows are S_{Hmax} orientations (quality ranking A) obtained from borehole breakout and drilling-induced tensile fractures in vertical wells. Solid black lines represent fault traces inferred and compiled from Berberian (1995) and Talebian and Jackson (2004), where KF represents the Kazerun Fault.

The Balarud Lineament, like most seismogenic faults in the ZFTB, is not directly exposed at the surface (Casini *et al.*, 2018). However, its existence and long-lived activity are proven by the alignment of the dominant focal mechanism nodal planes. The major zone of current seismicity in the northern ZFTB, which is concentrated along the NWSE-trending Mountain Front Fault, abruptly changes its orientation by 20° to the east around Balarud (Sepehr and Cosgrove, 2007). Most of the major, well-constrained earthquakes in the vicinity of the lineament are thrust events. The Balarud

Lineament's presence is also inferred from the lateral thickness, the facies variation of the sediment across it, and the structural geology style at different sides lineament. All the anticlines in the north side of the shear zone tilt towards the lineament, and those in the south side are covered by a thick sequence of Miocene sediment (Sepehr and Cosgrove, 2007).

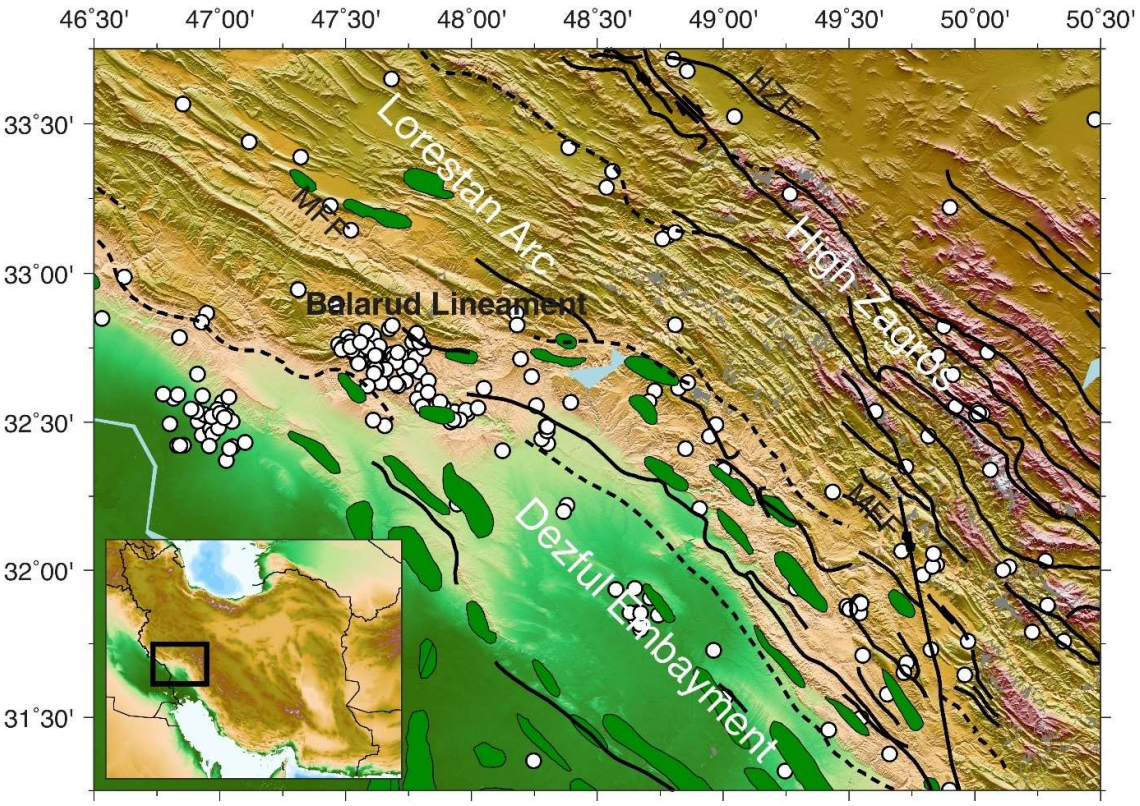

Figure 4-2: Topographic, structural and seismicity map of Balarud Lineament along with hydrocarbon fields. Each circle denotes a seismic event that occurred in the area between 2010 and 2020 (Iranian Seismological Centre catalog). Fault traces, the black lines in the background, are compiled from Berberian (1995) and Talebian & Jackson (2004). Major active faults are the HZF, High Zagros Fault; MFF, Mountain Front Fault; BL, Balarud Lineament.

4.3 Stress Orientation around Balarud Lineament

Method and Results

I used both borehole geophysical data from drilled oil and gas wells (3-4 km deep) and focal plane mechanisms (6 to 25 km deep) to constrain S_{Hmax} orientation in the vicinity of the Balarud Lineament. Borehole breakout and tensile-induced fracture are two reliable measures of the minimum and maximum horizontal stress orientations, respectively. In this study, I have examined borehole breakouts and tensile-induced fractures in eight wells drilled in the various oil fields in the southern part of the Balarud Lineament following World Stress Map (WSM) criteria (Heidbach *et al.*, 2018). Table A1 summarizes the stress orientations derived from borehole image logs. The blue inward-

pointing arrows in Figure 4-3 show the S_{Hmax} orientation with WSM quality ranking A extracted from borehole failures. Borehole geomechanics studies have demonstrated that the shallow state of stress in the Dezful Embayment is a normal/strike-slip regime (Amiri *et al.*, 2019; Haghi *et al.*, 2018; Taghipour *et al.*, 2019; Yaghoubi and Zeinali, 2009).

The local S_{Hmax} orientation around the Balarud Lineament is also indicated by both single earthquake focal mechanism solutions (FMS) and the formal stress inversion of focal mechanisms. Twenty-five well-constrained focal mechanisms have been compiled and extracted from previous publications (Hosseini *et al.*, 2019; Jackson and Fitch, 1981; Nissen *et al.*, 2011). These Twenty-five events occurred around the Baralud Lineament. This study is also supported by data on an additional 54 focal mechanisms recorded in the NW of the ZFTB which helped us to understand the regional stress orientation and relative stress magnitudes in the studied area. The related data are included in Supplementary Table A-2.

I have determined the S_{Hmax} orientation and the stress regime of every single earthquake focal mechanism solution, based on the plunge of P, B, and T axes according to Word Stress Map criteria (Table 3, Zoback (1992)). Individual focal mechanisms can only approximately indicate S_{Hmax} orientation, but inverting sets of earthquake focal mechanisms provides a more accurate estimation of the principal stress orientations (Gephart and Forsyth, 1984; Michael, 1984). Thus, I performed a formal inversion of fault plane mechanisms using MSATSI (Lund and Townend, 2007; Martínez-Garzón *et al.*, 2014) for both local and regional focal mechanisms datasets. MSATSI is an updated version of STASI algorithm (Hardebeck and Michael, 2006).

The formal inversion of focal plane mechanisms has been performed on two datasets, at a regional scale including 54 events in the northern ZFTB and a local scale including 25 events recorded nearby the lineament. The red lines crossing the beachballs in Figure 4-3 show the S_{Hmax} orientations inferred from individual focal mechanisms, while the inward-pointing black arrows represent the S_{Hmax} direction calculated from formal stress inversion in the northern DE (Figure 4-3). The results of our formal stress inversion are presented in Table 4.1. Seismologically determined S_{Hmax} orientations show more overall consistency than those obtained from borehole wall examinations. The observations of borehole breakouts and tensile-induced fractures (the blue inward-pointing arrows) represent a counter-clockwise rotation of stress orientation from the reference NE-SW S_{Hmax} direction by about 30°–35° in the northern part of the DE.

The relative stress magnitude and the stress ratio for each focal mechanism were also determined, using the Anderson fault parameter A_{φ}. The relative stress magnitude for each focal mechanism data is important for this study to identify the Balarud Lineament plane. Simpson (1997) generalized the parameter $\phi = (S_2 - S_3/S_1 - S_3)$ values to provide a quantitative measure as an equation, $A_{\varphi} = (n + 0.5) + (-1)^n(\varphi - 0.5)$, where n=0, 1, 2, for normal, strike-slip and reverse

types of faulting respectively. The Anderson fault parameter A_φ ranges continuously from 0 to 1 for normal, 1 to 2 for strike-slip, and 2 to 3 for reverse faults (Yang and Hauksson, 2013). Figure 4-3 shows the results of focal-mechanism analysis and the fault-type regimes on each focal mechanism using Simpson's (1997) approach. The color inside each focal beachball indicates the style of faulting based on A_φ values. The mean frequency value A_φ around the Balarud Lineament extracted from the 25 focal mechanism is ~2.11, and for the rest of the Dezful Embayment from the 54 focal mechanisms is calculated to be ~2.37. These findings indicate that the area adjacent to the Balarud Lineament is under less tectonic compression than the rest of the ZFTB. A_φ for each focal mechanism is used to identify the Balarud Lineament plane, discussed in the next section.

Table 4-1: Stress inversion results around the Balarud Lineament and the rest of the DE.

Location	Number of Focal Mechanisms	S_1 Azimuth (°)	S_1 Plunge (°)	Faulting Regime	φ
Northern ZFTB	53	221 (41)	5.4	R	0.37
Balarud	22	209 (29)	10.0	R	0.11

4.4 Balarud Fault Plane Identification

The ZFTB is a classic case of active basement tectonics within quiescent faulted and folded sedimentary rocks, with numerous seismogenic basement faults hidden within those rocks (Berberian, 1995; Hurd and Zoback, 2012a). Due to the depth of local earthquakes (6-15 km), neither 2D/3D reflection seismic nor geological mapping can diagnose structural features in the basement. Therefore, little is known about the seismogenic faults' properties in the ZFTB. However, recorded seismicity in the area demonstrates that there are critically stressed faults in the basement. The presence of seismicity (well-constrained focal mechanisms) in an area with a known state of stress provides useful information on seismogenic fault properties such as strike, dip direction, size, and the coefficient of friction. This section investigates which of the two existing nodal planes around the Balarud Lineament is geometrically optimal for fault slip. Knowing Balaroud fault properties is important in this study because slip along fault planes depends on the angle between the fault plane and the principal stress directions.

The Mohr-Coulomb shear criterion is used to define and identify the Balarud Fault plane as (Hurd and Zoback, 2012a; Morris *et al.*, 1996) $\tau = \mu(S_n - P_p) = \mu\sigma_n$ where τ and S_n are respectively the shear and normal stress acting on a pre-existing fault plane, and μ is the coefficient of friction. I assumed that the pre-existing Balarud Fault is cohesionless because it continues to be active. Slip is likely to occur on a fault plane when the resolved shear stress, τ, equals or exceeds the frictional

resistance of the fault's surface ($\tau/\sigma_n \geq \mu$), in which case the fault is considered to be critically stressed. A MATLAB™ code has been developed for fault slip-tendency analysis (Yaghoubi, 2019). For each focal mechanism, I calculate the ratio τ/σ_n on each nodal plane based on the value A_φ value. The nodal plane with a larger ratio of resolved shear to normal stresses is chosen as the preferred fault orientation.

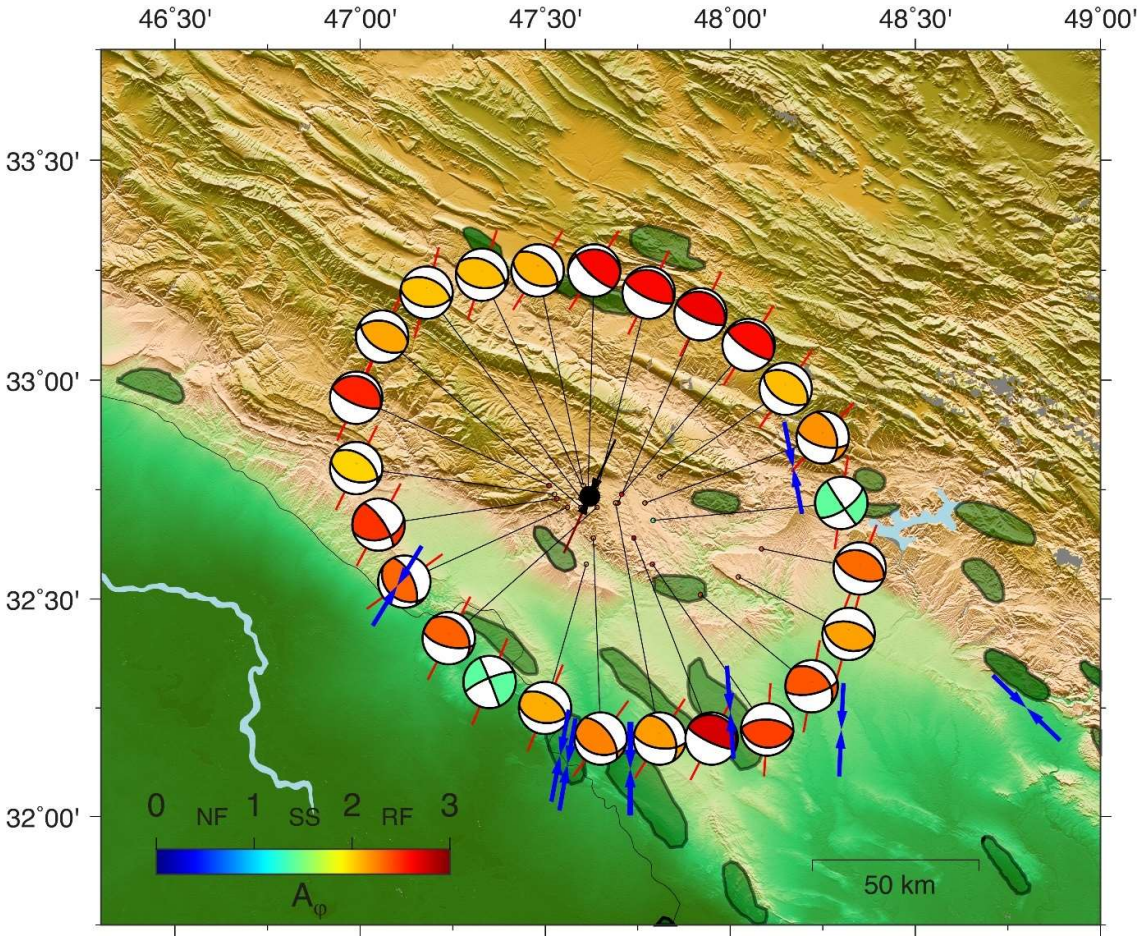

Figure 4-3: Map view of the value of Twenty-five interpreted focal mechanisms in the vicinity of BL. Colors show the stress regimes with A_φ ranging from 0.0 to 1.0 for normal faulting, 1.0 to 2.0 for strike-slip faulting, 2.0 to 3.0 for reverse faulting. Red and black lines indicate the orientation of S_{Hmax} for individual focal earthquakes and formal stress inversion respectively. Blue inward arrows show the S_{Hmax} direction derived from borehole breakouts and induced tensile fractures of A quality.

Figure 4-4 illustrates a 3D Mohr diagram with a representative reverse focal event (M_W 6.2, 2014-08-18). The stress magnitude in the diagram is based on the average A_φ value (≈2.1) calculated around the Balarud Lineament. The colors in the figure show the slip-tendency ($\tau/\sigma_n = \mu$) in the reverse faulting regime with an average S_{Hmax} orientation of 20° and hydrostatic pore pressure. The circle points in Figure 4-4 correspond to the shear and normal stresses acting on each nodal plane. The nodal plane with a larger ratio of resolved shear to normal stresses is chosen as the preferred fault

orientation. For this case, the red circle point (fault pole) represents the possible or preferred fault plane that is consistent with the local stress field. The black circle point, therefore, represents the auxiliary nodal planes. As can be seen, given the state of stress, for faults striking NW-SE (normally in the direction of S_{Hmax}) and dipping 30°-40°, either NE or SW is most likely to slip (critically stressed faults). The same analysis (Figure 4-4) was performed for each of the 25 focal mechanisms to evaluate the preferred and auxiliary nodal planes.

Figure 4-5 shows a rose diagram of the strike and a histogram of the dip angle for both the preferred and conjugate (auxiliary) nodal planes for the 25 earthquake focal planes. The nodal planes are striking NWW or SEE but at a different dip angle and direction. The result shows that seismogenic Balarud Lineament consists of some patches that have opposite dip directions. Given the state of stress in the northern Dezful Embayment, faults striking NW-SE (normal to the direction of S_{Hmax}) and dipping 40°-80°, either a NE or a SW direction are most likely to slip (critically stressed faults).

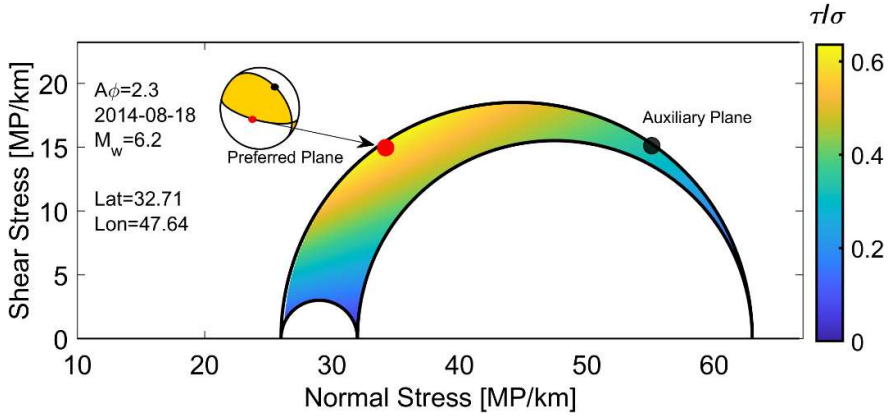

Figure 4-4: 3D Mohr's circle showing representative reverse focal plane mechanism and resolved shear and normal stresses for preferred (red circle point) and auxiliary planes (black circle point).

4.5 Stress Reorientation

Method and Results

Stress deflection in uniform lithospheric stress fields can be observed due to lateral density/strength contrasts, flexural stresses, or superimposed geological structures such as faults (Sonder, 1990; Zoback, 1992) and salt diapirs (Dusseault *et al.*, 2004). The amount of stress re-rotation depends on the degree of lateral density/strength contrasts and their orientation relative to the regional stress field. Figure 4-5 shows the geometry for evaluating stress reorientation due to local uniaxial stress. The schematic in Figure 4-5a illustrates the stress orientations ($X - Y$) in the reference state of stress (in this case, the ZFTB's principal horizontal stress orientations) where X and Y correspond to the orientations S_{Hmax} and S_{hmin}, respectively. Figure 4-5b shows the new coordinates ($X' - Y'$) where X'

is the strike of the local discontinuity (in this case, the Balarud Lineament strike) and Y' is normal to the structure. Figure 4-5c shows the resultant orientation due to the local source of stress.

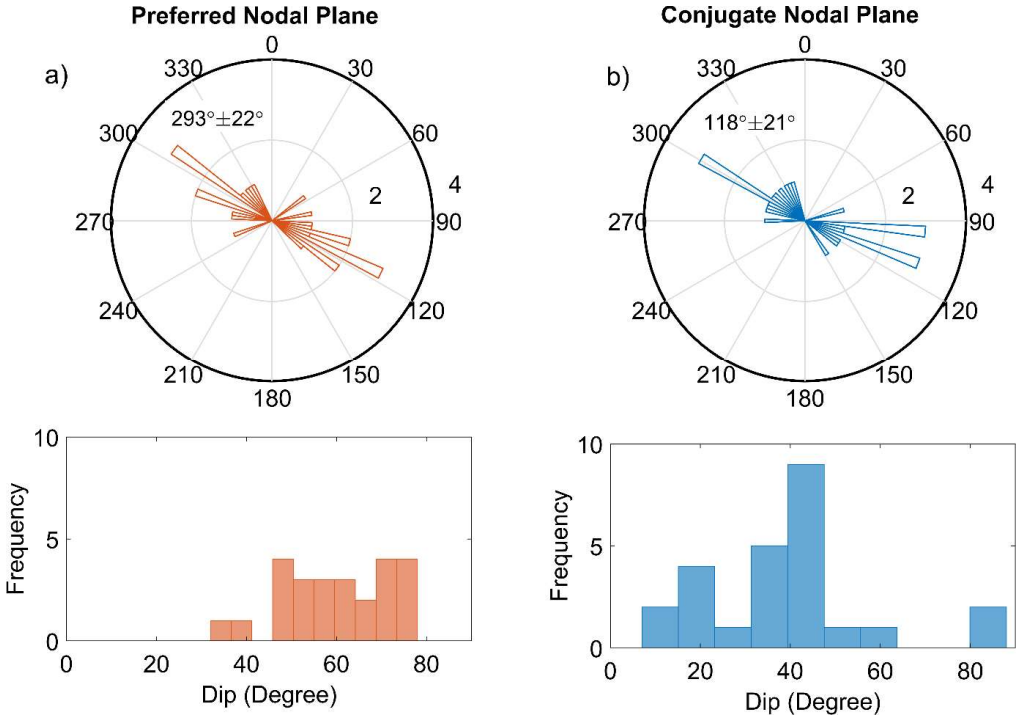

Figure 4-5: Strike and dip of the preferred (a) and the conjugate (b) nodal planes for 22 earthquake plane mechanisms. Both the preferred and conjugate nodal planes have almost the same strike (~300° or 120°); however, the preferred dip angle (34.1°±10.8°) is less the conjugate one (60°±10.3°).

In an unperturbed reference state of stress, the rotation of the principal stresses due to a local deviatoric compression or extension such as a fault can be evaluated with stress tensor transformation. The equations for transforming stress into a new coordinate system $(X' - Y')$ in a linear elastic medium are well documented (see section 2.3 in Jeagr and Cook). Assuming that one of the principal stresses is vertical, the horizontal principal stress rotation in the new coordinate system is given by

$$tan\, 2\gamma = \frac{2\tau_{xy}}{\sigma_x - \sigma_y} \tag{4-1}$$

Solving the equation in term of shear (τ) and normal (σ) stresses due to a superimposed local uniaxial stress (see Sonder (1990) and Zoback (1992) for more details), the Υ (Figure 4-5c) can be defined as a function of the reference and the local state of stresses as:

$$\gamma = \frac{sin\, 2\theta}{k - cos} \tag{4-2}$$

$$k = \frac{(S_{Hmax} - S_{hmin})}{S_L} \tag{4-3}$$

where θ (see Figure 4-6b) is the angle between regional maximum horizontal stress and the fault strike. The relative stress magnitudes of regional and local stresses ($k = \frac{(S_{Hmax} - S_{hmi})}{S_L}$) along with the angle (θ) between the local structure and regional stress orientation are significant parameters in the deviation of local stress orientation. In the case of thrust or normal faulting, the stress deflection is expected to be higher than that for a strike-slip regime (Sonder, 1990; Zoback, 1992).

Following this analytical approach (equation 4-2), I evaluate the stress rotation across the Balarud Lineament and whether it is a result of superimposed uniaxial local stress in the sedimentary cover. Figure 4-7 illustrates the rotation (Υ) contour (the angle between the regional stress orientation and the resultant local stress orientation) for various values of $\frac{(S_{Hmax} - S_{hmin})}{S_L}$. In the compressional state of stress, where $S_{Hmax} - S_{hmin}$ is high, (blue in Figure 4-7) the stress rotation is insignificant (less than 15°). However, where horizontal stress differences are relatively low (red in Figure 4-7), stress rotation is likely to occur, depending on the angle between regional stress state and fault strike.

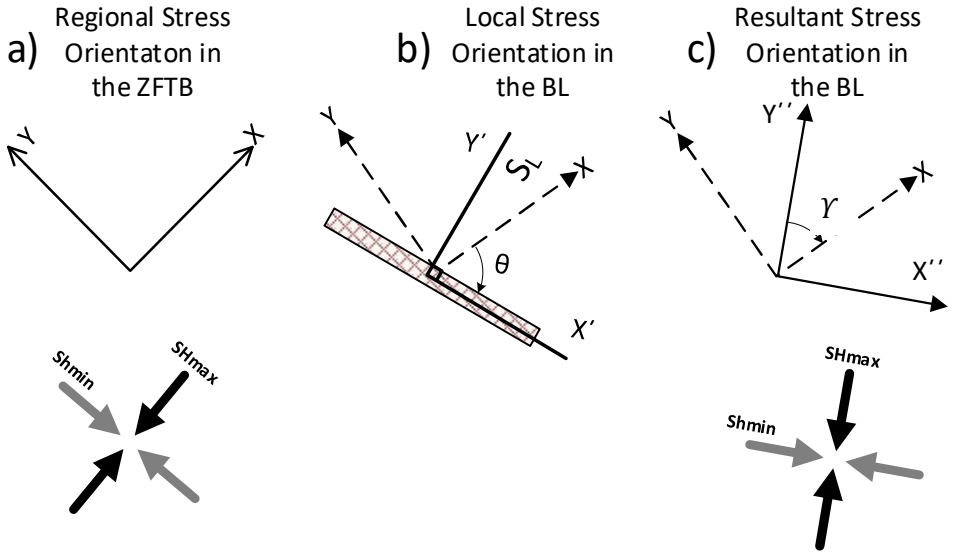

Figure 4-6: Schematic illustration of stress rotation due to local uniaxial stress: a) reference coordinate system in which the S_{Hmax} is the direction of X, b) local coordinate system where X' is aligned with the fault strike, and c) the resultant state of stress. The assumption is one principal stress that is assumed to be vertical (modified from Sonder (1990))

Since the regional orientation of S_{Hmax} in the ZFTB is 41°±15° and that for the Balarud Lineament strike is 293°±22° (113°±22°), the possible range of θ is around 72° to 90° (with average ≈75° - 80°) (please see Figure 4-7 inset). At seismogenic depths, the local stress changes (A_φ=2.1) are small with respect to the regional stress (A_φ=2.37). With this compressional stress state in the basement of the ZFTB, where S_{Hmax}-S_{hmin} ≈ 30 MPa/km (see Yaghoubi *et al.* (2021)), the local

uniaxial stress, σ_L, is not sufficient to deflect the stress orientations in the basement. For the case of the Balarud Lineament, the uniaxial stress perturbation (stress rotation due to the fault) at seismogenic depths is negligible. The regional stress difference dominates the local uniaxial stress ($\frac{(S_{Hmax}-S_{hmi})}{S_L} > 1$) at the seismogenic depth (10-15 km), causing the stress rotation to be insignificant ($|\Upsilon| \leq 15°$). This finding is consistent with the seismologically determined local S_{Hmax} direction around the Balarud Lineament, where the stress orientation is deflected around 10° counter-clockwise from the regional maximum horizontal orientation (the red box in Figure 4-7). The S_{Hmax} orientation around the BL has been constrained by the focal mechanism by 29°±8.5°, whereas the regional stress orientation in the ZFTB is 41°±15°. Note that, according to the World Stress Map criteria, the threshold for stress reorientation that acts as the second-order stress pattern is 15° (Zoback, 1992).

The stress orientation observed in eight exploration oil wells in the vicinity of the Balarud Lineament is 6°±11.0°. Assuming that the regional stress orientation follows the ZFTB in the S_{Hmax} direction of 41°±15° in the sedimentary cover, the average inferred rotation is therefore around 35°. As shown by the blue box in Figure 4-7, such a rotation implies that the ratio of the regional horizontal stress differences to local uniaxial stress in the southern part of Balarud Lineament is between 0.9 and 1.1. In the sedimentary rock where the regional state of stress has been constrained to be on the border between normal and that of the strike-slip faulting regime ($S_{hmin} < S_v \approx S_{Hmax}$), a moderate local uniaxial stress can cause stress deflection. This fact is the primary explanation of the variations in stress orientation seen in most of the oil and gas fields examined in the DE (Figure 4-1).

Our analysis of the regional and local stress fields in the vicinity of the Balarud Lineament indicates a second-order stress pattern occurring just in the sedimentary cover. In fact, the stress orientations in the sedimentary and the basement depths show two entirely distinct patterns due to the regional horizontal stress differences. The stress orientations constrained from inversion of the focal mechanisms are consistently in the NE-SW direction in all areas of the ZFTB. However, variations of stress orientations are seen in most of the investigated oil and gas fields in the area, from relatively abrupt changes of borehole breakouts to gradual variations over scales of several hundred meters (blue inward arrow in Figure 4-1).

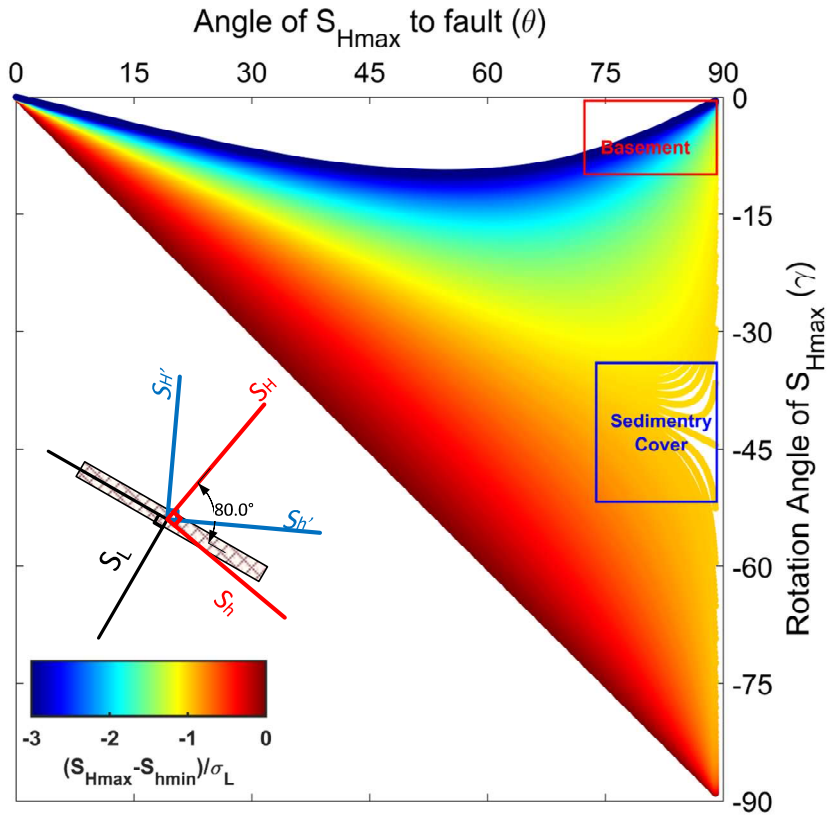

Figure 4-7: S_{Hmax} rotation as a function of the angle between local uniaxial stresses and regional maximum horizontal stresses around the Balarud Lineament. Colors represent the ratio of regional horizontal stress to the magnitude of local uniaxial stress (equation 4). The red and blue boxes indicate the possible stress variations (θ and Υ) due to the Balarud Lineament at seismogenic depths and the sedimentary cover, respectively. The inset is stress rotation (blue axes) from the reference stress (red axes) nearby the Balarud Lineament at shallow depths.

4.6 Wellbore Stability in the Northern DE's Hydrocarbon Fields

The Dezful Embayment within the ZFTB is one of the richest hydrocarbon regions in the world, hosting many onshore hydrocarbon fields. Major oil and gas fields are located in the southern part of the Balarud Lineament area, including the Danan, Chesmeh-Khush, Dalpari, Dehloran, Labsefied, and Paydar fields. Hydrocarbon resource extraction has been underway for more than 50 years. Many of the wells drilled in the vicinity of the Balarud Lineament for oil and gas production are vertical and highly deviated. Hence, it is necessary to understand the factors that control drilling performance in wells of different trajectories and orientations.

An unstable wellbore reduces drilling performance, resulting in penetration difficulties and, in the worst cases, loss of the hole through uncontrolled borehole sloughing and collapse. The optimum borehole trajectory that reduces the risk of instability directly depends on the principal stress magnitudes and orientations. The less difference between the largest and smallest stresses (S_1-S_3) acting normal to the borehole, the less instability a well will evidence. Therefore, finding the path

with the least deviatoric stress, given the requirement to develop an area strategically, helps to manage the potential instability for deviated and horizontal drilling (Dusseault *et al.*, 2001).

In the Zagros area, deviated oil and gas wells have traditionally been drilled in the NW-SW direction, perpendicular to the regional maximum horizontal stress orientation (S_{Hmax}). The ZFTB is typically considered to be NE-SW compressional, and NW-SW is believed to be the direction of lower drilling risk since the state of stress in the sedimentary cover is on the border of normal to the strike-slip faulting regime. However, in the area around the Balarud Lineament, where the stress orientation has been deflected in sedimentary cover by 35°, directional drilling in the NW-SW orientation has a high risk of failure and escalates the cost of drilling. In this section, utilizing the state of stress around the Balarud Lineament area, we briefly discuss wellbore stability analysis with a case study in the Paydar field.

Stress orientation was first determined from a detailed analysis of the ultrasonic image logs of two wells in the Paydar oil field (see Figure 3-3). The result indicates that the S_{hmin} direction (borehole breakout azimuth) in well P-7 is 100°±5, approximately the same as for well P-6, drilled about 4 km away (101°±12.1). Well P-7 has been drilled successfully, apart from mud loss problems in the 12¼" hole section drilled in the Gachsaran Formation. It was drilled vertically, with 130-138 pcf (2.08-2.21 g/cm^3) salt-saturated mud to 2963 m. An 8½" open hole was drilled into the Asmari Formation with 70 pcf (1.12 g/cm^3) oil-base mud (OBM) to 3910 m. After the insertion of a 7" liner, a 6½" open hole was drilled with OBM into the Sarvak Formation with 70 pcf (1.12 g/cm^3) mud to 4140 m (T.D. vertical hole).

Two sidetracks (ST-1 and ST-2) were successfully drilled into the Sarvak Formation from well P-7 using oil-based mud without encountering major instability, but the drilling experiences were different. For ST-2, it took 15 days to drill 717 meters at directional Azimuth 292° (S_{hmin} direction) with a mud weight of 63 pcf (1.01 g/cm^3), whereas for ST-1, it took 20 days to drill 212 meters at directional Azimuth 205° (S_{Hmax} direction) with a mud weight of 70 pcf (1.12 g/cm^3). The details for each sidetrack are presented in Table 4-2. The sidetrack drilled eastward took less time and had a lower mud weight than the one drilled southward.

Figure 4-8 shows the lower hemisphere representation of the minimum mud weight required to inhibit borehole breakouts at arbitrary wells in the northern DE, where the state of stress is on the border of normal and strike-slip faulting regimes in the N-S S_{Hmax} direction. For such a state of stress, the optimum borehole trajectory is in the minimum principal stress direction (E-S). For the case of ST-1 (Azimuth 205°), as shown in the figure, higher mud weights are needed because of the higher deviatoric stress acting on the borehole. The most unstable wells are those drilled in the direction of S_{Hmax}, and the most stable are those are drilled in the direction of S_{hmin} with deviations from vertical > 30°. Even though this is just one case study, we can generalize our experience to most of the well drilling planned in the northern Dezful Embayment where the S_{Hmax} follows a N-S direction. Since the

state of stress is on the border of a normal to a strike-slip faulting regime, the optimum borehole trajectory is in the direction of S_{hmin} (E-S).

Table 4-2: Detailed information on sidetracks of well PY-7.

ITEM	SD-1	SD-2
KOP	3928 m	3899 m
Azimuth	205^0	292^0
Final Inclination	90^0	90^0
Duration (Day)	20 Days	15 Days
Mud Weight	70 pcf	63 pcf
Drilled Meter	212 m	711m
Mud Type	OBM	OBM
MD	4140 m	4610 m
TVD	4025 m	4018m
Hole Size	6 1/8"	6 1/8"
Formation	Sarvak	Sarvak

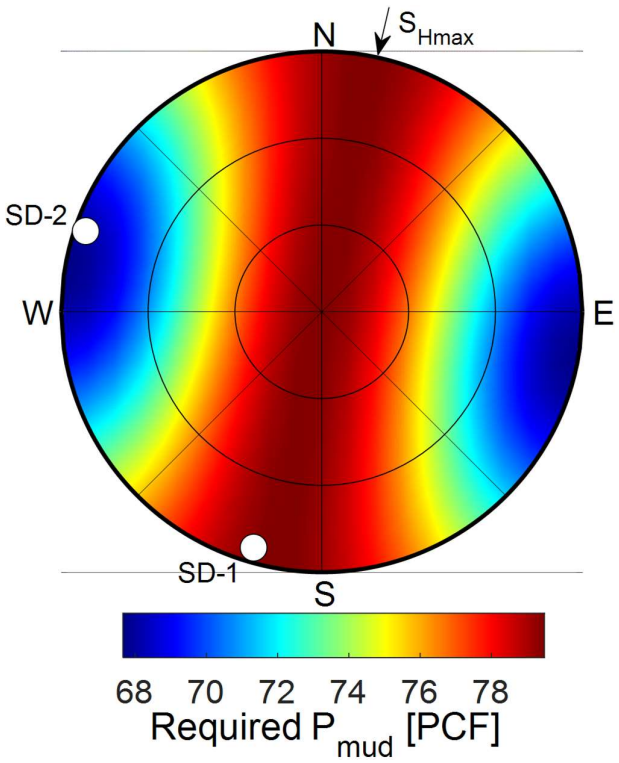

Figure 4-8: Required mud pressure to prevent borehole breakout in in arbitrarily oriented wells at depth of 4018m (Sarvak Formation), where $S_v=S_{Hmax}$=105 MPa, S_{hmin}=70 MPa, Pp=41MPa, and UCS=120 MPa.

4.7 Conclusion:

Stress deflection in the vicinity of the deep-seated Balarud Lineament in the Northern Dezful Embayment has been investigated using both borehole geophysical datasets and earthquake focal mechanism records. The seismologically determined local S_{Hmax} direction from 25 focal mechanisms (10-25 km) around the Balarud Lineament is 19.3°±8.5°. However, observations of borehole breakouts and tensile-induced fractures indicate that the dominant S_{Hmax} orientation is 5.7°±11.0° near the Balarud Lineament. Slip compatibility analysis on 22 earthquake focal mechanisms has demonstrated that the blind active BL is oriented 299.2°±16.0° (or 34.1°±10.8°). This local stress reorientation around the Balarud Lineament was evaluated quantitatively with the procedure presented by Sonder (1990). The relative regional and local stress magnitudes, along with the angle between local-fault and regional-stress orientations, are all significant parameters affecting the deviation of local stress orientation. We have found that the second-order stress pattern occurs just in the sedimentary cover in the vicinity of the Balarud Lineament, where the horizontal stress anisotropy is considerably less than that in the basement fault.

CHAPTER 5

Probabilistic Injection-Induced Fault Slip Assessment in Fox Creek Alberta[1]

Abstract

Energy extraction from underground resources triggers or induces seismic events because it changes pore pressure and temperature, leading to stress perturbation along pre-existing faults and fractures. A fault or fracture reactivates when the critical shear stress on the discontinuity plane exceeds the Coulomb criterion, causing slippage to occur. Slip constitutes an environmental and potential risk if induced seismic events are large enough to damage subsurface or surface infrastructure. Assessing stress state, pore pressure, and fault/fracture parameters as major input data for fault stability analysis is fraught with a broad range of uncertainties. This paper applies Monte Carlo probability assessment to estimate the potential slip tendency in a case study of Fox Creek, Alberta, Canada, involving seismic events induced by hydraulic fracturing (HF). Analyses of the local tectonic stress state and Mohr-Coulomb shear potential are displayed via a stability diagram, providing valuable insight for the fault slip tendency study. A probabilistic assessment is performed to identify the likelihood of induced seismicity and the slip tendency of faults crossing the Duvernay Formation shale. The results provide useful input for seismic hazard assessment and risk mitigation for local faults subjected to high-rate fluid injection.

5.1 Introduction

HF for energy extraction from underground conventional, unconventional, and geothermal resources is typically accompanied by anthropogenic seismicity (Bao and Eaton, 2016; Schultz *et al.*, 2017).

[1] An earlier version of this chapter was previously published as Yaghoubi, A., Dusseault, M., Mahbaz, S. and Leonenko, Y., 2020. Probabilistic Injection-Induced Fault Slip Assessment in Fox Creek Alberta. 54th US Rock Mechanics/Geomechanics Symposium.

Increasing pore pressure by injecting fluid into naturally fractured media leads to slip/shearing of faults and fractures, with resulting detectable earthquakes (Van der Baan *et al.*, 2013). The magnitude and rate of such human-made earthquakes are related to two sets of field parameters: controllable operational parameters, including fluid injection pressure, rate, and volume (Bao and Eaton, 2016); and uncontrollable subsurface parameters, including the state of stress, original pore pressure, size and density of pre-existing faults/fractures, fault/fracture orientation and frictional strength, permeability, compressibility, and other geomechanics parameters. The value of each uncontrollable parameter is characterized by wide inherent uncertainties; these uncertainties in rock mass properties are the key factors affecting the probabilistic assessment of fault/fracture slip. In HF treatments, accounting for parametric uncertainty by using appropriate statistical probability distributions leads to better decision-making/risk management for user-controlled parameters such as injection pressure.

Since December 2013, noticeably increased seismicity rates have been observed in Alberta's previously quiescent Fox Creek area (Figure 5-1). More than 200 Mw>2.5 earthquakes in the area are associated with HF operations, and include ones of M_W 4.1 on January 12, 2016 and M_W 3.9 on June 13, 2016 (Bao and Eaton, 2016; Schultz *et al.*, 2017). The recent anthropogenic seismicity for this area is among the largest magnitudes reported globally (Schultz *et al.*, 2018). To calculate the associated seismic risk due to fluid injection, the uncertainties associated with stress tensor, fault/fracture orientation, and frictional strength (Mohr-Coulomb parameters) must be incorporated in the evaluation process. Here, we apply a probabilistic assessment to investigate the potential slip tendency due to HF in a case study of Fox Creek incorporating the uncertainty distributions associated with Mohr Coulomb parameters.

5.2 Seismicity in Fox Creek

The Duvernay Formation, a prominent unconventional shale resource (Preston et al., 2016) that covers approximately 130,000 km^2 in west-central Alberta, is a source rock for conventional hydrocarbon resources. In recent years, shale gas and shale oil production from the Duvernay play has grown with the use of multi-stage HF technology. The formation is regionally heterogeneous; however, Fox Creek, in the northern part, has been evaluated as the highest and optimal development site in the Devonian West Shale Basin (Preston et al., 2016).

Fox Creek is also the only potential seismogenic region within the Duvernay depositional area (Atkinson 2016). Supported by high oil prices and new HF technology availability, development in the area started in 2012; since then, the seismicity rate has increased. Figure 5-1 shows the local cumulative seismicity since 2004. Most earthquakes in the area occur during HF treatments and are spatially and temporally restricted to the region around the horizontal wells. Bao and Eaton (2016) reported that the injection fluid volume is one of the main parameters controlling local induced seismicity. The clear example in Figure 5-2 shows that the cumulative fluid injection of 12.04×10^4

m^3 induced 115 earthquakes in one multistage well. The last post-treatment event was recorded 12 days after HF cessation. The same is true for spatial correlation; Figure 5-2b display the centroid depth distribution of earthquakes that occurred during HF completions, most of them restricted to the Duvernay Formation at 3.5 km. The small white circles in Figure 5-4a also represent earthquake events recorded in the area.

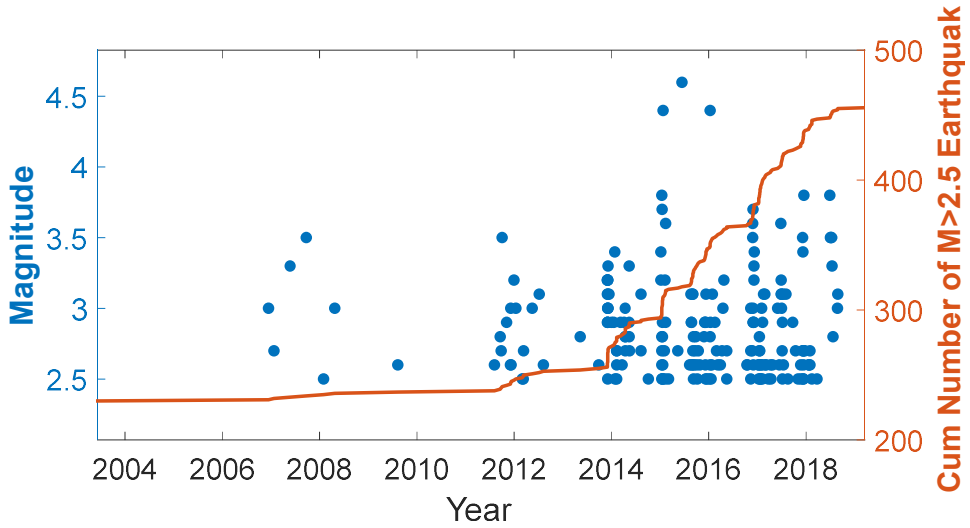

Figure 5-1: Cumulative number of earthquakes with Mw>2.5 around Fox Creek, Alberta, showing a rapid increase since 2012

The well-established linear Gutenberg-Richter (G-R) relation (Log(N)=a-bM) is a scientific scale for the magnitude versus frequency of seismicity occurring in any given area (Gutenberg & Richter, 1944). It expresses scale-independent behavior of earthquake magnitude. Both a- and b-values in the G-R relation can be estimated directly by plotting a cumulative number of earthquakes (N) with the magnitude ≥ M versus earthquake magnitude. Figure 5-3 shows the Gutenberg-Richter frequency-magnitude distribution (FMD) and b-values of 1087 induced earthquake events recorded during multistage HF treatment in Fox Creek. The dataset used to plot Figure 5-3 has been extracted from Bao and Eaton (2017). The recorded earthquake magnitudes range from $-0.54 \leq M_W \leq 3.2$, with a high frequency in the magnitude of -0.08 (magnitude threshold Mc). Since the b-value indicates the ratio between large versus small earthquakes, the relatively high b-value (≈2) indicates more small-to-large earthquakes recorded in the area, showing the typical seismicity range magnitude associated with HF. As can clearly be seen, the distribution shows two distinct b-values: b-value>1 (solid line) and b-value<1 (dashed line). This breakdown of G-R can occur when there are multiple seismic sources. Assuming a homogenous stress condition, we can explain the breakdown of G-R and two b-values by the existence of two fault/fracture geometry sets. As is the case with many HF treatments observed in different parts of the world, most earthquakes induced in the areas were recorded in response to small-size fracture slips (b-value>1). However, several anomalous large-magnitude-induced earthquakes have resulted from slip along a preexisting large-fault (>1000 m) reactivation.

The focus of this study is on assessing the potential for further slip along the existing fault that previously caused large earthquakes in the Fox Creek area.

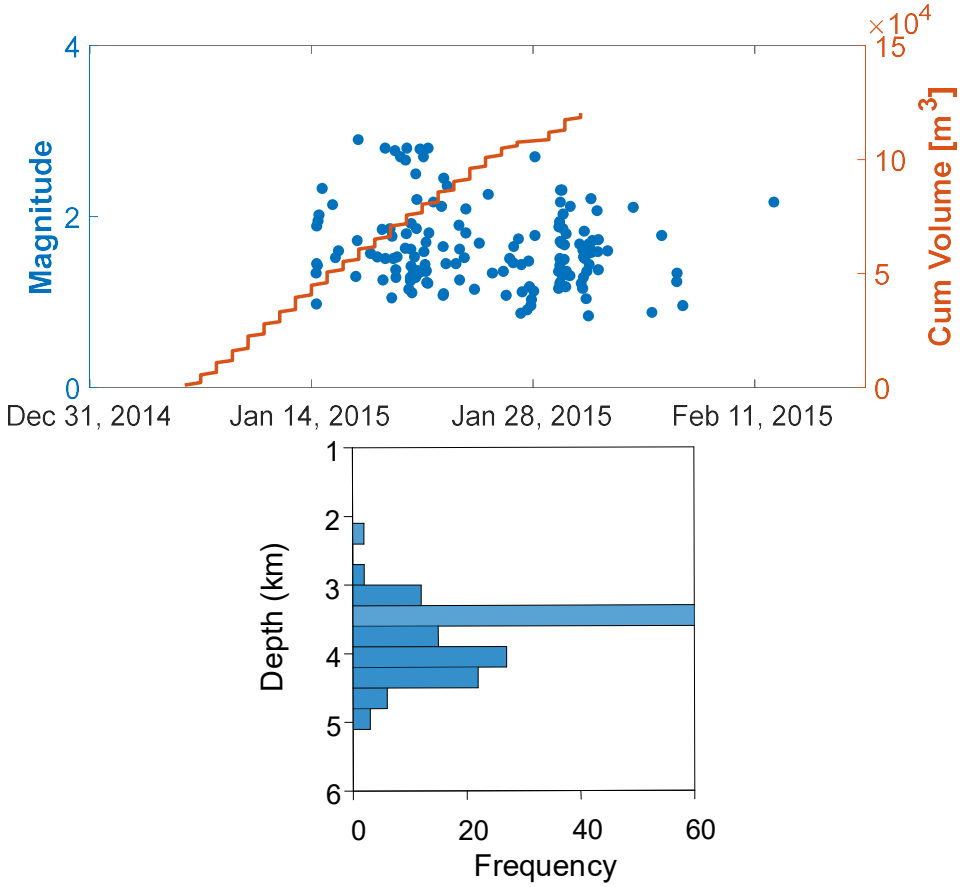

Figure 5-2: a) Cumulative fluid injection along with 115 induced earthquakes by magnitude through time in one multistage well in Fox Creek. b) Histogram showing the depth distribution of the local seismicity induced by 12.04×10^4 m3 fluid injection

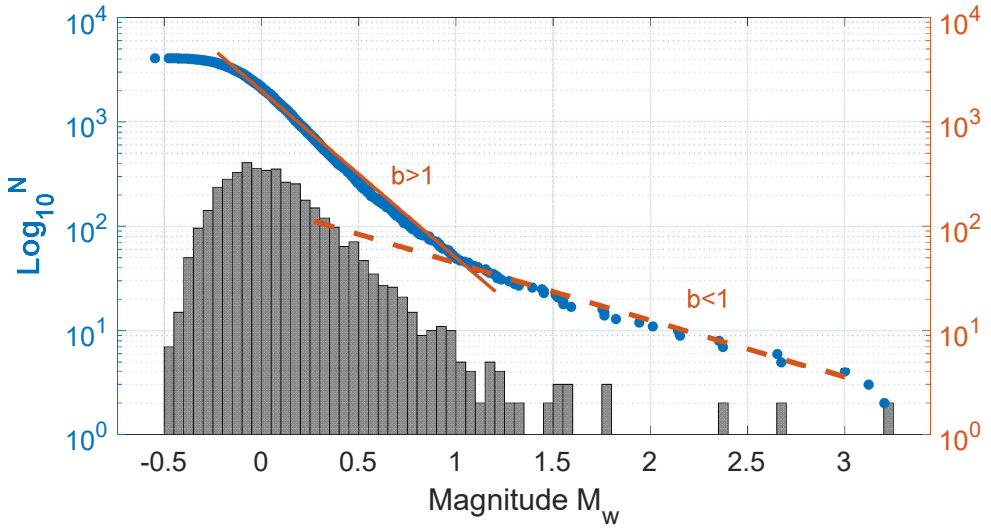

Figure 5-3: Gutenberg-Richter frequency-magnitude distribution of 1087 earthquakes recorded during multistage HF in Fox Creek

.

5.3 State of Stress in Fox Creek

Earthquake focal mechanisms provide valuable information on the relative stress magnitudes. Assuming that S_v is one of the principal stresses, an appropriate stress regime for each earthquake focal mechanism can be assigned based on the World Stress Map criteria (Table 3, Zoback (1992)). Assuming also that stress magnitudes at each depth are consistent with Coulomb frictional-failure theory for a coefficient of friction, Angelier (1984) introduced a quantity φ, measured by the equation ($\varphi = S_2\text{-}S_3/S_1\text{-}S_3$), where S1, S2, and S3 are respectively the greatest, intermediate, and minimum principal stresses. Depending on the magnitude of the intermediate relative to the other two, Angelier's shape parameter φ must fall between zero and one. Otherwise, none of the nodal planes will be geometrically consistent. Once the stress tensor is known, φ values and error limits can be computed along with the principal stresses and axes.

Simpson (1997) generalized the parameter φ values to provide a quantitative measure to determinate the relative stress magnitudes at each stress regime by expressing the equation, $A_\varphi = (n + 0.5) + (-1)^n(\varphi - 0.5)$ with n = 0, 1, 2, for normal, strike-slip and reverse faulting respectively. The Anderson fault parameter A_φ ranges continuously from 0 to 1 for normal, 1 to 2 for strike-slip, and 2 to 3 for reverse faults (Hurd, 2012; Yang and Hauksson, 2013). Applying the method to the 26 compiled focal mechanisms area of interest revealed that a strike-slip fault system ($A_\varphi \approx 1.56$) is dominant in the area. Note that we assume that the HF-induced stress perturbation and stress shadow effects are local and thus small relative to the regional stresses.

Different stress map studies have been performed around Alberta and particularly in the Fox Creek area. These studies also have indicated that the dominant state of stress in the area is the strike-slip stress regime where S_{Hmax} azimuth is NE-SW. I use the maximum likelihood method (MLEs) to find the best-fitting distribution for each uncertain parameter. The Normal, Lognormal, Gamma, and Weibull probability distribution have been tested for MLEs analysis. The best-fitting probability distribution value of each uncertain parameter is used as input for the Monte-Carlo simulation. Using inversion of the earthquake moment tensors and the study performed by Shen *et al.* (2019a) and Huge and Bell (2016) on the state of stress in Fox Creek, I constrained the three principal stress magnitudes at depth 3.4 km as S_v=85±0.85 MPa, S_{hmin}=69.4±3.1 MPa, and S_{Hmax}=103±5.2 MPa. A high pore pressure gradient with a mean value of 16±1.5 kPa/m in the Duvernay Formation plays an important role in seismicity generation during HF treatment. Drilling-induced tensile fractures and borehole breakouts observed in wellbore image logs indicate that the maximum horizontal stress (S_{Hmax}) azimuth is 35° in the region. The black inward-pointing arrow line in Figure 5-4 shows S_{Hmax} orientations around Fox Creek (Haug and Bell, 2016b).

5.4 Faults in Fox Creek

Prior to HF stimulation activity in the Fox Creek area, little was known about the possible existence of faults in the development area. Neither 2D/3D reflection seismic nor geological mapping detected diagnostic structural features in the Duvernay Formation that could be interpreted as significant faults before HF operation (Chopra 2017). However, existing faults can now be inferred from induced seismic events. Using earthquake focal mechanisms that provide two nodal planes, I can deduce the possible fault plane. Having applied a strike-slip faulting regime with the S_{Hmax} azimuth of 35°, we investigate which of two nodal planes of the earthquake focal mechanisms were geometrically optimal for the inferred fault plane (Figure 5-4). I also constrained the fault segment size based on the earthquake scaling relationship (Figure 5-5).

Figure 5-4b includes a Mohr Diagram with a representative strike-slip focal event (M_w=3, 2015-08-19). The interpreted focal mechanism was compiled by Schultz et al. (2017). The stress magnitudes in the diagram are defined based on the inversion of focal mechanisms. The uncertainties associated with the three principal stress magnitudes are shown with green error bars. The red and black circular points in Figure 5-4b corresponds to the shear and normal stresses acting on nodal planes. As shown, for this example, the fault plane (red) striking N-S and dipping 79° to the E is most likely to slip and is the preferred nodal plane. The same analysis has been performed for the other earthquake focal mechanisms shown in Figure 5-4a. The red line crossing each focal beachball represents the preferred fault plane. As illustrated, most diagnostic fault planes in the area are in the N-S direction, which seems already to be critically stressed.

Analyzing HF seismicity also provides fault locations and approximate fault spatial geometries. The area's fault sizes are constrained using earthquake event magnitudes, stress drop, and shear slip-induced during the simulation. The fault and slip length corresponds to the earthquake's magnitude. The relationship between earthquake magnitude, stress drop, and fracture/fault size slip follows (Kanamori and Anderson, 1975)

$$W = \sqrt[3]{\frac{4(\lambda+G)}{\pi(\lambda+2G)}\frac{M_0}{W\Delta\sigma}} \quad (1)$$

$$W = \sqrt{\frac{M_0}{\mathrm{GD}}\frac{1}{w}} \quad (2)$$

Where W is fault width, G is shear modulus, λ is Lamé's constant, M_w is moment magnitude, D is fault slip, w is length to width ratio, and Δσ is stress drop. The same approach was performed to constrain the size of fractures from induced seismicity magnitudes during HF in the Barnett shale (Yaghoubi, 2019). Figure 5-5 shows the fault sizes (dip interval) for each of the eleven focal earthquakes mapped in Figure 5-4a. The moment magnitude, fault/fracture size, and its shear slip have been plotted in Figure 5-5, assuming that μ is 10 GPa and $\frac{\mathrm{L}}{\mathrm{W}} = 0.01$. Holmgren *et al.* (2019)

shows that the average stress drop for induced seismicity in the Western Canada Sedimentary Basin is around 7.5±0.5 MPa. The length to width ratio of 0.01 has been chosen based on sensitivity analysis between fault length and seismicity cloud in the area.

The result shows that the approximate range of diagnostic fault dip dimensions in is ranging between 150 and 2600 m. Considering the figure, the maximum slip due to HF injection completions is estimated to be around 0.5 m. This may be among the largest fault slip values reported for fluid injection globally (Schultz *et al.*, 2018). The M_w 4.1 fault dip dimensions of 2600 meters and strike length 260 m of M_w 4.1 earthquake is consistent with appreciable dip direction seismicity in the area. This indicated long dip length indicates the injected-induced seismicity in this area are mostly involved with basement fault reactivation.

5.5 Probabilistic Fault Slip Assessment

Fault/fracture slip depends on the relative stress magnitude, the angle between the principal stress directions and the fault plane, and the coefficient of friction μ (Morris *et al.*, 1996). The slip tendency on a pre-existing cohesionless fault can be defined in terms of the Mohr-Coulomb shear failure:

$$\tau = \mu\sigma_n \quad (3)$$

Fault plane slip is more likely to occur when the resolved shear stress, τ, equals, or is very close to the frictional resistance of the fault surface; the fault is then called "critically stressed". The deterministic fault slip tendency is expressed as the ratio of normal stress to shear stress on a potential sliding surface ($\tau/\sigma_n \geq \mu$).

The deterministic approach considers just one single analysis as finite and therefore underestimates the potential risk. Figure 5-6 shows a lower hemisphere stereonet of the slip-tendency in a case where the state of stress is a strike-slip faulting regime with an average S_{Hmax} orientation of N35°E and hydrostatic pore pressure. Each location within the graph represents a pole perpendicular to a fault plane. The red color shows where less injection pressure is needed for reactive faults.

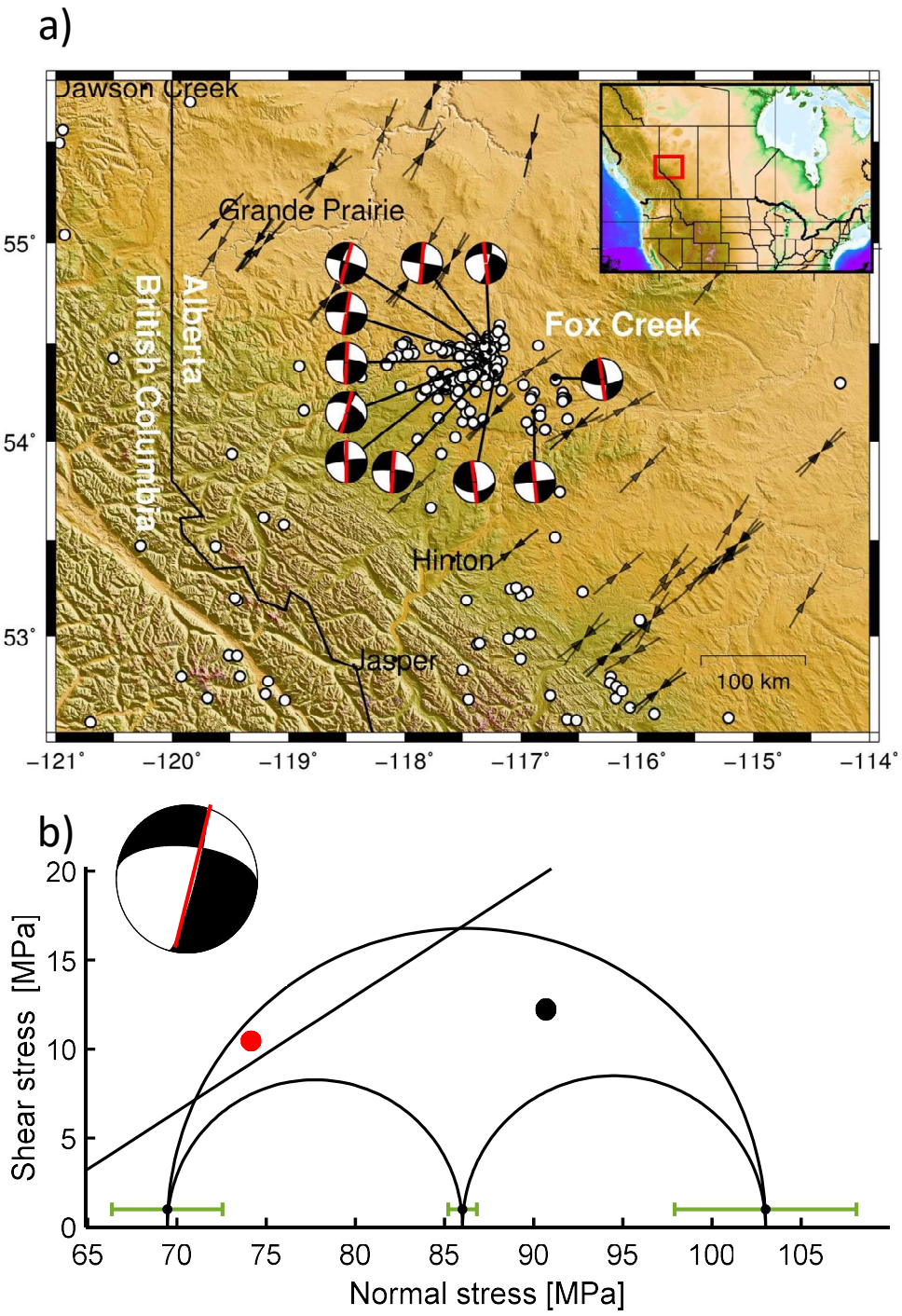

Figure 5-4: a) Seismicity around Fox Creek, Alberta. White circles represent earthquakes recorded in the area. The eleven interpreted focal mechanisms are compiled from Schultz et al. (2017), b) 3D Mohr's circle showing representative strike-slip earthquake focal (M_w=3, 2015-08-19) (Pp=60 MPa and μ=0.65).

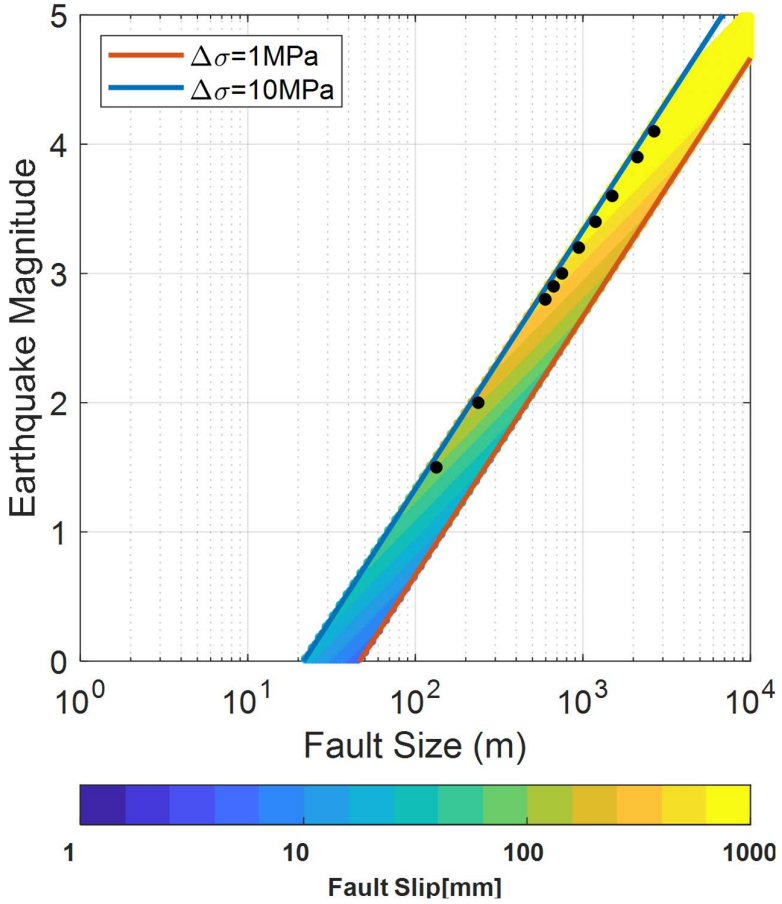

Figure 5-5: a) Relation between fault patch size and M_w (Moment magnitude). The straight lines give the relations for fault with two constant stress drops 0.1 and 10 MPa. Colors show the amount of fault slip corresponding to M_w and fault size. The black points represent eleven focal earthquakes displayed in Figure 5-4a. The color bar is a log10 base scale.

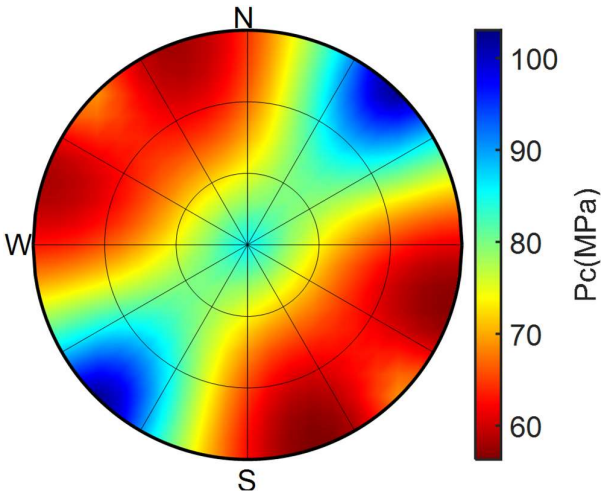

Figure 5-6: Lower hemisphere stereonet plot illustrates the deterministic approach to the slip-tendency (critical injection pressure).

The slip tendency in a probabilistic analysis, however, considers inherent uncertainties for each input variable, including stress magnitudes and orientation, fault dip direction, angle, and frictional

strength (Jones and Hillis, 2003; Walsh III and Zoback, 2016; Wang *et al.*, 2010). Each input variable effective in the Mohr-Coulomb shear failure can be assigned as a random sample with a specific mean and variance. An appropriate probability distribution has been an assignment for each of the uncertain input parameters in the model. The probability of failure can be defined as

$$P_f = P[\,\tau - \mu\sigma_n \leq 0] \tag{4}$$

Probabilistic slip tendency analysis is therefore comprehensive and suitable for evaluating multiple scenarios. In this work, a Monte Carlo simulation with 10000 scenarios have been applied to evaluate uncertainties associated with geomechanics parameters.

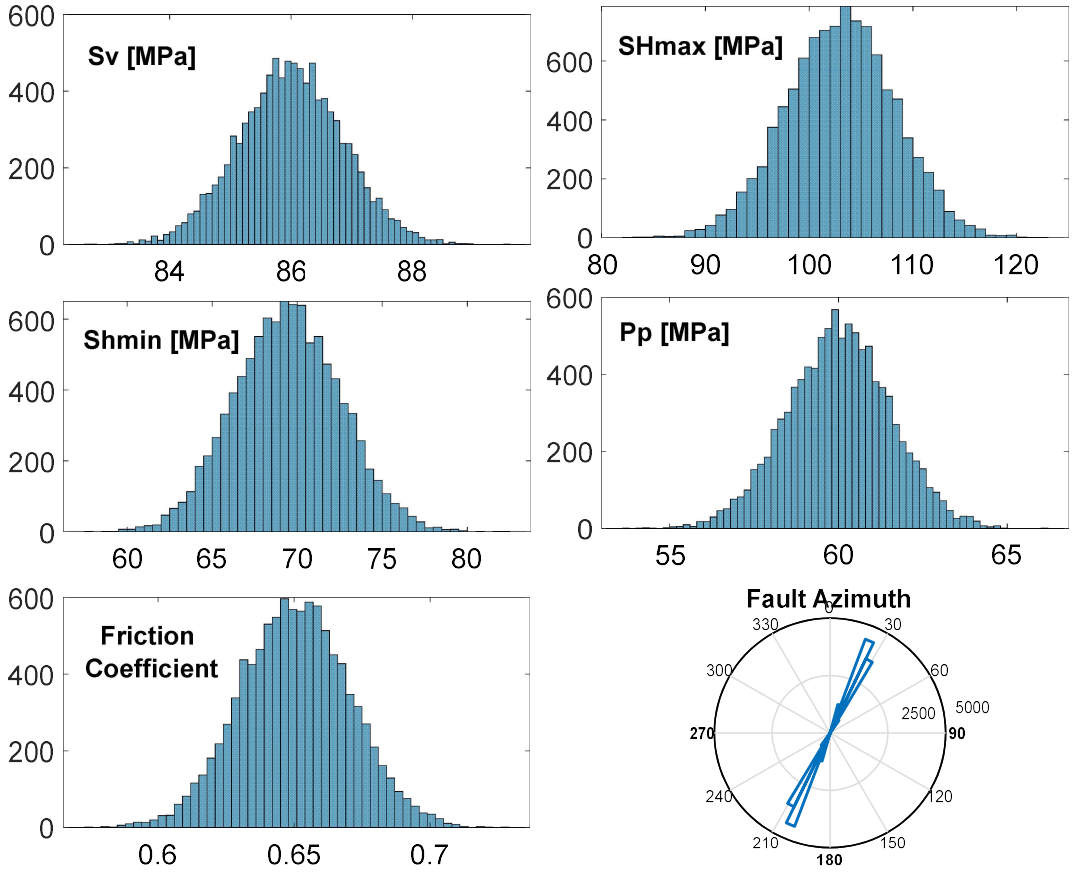

Figure 5-7: Statistical Mohr-Coulomb variables used in Monte Carlo simulation.

Figure 5-7 shows the statistical geomechanics variables used in the Monte Carlo simulation. A probabilistic assessment is performed to identify the likelihood of induced seismicity and the slip tendency of faults detected from the earthquake focal mechanism. The probability of faults slipping as a function of pressure injection is illustrated in Figure 5-7. The result is the cumulative distribution of the pore pressure required to prevent slip on each fault patch. The analysis shows a high likelihood of slip due to HF in faults crossing the Duvernay Formation shale. For faults inferred from the

earthquake focal mechanism at an injection pressure of 60 MPa, the probability of slip is between 60% to 80%. The result shows that N-S faults are likely to slip with even a small increase in pressure.

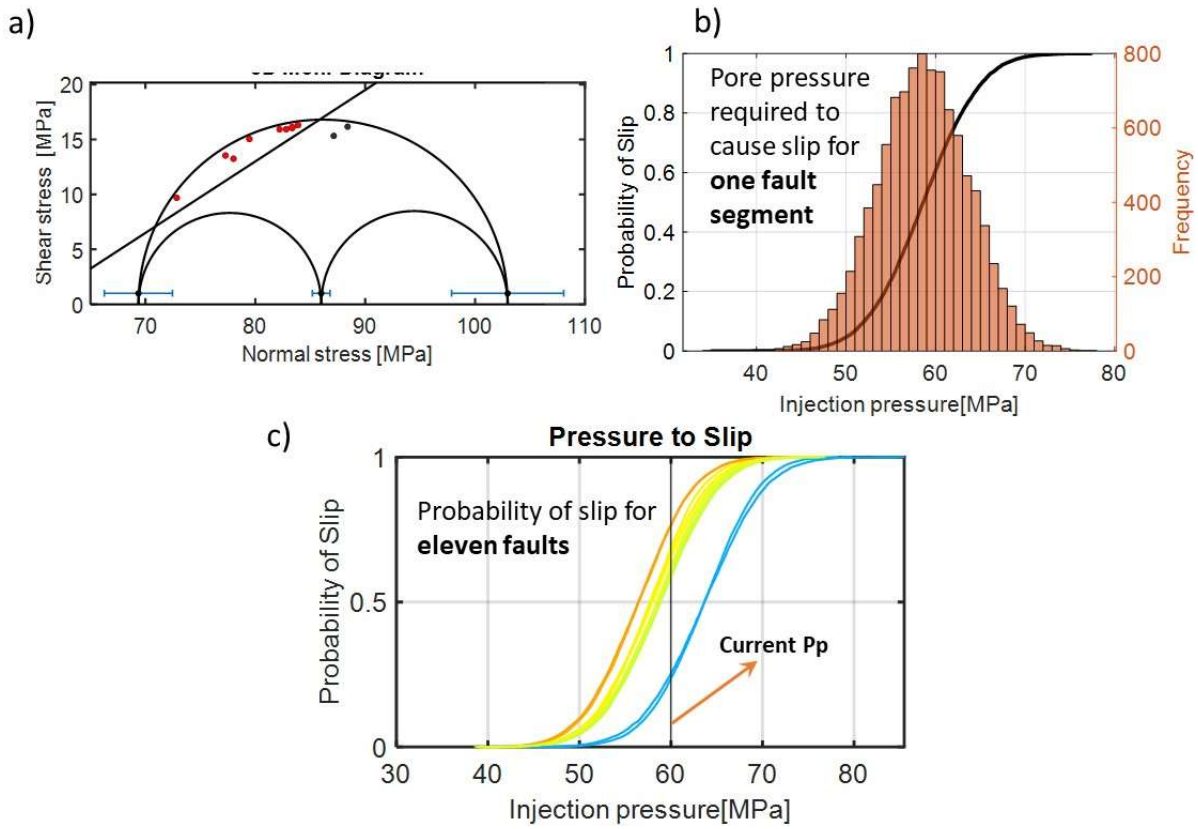

Figure 5-8: a) 3D Mohr's circle showing reactivated fault (red points) and stable faults (black points) b) injection pressure required to cause slip for one fault segment and c) Cumulative probability function of the injection pressure required to cause slip. Each curve represents one fault segment

5.6 Conclusions

I use a probabilistic approach to determine the likelihood of fault slip as a function of injection pressure due to HF treatment near Fox Creek. The approach allows us to account for the inherent uncertainties associated with geomechanics parameters. Mapped faults (location, strike, dip, length, depth) in the area need to be identified for a slip tendency probabilistic approach. Using the interpreted focal mechanics and induced seismicity, faults oriented approximately N-S were detected in the Fox Creek area. Formal stress inversion analysis of the focal plane mechanism solutions demonstrates that the dominant stress state in the area is a strike-slip faulting regime with A_{φ} =1. 56. A Monte Carlo simulation has been applied to address uncertainties associated with geomechanics parameter inputs. Each geomechanics parameter (Figure 5-8) was expressed as a stochastic distribution. The probabilistic analysis demonstrates that almost all the fault planes examined would become unstable with a modest change of pore pressure. Therefore, there is a heightened risk of induced earthquakes as a result of HF in the region.

CHAPTER 6

Injection-Induced Fault Slip Assessment in Montney Formation in Western Canada[1]

Abstract

Hydraulic stimulation to enhance energy extraction from geothermal and unconventional resources is typically accompanied by seismicity because injection changes pore pressures and temperatures, facilitating slippage of fractures and faults. Induced seismicity carries potential risk if events are large enough to damage infrastructure. The uncertainty invariably associated with the state of stress measurements and subsurface geomechanics parameters affects the analysis of fault slip and seismicity induced resulting from hydraulic fracturing. In this study, a probabilistic approach is used to assess the slip tendency of known faults crossing the compartmentalized Montney Formation of western Alberta and northeastern British Columbia. We first divide the formation into four different stress areas based on pore pressure deviations from hydrostatic. In each stress area, geomechanics parameters are expressed as probability distributions using multivariable datasets from borehole petrophysical data to injection-induced focal mechanisms. Monte Carlo simulations are applied to assess the potential slip tendency of local faults. We display the cumulative distribution function of critical pore pressure to cause slip on each fault by using analyses of the parameters of the Mohr–Coulomb shear failure criterion and local tectonic stress state. The results provide useful input for seismic hazard assessment and risk mitigation for local faults affected by high-rate fluid injection.

[1] A slightly shorter version of this chapter has been published as Yaghoubi, A., Dusseault, M. and Leonenko, Y., 2022. Injection-induced fault slip assessment in Montney Formation in Western Canada. Scientific reports, 12(1): 1-12.

6.1 Introduction

The Montney Formation, a prominent unconventional shale gas and liquids resource, covers approximately 130,000 km^2 in northwest Alberta and northeast British Columbia. The area is one of the most productive unconventional hydrocarbon resources in the Western Canada Sedimentary Basin (WCSB). According to a 2013 study by the British Columbia Oil and Gas Commission and the Alberta Energy Regulator, the Montney Formation can produce 12,719 billion m³ of marketable natural gas, 2,308 million m³ of marketable natural gas liquids (NGL), and 179 million m^3 of marketable oil (National Energy Board, 2013). By the end of 2019, more than 3600 wells had been completed in the Montney Formation just in British Columbia (BC Oil and Gas Commission, 2019).

Shale gas and shale oil production from the Montney play has grown with the use of multi-stage HF (Hydraulic Fracture stimulation) technology. Supported by high oil prices and new HF technology availability, development started in 2005 and accelerated significantly in 2011; since then, the seismicity rate has increased(Atkinson *et al.*, 2016; Babaie Mahani *et al.*, 2019; Babaie Mahani *et al.*, 2017; Ghofrani and Atkinson, 2020). More than 200 M_W >3 earthquakes within the area 52°N–60°N and 114°W-126°W are spatiotemporally associated with HF operations (Figure 6-1). In the last decade, noticeably higher seismicity rates have been observed in previously quiescent areas of British Columbia and western Alberta (Figure 6-1) (Atkinson *et al.*, 2016; Babaie Mahani *et al.*, 2019; Babaie Mahani *et al.*, 2017; Ghofrani and Atkinson, 2020). The anthropogenic seismicity for this area includes some of the largest M_W values reported globally, including events near Fort St. John of M_W 4.6 on August 17, 2015 (Babaie Mahani *et al.*, 2017), and M_W 4.2 on November 30, 2018 (Roth *et al.*, 2022). Most of these occur during HF treatments and are spatially and temporally restricted to the region around the wells(Atkinson *et al.*, 2016). M_W 4.6 on August 17, 2015, for example, occurred after five days of fluid injection of 65,000 m^3 in the Lower Montney Formation (depth of 1.9 km) (Babaie Mahani *et al.*, 2017) (Figure 6-2). The area between Fort St. John and Dawson Creek, BC (the Kiskatinaw area) and the northern Montney trend are the seismogenic regions within the Montney depositional area (Visser *et al.*, 2020) (Figure 6-3).

HF operations have not always resulted in injection-induced seismicity in the study area. Induced seismicity clouds show a high likelihood of slip due to HF in the area around the Kiskatinaw area as well as in the northwestern Montney area (Figure 6-3). Even in these areas, not all HF stimulation activities were associated with induced seismicity (Atkinson *et al.*, 2016; Ghofrani and Atkinson, 2020). Atkinson *et al.* (2016) highlight that of 12,289 wells drilled in the WSCB between 1985-and 2015 and hydraulically stimulated, only 0.3% were associated with injected-induced earthquakes of M≥3. A subsequent study by Ghofrani and Atkinson (2020) determined that 0.5 to 1% of HF wells drilled in WCSB between 2009 and 2019 were associated with induced seismicity M≥3, which indicates that the rate has steadily increased over time. They have observed that the associated rate of M ≥ 3 earthquakes appears to be formation related; the Montney Formation has an associated rate of

%2 whereas that rate for the Duvernay Formation is 6% and that of others is much lower. Questions arise as to which mechanisms are responsible and what parameters control regional injection-induced seismicity in the study area.

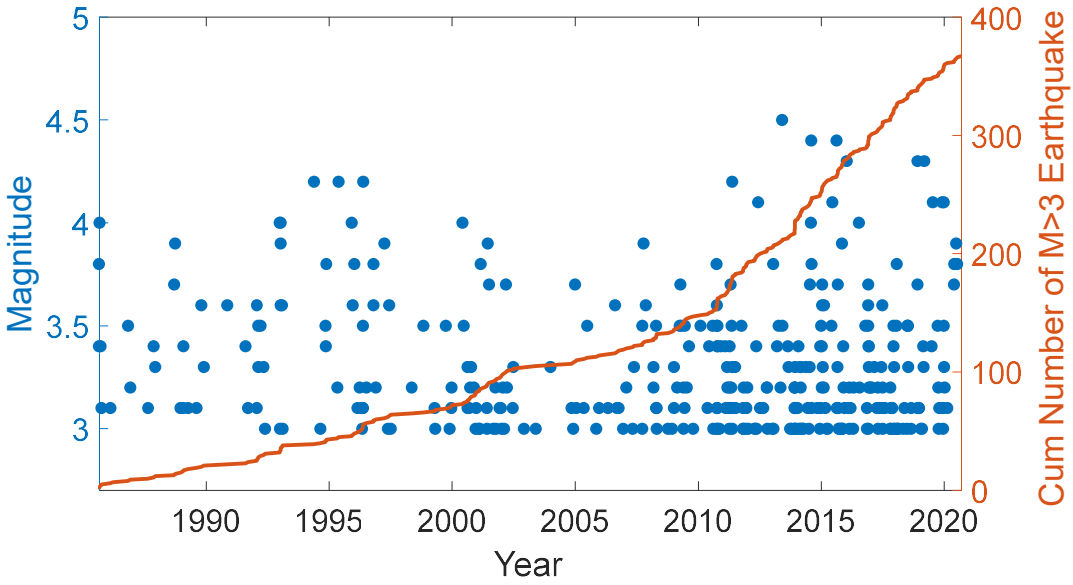

Figure 6-1: Cumulative number of earthquakes with Mw >3 within areas 52°N to 60°N and 114°W to 126°W in Western Canada, indicating a rapid increase in the last decade.

Three mechanisms can be considered for injection-induced seismicity. First, increasing pore pressure during HF decreases the normal effective stresses acting on fault/fracture surfaces, inducing shear slip, and causing earthquakes (Hennings *et al.*, 2019; Morris *et al.*, 1996; Morris *et al.*, 2021; Walsh III and Zoback, 2016). Second, coupled matrix poroelastic effects during HF in a fractured rock cause stress changes. Therefore, slippage/earthquakes may occur, perhaps not directly related to an increase in local pore pressure, but sufficient to trigger slip along a critically stressed discontinuity (Deng *et al.*, 2016; Wang *et al.*, 2019; Wang *et al.*, 2015; Yu *et al.*, 2019). Deng *et al.* (2016) performed a fully coupled poroelastic simulation to evaluate the spatiotemporal changes of solid matrix stresses and their relation to the 2013 Crooked Lake seismicity sequence in central Alberta. Their results showed that the poroelastic mechanism is responsible for both delayed and immediate injection-induced seismicity (Deng *et al.*, 2016). The same causative mechanism has been proposed by Wang *et al.* (2019) and Konstantinovskaya *et al.* (2021) to account for injection-induced seismicity in WCSB. Third, cases may arise in which faults can very slowly transform into a slippage state during HF, and fluid injection triggers aseismic (stable) slip (Eyre *et al.*, 2019; Eyre *et al.*, 2022; Yu *et al.*, 2021a) sufficiently far from the reservoir depth. Studies by Eyre *et al.* (2019), Yu *et al.* (2021a), and Eyre *et al.* (2022) suggest that induced earthquakes in WCSB may be attributed to aseismic slip loading. Another study (Yu *et al.*, 2019) suggests a combination of direct pore pressure diffusion and

poroelastic stress changes as the possible mechanism behind injection-induced seismicity in the Montney Formation. For this current study, the assessment of injection fault slips is based on the first mechanism: fluid injection causing normal stresses to decrease within the fault plane, which in turn, destabilizes the fault.

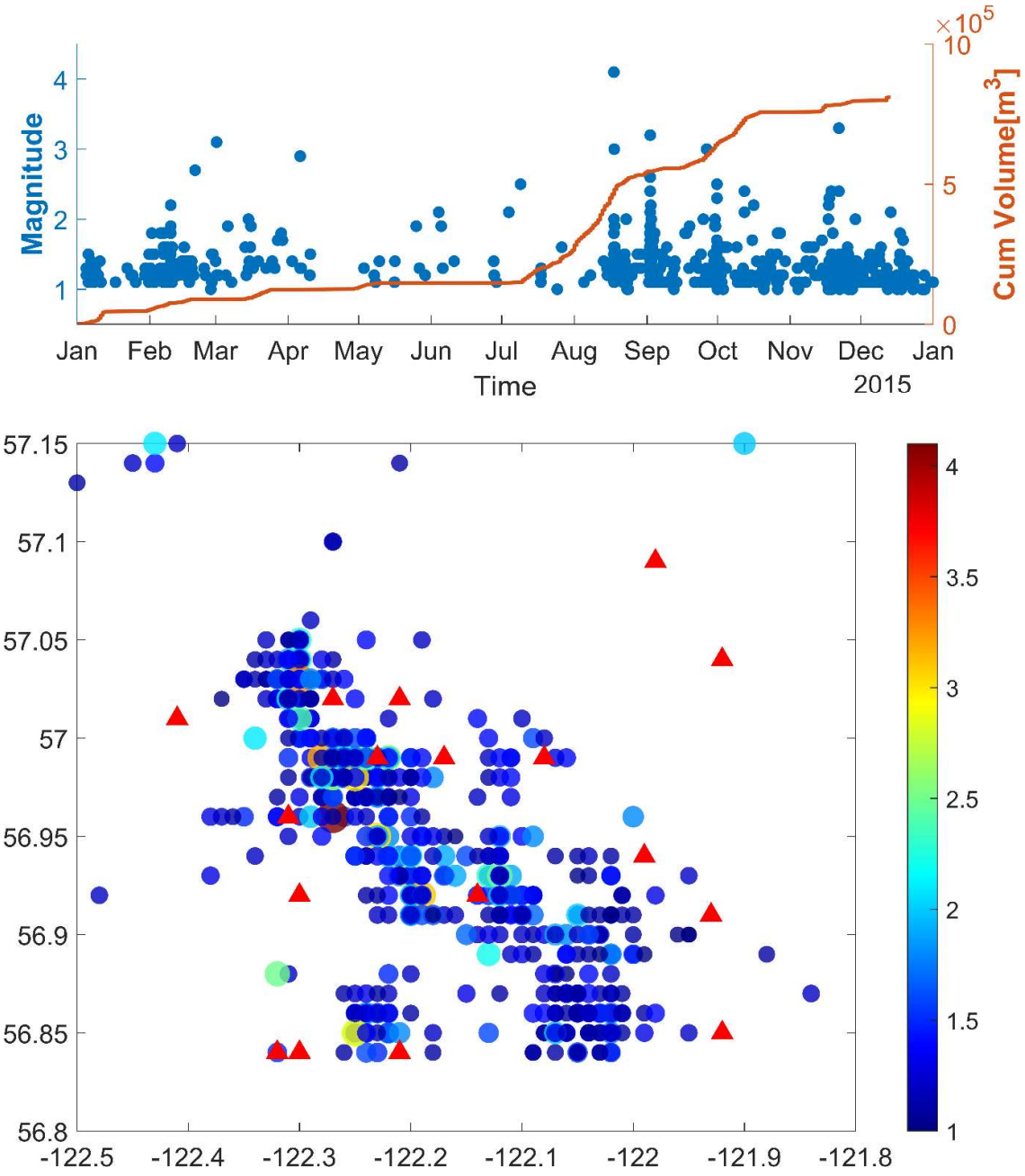

Figure 6-2: a) Approximately 8.2×10^5 m^3 of fluid have been injected in 16 wells in the Kiskatinaw area, resulting in 617 earthquakes, including event M_W 4.6 on August 17, 2015. b) Map showing the distribution of local seismicity (colored circles) and the locations of the 16 wells (green triangles). Color bars indicate the magnitude of the earthquake.

Three mechanisms can be considered for injection-induced seismicity. First, increasing pore pressure during HF decreases the normal effective stresses acting on fault/fracture surfaces, inducing shear slip, and causing earthquakes (Hennings *et al.*, 2019; Morris *et al.*, 1996; Morris *et al.*, 2021;

Walsh III and Zoback, 2016). Second, coupled matrix poroelastic effects during HF in a fractured rock cause stress changes. Therefore, slippage/earthquakes may occur, perhaps not directly related to an increase in local pore pressure, but sufficient to trigger slip along a critically stressed discontinuity (Deng *et al.*, 2016; Wang *et al.*, 2019; Wang *et al.*, 2015; Yu *et al.*, 2019). Deng *et al.* (2016) performed a fully coupled poroelastic simulation to evaluate the spatiotemporal changes of solid matrix stresses and their relation to the 2013 Crooked Lake seismicity sequence in central Alberta. Their results showed that the poroelastic mechanism is responsible for both delayed and immediate injection-induced seismicity (Deng *et al.*, 2016). The same causative mechanism has been proposed by Wang *et al.* (2019) and Konstantinovskaya *et al.* (2021) to account for injection-induced seismicity in WCSB. Third, cases may arise in which faults can very slowly transform into a slippage state during HF, and fluid injection triggers aseismic (stable) slip (Eyre *et al.*, 2019; Eyre *et al.*, 2022; Yu *et al.*, 2021a) sufficiently far from the reservoir depth. Studies by Eyre *et al.* (2019), Yu *et al.* (2021a), and Eyre *et al.* (2022) suggest that induced earthquakes in WCSB may be attributed to aseismic slip loading. Another study (Yu *et al.*, 2019) suggests a combination of direct pore pressure diffusion and poroelastic stress changes as the possible mechanism behind injection-induced seismicity in the Montney Formation. For this current study, the assessment of injection fault slips is based on the first mechanism: fluid injection causing normal stresses to decrease within the fault plane, which in turn, destabilizes the fault.

The magnitude and rate of anthropogenic earthquakes are influenced by two sets of field parameters directly: the controllable operational parameters, including fluid injection pressure (Walsh III and Zoback, 2016), rate (Weingarten *et al.*, 2015), viscosity (Cornelio *et al.*, 2020), volume (McGarr, 2014), and type (Ries *et al.*, 2020); and, the uncontrollable subsurface parameters, including stress state (Hennings *et al.*, 2019) and pore pressure (Eaton and Schultz, 2018), size and density of pre-existing faults/fractures (Yaghoubi, 2019), fault/fracture orientation (Yaghoubi, 2019) and frictional strength, steady-state coefficient of friction (Kohli and Zoback, 2013) and rock's permeability and compressibility (Chang and Yoon, 2022). However, wide inherent uncertainty affects the value of each uncontrollable parameter. In HF treatments, accounting for parametric uncertainty by using appropriate probability distributions (Morris *et al.*, 2021; Walsh III and Zoback, 2016) leads to better decision-making for user-controlled parameters such as injection pressure. Because of large-scale injection-induced earthquakes in the Montney Formation, probabilistic fault slip assessment is essential to improve understanding of seismic hazards in the region. This is of importance because no studies on such a scale have been presented in the Montney Formation. Similar studies have been performed in Fox Creek, Alberta (Shen *et al.*, 2019b), north-central Oklahoma (Walsh III and Zoback, 2016), the Fort Worth Basin (Hennings *et al.*, 2019), and the Delaware Basin in Texas (Morris *et al.*, 2021).

This paper aims to assess the fault slip tendency resulting from fluid injection into the Montney Formation. Herein, we define a geomechanical zoning or stress area model based on pore pressure variation in the Montney Formation. I then assess all known faults as potential sites of injection-induced seismicity. In each stress area, we constrain uncertainties associated with each effective uncontrollable geomechanical parameter, such as stress tensors, pore pressure, multiple fault/fracture orientations, and frictional strengths. Then, we apply a probabilistic assessment to investigate the potential fault slip tendency due to HF in the formation, incorporating the uncertainty distributions associated with Mohr-Coulomb strength parameters. Besides the HF stimulations, the resulting probabilistic fault stability map in the region can be used as a baseline map for any fluid injection projects such as wastewater disposal, CO_2 sequestration as well as geothermal energy extraction.

6.2 State of Stress in the Montney Formation

Pore pressure is an integral part of the state of stress in a region. Different studies have shown that pore pressure distribution in the Montney Formation is hydrologically subdivided and, consequently, the formation is compartmentalized (Chatellier and Euzen, 2021; Chatellier et al., 2018; Euzen et al., 2021). Figure 6-4 sets out the lateral pore pressure variation of the Montney Formation mapped from direct pore pressure measurements taken from datasets provided by geoLOGIC™ Systems and Wozniakowska and Eaton (2020). The study by Chatellier and Euzen (2021); (Chatellier et al., 2018) shows that the Montney Formation pore pressure compartments are due to hidden faults that do not appear in the 3D seismic dataset but rather have been determined by analyzing drilling cuttings and gas compositions (gas chromatography) and Diagnostic Fracture Injection Test (DFIT) results. Spatial variations of the pore pressure gradient (Figure 6-4) indicate that the deeper, western side of the formation (in British Columbia) has a higher value than the shallower, eastern side (in Alberta).

Based on pore pressure variation, we subdivided the Montney Formation into four different areas and used the K-means MATLAB™ function to group pore pressure gradient datasets. The main reason for subdividing the formation is three principal stress magnitudes are intrinsically linked to the pore pressure. Therefore, when the pore pressure is high, there is little difference between the three principal stresses. Due to the fact that pore pressure is an important parameter in fault stability assessment, and since our analysis is based on injection pressure, dividing the formation into distinct areas allows a more accurate fault assessment. Note that the clustering is solely based on the value of the pore pressure gradient. The existence of faults or other factors such as stratigraphic variations and oil compositional differences in reservoir compartments has not been considered for the clustering. For the purpose of our assessment, we used the pore pressure that corresponded most closely with each fault patch (Figure 6-4).

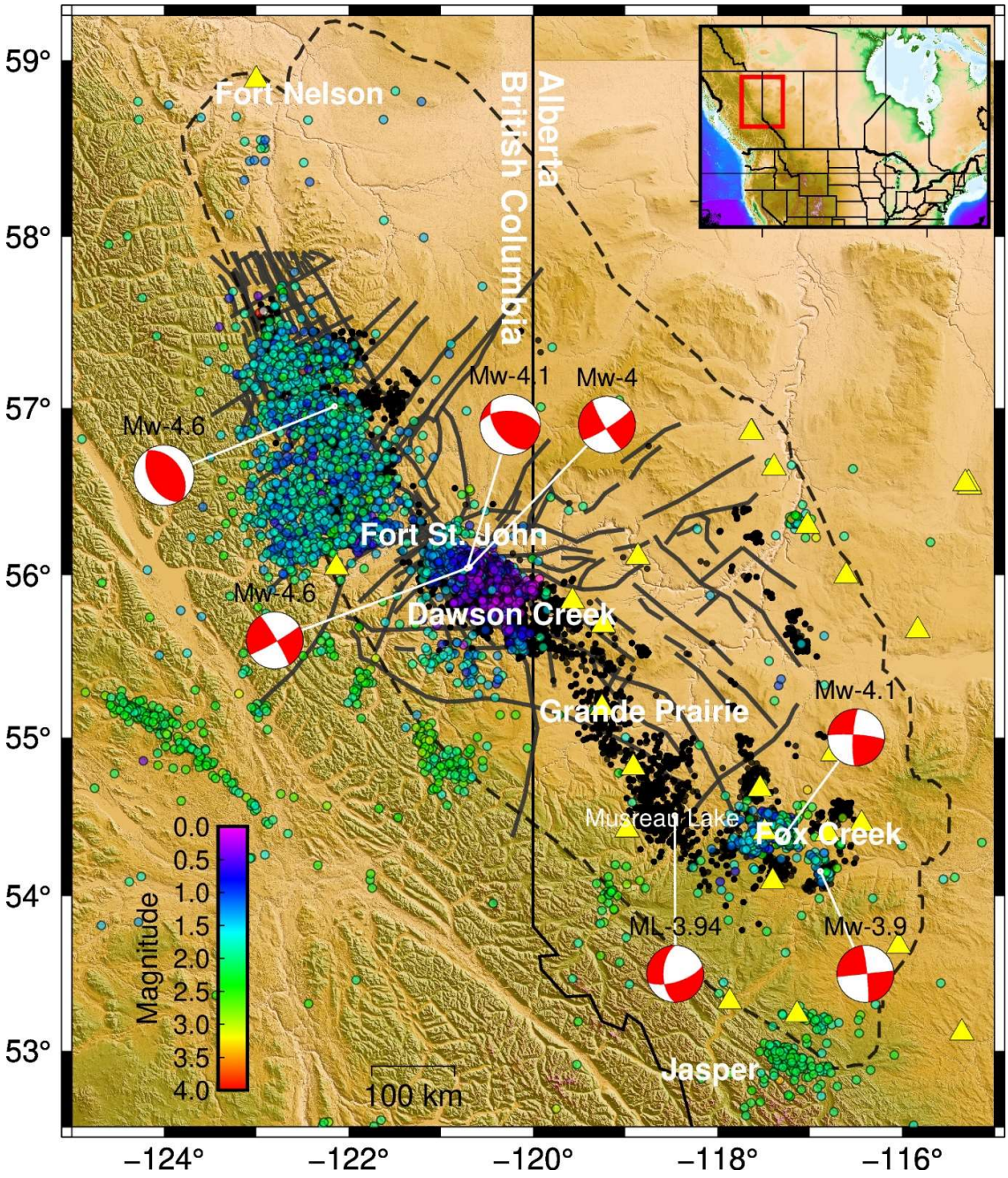

Figure 6-3: Seismicity, fault traces, HF wells in the Montney Formation. The dashed line defines the Montney Formation area. The colored circles are seismicity reported by Visser *et al.* (2017) and Visser *et al.* (2020). Not all these earthquakes are within the Montney Formation; the colored circles outside of the area of the Montney Formation are natural tectonic earthquakes. The earthquakes around Fox Creek have resulted from HF in the Duvernay Formation and wastewater disposal near Musreau Lake (event M_L 3.94) (Li *et al.*, 2021). Grey thick lines are the main faults in the studied area. Black dots show wells drilled into the Montney Formation. Geographical locations of seismic stations are indicated by yellow triangles (Schultz and Stern, 2015). The focal mechanism events represent some major earthquakes recorded in the area.

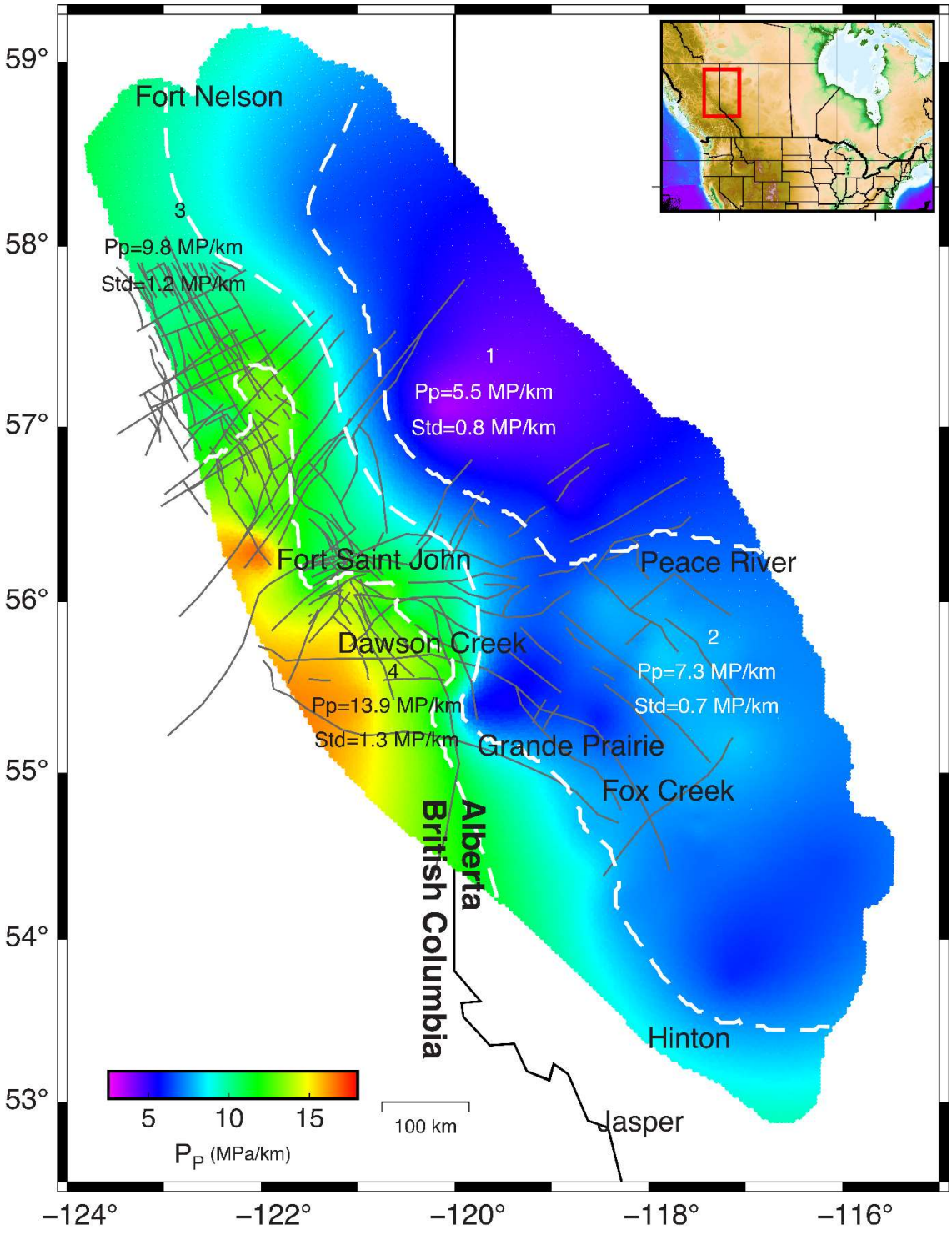

Figure 6-4: Spatial pore pressure gradient values in the Montney Formation. Extremely low Pp (5 MPa/km) are observed around Peace River and Grande Prairie where less seismicity has been recorded. Pore pressure gradients are highest (15 MPa/km) in the areas around Fort St. John and Dawson Creek. The western parts of the formation have relatively higher pore pressure values and gradients than the eastern parts. Gray lines indicate faults crossing one another in the Montney play. The white dashes show the zoning of the Montney Formation based on pore pressure gradients at various locations. Each zone is represented by a mean pore pressure value (Pp) and a standard deviation (Std).

Comprehensive studies of principal stress orientations in British Columbia and Alberta have been conducted since the late 1970s (Bell and Bachu, 2004; Bell and Grasby, 2012; Bell and McCallum, 1990; Dusseault, 1977; Gough and Bell, 1981; Haug and Bell, 2016a). Principal stress orientations in the region have been determined using different methods such as borehole failures (borehole breakouts and tensile-induced fractures) and earthquake focal mechanisms. Compilations of maximum horizontal compressive orientation (S_{Hmax}) and relative stresses are available in the 2018 edition of the World Stress Map (WSM) databases (Heidbach *et al.*, 2018). Except around the Peace River Arch (Bell and McCallum, 1990), where S_{Hmax} is deflected because of the presence of complex fault systems, S_{Hmax} azimuth often strikes NE-SW in the region. Of 211 S_{Hmax} orientations provided by the World Stress Map in the study region, 19 have an A quality ranking, indicating that the dominant S_{Hmax} orientation is NE-SW. Enlighten Geoscience (2021) also determined fifty-eight (including 40 A quality data) S_{Hmax} orientations from borehole failures through various wellbores drilled in the Kiskatinaw area. The black arrows in Figure 6-5 indicate the S_{Hmax} azimuth (including all quality rankings) within the region, derived from borehole breakouts and tensile-induced fractures provided by the World Stress Map and Enlighten Geoscience. Figure 6-5's inset rose diagram, which includes all available datasets with different quality rankings, shows the consistency of S_{Hmax} orientations in the region. In this study, based on available borehole stress orientation indicators, we have assigned a mean of 45° and a standard division of 5° to S_{Hmax} azimuth in all stress areas. It should be pointed out that the stress orientation perturbation due to HF is assumed to be small relative to the regional stresses' orientation.

The Vertical Stress is assumed to be equal to the average specific weight of the geomaterials multiplied by the depth. S_v can be obtained from the typical density logs that are abundant for most drilled wells. Because of density log availability, less uncertainty is associated with the vertical stress component in stress tensors. Several studies have investigated the vertical stress variation in the Western Sedimentary Basin (Bell and Gough, 1979; Bell and Grasby, 2012; Bell *et al.*, 1990; Haug and Bell, 2016a). Bell and Grasby (2012) showed that S_v varies between 22-25 MPa/km at a depth between 0.5 km and 1 km beneath the surface in the study area. The study of the Kiskatinaw area reported in Enlighten Geoscience (2021) indicates vertical stresses ranging from 24.6 to 25.5 MPa/km at the depth of the Montney Formation (~2.5 km). The same values were reported in Hayes *et al.* (2020) and Shen *et al.* (2018). In our study, we consider an S_v range of between 24 and 26 MPa/km.

The Vertical Stress is assumed to be equal to the average specific weight of the geomaterials multiplied by the depth. S_v can be obtained from the typical density logs that are abundant for most drilled wells. Because of density log availability, less uncertainty is associated with the vertical stress component in stress tensors. Several studies have investigated the vertical stress variation in the Western Sedimentary Basin (Bell and Gough, 1979; Bell and Grasby, 2012; Bell *et al.*, 1990; Haug and Bell, 2016a). Bell and Grasby (2012) showed that S_v varies between 22-25 MPa/km at a depth

between 500 m to 1 km in the area of interest. The study of the Kiskatinaw area reported in Enlighten Geoscience (2021) indicates vertical stresses ranging from 24.6 to 25.5 MPa/km at the depth of the Montney Formation (~2.5 km). The same values were reported in Hayes *et al.* (2020) and Shen *et al.* (2018). In our study, I consider an S_v range of between 24 and 26 MPa/km.

Many wells drilled in the Montney Formation have undergone a Diagnostic Fracture Injection Test (DFIT) or mini-frac, which provides reliable determinations of minimum in situ stresses. In DFIT, closure pressure is considered to be a good estimate for minimum principal stress magnitudes (Nicholson *et al.*, 2019). Enlighten Geoscience (2021) after re-interpretating DFIT tests in the Kiskatinaw area provided by geoLOGIC systems, generated a map of the minimum principal stresses around Fort St John. S_{hmin} values were inferred to follow a normal distribution, ranging from 13.8 to 24 MPa/km, with a mean of 18.7 and standard deviations of 1.9 MPa. Using the closure pressure reported by Enlighten Geoscience (2021), along with operator-reported closure pressure gradients provided by geoLOGIC™ systems, Figure 6-5 shows a map of the minimum stress magnitude gradients in the Montney Formation. In our study, I assume that the S_{hmin} gradients in the upper-middle Montney, lower-middle Montney, and lower Montney are the same. Figure B1 in Supplementary Information presents the map-inferred S_{hmin} gradients derived from the dataset provided in Figure 6-5. Note that we also assume that the HF-induced stress perturbation and stress shadow effects are local and thus small relative to the regional stresses.

The spatial variations of the S_{hmin} gradients (Figures 6-5 and Figure B1) indicate that minimum principal stress magnitudes are slightly higher on the British Columbia side than in Alberta, similar to the case for spatial pore pressure gradient values. A study of 134 DFITs in the Montney Formation indicated a direct relationship between pore pressure variation and S_{hmin} gradients (Haghshenas and Qanbari, 2020). Based on pore pressure zoning (Figure 6-4) and the available minimum principal stress datasets (Figure 6-5), we have derived statistical measures of the S_{hmin} magnitude variables in each stress area. Table 6-1 provides information about the mean and standard deviations of the S_{hmin} gradients.

The maximum principal stress magnitude is the most difficult parameter to measure in a strike-slip (or thrust) stress state tensor. However, its range can be constrained by utilizing borehole failure data along with knowledge of minimum principal stresses and vertical stresses. Earthquake focal mechanisms also provide valuable information on the relative stress magnitudes and maximum principal stress magnitudes. In this study, we have used the injection-induced earthquake focal mechanisms recorded in the Western Canadian Sedimentary Basin (WCSB) to constrain the maximum principal stress magnitudes. The dataset includes 64 HF-induced earthquakes around Fort St John, and 39 wastewater-induced earthquakes near Musreau Lake, Alberta (Li et al., 2021).

One of the parameters that can be derived from the inversion of the focal mechanism is Angelier's shape parameter $\varphi = \frac{S_2 - S_3}{S_1 - S_3}$, in which S is the principal stress magnitude and $S_1 > S_2 > S_3$. Simpson (1997) generalized the parameter φ values to provide a quantitative measure with which to determine the relative stress magnitudes in each stress regime by expressing the equation as $A_\varphi = (n + 0.5) + (-1)^n(\varphi - 0.5)$ with n = 0, 1, 2, for normal, strike-slip and reverse faulting respectively. The Anderson fault parameter A_φ ranges continuously from 0 to 1 for normal, 1 to 2 for strike-slip, and 2 to 3 for reverse faults (Hurd and Zoback, 2012b; Yaghoubi *et al.*, 2021; Yang and Hauksson, 2013).

Applying Simpson's approach to the combined 103 compiled focal mechanisms revealed that a strike-slip fault system is the dominant tectonic regime in the area, with an average Anderson fault parameter of $A_\varphi \approx 1.20$ around Musreau Lake and $A_\varphi \approx 1.7$ around Fort St John. Of the 103 focal mechanisms, 93 are strike-slip faulting events and the remainder are large-magnitude reverse faulting events that occurred in the Fort St. John Graben system (Roth *et al.*, 2022) in the northern part of the study area. Roth *et al.* (2022) states that there is no obvious relationship between the faulting style events and hypocentral depth. Note that earthquake events recorded around Musreau Lake are not the result of injection operations in the Montney Formation but rather the result of injection at deeper depths in the Winterburn Formation (Li *et al.*, 2021). However, injection-induced earthquakes that have occurred above and below the injection depth can provide valuable information on the region's state of stress.

Figure 6-5 illustrates some of the focal mechanisms in the study area, with A_φ representing the value above each beachball. Table B1 lists the focal mechanism source data used in this study and the result of A_φ on each focal mechanism. Applying the same approach to eleven earthquake focal mechanisms resulting from HF operations around Fox Creek, Yaghoubi *et al.* (2020) also concluded that A_φ is 1.56 (strike-slip regime).

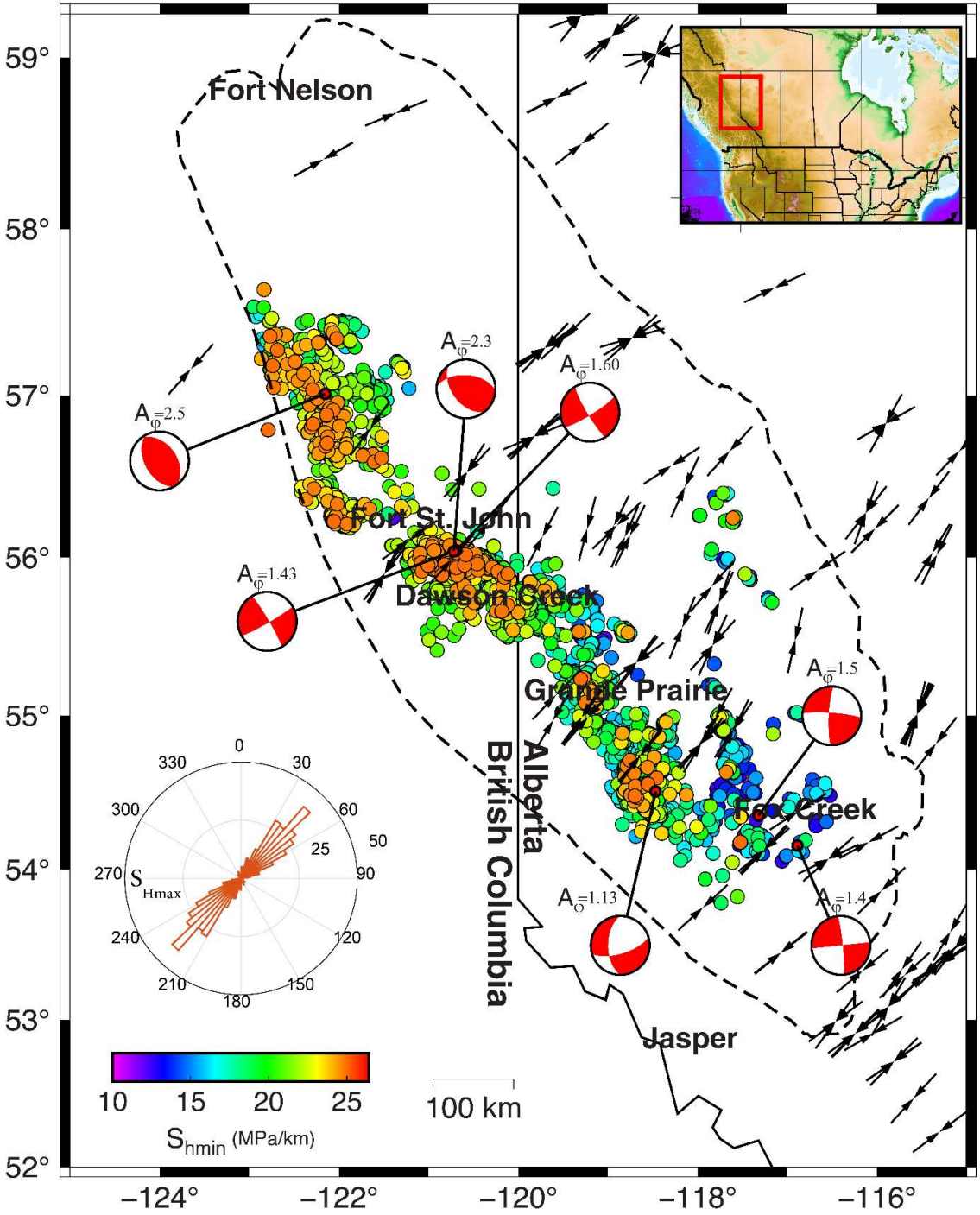

Figure 6-5: Map of S_{hmin} gradients in the Montney Formation. The data have been extracted from geoLOGIC™ systems. The black arrows, extracted from World Stress Map datasets (Heidbach *et al.*, 2018), represent the maximum horizontal principal stress (S_{Hmax}) orientation (inset rose diagram). Beachballs present large-magnitude injection-induced focal mechanisms recorded in the studied area.

I constrain the magnitude of maximum horizontal principal stress, S_{Hmax}, using A_φ. For stress area 4, for example, where the mean S_{hmin} and S_v gradients are 19.4 MPa/km and 25 MPa/km respectively, and the relative stress ratio is $A_\varphi \approx 1.67$, the ratio S_{Hmax}/S_{hmin} is equal to 1.78. Consequently, the

maximum horizontal stress is around 34 MPa/km. The same value is assumed for stress area 3. For stress area 2, using Musreau Lake's focal mechanism dataset, A_φ is assigned a value of 1.2. Unfortunately, sufficient focal mechanisms for determining the relative stress ratio (A_φ) are not available for stress area 1. Consequently, we assume a stress ratio $of\ A_\varphi \approx 1.2$ for this area.

Table 6-1: S_{hmin}, S_V and S_{Hmax} and fault properties statistical measures are used in Monte Carlo Simulation for each stress area. The number of earthquakes reported by Visser et al. (2017 and 2020) represents the number of occurrences in each stress area.

Stress Area	S_{hmin} (MPa/km)		S_V (MPa/km)		S_{Hmax} (MPa/km)		Number of DFIT test	Number Earthquakes
	mean	Std	mean	Std	mean	Std		
1	16.1	1.6	25	0.3	27.4	2.7	10	13
2	16.5	2.1	25	0.3	28	2.5	936	855
3	17.8	1.7	25	0.3	30.2	3.1	1742	1533
4	19.4	1.85	25	0.3	34	3.1	2299	13208

6.3 Pre-existing Faults in the Region

To evaluate fault slip assessment, we need information on the dip direction and dip angle. Most of the faults in the studied regions are hidden and completely buried under sedimentary rock units. Different studies have been performed to map faults in the region using high-resolution aeromagnetic (HRAM) data integrated with regional seismic, remote sensing, and drilled well information. The faults mapped in Figure 6-3 are inferred and compiled from published studies, including those by Barclay *et al.* (1990), Berger (1994), Davies (1997b), Davies (1997a), Davies *et al.* (1997), Berger (2005), Berger *et al.* (2009), Furlong *et al.* (2020), and Hayes *et al.* (2020).

Since faults in the studied area are hidden, the three-dimensional geometry and dip angles are either unknown or are associated with uncertainties. However, the presence of seismicity in an area with a known state of stress provides useful information on seismogenic fault properties such as strike, dip direction, size, and the coefficient of friction. Considering the state of stress in the Montney Formation and slip compatibility analysis of 103 complied focal mechanisms, the hidden faults are expected to dip more than 60°. In this study, the dip angle of each fault is described as a probability distribution. Figure 6-6 presents a Mohr Diagram with a representative strike-slip focal event (M_w=4.6, 2018-11-30) and resolved shear and normal stresses for each nodal plane. The nodal plane with high τ/σ_n is selected as the actual plane. These nodal planes are shown in bold in Table B1. No laboratory studies or in-situ tests have been conducted to investigate the magnitude of coefficients of friction for regional faults. Based on experimental studies, Byerlee (1978) has shown that for different rock types, the coefficient of friction lies between 0.6 and 1. In our study, we assumed that the coefficient of friction ranges from 0.5 to 0.8. A similar value has been assigned to fault slip

tendencies in Oklahoma (Walsh III and Zoback, 2016), the Delaware Basin of Texas, and New Mexico (Morris *et al.*, 2021). It should also be noted that some faults in this region have been mapped at slightly different locations in different studies. In this study, we mapped and considered both versions for slip assessment. Additionally, there are some areas where earthquakes are not associated with faults that have been mapped. Injection-induced earthquakes around the Fox Creek area, for example, are due to HF in parts of the Duvernay Formation that lie near critically stressed faults that had been unknown before the operation started (Schultz *et al.*, 2017). Similarly, seismic activity around Musreau Lake has been linked to the reactivation of an unknown N-S fault due to wastewater injection at a depth of 3 to 4 km. These examples suggest that other areas with as-yet unrecognized critically stressed faults probably exist and will also be susceptible to HF-induced earthquakes.

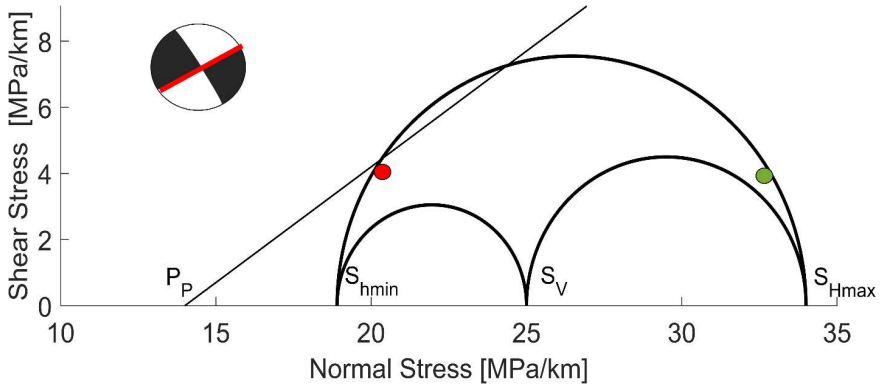

Figure 6-6: The Mohr-Coulomb shear failure criterion (the diagonal line), Mohr's circles representing and a representative strike-slip earthquake focal mechanism (M_w=4.6, 2018-11-30). The red line on the focal beach ball indicates the actual fault plane.

6.4 Assessment of Fault-Slip Potential

Fault or fracture slip depends on the relative stress magnitude, the angle between the principal stress directions and the fault plane, and the coefficient of friction μ based on Coulomb faulting theory (Morris *et al.*, 1996). The slip tendency in a pre-existing cohesionless fault can be defined in terms of the Mohr-Coulomb shear failure criterion, where σ_n is the effective normal stress across the slip surface

$$\tau = \mu\sigma_n \tag{6-1}$$

Fault plane slippage is more likely to occur when the resolved shear stress, τ, equals, or is very close to, the frictional resistance of the fault surface; the fault is then called “critically stressed”. The deterministic fault slip tendency is expressed as the ratio of effective normal stress to shear stress on a potential sliding surface ($\tau/\sigma_n \geq \mu$).

The deterministic approach considers just one single analysis as finite and therefore underestimates potential risks (Figure B2). The slip tendency in a probabilistic analysis, however, considers inherent uncertainties for each input variable, including stress magnitudes and orientations, fault dip directions, angles, and frictional strengths (Jones and Hillis, 2003; Walsh III and Zoback, 2016; Wang *et al.*, 2010). Each input variable effective in Mohr-Coulomb shear failure can be assigned as a random sample with specific statistical parameters. An appropriate probability distribution should be assigned for each of the uncertain input parameters in the model. The probability of failure can be defined as

$$P_f = P[\,\tau - \mu\sigma_n \leq 0] \qquad (6\text{-}2)$$

Probabilistic slip tendency analysis is, therefore, more comprehensive and more suitable for evaluating risk in multiple scenarios. In this study, for each fault patch, a Monte Carlo simulation with 5,000 scenarios has been applied to evaluate the slip tendency of faults in the Montney Formation. In determining the size of the simulation sample, we considered the probability of fault slip (with two-digit precision) compared to the number of realizations (see Figure B3 in Supplementary Information). The analysis includes uncertainty associated with the uncontrollable subsurface parameters, such as the state of stress, pore pressure, pre-existing fault/fracture orientation, and frictional strength. Figures B5 to B7 show the statistical geomechanics variables used in the Monte Carlo simulation in each stress area (Table 6-1). The result is a cumulative distribution of the probability of slip for each mapped fault. Figure 6-7 shows an example of the cumulative probability function of the injection pressure required to cause slip at a depth of 2.5 km in all fault segments located in stress area 4.

In Figure 6-7, I use the uncertainty distributions in Figure B7 to apply Monte Carlo simulation to the faults mapped in study area 4. For this case, some segments of faults are likely to slip with an injection pressure of 37 MPa (at a depth of 2.5 km), and the probability of slip at the current injection pressure is 76%. The same analyses were performed for each fault patch mapped in Figure 6-3 in different stress areas (see Figures B8, B9, B10). For each fault segment, I calculated the probability of slip in response to 2 MPa pore pressure perturbations ($\Delta P(P_{inj}\text{-}P_p)$ = 2 MPa) as presented in Figure 6-7. Figure 6-8 shows faults mapped in the study area color-coded with the probability of slip. The red fault lines imply a higher likelihood of slip. Recorded earthquakes and wells drilled in the area are represented with black and red circles respectively.

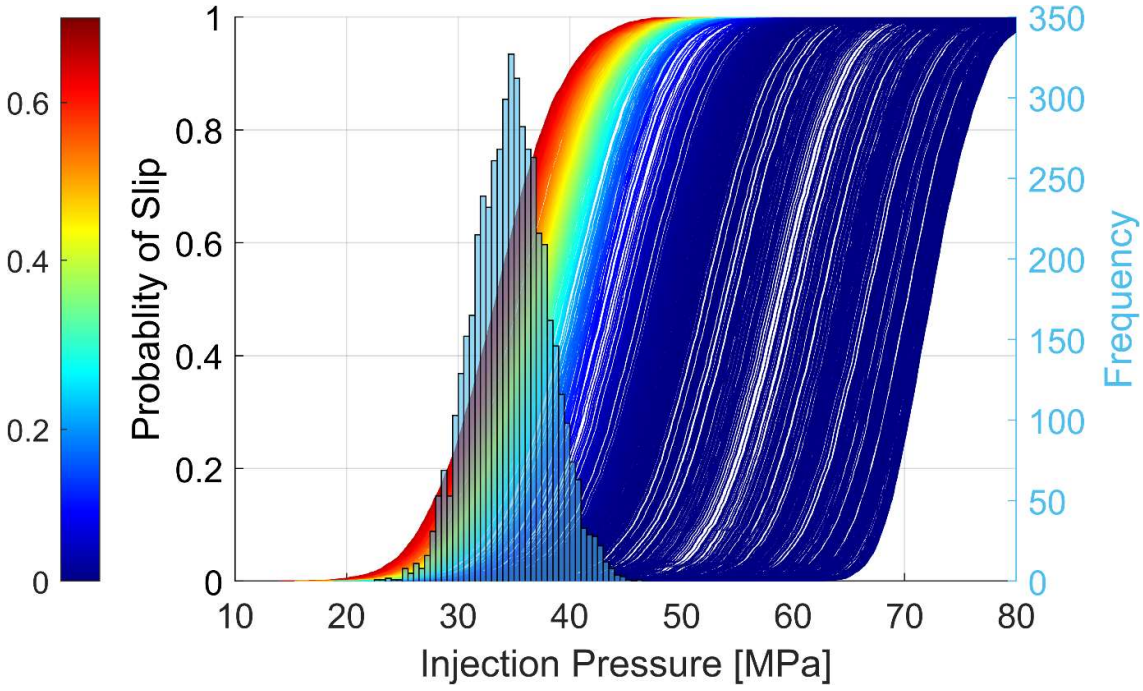

Figure 6-7: The cumulative probability function of the required injection pressure to cause slip on faults located in stress area 4. The histogram presents the pore pressure distribution in the stress area 4. Each curve represents the cumulative probability function of slip on each fault segment. The difference between current injection pressure and mean Pp distribution is 2 MPa. The depth of injection is assumed to be 2.5 km.

6.5 Discussion

The results of the study indicate that pore pressure gradient and fault orientation are important factors affecting seismic activity in the studied area. In overpressured areas, the principal stress magnitudes approach the vertical stress value regardless of the region's fault regime environment. This fact is important in assessing fault/fracture stability because, in overpressured regions where the difference between the minimum and maximum principal stresses is smaller, a fault in the optimum orientation is likely to slip more easily. Of the 15,609 induced earthquakes presented by Visser *et al.* (2017) and Visser *et al.* (2020), only 13 are located in stress area 1, whereas more than 13,000 occurred in stress area 4, where the mean pore pressure gradient is 13.5 MPa/km. Around Grande Prairie, where the Montney Formation's pore pressure gradient is around 7 MPa/km, no significant and large seismicity ($M \geq 4$) has been reported even though more than 680 HF wells (represented by black circles in Figure 6-8) have been stimulated with around 9 $\times 10^6$ m^3 cumulative fluid injection (geoLOGIC™ Systems) into both the Duvernay and Montney Formations. As the seismic network in this area is sufficiently dense (Figure 6-8), it can be concluded that there has been no seismic activity caused by fluid injection into the formations in the Grande Prairie area. This finding may be due to the relatively low pore pressure gradients in the Montney Formation or because pre-existing local faults are not in a critically stressed condition in the Grande Prairie area. However, Fox Creek (about 200 km southeast of Grande Prairie) is associated with large earthquakes, including one of M_W 4.1 on January 12, 2016,

which has been associated with HF injected volume into the Duverney Formation (Schultz *et al.*, 2018). Among the principal geomechanics differences is that the mean pore pressure gradient in Duverney is approximately 9 MPa/km higher than in Montney in Grande Prairie. Thus, the importance of pore pressure gradient on induced seismicity in the Montney Formation is therefore evident.

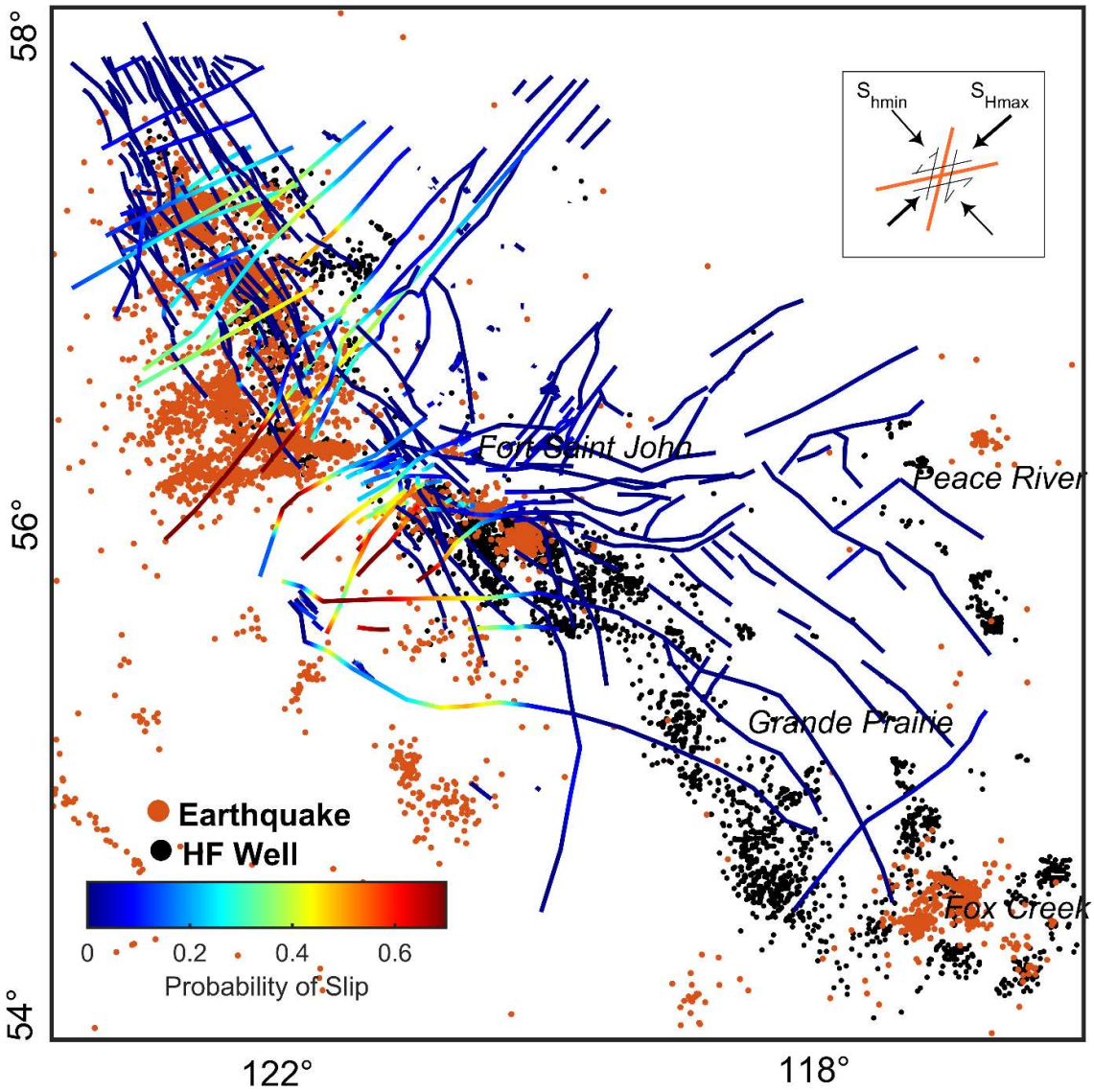

Figure 6-8: Fault map color-coded to highlight the probability of slip in the Montney Formation. Black points represent wells that were hydraulically stimulated. The red circles are seismicity reported by Visser *et al.* (2017) and Visser *et al.* (2020).

Other factors in earthquake nucleation in the Montney Formation are the fault dip angle and dip direction. Slip compatibility analysis of 64 complied focal mechanisms (Figure 6-6) in the Kiskatinaw area shows that nodal planes optimal for slippage are expected to be in the Azimuth of 5° (or 185°) and 65° (or 245°). The observation is consistent with the frictional faulting theory and what we have

illustrated in Figure 6-8. The stereonet in Figure B2 shows fault slip tendency with an average S_{Hmax} orientation of 45° and $A_{\varphi} = 1.7$ for stress area 4. The slip compatibility analysis of 39 focal mechanisms near Musreau Lake indicates a similar probability of slip between the two nodal planes (strike=170±20 dip=60±24 and strike=85±17 and dip=65±22); however, the nodal planes with a higher dip angle have a higher tendency to slip. In Figure 6-8, the upper top inset shows the direction of a critically stressed fault.

This study is based on the mechanism by which earthquake nucleation occurs due to direct pore pressure diffusion along known faults in the Montney Formation. Similar studies have been performed in Fox Creek, Alberta (Shen *et al.*, 2019b), north-central Oklahoma (Walsh III and Zoback, 2016), the Fort Worth Basin (Hennings *et al.*, 2019), and the Delaware Basin in Texas (Morris *et al.*, 2021). Similar to finding for those areas (Johann *et al.*, 2018; Zhai *et al.*, 2021), injection-induced seismicity in the Montney Formation has been attributed to two other mechanisms as well: a) poroelastic coupling stress evolution of the rock matrix between the injection zone and nearby fault (Deng *et al.*, 2016) and b) an aseismic slip loading mechanism that causes delayed dynamic rupture events far from points of injection (Eyre *et al.*, 2019; Eyre *et al.*, 2022; Yu *et al.*, 2021a).

Based on observations and evidence, all three mechanisms, individually or in combination, are plausible causes of earthquake nucleation in the Montney Formation at different locations of WCSB. However, the different mechanisms can be distinguished from one another by their spatiotemporal patterns of injection-induced seismicity. For example, the primary support for this aseismic loading mechanism is that most of the large events in WCSB are vertically offset from the injection zone and occur below (at crystalline basement depth) and above reservoir depth. In contrast to aseismic loading mechanisms, numerical stress modeling by Peña Castro *et al.* (2020) has argued that highly permeable fault zones allow fluid from the injection zone to reach basement-rooted faults in WCSB. The authors have indicated that rapid change in pore pressure along the fault is the dominant mechanism for the November 30, 2018, M_w 4.2 earthquake around Fort St John at a depth of 4.5 km, precipitated by HF in the Montney Formation (~2.5 km depth). The existence of a permeable conduct/fault network is supported by a low flow rate for WCSB HF wells, as half of the injected fluid is lost during HF operations (Bao and Eaton, 2016).

Different effective parameters might be responsible for the various injection-induced seismicity mechanisms. Matrix permeability and compressibility are major factors in the poroelastic stress evaluation mechanism. Slow-slip-induced seismicity is likely to occur in shale-hosted faults with high clay and total organic content (TOC). However, the feature common to all three is the existence of critically stressed host faults in the region. In the context of Mohr-Coulomb failure criteria, as illustrated in the upper right inset in Figure 6-8 and Figure B2, those faults striking ENE (Azimuth≈60° and 240°) and NEN (Azimuth≈10° and 190°) and dipping more than 60° are most likely to slip, as are the well-oriented fault planes in the studied area. The same analysis for reverse

fault events shows the faults striking NWN and dipping from 15° to 60° have a high likelihood to slip (Figure 6-9). That finding is consistent with most of the reverse fault events in the study area. Even for those faults that are not critically stressed (where $\sigma_n \gg \tau$), fault reactivation and related induced seismicity can only be attributed to the aseismic loading mechanism. Hence, regardless of which mechanism is causing the significant anthropogenic seismicity in the region, this study provides information on known seismogenic faults in one of the largest unconventional shale gas resources in the world, the Montney Formation.

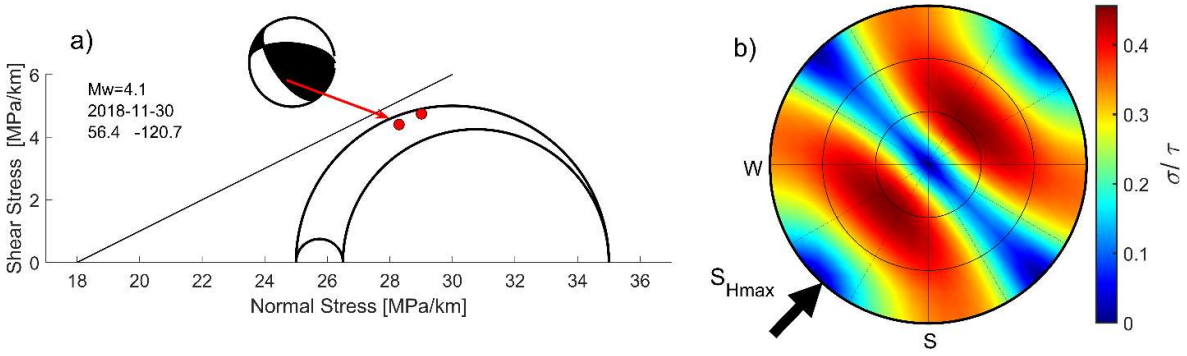

Figure 6-9: a) The Mohr-Coulomb shear failure criterion (the diagonal line) and 3D Mohr's circle, depicting the reverse focal mechanism and resolved normal and shear stresses for each nodal plane. (b) Lower hemisphere stereonet plot for the case that state of stress is reverse faulting regime. Colors show the ratio of shear to effective normal stresses (required μ) needed for shear failure on a fault plane. In a reverse faulting regime, faults dipping from 15° to 60° and striking northwest to southeast are critically stressed.

6.6 Conclusions

I have used a probabilistic approach to determine the likelihood of fault slip as a function of injection pressure due to HF treatment in the Montney Formation. We first determined the state of stress and mapped faults as potential sites of injection-induced seismicity. The stress areas are defined by spatial pore pressure gradient variation. Strike-slip faulting regimes with A_φ=1.2 to 1.8 were determined using multivariable datasets from borehole petrophysical data to injection-induced focal mechanisms. Published known faults mapped for the Montney Formation were examined for slip tendency, considering the uncertainties associated with geomechanics parameters. Each geomechanical parameter was expressed as a probability distribution. Based on probabilistic analysis, it appears that most fault planes in the Kiskatinaw area and the northwestern Montney Formation would become unstable with only a moderate change in pore pressure. However, some areas have only a low probability of slip, having relatively low initial pore formation pressure. This finding is consistent with major injection-induced seismicity that has occurred in the area. In the Montney Formation, pore pressure spatial inhomogeneity plays a significant role in fault stability and injection-induced earthquakes. These results prompted us to discuss two important factors influencing fault stability in

the Montney Formation: pore pressure gradient and fault direction. The areas with the highest pore pressure gradient and nearly vertical faults-oriented ENE (Azimuth≈60°) and NEN (Azimuth≈10°) are the most seismogenic regions in this unconventional play. The resulting probabilistic fault stability map can be used as a base map for fluid injection projects involving wastewater disposal, carbon sequestration and storage, and geothermal energy extraction.

CHAPTER 7

Injection- Induced Seismicity assessment at the Alberta No. 1 Geothermal Project site[1]

Abstract

Alberta No.1 is a geothermal project targeting deep carbonate, conglomerates, and sandstone formations in a potential production and injection zone for geothermal energy exploitation within the Municipal District of Greenview south of Grande Prairie, Alberta, Canada. In geothermal systems without a steam fraction (typically systems under 170°C), rapid widespread pore pressure changes and slow temperature changes have led to increased deviatoric stresses, resulting in induced seismicity. A concern for the Alberta No.1 Geothermal Project is that anthropogenic seismicity from oil, gas, and well field fluid injection has created felt events in Alberta. Thus, at the beginning of this type of project, it is prudent to review the potential for induced seismicity. In this study, a geomechanical study of the Leduc and Granite Wash Formations, two potential geothermal fluid exploitation zones, has been undertaken based on borehole geophysics and regional injection-induced earthquake data. Determining subsurface properties such as state of stress, pore pressure, and fault properties, however, poses uncertainties in the absence of actual data from the target formations. Geomechanical analysis results (with associated uncertainties) are used to assess the potential for injection-induced earthquakes. A Monte Carlo probability analysis is employed to estimate the likelihood of slippage of the known faults close to the Alberta No.1 Geothermal Project. A cumulative distribution function of the critical pore pressure on each fault is derived from the local tectonic stress state and Mohr-Coulomb shear parameter analyses. The resultant probabilistic fault stability maps can serve as a baseline for future fluid injection projects in the region including wastewater disposal, hydraulic fracture stimulation, CO2 sequestration, as well as geothermal energy extraction.

[1] A version of this chapter has been submitted in Canadian Journal of Earth Science.

7.1 Introduction

Renewable baseload geothermal energy can contribute significantly to meeting energy demand and decarbonizing the world's energy sources (Amponsah *et al.*, 2014; Frick *et al.*, 2010). In the last few decades, geothermal energy has increasingly gained prominence as a means of reducing greenhouse gas emissions (Amponsah *et al.*, 2014; Frick *et al.*, 2010). In Canada, geothermal energy can help to attain net-zero emissions goals of provinces with suitable geothermal assets in the Western Canadian Sedimentary Basin (WCSB) (Downey *et al.*, 2021). In the central regions of the WCSB, Alberta has been identified as a significant source of underground geothermal energy, with an average geothermal gradient of 25-35 °C/km (Champollion *et al.*, 2021; Grasby *et al.*, 2011; Hickson *et al.*, 2020; Hickson *et al.*, 2021; Hofmann *et al.*, 2014; Huang *et al.*, 2021a). The WCSB Alberta portion has been subjected to various studies in order to identify a suitable geothermal project site. It has been determined that the Municipal District of Greenview (MDGV) is likely to have economically viable deep geothermal resources, particularly south of Grande Prairie. The MDGV is bordered by the Wapiti River on the north, just south of the City of Grande Prairie (Banks, 2016; Banks and Harris, 2018; Hickson and Colombina, 2021; Huang *et al.*, 2021a).

The Alberta No. 1 (ABNo1) geothermal project, located within MDGV, just south of the City of Grande Prairie, will be the province's first conventional geothermal electrical energy producing facility (Hickson *et al.*, 2021; Huang *et al.*, 2021b) . Grande Prairie is the largest city in the region with a population of 55,000 spread over 72.8 km^2 (Banks, 2016). According to Hickson (2022), ABNo1 is expected to produce 80,000 MWhr of electrical power per year, offset 96,000 tCO_2/year, and produce 985 TJ/year of thermal energy (Hickson, 2022). Nearby facilities include the Grovedale light industrial park and Greenview Industrial Gateway. The project is planning for three production and two injection wells at its first site. In ABNo1, the primary target formation is a Devonian carbonate unit consisting of interbedded dolomite and sandstone units (Hickson *et al.*, 2021; Huang *et al.*, 2021a; Huang *et al.*, 2021b)

One of the technical/environmental issues that needs to be addressed before starting a deep geothermal development in Alberta is the potential for induced seismicity due to local fault reactivation as a result of fluid injection (Atkinson *et al.*, 2016; Bao and Eaton, 2016; Mahbaz *et al.*, 2021; Schultz *et al.*, 2017). Upon injection of fluid into the fractured rock mass, pore pressure is increased along pre-existing faults and fracture planes; if the resolved shear stress on the plane exceeds the normal effective stress limit, the fault slips and thereby

triggers an earthquake (Yaghoubi, 2019). Anthropogenic seismic events in Alberta arising from oil and gas operations are among the largest Mw (moment magnitude) events reported globally (Atkinson *et al.*, 2016), including events near Fox Creek at Mw 4.1 on January 12, 2016 (Schultz *et al.*, 2017), and Musreau Lake at M_L 3.94 (local magnitude) on December 25, 2019 (Li *et al.*, 2021). In terms of distance, Fox Creek is approximately 200 kilometers southeast of the ABNo1 development site. Musreau Lake is approximately 100 km south (Figure 7-1) of ABNo1. Thus, at the beginning of this type of project in Alberta a precautionary assessment is prudent.

Prior to the development of a deep geothermal project, an injection-induced earthquake assessment should be performed. For example, in Switzerland, The Deep Heat Mining Basel Project implemented in a densely populated suburb of Basel was shut down due to a M_L3.4 injection-induced seismic event that occurred on December 8, 2006. The project was initiated for geothermal reservoir enhancement from the granitic basement ("hot dry rock"). During six days of hydraulic fracturing (HF) stimulation, approximately 13,000 induced seismic events were detected at a depth of 5-6 km (Häring *et al.*, 2008; Kraft and Deichmann, 2014; Mukuhira *et al.*, 2013). Even though the geologic and operational characteristics of the ABNo1 and Basel projects are different, it is still important to apply the lessons learned from Basel to the assessment of the likelihood and risk of injection-induced seismicity in ABNo1.

Two kinds of parameters impact the rate and magnitude of injection-indued seismicity. First, extrinsic parameters that can be controlled, such as injection pressure, flow rate, viscosity, volume, and type of fluid, and second, subsurface intrinsic parameters that are uncontrollable. These intrinsic parameters may include stress state and pore pressure, size and density of fissures and fractures, fault orientation and frictional strength, steady-state coefficient of friction, rock permeability, and compressibility, as well as other geomechanical parameters such as brittleness and deformation properties (Yaghoubi *et al.*, 2022). However, substantial levels of inherent uncertainty are associated with the value of each intrinsic parameter. In fluid injection projects (well field brine disposal for example), understanding the uncertainty associated with any intrinsic parameter can assist the user in making better decisions concerning user-controlled parameters such as injection pressure.

Herein, using borehole geophysics data and earthquake focal mechanism reports from nearby locations, we establish a constraint for the region's state of stress in two target formations, the Leduc and Granite Wash Formations. We have conducted a geomechanical characterization of both formations and identified a range of uncertainties with respect to

stress tensors, pore pressure, and fault properties. We then employ a probabilistic approach to determine the potential fault slip tendency for fluid injection in the formations, incorporating the uncertainty distributions associated with Mohr-Coulomb strength parameters (friction angle, normal and shear stress). A benefit of this approach is the generation of probabilistic fault stability maps that may provide a basis for future fluid injection projects in the region, such as carbon sequestration projects or well field fluid disposal.

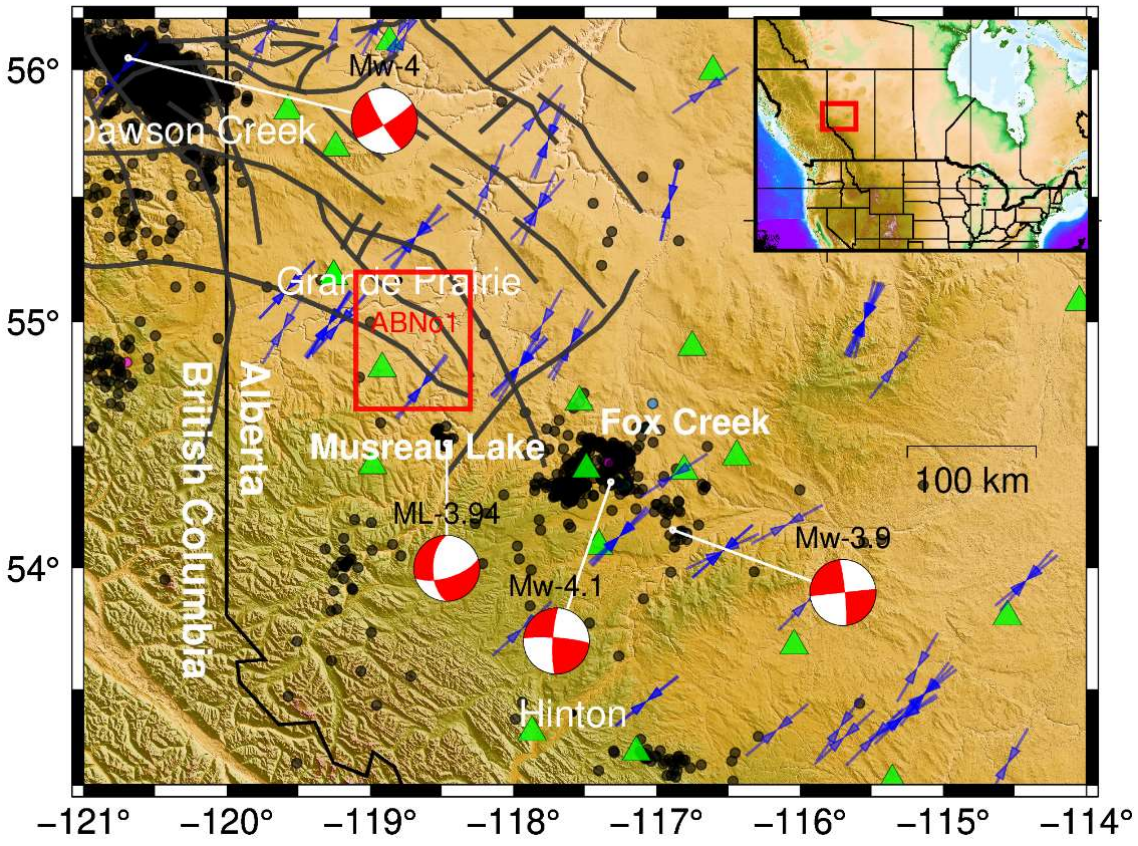

Figure 7-1: The location of Alberta No. 1 geothermal project (red box). Black circles represent earthquakes reported in the area. The blue arrows, extracted from World Stress Map datasets (Heidbach *et al.*, 2018), represent the maximum horizontal principal stress (S_{Hmax}) orientation. Grey thick lines are the main faults in the studied area. The green triangles represent the locations of seismic stations. Details of the seismic stations are provided in Stern *et al.* (2011) Table 1. The strike-slip focal mechanism events represent major induced earthquakes recorded in the area.

7.2 Geology Setting

Because of extensive drilling and public data availability, the stratigraphic columns in northwest Alberta are well established, but data is still sparse for deep formations such as the Granite Wash (Dec *et al.*, 1996; Glass, 1990; Porter *et al.*, 1982). From the oldest to

youngest in northwest Alberta, the Devonian stratigraphy is made up of the Lower Devonian strata, the Elk Point Group, the Beaverhill Lake Group and the Woodbend Group (Dec *et al.*, 1996; Glass, 1990; Porter *et al.*, 1982). Figure 7-2 shows the stratigraphic column near the ABNo1 geothermal project. Based on the geothermal gradient, lithology, and hydrogeologic properties, Banks (2016) and Banks and Harris (2018) reported that two formations in Grande Prairie County and the Municipal District of Greenview region could be suitable for geothermal energy extraction: the Leduc and Granite Wash Formations. Formation selection is determined by a variety of factors, including formation temperature gradient and depth, as well as the rock physics characteristics of the formation, such as porosity and permeability (Banks and Harris, 2018). This work was corroborated by the studies for ABNo1 (Hickson *et al.*, 2020).

The Leduc Formation (Woodbend Group), is approximately 175-300 m thick in the Grande Prairie area, contains dominantly limestone and dolomitized limestone regions (Banks and Harris, 2018). The formation is highly porous because of widespread dolomitization during diagenesis (Amthor *et al.*, 1994). The Granite Wash Formation is another target geothermal fluids zone and consists of sandstone and conglomeratic sandstone of 100-200 m thickness lying directly on the Precambrian crystalline basement. This formation is also known for its high porosity and permeability (Banks, 2016; Banks and Harris, 2018). The Leduc and Grant Wash Formations lie at depths of approximately 3500 m and 3800 m, respectively, in the study area.

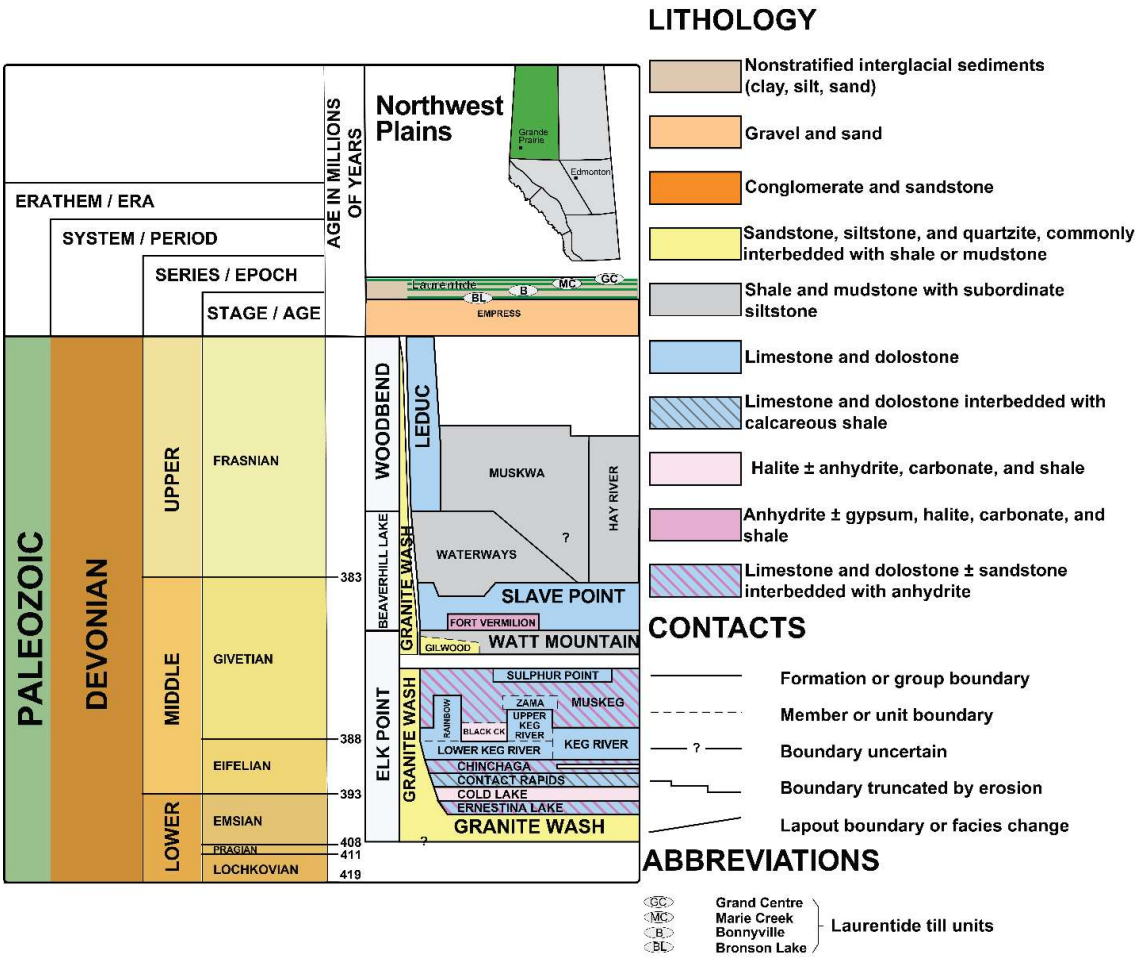

Figure 7-2: Stratigraphic column and table of formations in the Alberta No. 1 geothermal project in Grande Prairie in Northwest Alberta (modified from Alberta Geological Survey (2019). The vector version of this figure can be found in the supplementary information or online at https://ags.aer.ca/publication/alberta-table-formations

Over 2920 wells have been drilled in Grande Prairie County to extract fossil fuel, primarily from the Montney and Duvernay Formations (geoSCOUT™). Geomechanical parameters are available only for the Montney and Duvernay Formations, although drilled wells provide information on depth, thickness, lithology, and rock physics properties of subsurface layers such as the Leduc and Granite Wash Formations. The Duvernay and Montney Formations are "tight" shales that require hydraulic fracturing in order to release hydrocarbons. Hydraulic Fracturing (HF) is a process used to develop oil and gas wells using high-pressure injection of water, sand, and chemicals into rock formations.

HF is rarely used in conventional geothermal operations where steam or extremely hot fluids are present, but in the case of "hot dry rock" (Enhanced or Engineered Geothermal Systems "EGS"), operations this technique is used to create a fractured reservoir from which

to extract the heat. Basel Switzerland is an example of an HF EGS system. In conventional geothermal operations, injection takes place directly, at lithostatic pressure, and no proppants or other chemicals are added other than scale inhibitors which might be necessary. Nonetheless, in geothermal projects similar to the ABNo1 project, limited HF may be used to increase the flow capacity of individual wells upon analysis of initial pumping tests.

In this region, only eight wells have been drilled through to the Granite Wash Formation and an additional 28 have reached the top of the Leduc Formation. Figure 7-3 shows the location of wells with the color denoting the top (depth) of the Leduc (Figure 7- 3a) and Granite Wash Formations (Figure 7- 3b). The depth of both formations increases from northeast to southwest as shown in the Figure 7-3. For geothermal projects to be commercially viable, Huang *et al.* (2021b) proposed that the target formation should be no deeper than 4500 meters and its temperature should be no lower than 120°C. Thus, the southwest area of Grande Prairie County could be a promising site for injection and production wells (Champollion *et al.*, 2021; Hickson *et al.*, 2021; Huang *et al.*, 2021b).

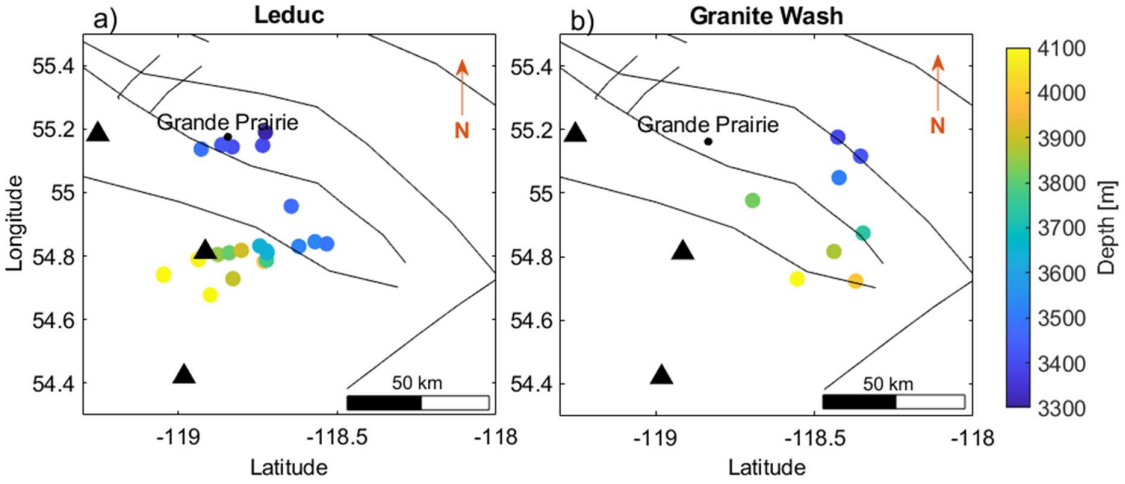

Figure 7-3: Top of the (a) Leduc and (b) Granite Wash Formations as seen in drilled wells in the region. Black lines are the main faults in the studied area. Seismic stations are indicated by black triangles.

7.3 Seismicity in the Region

A positive attribute of the Grande Prairie area is that despite the large number of HF operations carried out as part of oil and gas operations (mostly in the Duvernay and Montney Formations, stratigraphically above the Leduc and Granite Wash formations), no triggered seismic activity has been recorded. The number of seismic stations in a region will affect the

level of seismic activity observed/reported in that region. The triangles in figures show the location of regional seismic stations. One of these stations has been operating since 2009, 30 kilometers west of Grande Prairie and north of the Wapiti River (Stern *et al.*, 2011). There are three seismic stations within 100 km of the region of interest. The seismic network in this area is sufficiently dense that it is certain that no significant seismic activity M≥3 has resulted from fluid injection into different geological formations in the Grande Prairie area. However, in the region south and east of Grande Prairie, there are two seismogenic regions: Fox Creek and Musreau Lake (Figure 7-1), which were both quiescent prior to the fluid injection associated with oil and gas development.

There has been a noticeable increase in seismicity rates in Fox Creek since December 2013. More than 200 earthquakes of magnitude >2.5 have occurred in this area in association with HF operations in the Duvernay Formation, including Mw 4.1 on January 12, 2016, and Mw 3.9 on June 13, 2016 (Bao and Eaton, 2016; Schultz *et al.*, 2017). Most earthquakes in the Fox Creek area occurred during HF treatments and were spatially and temporally restricted to the region around the horizontal wells. Seismicity around Musreau Lake resulted from oil field wastewater injection into the Winterburn Formation at a depth of 3 to 4 km, the largest event being M_L 3.94 on December 25, 2019. Like Fox Creek, seismicity in Musreau Lake was spatially and temporally confined to the injection site activity. A point that should be emphasized is that induced seismicity near Fox Creek is due to HF occurring in parts of the Duvernay Formation that lay near critically stressed faults unknown before the operation began. This implies that there may be other, as-yet-unrecognized, critically stressed faults which are also susceptible to HF-induced earthquakes.

From 706 multistage HF wells, 9 $\times 10^6$ m^3 cumulative fluid volume (geoSCOUT™) was injected into both the Duvernay and Montney Formations in the Grande Prairie region (Figure 7-4 and Figure 7-5). That is important to highlight because, in a multistage HF well in Fox Creek, fluid injections of 2.04×10^4 m^3 triggered 115 earthquakes with a moment magnitude from 1 to 2.9 (Yaghoubi *et al.*, 2020). Although both regions have a comparable level of HF activity, there is a question as to why Fox Creek is a seismogenic region whereas Grande Prairie is a quiescent area. This paper addresses this question as one of its objectives.

7.4 Pre-existing Faults in Grande Prairie

When evaluating fault slip, it is necessary to know the dip and dip directions of the faults that underlie the region. Berger *et al.* (2009) mapped faults around the Peace River Arch, a

geological structure most prominent north of Grande Prairie using regional high-resolution aeromagnetic data (HRAM). Specifically, Berger *et al.* (2009) explain that the Grande Prairie tectonic state is controlled by a northwest-southeast down-to-the-basin listric fault, as well as a northeast-southwest basement-involved strike-slip fault (Berger *et al.*, 2009). The latter may be responsible for the induced seismicity in Musreau Lake arising from wastewater injection. Because strike-slip faults may have a small or negligible vertical movement component, they are difficult to identify on seismic surveys.

In this study, the range of dip angle of each fault is described as a uniform probability distribution with the value of 80° ±10°. It should also be noted that no laboratory study or in-situ experiment has been conducted to estimate the coefficient of friction of regional faults in the study area. Byerlee (1978) has demonstrated, based on experimental studies, that the coefficient of friction of faults varies between 0.6 and 1.0 for different rock types. In our study, we assumed that the coefficient of friction is in the range 0.7±0.1. A further important point to emphasize is that our study is based on known faults in the region. As mentioned above, injection-induced seismicity around the Fox Creek area occurred on previously unknown critically stressed faults.

7.5 State of Stress around Grande Prairie

An integral part of a region's stress state is the pore pressure. Formation pore pressure can be directly measured from direct wellbore tests such as Drill Stem Test, Repeat Formation Test, or predicted from borehole geophysics data. For this study, we determine pore pressures within two target formations, the Leduc and Granite Wash Formations, using the datasets provided by geoSCOUT™ data services. Of 856 direct pore pressure measurements in the Leduc Formation in the WCSB, six wells including 30 tests are in the region of study. Figure 7-6.a and 6.b display the Leduc Formation's pore pressure gradient and its histogram presented from wells drilled in the WSCB and around Grande Prairie respectively (Figure 7-6.c and 6.d). Similar to the Leduc Formation, Figure 7-7 provides pore pressure gradient variations from wells that have available direct measurements in the Granite Wash Formation. Both formations, as can be seen from the Figures, are almost at hydrostatic pressure. In our study, we use a Pore pressure (Pp) gradient of 9±2 MPa/km for the Leduc and Granite Wash Formations. Note that pore pressure and other stress parameters are presented as gradients in this section since the depth of the target formations differs at different locations (Figure 7-3).

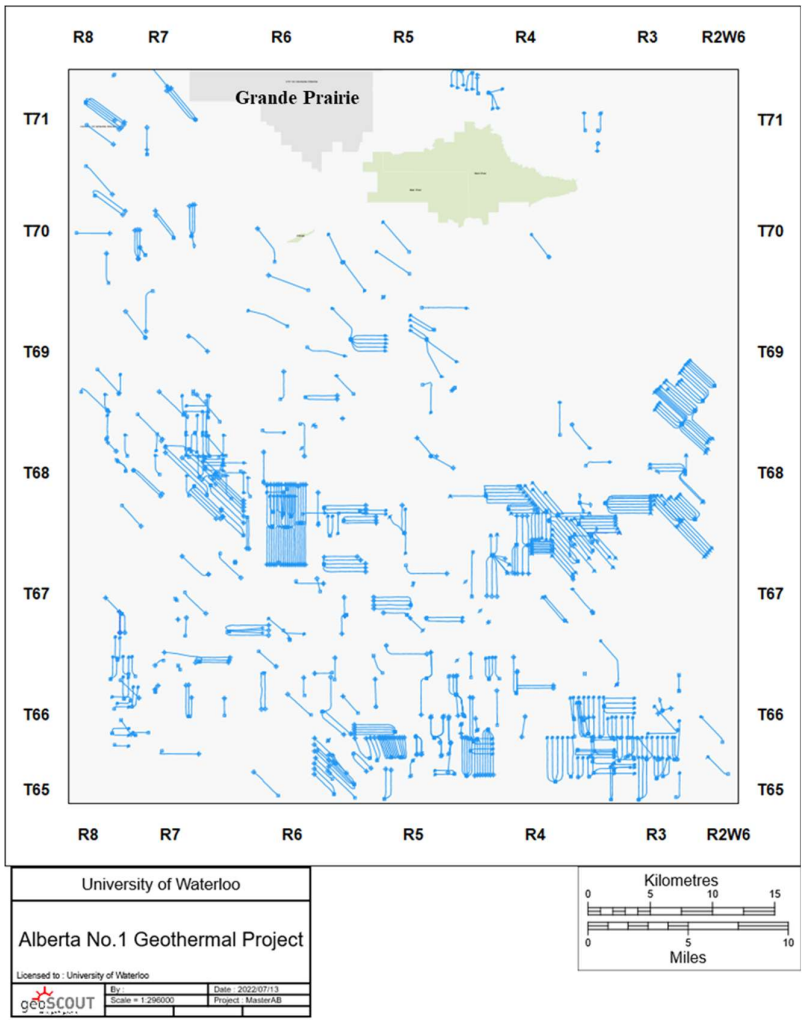

Figure 7-4: A top view of 706 HF wells drilled in the Grande Prairie area. The majority of these wells were drilled into the Montney and Duverney formations. The area in this figure is represented by a red square in Figure 1.

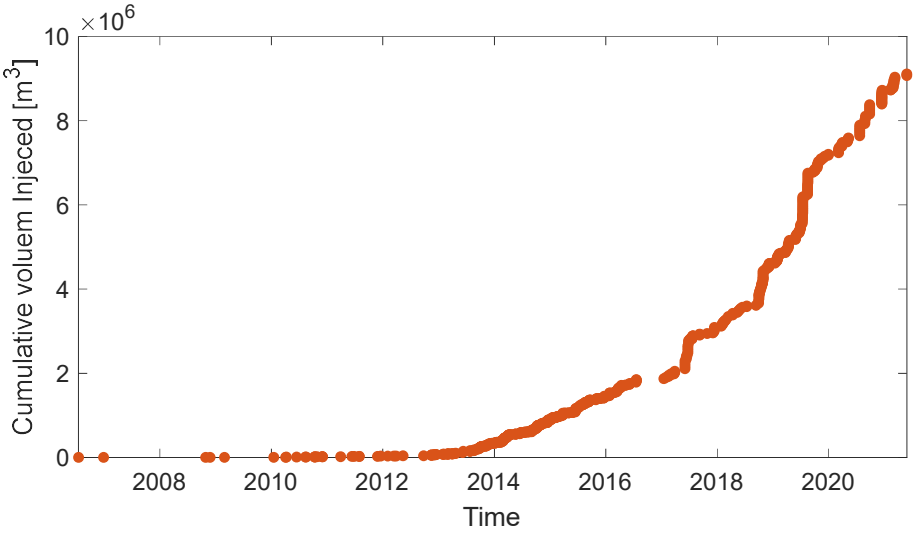

Figure 7-5: 706 HF wells in the Grande Prairie region have been injected around 9×10^6 m^3, yet no major injection-induced seismicity has been reported in the area.

Since the late 1970s, extensive studies have been conducted on the principal stress orientations in British Columbia and Alberta (Bell and Bachu, 2004; Bell and Grasby, 2012; Bell and McCallum, 1990; Dusseault, 1977; Gough and Bell, 1981; Haug and Bell, 2016a). Various methods have been used to determine the maximum horizontal compressive (S_{Hmax}) orientations in the region, including borehole failures (borehole breakouts and tensile-induced fractures) and earthquake focal mechanisms. The 2018 edition of the World Stress Map (WSM) databases include compilations of S_{Hmax} and relative stresses (Heidbach *et al.*, 2018). The blue arrows in Figure 7-1 represent the azimuth of the S_{Hmax} within the region and are based on borehole breakouts and tensile-induced fracture data from the World Stress Map. We have assigned a mean of 45° and a standard division of 5° to S_{Hmax} azimuth values in all areas.

The vertical stress (S_v) can be calculated by integrating the density logs from the surface to the depth of interest. Most drilled wells in the region have density logs that can be used to compute S_v. The vertical stress component in stress tensors is less uncertain due to the availability of these density logs. The Western Canada Sedimentary Basin has been the subject of several studies that have investigated vertical stress variations, which indicate vertical stress gradients ranging from 24.6 to 25.5 MPa/km at depths greater than 2000 m (Bell and Gough, 1979; Bell and Grasby, 2012; Bell *et al.*, 1990; Haug and Bell, 2016a; Shen *et al.*, 2018). In our study, we consider an S_v range of between 24 and 26 MPa/km.

The vertical stress (S_v) can be calculated by integrating the density logs from the surface to the depth of interest. Most drilled wells in the region have density logs that can be used to compute S_v. The vertical stress component in stress tensors is less uncertain due to the availability of density logs. The Western Canada Sedimentary Basin has been the subject of several studies that have investigated vertical stress variations, which indicate vertical stress gradients ranging from 24.6 to 25.5 MPa/km at depths greater than 2000 m (Bell and Gough, 1979; Bell and Grasby, 2012; Bell *et al.*, 1990; Haug and Bell, 2016a; Shen *et al.*, 2018). In our study, we consider an S_v range of between 24 and 26 MPa/km.

There are 706 multistage HF wells in the Grande Prairie region that have been subjected to Diagnostic Fracture Injection Testing (DFIT) or mini-frac, which can determine the minimum in-situ stress magnitude (S_{hmin}). Only one DFIT well has been completed in the Granite Wash Formation, indicating a fracture closure pressure of 16.55 MPa/km. The closure pressure is approximately equal to S_{hmin}. The majority of the HF wells were completed in the Montney and Duvernay Formations in the Grande Prairie region. There are DFIT tests available in the Watt Mountain and Muskeg Formations, both of which are

situated between the Leduc and Granite Wash Formations, but available data are laterally remote from the Grande Prairie area (Figure 7-8). In the Muskeg Formation, 31 measurements of closure pressure indicate a S_{hmin} gradient of between 17 and 23 MPa/km. With 28 reported DFITs, the Watt Mountain Formation shows a S_{hmin} gradient of 16 to 25 MPa/km. Weides *et al.* (2014) use a range of 13.6 to 19.7 MPa/km for S_{hmin} as input for the likelihood of fault slip due to fault injection in the Granite Wash Formation around the town of Peace River. In our study, we consider a S_{hmin} range of between 16 and 24 MPa/km in both the Leduc and Granite Wash Formations.

When determining a strike-slip (or thrust) stress state tensor, the most difficult parameter to determine is the maximum principal stress magnitude (S_{Hmax}). However, borehole failure data, together with knowledge of horizontal and vertical stresses, can be utilized to limit the range of S_{Hmax} magnitude (Yaghoubi *et al.*, 2021). Additionally, earthquake focal mechanisms provide helpful information on the relative stress magnitude as well as the maximum principal stress. To constrain the maximum principal stress magnitudes, we used injection-induced earthquake focal mechanisms recorded around the Grande Prairie region. The dataset includes 11 HF-induced earthquakes around Fox Creek and 39 wastewater-induced earthquakes near Musreau Lake, Alberta (Li *et al.*, 2021).

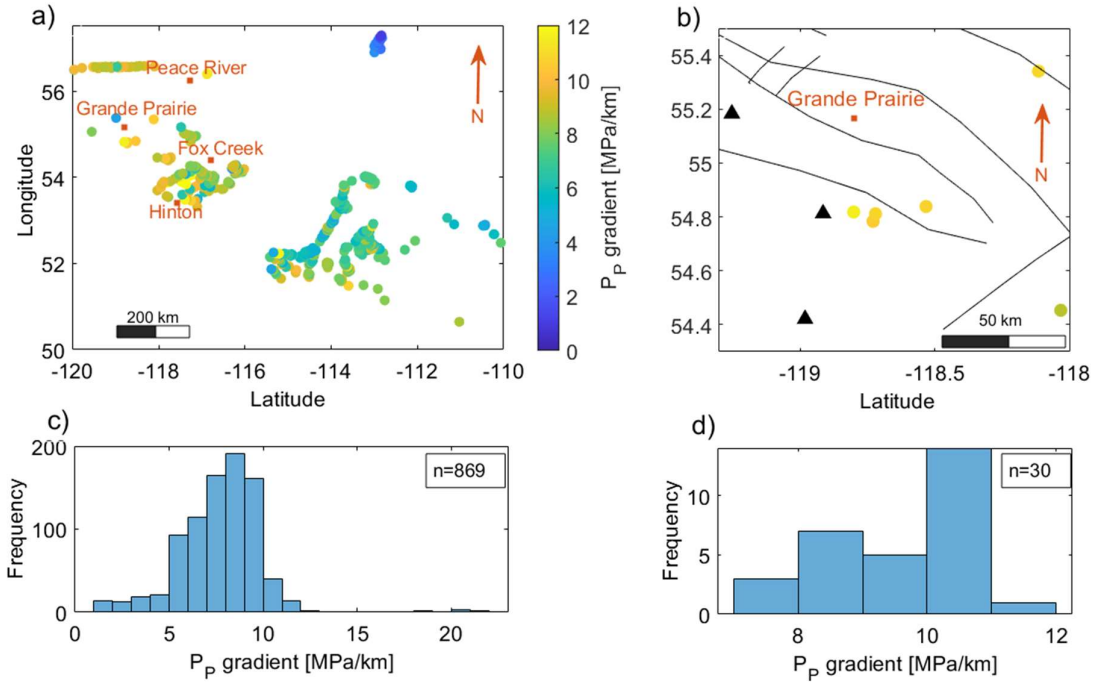

Figure 7-6: Pore pressure (Pp) gradient in the Leduc Formation from drilled wells in a) WCSB and b) around Grande Prairie. Pp gradient frequency in c) WCSB and d) around Grande Prairie are shown in the histogram. Each point represents the location of the well and the color display represents the Pp gradient. High pore pressure was observed around Fox Creek. Black triangles indicate seismic stations.

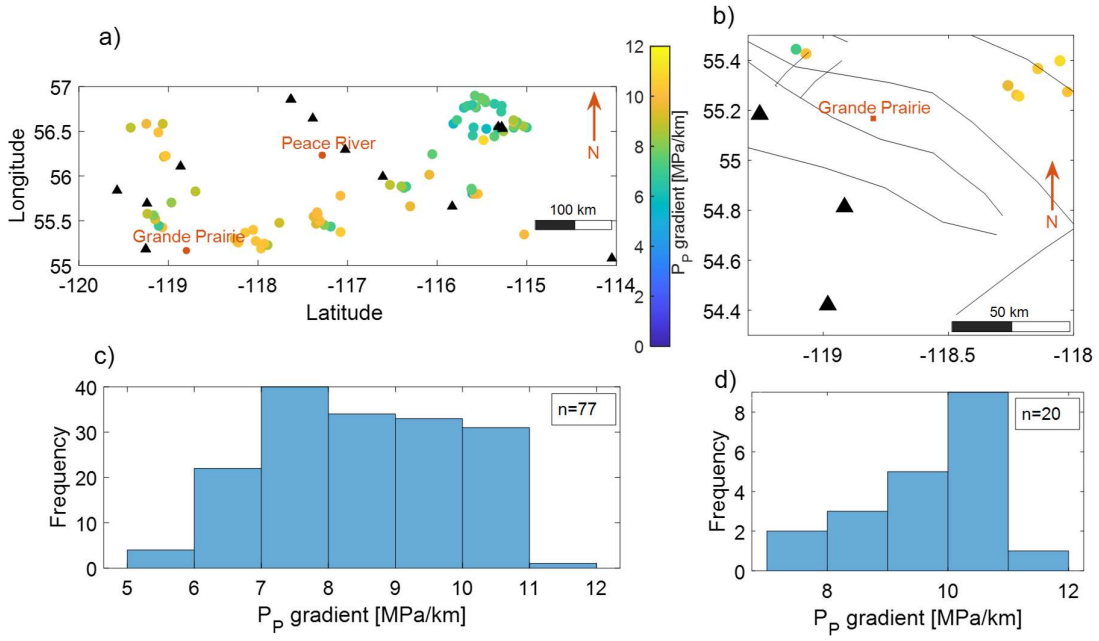

Figure 7-7: Pore pressure gradient for the Granite Wash Formation from drilled wells in a) WCSB and b) around Grande Prairie. Pp gradient frequency in c) WCSB and d) around Grande Prairie are shown in the histogram. Each point represents the location of the well and the color display Pp gradient. Black triangles indicate seismic stations.

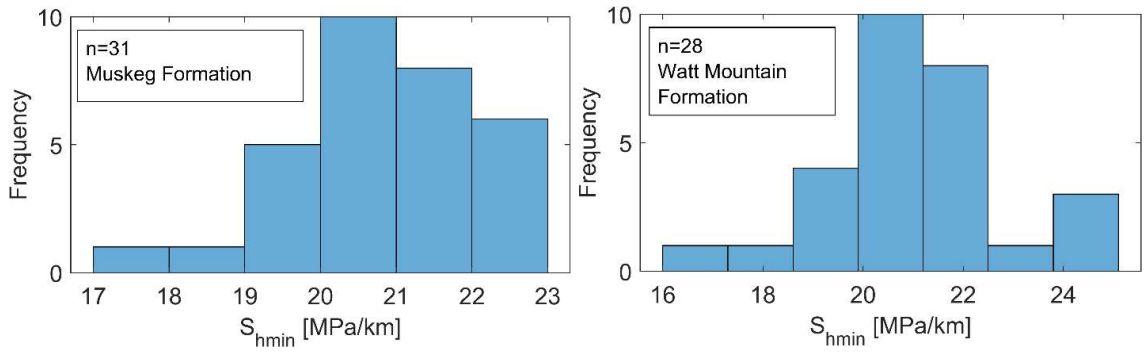

Figure 7-8: The minimum stress gradient in Muskeg and Watt Mountain formations derived from DFIT

Using the inversion of the focal mechanism, the Angelier's shape parameter can be determined by $\varphi = \frac{S_2 - S_3}{S_1 - S_3}$ (Angelier, 1979), in which S_1 represents the maximum principal stress magnitude, S_2 represents the intermediate principal stress magnitude, and S_3 represents the minimum principal stress magnitude. Simpson (1997) generalized the φ values in order to determine the relative stress magnitudes in each stress regime by the equation: $A_\varphi = (n + 0.5) + (-1)^n(\varphi - 0.5)$ where n = 0, 1, 2, for normal, strike-slip and reverse faulting respectively. A_φ ranges continuously from 0 to 1 for normal faults, 1 to 2 for strike-slip

faults, and 2 to 3 for reverse faults (Hurd and Zoback, 2012b; Yaghoubi *et al.*, 2021). Simpson's approach was applied to the 50 compiled focal mechanisms, showing that a strike-slip fault system dominates the area, with an average Anderson fault parameter of $A_\varphi \approx 1.19$ around Musreau Lake and $A_\varphi \approx 1.5$ around Fox Creek. In this study, we consider $A_\varphi \approx 1.2$ to 1.5 for the slip tendency of faults located around Grande Prairie. That means the vertical stress is closer to the minimum horizontal stress than to the maximum horizontal stress.

7.6 Assessment of Fault-Slip Potential

In accordance with Coulomb faulting theory, fault slip depends on the relative stress magnitudes, the angle between the principal stress directions and the fault plane, and the coefficient of friction μ. The slip tendency in a pre-existing cohesionless fault can be calculated in terms of the effective normal stress across the fault, σ_n, to the shear stress along the fault, τ. The likelihood for fault plane slip increases when the resolved shear stress, τ , equals or approaches the frictional resistance of the fault surface; the fault is then referred to as being "critically stressed". Deterministic fault slip tendencies can be defined as the ratio between the effective normal stress and the shear stress on a potential sliding surface ($\tau/\sigma_n \geq \mu$). Figure 7- 9 illustrates the lower hemisphere stereonet for a strike-slip fault regime with an average S_{Hmax} orientation of N45°E and a hydrostatic pore pressure. A pole perpendicular to a fault plane corresponds to each location within the stereonet graph. The red color indicates faults that are prone to slipping or that require less pressure to slip. Thus, nearly vertical faults striking at azimuths of 75° and 15° are critically stressed.

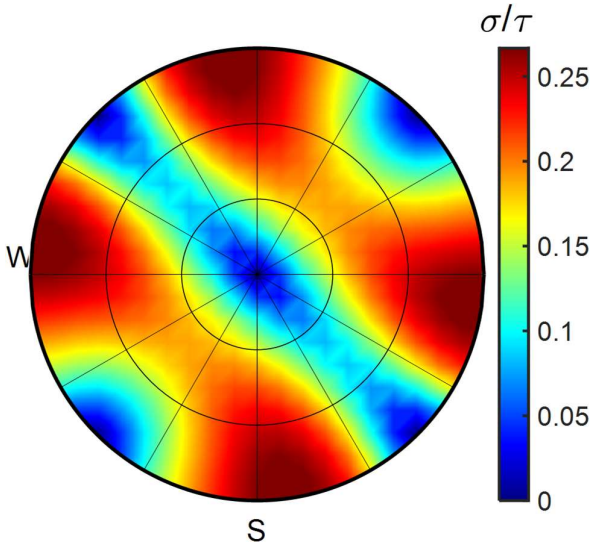

Figure 7-9: A stereonet plot illustrating the slip-tendency (ratio of resolved shear stress to normal stress) around Grande Prairie in the strike-slip faulting regime

Deterministic analyses consider only one analysis as finite and, therefore, significantly underestimate potential risks (Figure 7-9). Based on the evidence provided in the previous section, each geomechanics parameter is associated with some level of uncertainty. A probabilistic analysis, on the other hand, examines slip tendencies by considering uncertainties inherent to each input variable, such as stress magnitudes and directions, fault dip directions, angles, and friction coefficients (Jones and Hillis, 2003; Walsh III and Zoback, 2016; Wang *et al.*, 2010). Various input variables can be assigned as random samples with specific statistical parameters in a Mohr-Coulomb shear failure assessment. The probabilities of failure P_f can be described as follows: $P_f = P[\,\tau - \mu\sigma_n \leq 0]$.

Probabilistic slip tendency analysis is, therefore, more comprehensive and more appropriate for assessing risk in a variety of scenarios. This study examined the slip tendency of faults in injection formations using a Monte Carlo simulation for each fault segment. We evaluated 5000 scenarios within each fault segment as a function of pore pressure perturbation using the Mohr-Coulomb faulting theory. A sample size of 5000 was determined based on the sensitivity analysis of slip probability (with two-digit precision) versus the number of realizations in one segment fault. Uncertainties associated with intrinsic subsurface parameters, such as the state of stress, pore pressure, fault/fracture orientation, and frictional strength, are involved in the analysis. Considering that both the Leduc and Granite Wash Formations exhibit relatively similar geomechanical behavior, one analysis has been conducted to examine fault slip potential in both formations. We present the statistics that

were used as inputs to the Monte Carlo simulation for fault slip tendency in the Grande Prairie region in Figure 7- 10.

Some points should be noted regarding Figure 7- 10. First, pore pressure and principal stress magnitudes in the target formations are assumed to follow a Gaussian distribution. Second, we assume that both the Leduc and Granite Wash Formations exhibit similar geomechanical properties. Finally, as mentioned above, since the depth of both formations varies at different locations, pore pressure and principal stress magnitudes are expressed as gradients (MPa/km). In the fault tendency analysis, however, a depth of 4000 m was applied as the injection depth.

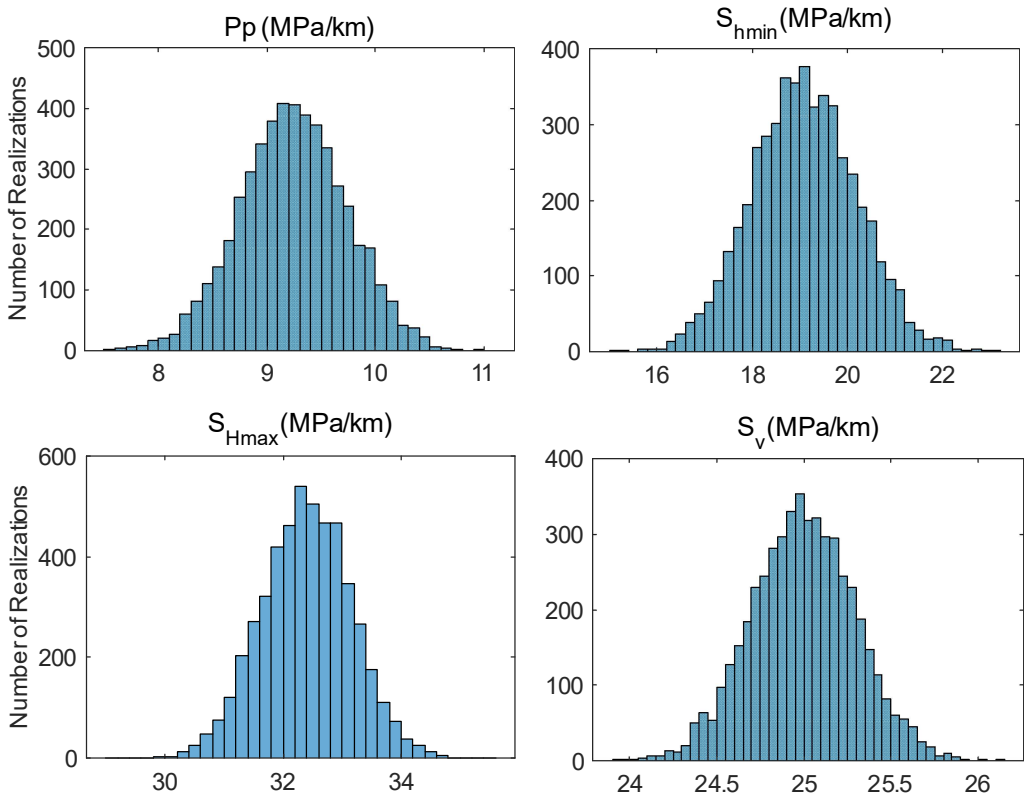

Figure 7-10: Statistics used in Monte Carlo simulations of fault slip around Grande Prairie. It is assumed that pore pressure and principal stress magnitudes in both target formations follow the Gaussian distribution

The result is the cumulative distribution function of the critical pore pressure on each fault derived from the local tectonic stress state and the Mohr-Coulomb shear parameter analyses (Figure 7-11). As shown in the Mohr-Coulomb diagram, the mean of the principal stress magnitudes is accompanied by the associated uncertainty (green error bar). I calculated the shear stress and normal stress acting on each fault plane based on the state of stress and fault dip direction and angle. I then calculated the probability of slip for each fault segment in

response to injection pressures up to 100 MPa (Figure 7-11b). The vertical black straight line in the figure indicates an injection pressure of +2 MPa greater than the pore pressure (ΔP (P_{inj}-Pp) = 2 MPa). In Figure 7-12, faults are colored according to their slip probability when injection pressure is greater than mean formation pore pressure by 2 MPa. According to the results, for this case (ΔP= 2 MPa), there is a low probability of slippage of the faults as a result of fluid injection. The northeast-southwest basement-involving strike-slip fault in the study region has a higher probability of slip. The current result is consistent with a low level of seismicity in the region. As pore pressure increases, the probability of each fault slipping increases. For instance, the red vertical line in Figure 7-11b illustrates an injection pressure of 45 MPa in which the most probable fault has a probability slip of 50%. An increase in injection pressure to 60 MPa is certain to trigger a strike-slip fault in the northeast-southwest basement.

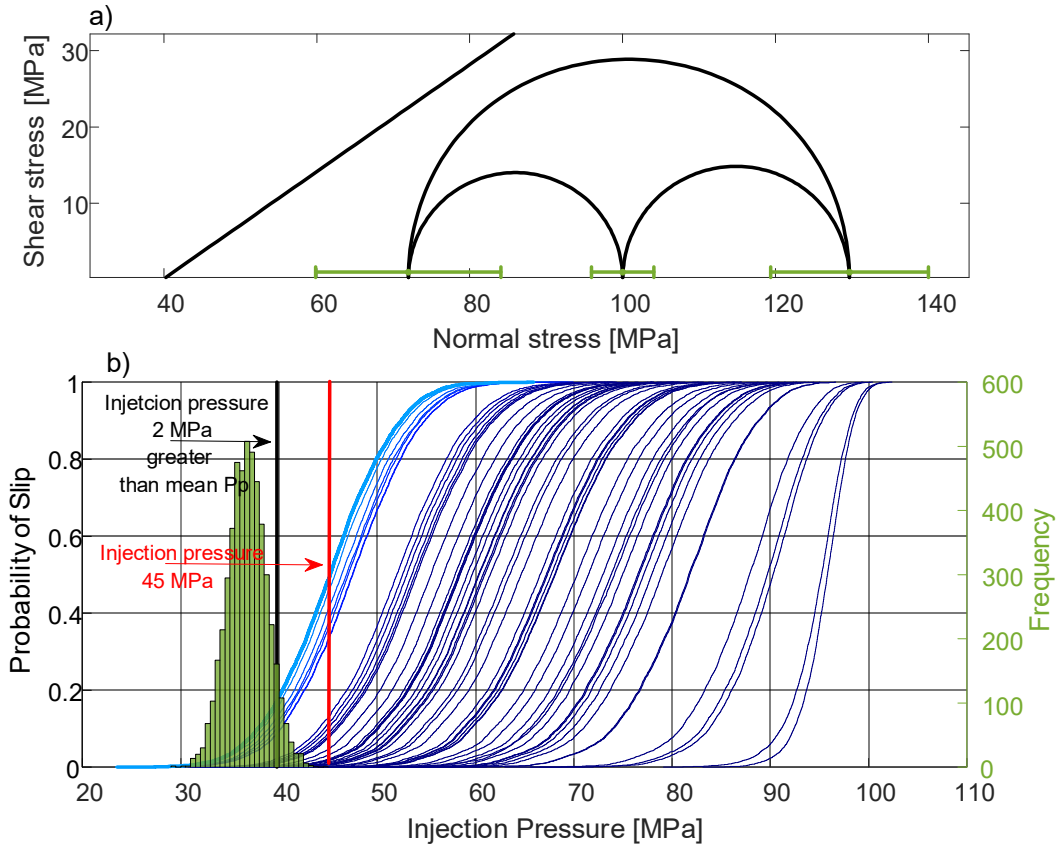

Figure 7-11: a) 3D Mohr diagram presenting principal stress magnitudes acting on known faults located in the Grande Prairie area. b) The cumulative probability function of the required injection pressure to cause slip on each fault segment patch. Note that the injection depth is assumed to be 4 km.

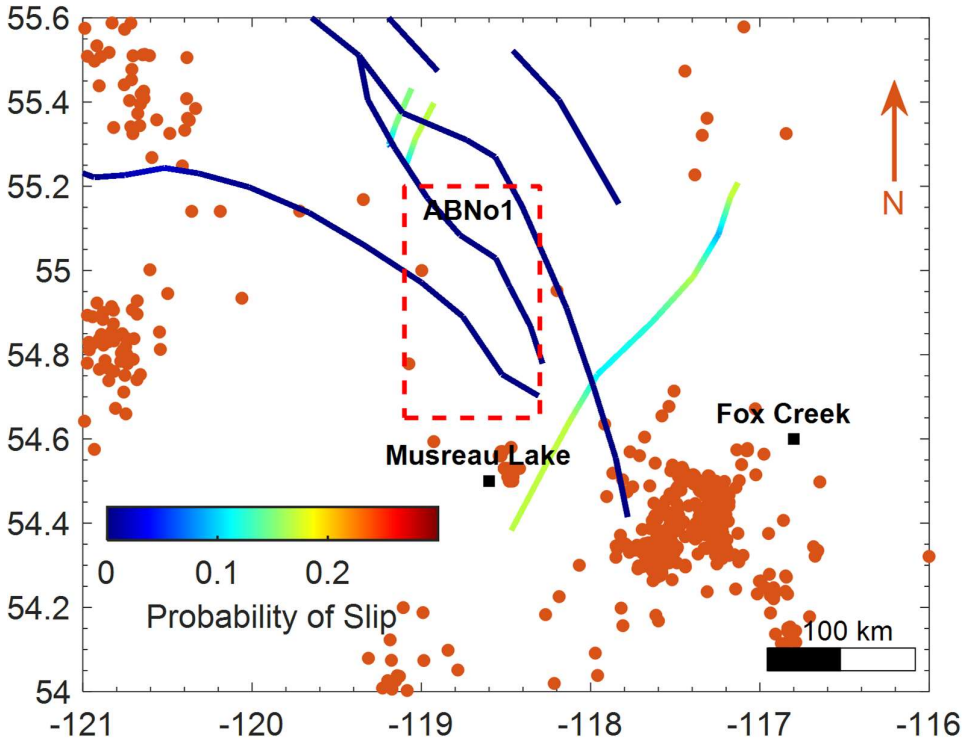

Figure 7-12: Map of faults in the Grande Prairie region colored according to the probability of slip. The red circles represent seismicity reported by Visser et al. (2017) and Visser et al. (2020). Fox Creek earthquakes were caused by HF in the Duvernay Formation, where the Pp gradient is 18 MPa/km.

7.7 Discussion

The results of our study are consistent with the lower level of induced seismic activity observed around Grande Prairie when compared with other areas in Alberta and British Columbia that have been affected by HF (Visser *et al.*, 2020). This theoretical calculation is corroborated by numerous multistage hydraulic fractures having been conducted in this area that have not triggered seismic events. However, Fox Creek, about 200 km southeast of Grande Prairie, experienced some large HF induced earthquakes (Schultz *et al.*, 2017; Yaghoubi *et al.*, 2020). HF seismicity occurred in Fox Creek as a result of multistage HF operations in the Duvernay Formation (Schultz *et al.*, 2017). The Duvernay Formation differs significantly from other formations in the region in terms of pore pressure gradients, one of its primary geomechanics properties. Pore pressure measurements indicate a gradient of 18 MPa/km in the Duvernay Formation around Fox Creek, which is twice as great as that in the Leduc and Granite Wash Formations in the ABNo1 study area.

Another question that might be raised is about seismicity in Musreau Lake, located less than 100 km south of Grande Prairie. The ML 3.9 earthquake occurred in Musreau Lake as a

result of *long-term* wastewater being disposed into the low-pore-pressure Winterburn Group. First, the Musreau Lake area is located closest to a northeast-southwest strike-slip fault, and our results indicate that the fault is more likely to slip than other faults in the region, but the likelihood is as low as 20%. Second, it is suggested by Yu *et al.* (2021b) that an aseismic loading slip mechanism is a triggering mechanism for the earthquake swarm around Musreau Lake. As proposed by Li *et al.* (2021), long-term fluid injection in the Musreau Lake region leads to slip of faults striking in an unfavorable orientation along the NW-SE direction. The sequence of events at Musreau Lake may be a sign that stress accumulation has triggered a hidden fault striking in an unfavorable orientation in the region. If this is the case, long-term fluid injection in the Grande Prairie region might also cause slow-slip injection-induced seismicity on northwest-southeast down-to-the-basin listric faults.

As pore pressure increases, each fault is more likely to slip. Figure 7- 13 illustrates the impact of injection pressure (pore pressure) on fault slip in the study region. As can be seen, the northwest-southeast fault patches require an injection pressure of 80 MPa in order to slip, which is twice the current pore pressure in the Leduc and Granite Wash Formations. Another possible explanation for Grande Prairie's quiescence is that pre-existing local faults are not in critically stressed orientations in the Grande Prairie region compared to faults in the Duvernay Formation in the Fox Creek area.

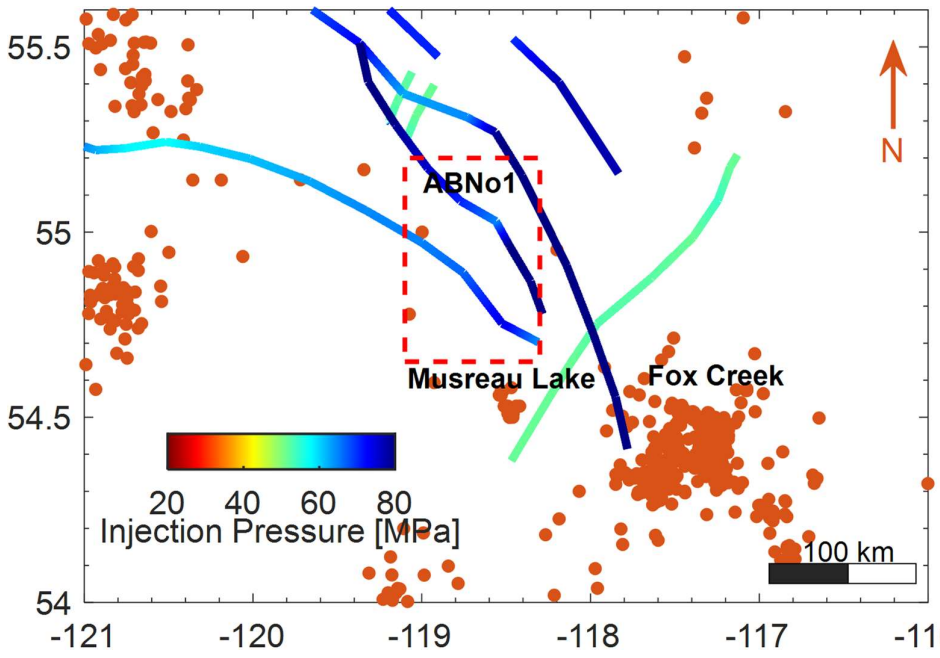

Figure 7-13: Required injection pressures for fault reactivation in the Grande Prairie region. Faults are color-coded according to the critical pore pressure that would cause them to slip.

7.8 Conclusion

We developed and presented a method for calculating the likelihood of fault slip caused by fluid injection in a section of the Western Canadian Sedimentary Basin. The method can be applied generally, wherever sufficient information is available to evaluate parametric uncertainty, and where faults can be identified from data sources. The major characteristics of the method are:

- Data-driven parametric uncertainty in the Mohr-Coulomb slip criteria is included.
- Data-driven parametric uncertainty in stress state, including pore pressure, is included.
- We evaluate various injection scenarios to generally assess the probability of slip.

This approach is applied to known mapped faults in the region that surrounds the Alberta No 1 geothermal site, a proposed geothermal energy development project south of Grande Prairie. Major analysis characteristics and results are:

- Target Leduc and Granite Wash Formations possess moderate porosity and permeability, reasonable depth, and constitute potential geothermal energy extraction zones.
- In both target formations, strike-slip faulting is the dominant stress state.
- Given state parameters extracted from data bases, there is a low probability of fault slip under moderate changes in pore pressure. This finding consistent with the lack of observed seismic events in the area, despite numerous multistage hydraulic fracture installations.
- Nearly vertical faults oriented NEN and ENE are likely critically stressed orientations, but they are stable under moderate changes in pore pressure perturbations.
- Induced seismicity in this region is less likely than in surrounding regions.

It is necessary to have mapped faults in order to use this approach, and this may be a challenge in strike-slip and reverse fault domains. At Fox Creek and Musreau Lake, more distant from the ABNo1 site, events were triggered on faults that were previously unmapped, demonstrating the importance of fault identification prior to a project.

CHAPTER 8

Conclusions and Recommendations:

8.1 Publications

The research work in this thesis has resulted in a series of refereed journal articles and conference articles. The published papers are open access and I am the first author on all of them which were written under supervision of Maurice Dusseault and Yuri Leonenko.

8.1.1 Refereed Publications:

- Yaghoubi, A., Mahbaz, S., Dusseault, M. B., & Leonenko, Y. (2021). Seismicity and the State of Stress in the Dezful Embayment, Zagros Fold and Thrust Belt. Geosciences, 11(6), 254. (Chapter 3).

- Yaghoubi, A., Dusseault, M. B., & Leonenko, Y. (2022). Injection-induced fault slip assessment in Montney Formation in Western Canada. Scientific Reports, 12(1), 1-12. (Chapter 6)

- Yaghoubi, A., Hickson, C., Dusseault, M. B., & Leonenko, Y. (2022). Probabilistic Assessment of Induced Seismicity at the Alberta No. 1 Geothermal Project Site, accepted in Canadian Journal of Earth Science. (Chapter 7)

- Yaghoubi, A., Dusseault, M. B., & Leonenko, Y. (2022). Stress Variation around the Balarud Lineament in the Zagros Fold and Thrust Belt and its Implication for Reservoir Geomechanics, in progress (Chapter 4).

8.1.2 Conference Publications

- Yaghoubi, A., Dusseault, M. B., Mahbaz, S. B., & Leonenko, Y. (2020, June). Probabilistic injection-induced fault slip assessment in Fox Creek Alberta. In *54th US Rock Mechanics/Geomechanics Symposium*. OnePetro. (Chapter 4)

- Yaghoubi, A., Dusseault, M. B., Mahbaz, S., & Leonenko, Y. (2020) Injection-induced Seismic Hazard in Fox Creek Alberta, GeoConvention,, Calgary, Canada. (Chapter 4)

- Yaghoubi, A., Dusseault, M. B., & Leonenko, Y. (2022). Induced Seismicity in Low-Temperature Geothermal Development, ARMA Letters. Issue 33. (Chapter6)
- Yaghoubi, A., Hickson, C., Dusseault, M. B., & Leonenko, Y. (2022). Induced Seismicity Assessment at the Alberta No.1 Geothermal Project, Geothermal Rising Conference, Reno, Nevada, USA. (Chapter 7)

8.2 Conclusions

In this dissertation, the state of stress and style of faulting has been investigated for the Dezful Embayment in the ZFTB (*Chapters 3, 4*), as well as for the Montney and Duvernay Formations in Alberta and British Columbia (*Chapters 5 and 6*). To achieve this objective, I have examined data from boreholes drilled for hydrocarbon resource development and earthquake focal mechanism records. Another achieved objective is the implementation of a probabilistic approach for assessing injection-induced fault slip in unconventional and geothermal resources in WCSB.

Throughout the upper five kilometers of sedimentary cover of the Dezful Embayment, borehole geomechanics studies of 25 wells indicate that strike-slip faulting and normal faulting are the dominant states of stress (*Chapter 3*). However, 108 well-constrained earthquake focal mechanisms deeper than five kilometers in the basement, which is seismically active, indicate a regime of stress in a reverse/strike-slip faulting condition. These results are in agreement with the low seismicity level in the sedimentary cover of the Dezful Embayment and may indicative the result of stress decoupling due to the presence of salt layers. The seismologically determined S_{Hmax} direction is 37° ± 10°, nearly perpendicular to the strike of most faults in the Dezful Embayment. However, stress orientation deflection has been observed in different locations of the sedimentary cover. Using borehole geophysical datasets and records of earthquake focal mechanisms, stress deflection has been investigated in the vicinity of the deep Balarud Lineament in the Northern Dezful Embayment. I found that the second-order stress pattern occurs just in the sedimentary cover in the vicinity of the Balarud Lineament, where the horizontal stress anisotropy (S_{Hmax}-S_{hmin}) is considerably less than that in the basement fault (*Chapter 4*). The regional horizontal stress difference is the determining factor for these anomalies in the folded and faulted sedimentary cover in the ZFTB. With this compressional state of the stress field at seismogenic depths (around 10 km) in the ZFTB, where S_{Hmax}-$S_{hmin} \approx 30$ MPa/km, the local uniaxial stress is not sufficient to deflect the general stress orientation. However, in the sedimentary rock where the regional state of stress has been constrained to be on the border between a normal and a strike-slip faulting regime ($S_{Hmax} \cong S_V > S_{hmin}$), a moderate local horizontal stress difference can cause stress deflection. Thus, variations in stress orientations are seen in most of the oil and gas fields examined in the Dezful Embayment.

Stress states have also been determined using the same approach in the Montney Formation in Alberta and British Columbia as well as in the Duvernay Formation near Fox Creek, Alberta

(*Chapters 5 and 6*). Except around the Peace River Arch, where S_{Hmax} is deflected because of the presence of complex fault systems, S_{Hmax} azimuth generally is NE-SW in the Montney and Duvernay Formations. Measurements of the pore pressure gradient in the Montney Formation indicate that it is compartmentalized with the deeper, western part of the Formation (in British Columbia) having a greater pore pressure gradient value than the shallower, eastern part (in Alberta) (*Chapter 6*). The spatial variations of the S_{hmin} gradients derived from DFIT indicate that minimum principal stress magnitudes are slightly higher on the British Columbia side than in Alberta, similar to the case for spatial pore pressure gradient values (i.e., higher Pp → higher S_{hmin}). Using borehole geomechanics and 103 compiled focal mechanisms, it was determined that a strike-slip fault system was the dominant tectonic regime in the area, with an Anderson fault parameter of $A_\varphi \approx 1.2$ to 1.8. Applying the same approach to eleven earthquake focal mechanisms resulting from HF operations around Fox Creek indicates that A_φ is 1.56 (strike-slip regime) (*Chapter 5*).

A probabilistic approach was used to determine the likelihood of fault slip induced by elevated injection pressure in three different project sites: 1) Duvernay Formation near Fox Creek (*Chapter 5*), 2) Montney Formation in Alberta and British Columbia (*Chapter 6*), and 3) Alberta No.1 geothermal project near Grande Prairie (*Chapter 7*). By using this approach, I accounted for the inherent uncertainties associated with geomechanics parameters. In each project, mapped faults (location, strike, dip, length, depth) were identified for a slip tendency probabilistic approach. The slip tendency of published faults mapped in the Montney Formation was examined, taking into account the uncertainties associated with geomechanics parameters (*Chapter 6*). The probabilistic analysis indicated that most fault planes in the Kiskatinaw area and the northwestern Montney Formation would become unstable with only a moderate increase in pore pressure. On the other hand, some areas possess only a low probability of injection-induced slippage due to relatively low initial pore pressures. The findings are in agreement with the major injection-induced seismicity that has occurred in the area. Pore pressure spatial heterogeneity is a significant factor affecting fault stability and injection-induced earthquakes in the Montney Formation (*Chapter 6*). The same conclusion has been reached in assessing the induced seismicity that has been recorded during hydraulic stimulation of the Duvernay Formation near Fox Creek, Alberta (*Chapter 5*). Based on these findings, two important factors affecting fault stability in the Montney, and Duverney formations are addressed: pore pressure gradient and fault orientation. In these unconventional plays involving low-permeability strata, regions characterized by the highest pore pressure gradients and faults that are nearly vertical and inclined ENE and NEN are the most seismically active. The resulting probabilistic fault stability map can be used as a base map for fluid injection projects involving wastewater disposal, carbon sequestration and storage, and geothermal energy extraction.

Additionally, this dissertation examines the potential effects of fault slip in the Alberta No.1 geothermal project in Alberta within the Municipal District of Greenview south of Grande Prairie,

Alberta, Canada (*Chapter 7*). The Leduc and Granite Wash Formations, potential geothermal development zones in the Grande Prairie area, have been subjected to geomechanical analyses. This study area is characterized by strike-slip faulting as the dominant stress state in both target formations. The result of cumulative injection pressure shows a low probability of reactivating known faults located around the Grande Prairie region. This finding is consistent with a low level of seismic activity reported around Grande Prairie, despite numerous multistage hydraulic stimulation activities in this area. This study shows that faults orientated in NEN and ENE directions, which are related to the critical stress orientations, are stable after perturbations in pore pressure of 2 MPa. As the injection pressure increases, however, the likelihood of fault reactivation and consequent injection-induced seismic activity increases.

8.3 Recommendations

One of the areas not fully addressed in this analysis of injection-induced seismicity in the WCSB is basement fault reactivation. Several large basement-rooted injection-induced earthquakes have been observed near Fox Creek and Fort St. John. Earthquake events are noted first at the depth of the Duvernay or Montney Formation intervals during hydraulic stimulation activity, and additional events are observed to extend downward into the Precambrian crystalline basement. There are three possible mechanisms for injection-induced seismicity in the basement. First, highly permeable fault zones allow fluid pressurization from the Duvernay or Montney injection zone to reach basement-rooted faults. During HF, an increase in pore pressure reduces the normal stresses acting on fault surfaces, leading to shear slip and thereby causing seismic activity. Second, HF in fractured rocks results in coupled matrix poroelastic effects that are transmitted through the solid matrix of the rock mass as a mechanical strain. Thereby, slippage/earthquakes may occur, perhaps not directly related to an increase in local pore pressure, but sufficient to trigger slip along a critically stressed fault in the Precambrian basement rocks. Third, there may be situations where fluid injection and the resulting elevated pressures cause faults to slowly slip, so that the fluid injection induces aseismic (stable) slip sufficiently far from the reservoir depth that the basement is impacted in a process of strain transfer. In this dissertation, just the first possible mechanism is fully discussed. A three-dimensional coupled poroelastic simulation is recommended to evaluate the spatiotemporal changes of solid matrix stresses, transmitted strains, and their relation to basement fault reactivation. Three-dimensional finite element simulation is also needed to examine the stress and strain responses (stress shadowing) that arise during multistage HF stimulation. Stress perturbations during fluid injection in multistage HF operations are cyclic in nature (stages of pressurization followed by pressure decay), but not reversible, as each stage creates some permanent displacement and stress changes in the rock mass. These effects are undoubtedly linked to the induced seismicity during HF and other stimulation

events, and there is a need for them to be investigated. I recommend using the Coulomb failure theory as the slip criterion for each HF treatment to examine the susceptibility of fault reactivation beneath the injection area in the crystalline basement during the cyclic pressurization associated with multi-stage hydraulic fracture.

Another domain of interest that largely remains unstudied is the potential for seismic activity generation with time as geothermal projects gradually create large, cooled volumes of rock in the subsurface. This is particularly relevant for the Geothermal Alberta No. 1 project, for which I have not considered the effect of temperature in my analysis.

The probabilistic fault slip assessment in this dissertation is based on the known mapped faults in the region; however, it is possible that there may be unrecognized critically stressed faults buried in the study area in western Canada. Even with high-resolution 3D seismic data, not all faults can be detected. Therefore, before any fluid injection project is initiated, the location, dip direction, and dip angle of the preexisting faults should be determined with reasonable accuracy. The importance of this is particularly evident in the case of Alberta No. 1 geothermal project.

The selection of the probability distribution is of fundamental importance in probabilistic assessment since it directly impacts the result of the calculation. In this study, stress tensor parameters are assumed to be characterized statistically by a Gaussian distribution defined by a mean and a standard deviation. In order to determine the most appropriate distribution, it is recommended to use other techniques such as probability paper plots, maximum likelihood estimations, or bootstrapping.

One of the limitations of the comprehensive geomechanical model in the ZFTB case study is the absence of direct measurement of the minimum principal stress. Therefore, I recommend measuring S_{hmin} at various locations within the Dezful embayment when the opportunity arises. Particularly important for this measurement is the area near the Balarud Lineament and Kazerun Fault Systems, where stress deflections have been reported in the sedimentary cover. Exploration could be conducted at different depths, particularly in the Asmari and Sarvak Formations, to determine how in-situ stresses change with depth.

Bibliography

Adams, A., Brazier, R., Nyblade, A., Rodgers, A. and Al-Amri, A., 2009. Source parameters for moderate earthquakes in the Zagros Mountains with implications for the depth extent of seismicity. Bulletin of the Seismological Society of America, 99(3): 2044-2049.

Ahlers, S., Hergert, T. and Henk, A., 2019. Numerical Modelling of Salt-Related Stress Decoupling in Sedimentary Basins–Motivated by Observational Data from the North German Basin. Geosciences, 9(1): 19.

Alavi, M., 1994. Tectonics of the Zagros orogenic belt of Iran: new data and interpretations. Tectonophysics, 229(3-4): 211-238.

Alavi, M., 2007. Structures of the Zagros fold-thrust belt in Iran. American Journal of science, 307(9): 1064-1095.

Alberta Geological Survey, 2019. Alberta Table of Formations; Alberta Energy Regulator, URL <https://ags.aer.ca/publications/Table_of_Formations_2019.html>.

Allen, M., Saville, C., Blanc, E., Talebian, M. and Nissen, E., 2013. Orogenic plateau growth: Expansion of the Turkish-Iranian Plateau across the Zagros fold-and-thrust belt. Tectonics, 32(2): 171-190.

Amiri, M., Lashkaripour, G.R., Ghabezloo, S., Moghaddas, N.H. and Tajareh, M.H., 2019. Mechanical earth modeling and fault reactivation analysis for CO 2-enhanced oil recovery in Gachsaran oil field, south-west of Iran. Environmental Earth Sciences, 78(4): 112.

Amponsah, N.Y., Troldborg, M., Kington, B., Aalders, I. and Hough, R.L., 2014. Greenhouse gas emissions from renewable energy sources: A review of lifecycle considerations. Renewable and Sustainable Energy Reviews, 39: 461-475.

Amthor, J.E., Mountjoy, E.W. and Machel, H.G., 1994. Regional-scale porosity and permeability variations in Upper Devonian Leduc buildups: implications for reservoir development and prediction in carbonates. AAPG bulletin, 78(10): 1541-1558.

Anderson, E.M., 1951. The dynamics of faulting and dyke formation with applications to Britain Edinburgh Oliver and Boyd.

Angelier, J., 1979. Determination of the mean principal directions of stresses for a given fault population. Tectonophysics, 56(3-4): T17-T26.

Angelier, J., 1984. Tectonic analysis of fault slip data sets. Journal of Geophysical Research: Solid Earth, 89(B7): 5835-5848.

Asadi, S., Maleki, J.M., Bohloli, B. and Mutabashiani, S., 2013. Experimental, Numerical and Analytical Investigation the Initiation and Propagation of Hydraulic Fracturing. World Applied Sciences Journal, 22(5): 637-646.

Asef, M.R. and Farrokhrouz, M., 2010. Governing parameters for approximation of carbonates UCS. Electron.J.Geotech.Eng, 15: 1581–1592.

Atashbari, V., 2016. Origin of overpressure and pore pressure prediction in carbonate reservoirs of the Abadan Plain Basin. Doctoral dissertation Thesis, University of Adelaide.

Atkinson, G.M., Eaton, D.W., Ghofrani, H., Walker, D., Cheadle, B., Schultz, R., Shcherbakov, R., Tiampo, K., Gu, J. and Harrington, R.M., 2016. Hydraulic fracturing and seismicity in the Western Canada Sedimentary Basin. Seismological research letters, 87(3): 631-647.

Atkinson, G.M., Eaton, D.W. and Igonin, N., 2020. Developments in understanding seismicity triggered by hydraulic fracturing. Nature Reviews Earth & Environment, 1(5): 264-277.

Babaie Mahani, A., Kao, H., Atkinson, G.M., Assatourians, K., Addo, K. and Liu, Y., 2019. Ground-motion characteristics of the 30 November 2018 injection-induced earthquake sequence in northeast British Columbia, Canada. Seismological Research Letters, 90(4): 1457-1467.

Babaie Mahani, A., Schultz, R., Kao, H., Walker, D., Johnson, J. and Salas, C., 2017. Fluid injection and seismic activity in the northern Montney play, British Columbia, Canada, with special reference to the 17 August 2015 M w 4.6 induced earthquake. Bulletin of the Seismological Society of America, 107(2): 542-552.

Bahroudi, A. and Koyi, H.A., 2003. Effect of spatial distribution of Hormuz salt on deformation style in the Zagros fold and thrust belt: an analogue modelling approach. Journal of the Geological Society, 160(5): 719-733.

Bahroudi, A. and Koyi, H.A., 2004. Tectono-sedimentary framework of the Gachsaran Formation in the Zagros foreland basin. Marine and Petroleum Geology, 21(10): 1295-1310.

Baker, C., Jackson, J. and Priestley, K., 1993. Earthquakes on the Kazerun Line in the Zagros Mountains of Iran: strike-slip faulting within a fold-and-thrust belt. Geophysical Journal International, 115(1): 41-61.

Banks, J., 2016. Deep-Dive Analysis of the Best Geothermal Reservoirs for Commercial Development in Alberta. University of Alberta.

Banks, J. and Harris, N.B., 2018. Geothermal potential of Foreland Basins: a case study from the Western Canadian Sedimentary Basin. Geothermics, 76: 74-92.

Bao, X. and Eaton, D.W., 2016. Fault activation by hydraulic fracturing in western Canada. Science, 354(6318): 1406-1409.

Barclay, J., Krause, F., Campbell, R. and Utting, J., 1990. Dynamic casting and growth faulting: Dawson Creek graben complex, Carboniferous–Permian Peace River embayment, western Canada. Bulletin of Canadian Petroleum Geology, 38(1): 115-145.

Barton, C.A., Zoback, M.D. and Burns, K.L., 1988. In-situ stress orientation and magnitude at the Fenton geothermal site, New Mexico, determined from wellbore breakouts. Geophys Res Lett, 5: 467–70.

Barton, C.A., Zoback, M.D. and Moos, D., 1995. Fluid flow along potentially active faults in crystalline rock. Geology, 23(8): 683-686.

BC Oil and Gas Commission, 2019. British Columbia's Oil and Gas Reserves and production report. https://www.bcogc.ca/files/reports/Technical-Reports/2015-oil-and-gas-reserves-and-production-report_4.pdf.

Bell, J. and Bachu, S., 2004. In-situ stress magnitudes in the Alberta Basin-regional coverage for petroleum engineers, Canadian International Petroleum Conference. OnePetro.

Bell, J. and Gough, D.I., 1979. Northeast-southwest compressive stress in Alberta: evidence from oil wells. Earth Planet Sci Lett 475–82.

Bell, J. and Grasby, S., 2012. The stress regime of the Western Canadian sedimentary basin. Geofluids, 12(2): 150-165.

Bell, J. and McCallum, R., 1990. In situ stress in the Peace River Arch area, western Canada. Bulletin of Canadian Petroleum Geology, 38(1): 270-281.

Bell, J., Price, P. and McLellan, P., 1990. In-situ stress in the western Canada Sedimentary Basin. Bulletin of Canadian Petroleum Geology, 38(1): 157-157.

Berberian, M., 1995. Master "blind" thrust faults hidden under the Zagros folds: active basement tectonics and surface morphotectonics. Tectonophysics, 241(3-4): 193-224.

Berger, Z., 1994. The Fort St. John Graben, Western Canada. Satellite Hydrocarbon Exploration: 239-248.

Berger, Z., 2005. Aeromag/tectonic study of northeast British Columbia, summary tectonic map. Image interpretation Technologies Inc.(IITech.).

Berger, Z., Boast, M. and Mushayandebvu, M., 2009. Basement structures control on the development of the Peace River Arch's Montney/Doig resource plays. Reservoir, Canadian Society of Petroleum Geologists, 36: 40-45.

Bordenave, M.L. and Burwood, R., 1995. The Albian Kazhdumi Formation of the Dezful Embayment, Iran: One of the Most Efficient Petroleum Generating Systems. In: B.J. Katz (Editor), Petroleum Source Rocks. Springer Berlin Heidelberg, Berlin, Heidelberg, pp. 183-207.

Bordenave, M.L. and Hegre, J.A., 2010. Current distribution of oil and gas fields in the Zagros Fold Belt of Iran and contiguous offshore as the result of the petroleum systems. Geological Society, London, Special Publications, 330(1): 291-353.

Brace, W. and Kohlstedt, D., 1980. Limits on lithospheric stress imposed by laboratory experiments. Journal of Geophysical Research: Solid Earth, 85(B11): 6248-6252.

Byerlee, J., 1978. Friction of rocks, Rock friction and earthquake prediction. Springer, pp. 615-626.

Casini, G., Romaire, I., Casciello, E., Saura, E., Vergés, J., Fernández, N. and Hunt, D.W., 2018. Fracture characterization in sigmoidal folds: Insights from the Siah Kuh anticline, Zagros, Iran. AAPG Bulletin, 102(3): 369-399.

Champollion, Y., Hickson, C. and Huang, K., 2021. Comparing Temperature Data from Oil and Gas and Geothermal Logs. Geoconvention Conference 2021.

Chang, K.W. and Yoon, H., 2022. Permeability-controlled migration of induced seismicity to deeper depths near Venus in North Texas. Scientific Reports, 12(1): 1-12.

Chatellier, J.-Y. and Euzen, T., 2021. New Approach to Reveal Compartmentalization in Montney Horizontal Wells for Completion Design Optimization. SPE/AAPG/SEG Unconventional Resources Technology Conference.

Chatellier, J.-Y., Simpson, K., Perez, R. and Tribovillard, N., 2018. Geochemically focused integrated approach to reveal reservoir characteristics linked to better Montney productivity potential. Bulletin of Canadian Petroleum Geology, 66(2): 516-551.

Cornelio, C., Passelègue, F., Spagnuolo, E., Di Toro, G. and Violay, M., 2020. Effect of fluid viscosity on fault reactivation and coseismic weakening. Journal of Geophysical Research: Solid Earth, 125(1): e2019JB018883.

Cornet, F.H. and Röckel, T., 2012. Vertical stress profiles and the significance of "stress decoupling". Tectonophysics, 581: 193-205.

Davies, G., 1997a. The Triassic of theWestern Canada Sedimentary Basin: Tectonic and stratigraphic framework, paleogeography, paleoclimate and biota. Bulletin of Canadian Petroleum Geology, 45(4): 434-460.

Davies, G., 1997b. The Upper Triassic Baldonnel and Pardonet formations, Western Canada Sedimentary Basin. Bulletin of Canadian Petroleum Geology, 45(4): 643-674.

Davies, G., Moslow, T.F. and Sherwin, M.D., 1997. The lower Triassic Montney formation, west-central Alberta. Bulletin of Canadian Petroleum Geology, 45(4): 474-505.

Dec, T., Hein, F.J. and Trotter, R.J., 1996. Granite wash alluvial fans, fan-deltas and tidal environments, northwestern Alberta: implications for controls on distribution of Devonian clastic wedges associated with the Peace River Arch. Bulletin of canadian petroleum geology, 44(3): 541-565.

Deng, K., Liu, Y. and Harrington, R.M., 2016. Poroelastic stress triggering of the December 2013 Crooked Lake, Alberta, induced seismicity sequence. Geophysical Research Letters, 43(16): 8482-8491.

Downey, B., Henry, M., Finley, R., Korney, S. and Zhou, J., 2021. Pathways to Net-Zero: Opportunities for Canada in a Changing Energy Sector. Alberta Law Review: 225-225.

Dusseault, M.B., 1977. Stress state and hydraulic fracturing in the Athabasca oil sands. Journal of Canadian Petroleum Technology, 16(03).

Dusseault, M.B., 2011. Geomechanical challenges in petroleum reservoir exploitation. KSCE Journal of Civil Engineering, 15(4): 669-678.

Dusseault, M.B., Bruno, M.S. and Barrera, J., 2001. Casing shear: causes, cases, cures. SPE Drilling & Completion, 16(02): 98-107.

Dusseault, M.B., Maury, V., Sanfilippo, F. and Santarelli, F.J., 2004. Drilling around salt: risks, stresses, and uncertainties, Gulf Rocks 2004, the 6th North America Rock Mechanics Symposium (NARMS). American Rock Mechanics Association.

Eaton, D.W. and Schultz, R., 2018. Increased likelihood of induced seismicity in highly overpressured shale formations. Geophysical Journal International, 214(1): 751-757.

Enlighten Geoscience, L., 2021. Pressure, Stress and Fault Slip Risk Mapping in the Kiskatinaw Seismic Monitoring and Mitigation Area, British Columbia, BC Oil and Gas Research and Innovation Society (ER-Seismic-2020-01).

Enlighten Geoscience Ltd., 2021. Pressure, Stress and Fault Slip Risk Mapping in the Kiskatinaw Seismic Monitoring and Mitigation Area, British Columbia. BC Oil and Gas Research and Innovation Society (ER-Seismic-2020-01).

Euzen, T., Watson, N., Fowler, M., Mort, A. and Moslow, T.F., 2021. Petroleum distribution in the Montney hybrid play: Source, carrier bed, and structural controls. AAPG Bulletin, 105(9): 1867-1892.

Eyre, T.S., Eaton, D.W., Garagash, D.I., Zecevic, M., Venieri, M., Weir, R. and Lawton, D.C., 2019. The role of aseismic slip in hydraulic fracturing–induced seismicity. Science advances, 5(8): eaav7172.

Eyre, T.S., Samsonov, S., Feng, W., Kao, H. and Eaton, D.W., 2022. InSAR data reveal that the largest hydraulic fracturing-induced earthquake in Canada, to date, is a slow-slip event. Scientific reports, 12(1): 1-12.

Farrokhrouz, M., Asef, M.R. and Kharrat, R., 2014. Empirical estimation of uniaxial compressive strength of shale formations. GEOPHYSICS, 79(NO. 4): D227–D233.

Fredrich, J.T., Coblentz, D., Fossum, A.F. and Thorne, B.J., 2003. Stress perturbations adjacent to salt bodies in the deepwater Gulf of Mexico, SPE Annual Technical Conference and Exhibition. Society of Petroleum Engineers.

Frick, S., Kaltschmitt, M. and Schröder, G., 2010. Life cycle assessment of geothermal binary power plants using enhanced low-temperature reservoirs. Energy, 35(5): 2281-2294.

Frohlich, C., Ellsworth, W., Brown, W.A., Brunt, M., Luetgert, J., MacDonald, T. and Walter, S., 2014. The 17 May 2012 M4. 8 earthquake near Timpson, East Texas: An event possibly triggered by fluid injection. Journal of Geophysical Research: Solid Earth, 119(1): 581-593.

Furlong, C.M., Gingras, M.K. and Zonneveld, J.P., 2020. High-resolution sequence stratigraphy of the Middle Triassic Sunset Prairie Formation, Western Canada Sedimentary Basin, north-eastern British Columbia. The Depositional Record, 6(2): 383-408.

Gaarenstroom, L., 1993. et al. Overpressures in the Central North Sea: implications for trap integrity and drilling safety, Geology of Northwest Europe: Proceedings of the Fourth Conference.

Gephart, J.W. and Forsyth, D.W., 1984. An improved method for determining the regional stress tensor using earthquake focal mechanism data: application to the San Fernando earthquake sequence. Journal of Geophysical Research: Solid Earth, 89(B11): 9305-9320.

Ghofrani, H. and Atkinson, G.M., 2020. Activation rate of seismicity for hydraulic fracture wells in the Western Canada sedimentary basin. Bulletin of the Seismological Society of America, 110(5): 2252-2271.

Glass, D., 1990. Lexicon of Canadian Stratigraphy, Volume 4, Western Canada, including Eastern British Columbia, Alberta, Saskatchewan and Southern Manitoba. Canadian Society of Petroleum Geologists, 772.

Gough, D. and Bell, J., 1981. Stress orientations from oil-well fractures in Alberta and Texas. Canadian Journal of Earth Sciences, 18(3): 638-645.

Grasby, S.E., Jessop, A., Kelman, M., Ko, M., Chen, Z., Allen, D., Bell, S., Ferguson, G., Majorowicz, J. and Moore, M., 2011. Geothermal energy resource potential of Canada.

Haghi, A., Chalaturnyk, R. and Ghobadi, H., 2018. The state of stress in SW Iran and implications for hydraulic fracturing of a naturally fractured carbonate reservoir. International Journal of Rock Mechanics and Mining Sciences, 105: 28-43.

Haghnejad , A., Ahangari, K. and Ali, N., 2014. Investigation on Various Relations Between Uniaxial Compressive Strength, Elasticity and Deformation Modulus of Asmari Formation in Iran. Arab J Sci Eng, 39: 2677–2682.

Haghshenas, B. and Qanbari, F., 2020. Field-Wide Review of Diagnostic Fracture Injection Tests DFIT in Montney and Duvernay Formations–Part 1: Stress and Pressure Distributions. SPE Canada Unconventional Resources Conference.

Haimson, B.C. and Herrick, C.G., 1989. Borehole breakouts and in situ stress. In: 12th Annual Energy-Sources Technology Conference and Exhibition, Houston, TX.

Hardebeck, J.L. and Hauksson, E., 2001. Crustal stress field in southern California and its implications for fault mechanics. Journal of Geophysical Research: Solid Earth, 106(B10): 21859-21882.

Hardebeck, J.L. and Michael, A.J., 2006. Damped regional-scale stress inversions: Methodology and examples for southern California and the Coalinga aftershock sequence. Journal of Geophysical Research: Solid Earth, 111(B11).

Häring, M.O., Schanz, U., Ladner, F. and Dyer, B.C., 2008. Characterisation of the Basel 1 enhanced geothermal system. Geothermics, 37(5): 469-495.

Hatzfeld, D., Authemayou, C., Van Der Beek, P., Bellier, O., Lavé, J., Oveisi, B., Tatar, M., Tavakoli, F., Walpersdorf, A. and Yamini-Fard, F., 2010. The kinematics of the Zagros mountains (Iran). Geological Society, London, Special Publications, 330(1): 19-42.

Haug, K. and Bell, J., 2016a. Compilation of in situ stress data from Alberta and Northeastern British Columbia (tabular data, tab delimited). Alberta Energy Regulator, AER/AGS Digital Data, 40.

Haug, K. and Bell, J., 2016b. Compilation of in situ stress data from Alberta and Northeastern British Columbia (tabular data, tab delimited). Alberta Energy Regulator, Edmonton.

Hauksson, E., 1994. State of stress from focal mechanisms before and after the 1992 Landers earthquake sequence. Bulletin of the Seismological Society of America, 84(3): 917-934.

Hayes, B., Anderson, J., Cooper, M., McLellan, P., Rostron, B. and Clarke, J., 2020. Wastewater Disposal in the Maturing Montney Play Fairway, Northeastern British Columbia (NTS 093P, 094A, B, G, H). Geoscience BC Summary of Activities: 2021-02.

Heidbach, O., Barth, A., Müller, B., Reinecker, J., Stephansson, O., Tingay, M. and Zang, A., 2016a. WSM quality ranking scheme, database description and analysis guidelines for stress indicator.

Heidbach, O., Rajabi, M., Cui, X., Fuchs, K., Müller, B., Reinecker, J., Reiter, K., Tingay, M., Wenzel, F. and Xie, F., 2018. The World Stress Map database release 2016: Crustal stress pattern across scales. Tectonophysics, 744: 484-498.

Heidbach, O., Rajabi, M., Reiter, K. and Ziegler, M., 2016b. World stress map 2016. Science, 277: 1956-1962.

Heidbach, O., Tingay, M., Barth, A., Reinecker, J., Kurfeß, D. and Müller, B., 2010. Global crustal stress pattern based on the World Stress Map database release 2008. Tectonophysics, 482(1-4): 3-15.

Hennings, P.H., Snee, J.E.L., Osmond, J.L., DeShon, H.R., Dommisse, R., Horne, E., Lemons, C. and Zoback, M.D., 2019. Injection-Induced Seismicity and Fault-Slip Potential in the Fort Worth Basin, TexasInjection-Induced Seismicity and Fault-Slip Potential in the Fort Worth Basin, Texas. Bulletin of the Seismological Society of America, 109(5): 1615-1634.

Hickson, C., 2022. Geothermal Energy: The Full Value Chain in a Decarbonizing World, Gobal Energy Show Conference, Calgary, Alberta, Canada.

Hickson, C. and Colombina, M., 2021. Launching Conventional Deep Geothermal Development Projects in Oil and Gas Dominated Regions of Canada, Geothermal Rising Conference, San Diego.

Hickson, C., Huang, K., Cotterill, D., Gosnold, W. and Benoit, D., 2020. Updated Resource Assessment Alberta No. 1, Terrapin Internal Report.

Hickson, C.J., Raymond, J., Dusseault, M., Fraser, T., Huang, K., Marcia, K., Miranda, M., Poux, B., Fiess, K. and Ferguson, G., 2021. Geothermal Energy in Canada–Times Are “a Changing”.

Hofmann, H., Weides, S., Babadagli, T., Zimmermann, G., Moeck, I., Majorowicz, J. and Unsworth, M., 2014. Potential for enhanced geothermal systems in Alberta, Canada. Energy, 69: 578-591.

Hojka, K., Dusseault, M. and Bogobowicz, A., 1993. Analytical solutions for transient thermoelastic stress fields around a borehole during fluid injection into permeable media. Journal of Canadian Petroleum Technology, 32(04).

Holmgren, J.M., Atkinson, G.M. and Ghofrani, H., 2019. Stress Drops and Directivity of Induced Earthquakes in the Western Canada Sedimentary Basin. Bulletin of the Seismological Society of America, 109(5): 1635-1652.

Hosseini, E., Ghojogh, J.N. and Habibnia, B., 2015. Study of Faults in Asmari Formation by FMI Image Log, Case Study: Lali Oilfield. American Journal of Oil and Chemical Technologies: Volume, 3(5).

Hosseini, H., Pakzad, M. and Naserieh, S., 2019. Iranian regional centroid moment tensor catalog: Solutions for 2012–2017. Physics of the Earth and Planetary Interiors, 286: 29-41.

Huang, K., Champollion, Y. and Hickson, C., 2021a. Preliminary Results and New Insights from a Deep Temperature Log in the Western Canada Sedimentary Basin.

Huang, K.K., Hickson, C.J., Cotterill, D. and Champollion, Y., 2021b. Geothermal Assessment of Target Formations Using Recorded Temperature Measurements for the Alberta No. 1 Geothermal Project. Applied Sciences, 11(2): 608.
Hurd, O. and Zoback, M.D., 2012a. Intraplate earthquakes, regional stress and fault mechanics in the Central and Eastern US and Southeastern Canada. Tectonophysics, 581: 182-192.
Hurd, O. and Zoback, M.D., 2012b. Regional stress orientations and slip compatibility of earthquake focal planes in the New Madrid seismic zone. Seismological Research Letters, 83(4): 672-679.
Hurd, O.V., 2012. Geomechanical analysis of intraplate earthquakes and earthquakes induced during stimulation of low permeability gas reservoirs, Stanford University.
Jackson, J. and Fitch, T., 1981. Basement faulting and the focal depths of the larger earthquakes in the Zagros mountains (Iran). Geophysical Journal International, 64(3): 561-586.
Jackson, J. and McKenzie, D., 1984. Active tectonics of the Alpine—Himalayan Belt between western Turkey and Pakistan. Geophysical Journal International, 77(1): 185-264.
Jaeger, J.C., Cook, N.G. and Zimmerman, R., 2009. Fundamentals of rock mechanics. John Wiley & Sons.
Jahani, S., Callot, J.-P., de Lamotte, D.F., Letouzey, J. and Leturmy, P., 2007. The Salt Diapirs of the Eastern Fars Province (Zagros, Iran): A Brief Outline of their Past and Present. In: O. Lacombe, F. Roure, J. Lavé and J. Vergés (Editors), Thrust Belts and Foreland Basins: From Fold Kinematics to Hydrocarbon Systems. Springer Berlin Heidelberg, Berlin, Heidelberg, pp. 289-308.
Johann, L., Shapiro, S.A. and Dinske, C., 2018. The surge of earthquakes in Central Oklahoma has features of reservoir-induced seismicity. Scientific reports, 8(1): 1-14.
Jones, R.M. and Hillis, R.R., 2003. An integrated, quantitative approach to assessing fault-seal risk. AAPG bulletin, 87(3): 507-524.
Kanamori, H. and Anderson, D.L., 1975. Theoretical basis of some empirical relations in seismology. Bulletin of the seismological society of America, 65(5): 1073-1095.
Kastrup, U., Zoback, M.L., Deichmann, N., Evans, K.F., Giardini, D. and Michael, A.J., 2004. Stress field variations in the Swiss Alps and the northern Alpine foreland derived from inversion of fault plane solutions. Journal of Geophysical Research: Solid Earth, 109(B1).
Kaven, J.O., Hickman, S.H., McGarr, A.F., Walter, S. and Ellsworth, W.L., 2014. Seismic monitoring at the Decatur, IL, CO2 sequestration demonstration site. Energy Procedia, 63: 4264-4272.
Kohli, A.H. and Zoback, M.D., 2013. Frictional properties of shale reservoir rocks. Journal of geophysical research: solid earth, 118(9): 5109-5125.
Koleini, M., 2012. Engineering geological assessment and rock mass characterization of the Asmari formation (Zagros range) as large dam foundation rocks in southwestern Iran, University of Pretoria.
Konstantinovskaya, E., Li, Q., Zhmodik, A., Ibelegbu, C., Schultz, R. and Shipman, T., 2021. Lateral fluid propagation and strike slip fault reactivation related to hydraulic fracturing and induced seismicity in the Duvernay Formation, Fox Creek area, Alberta. Geophysical Journal International, 227(1): 518-543.
Kraft, T. and Deichmann, N., 2014. High-precision relocation and focal mechanism of the injection-induced seismicity at the Basel EGS. Geothermics, 52: 59-73.
Lachenbruch, A.H. and Sass, J., 1980. Heat flow and energetics of the San Andreas fault zone. Journal of Geophysical Research: Solid Earth, 85(B11): 6185-6222.
Lacombe, O., Mouthereau, F., Kargar, S. and Meyer, B., 2006. Late Cenozoic and modern stress fields in the western Fars (Iran): Implications for the tectonic and kinematic evolution of central Zagros. Tectonics, 25(1): n/a-n/a.
Levandowski, W., Herrmann, R.B., Briggs, R., Boyd, O. and Gold, R., 2018. An updated stress map of the continental United States reveals heterogeneous intraplate stress. Nature Geoscience, 11(6): 433-437.
Li, T., Gu, Y.J., Wang, J., Wang, R., Yusifbayov, J., Canales, M.R. and Shipman, T., 2021. Earthquakes Induced by Wastewater Disposal near Musreau Lake, Alberta, 2018–2020. Seismological Research Letters.

Lund, B. and Townend, J., 2007. Calculating horizontal stress orientations with full or partial knowledge of the tectonic stress tensor. Geophysical Journal International, 170(3): 1328-1335.
Maggi, A., Jackson, J., Priestley, K. and Baker, C., 2000. A re-assessment of focal depth distributions in southern Iran, the Tien Shan and northern India: Do earthquakes really occur in the continental mantle? Geophysical Journal International, 143(3): 629-661.
Mahbaz, S.B., Yaghoubi, A., Dehghani-Sanij, A., Sarvaramini, E., Leonenko, Y. and Dusseault, M.B., 2021. Well-Doublets: A First-Order Assessment of Geothermal SedHeat Systems. Applied Sciences, 11(2): 697.
Martínez-Garzón, P., Kwiatek, G., Ickrath, M. and Bohnhoff, M., 2014. MSATSI: A MATLAB package for stress inversion combining solid classic methodology, a new simplified user-handling, and a visualization tool. Seismological Research Letters, 85(4): 896-904.
Mastin, L., 1988. Effect of Borehole Devition on Breakout Orientation. J Geophys Res, 93: 9187-9195.
Mazidi Saber Mehrabi , Haftani Mohammad , Bohloli Bahman and Akbar, C., 2012. Measurement of uniaxial compressive strength of rocks using reconstructed cores from rock cuttings. Journalof Petroleum Science and Engineering, 86: 39-43.
McClure, M. and Horne, R., 2011. Investigation of injection-induced seismicity using a coupled fluid flow and rate/state friction model. GEOPHYSICS, 76(6): WC181-WC198.
McGarr, A., 2014. Maximum magnitude earthquakes induced by fluid injection. Journal of Geophysical Research: solid earth, 119(2): 1008-1019.
McGarr, A., Simpson, D., Seeber, L. and Lee, W., 2002. Case histories of induced and triggered seismicity. International Geophysics Series, 81(A): 647-664.
McKenzie, D., 1972. Active tectonics of the Mediterranean region. Geophysical Journal International, 30(2): 109-185.
Michael, A.J., 1984. Determination of stress from slip data: faults and folds. Journal of Geophysical Research: Solid Earth, 89(B13): 11517-11526.
Moeck, I., Kwiatek, G. and Zimmermann, G., 2009. Slip tendency analysis, fault reactivation potential and induced seismicity in a deep geothermal reservoir. Journal of Structural Geology, 31(10): 1174-1182.
Molinaro, M., Leturmy, P., Guezou, J.C., Frizon de Lamotte, D. and Eshraghi, S., 2005. The structure and kinematics of the southeastern Zagros fold-thrust belt, Iran: From thin-skinned to thick-skinned tectonics. Tectonics, 24(3).
Moos, D.B. and Zoback, M.D., 1990. Utilization of observations of well bore failure to constrain the orientation and magnitude of crustal stresses: application to continental deep sea drilling project and ocean drilling program boreholes. J Geophys Res, 95: 9305–25.
Morris, A., Ferrill, D.A. and Henderson, D.B., 1996. Slip-tendency analysis and fault reactivation. Geology, 24(3): 275-278.
Morris, A.P., Hennings, P.H., Horne, E.A. and Smye, K.M., 2021. Stability of basement-rooted faults in the Delaware Basin of Texas and New Mexico, USA. Journal of Structural Geology, 149: 104360.
Motiei, H., 1994. Stratigraphy of Zagros (In Farsi). Geological Survey of Iran.
Mouthereau, F., Lacombe, O., Tensi, J., Bellahsen, N., Kargar, S. and Amrouch, K., 2007. Mechanical constraints on the development of the Zagros Folded Belt (Fars), Thrust Belts and Foreland Basins. Springer, pp. 247-266.
Mukuhira, Y., Asanuma, H., Niitsuma, H. and Häring, M.O., 2013. Characteristics of large-magnitude microseismic events recorded during and after stimulation of a geothermal reservoir at Basel, Switzerland. Geothermics, 45: 1-17.
Nabaei, M., Moazzeni, A.R., Ashena, R. and Roohi, A., 2011. Complete Loss, Blowout and Explosion of Shallow Gas, Infelicitous Horoscope in Middle East, SPE European Health, Safety and Environmental Conference in Oil and Gas Exploration and Production. Society of Petroleum Engineers.
Najibi, A.R. and Asef, M.R., 2014. Prediction of seismic-wave velocities in rock at various confining pressures based on unconfined dataPrediction of seismic-wave velocities in rock at various confining pressures based on unconfined data. GEOPHYSICS, 79: 235-242.

Najibi, A.R., Ghafoori, M., Lashkaripour, G.R. and Asef, M.R., 2015. Empirical relations between strength and static and dynamic elastic properties of Asmari and Sarvak limestones, two main oil reservoirs in Iran. Journal of Petroleum Science and Engineering, 126: 78-82.

National Energy Board, 2013. The Ultimate Potential for Unconventional Petroleum from the Montney Formation of British Columbia and Alberta - Energy Briefing Note, BC Oil and Gas Commission, Alberta Energy Regulator, BC Ministry of Natural Gas Development.

Nelson , E.J., Meyerb, J.J., Hillisa, R.R. and Mildrenb, S.D., 2005. Transverse drilling-induced tensile fractures in the West Tuna area, Gippsland Basin, Australia: implications for the in situ stress regime. Int J Rock Mech Min Sci,, 42: 361-371.

Ni, J. and Barazangi, M., 1986. Seismotectonics of the Zagros continental collision zone and a comparison with the Himalayas. Journal of Geophysical Research: Solid Earth, 91(B8): 8205-8218.

Nicholson, A.K., Hawkes, R.V. and Bachman, R.C., 2019. Early Warning Systems-Using PTA Analysis of DFITs to Understand Complex Hydraulic Fractures and Optimize Treatment Designs, SPE Annual Technical Conference and Exhibition. OnePetro.

Nissen, E., Tatar, M., Jackson, J.A. and Allen, M.B., 2011. New views on earthquake faulting in the Zagros fold-and-thrust belt of Iran. Geophysical Journal International, 186(3): 928-944.

Pandey, M., 2020. Risk and Reliability: Basic Concepts (CIVE 601 courese). Unversity of Waterloo.

Peña Castro, A., Roth, M., Verdecchia, A., Onwuemeka, J., Liu, Y., Harrington, R., Zhang, Y. and Kao, H., 2020. Stress chatter via fluid flow and fault slip in a hydraulic fracturing-induced earthquake sequence in the Montney Formation, British Columbia. Geophysical Research Letters, 47(14): e2020GL087254.

Peska, P. and Zoback, M.D., 1995. Compressive and tensile failure of inclined borehole and determination of in situ stress and rock strength. J Geophys Res, 100(B7): 12791–811.

Peyret, M., Rolandone, F., Dominguez, S., Djamour, Y. and Meyer, B., 2008. Source model for the Mw 6.1, 31 March 2006, Chalan-Chulan earthquake (Iran) from InSAR. Terra Nova, 20(2): 126-133.

Pirouz, M., 2018. Post-collisional deposits in the Zagros foreland basin: Implications for diachronous underthrusting. International Journal of Earth Sciences, 107(5): 1603-1621.

Plumb, R.A. and Cox, J.W., 1987. Stress directions in eastern North America determined to 4.5 km from borehole elongation measurements. . J Geophys Res, 90: 5513-5522.

Porter, J., Price, R. and McCrossan, R., 1982. The western Canada sedimentary basin. Philosophical Transactions of the Royal Society of London. Series A, Mathematical and Physical Sciences, 305(1489): 169-192.

Priestley, K., Baker, C. and Jackson, J., 1994. Implications of earthquake focal mechanism data for the active tectonics of the South Caspian Basin and surrounding regions. Geophysical Journal International, 118(1): 111-141.

Ries, R., Brudzinski, M.R., Skoumal, R.J. and Currie, B.S., 2020. Factors influencing the probability of hydraulic fracturing-induced seismicity in Oklahoma. Bulletin of the Seismological Society of America, 110(5): 2272-2282.

Roth, F. and Fleckenstein, P., 2001. Stress orientations found in north-east Germany differ from the West European trend. Terra Nova, 13(4): 289-296.

Roth, M., Kemna, K., Harrington, R. and Liu, Y., 2022. Source properties of hydraulic-fracturing-induced earthquakes in the Kiskatinaw area, British Columbia, Canada. Journal of Geophysical Research: Solid Earth: e2021JB022750.

Rudkiewicz, J.L., Sherkati, S. and Letouzey, J., 2007. Evolution of maturity in Northern Fars and in the Izeh Zone (Iranian Zagros) and link with hydrocarbon prospectivity, Thrust Belts and Foreland Basins. Springer, pp. 229-246.

Rutqvist, J., 2012. The geomechanics of CO2 storage in deep sedimentary formations. Geotechnical and Geological Engineering, 30(3): 525-551.

Salehi, M., Miri, A., Sherkati, S. and Bahroudi, A., 2012. Analysis of pore pressure effect on abnormal thickness variation of Dashtak Fm. as a detachment layer in Fars region of Zagros fold and thrust belt, Istanbul 2012-International Geophysical Conference and Oil & Gas Exhibition. Society of Exploration Geophysicists and The Chamber of Geophysical …, pp. 1-4.

Schmitt, D.R., Currie, C.A. and Zhang, L., 2012. Crustal stress determination from boreholes and rock cores: Fundamental principles. Tectonophysics, 580: 1-26.
Schultz, R., Atkinson, G., Eaton, D., Gu, Y. and Kao, H., 2018. Hydraulic fracturing volume is associated with induced earthquake productivity in the Duvernay play. Science, 359(6373): 304-308.
Schultz, R. and Stern, V., 2015. The regional Alberta observatory for earthquake studies network (RAVEN). CSEG Recorder, 40(8): 34-37.
Schultz, R., Wang, R., Gu, Y.J., Haug, K. and Atkinson, G., 2017. A seismological overview of the induced earthquakes in the Duvernay play near Fox Creek, Alberta. Journal of Geophysical Research: Solid Earth, 122(1): 492-505.
Sepehr, M. and Cosgrove, J., 2004. Structural framework of the Zagros fold–thrust belt, Iran. Marine and Petroleum geology, 21(7): 829-843.
Sepehr, M. and Cosgrove, J.W., 2007. The role of major fault zones in controlling the geometry and spatial organization of structures in the Zagros Fold-Thrust Belt. Geological Society, London, Special Publications, 272(1): 419-436.
Shen, L., Schmitt, D. and Haug, K., 2018. Measurements of the states of in situ stress for the Duvernay Formation near Fox Creek, west-central Alberta. Alberta Energy Regulator/Alberta Geological Survey, AER/AGS Report, 97: 29.
Shen, L.W., Schmitt, D.R. and Haug, K., 2019a. Quantitative constraints to the complete state of stress from the combined borehole and focal mechanism inversions: Fox Creek, Alberta. Tectonophysics, 764: 110-123.
Shen, L.W., Schmitt, D.R. and Schultz, R., 2019b. Frictional stabilities on induced earthquake fault planes at Fox Creek, Alberta: A pore fluid pressure dilemma. Geophysical Research Letters, 46(15): 8753-8762.
Sherkati, S. and Letouzey, J., 2004. Variation of structural style and basin evolution in the central Zagros (Izeh zone and Dezful Embayment), Iran. Marine and Petroleum Geology 21: 535–554.
Simpson, R.W., 1997. Quantifying Anderson's fault types. Journal of Geophysical Research: Solid Earth, 102(B8): 17909-17919.
Snee, J.E.L. and Zoback, M.D., 2016. State of stress in Texas: Implications for induced seismicity. Geophysical Research Letters, 43(19): 10,208-10,214.
Soleimani, B., Hassani-Giv, M. and Abdollahi fard, I., 2017. Formation Pore Pressure Variation of the Neocomian Sedimentary Succession (the Fahliyan Formation) in the Abadan Plain Basin, SW of Iran. Geofluids, 2017: 13.
Sonder, L.J., 1990. Effects of density contrasts on the orientation of stresses in the lithosphere: Relation to principal stress directions in the Transverse Ranges, California. Tectonics, 9(4): 761-771.
Stern, V., Schultz, R. and Jean, G., 2011. Alberta Microseismicity Project, Phase 1: Site assessments for the ATSN semipermanent stations and the PSEIP Strachan temporary seismic array, Energy Resources Conservation Board. ERCB/AGS Open-File Rept, 15: 75.
Taghipour, M., Ghafoori, M., Lashkaripour, G.R., Moghaddas, N.H. and Molaghab, A., 2019. Estimation of the current stress field and fault reactivation analysis in the Asmari reservoir, SW Iran. Petroleum Science, 16(3): 513-526.
Talebi, H., Alavi, S.A., Sherkati, S., Ghassemi, M.R. and Golalzadeh, A., 2018. In-situ stress regime in the Asmari reservoir of the Zeloi and Lali oil fields, northwest of the Dezful embayment in Zagros fold-thrust belt, Iran. 68-53 :27 ,فصلنامه علمی-پژوهشی علوم زمین.
Talebian, M. and Jackson, J., 2002. Offset on the Main Recent Fault of NW Iran and implications for the late Cenozoic tectonics of the Arabia–Eurasia collision zone. Geophysical Journal International, 150(2): 422-439.
Talebian, M. and Jackson, J., 2004. A reappraisal of earthquake focal mechanisms and active shortening in the Zagros mountains of Iran. Geophysical Journal International, 156(3): 506-526.
Tatar, M., Hatzfeld, D. and Ghafory-Ashtiany, M., 2004. Tectonics of the Central Zagros (Iran) deduced from microearthquake seismicity. Geophysical Journal International, 156(2): 255-266.

Tingay, M., Bentham, P., De Feyter, A. and Kellner, A., 2011. Present-day stress-field rotations associated with evaporites in the offshore Nile Delta. Bulletin, 123(5-6): 1171-1180.
Valley, B. and Evans, K.F., 2019. Stress magnitudes in the Basel enhanced geothermal system. International Journal of Rock Mechanics and Mining Sciences, 118: 1-20.
Van der Baan, M., Eaton, D. and Dusseault, M., 2013. Microseismic monitoring developments in hydraulic fracture stimulation, ISRM International Conference for Effective and Sustainable Hydraulic Fracturing. International Society for Rock Mechanics and Rock Engineering.
Visser, R., Kao, H., Smith, B., Goerzen, C., Kontou, B., Dokht, R., Hutchinson, J., Tan, F. and Babaie-Mahani, A., 2020. A comprehensive earthquake catalogue for the Fort St. John–Dawson Creek region, British Columbia, 2017–2018, Tech. rep., Open File 8718, Geological Survey of Canada.
Visser, R., Smith, B., Kao, H., Babaie Mahani, A., Hutchinson, J. and McKay, J., 2017. A comprehensive earthquake catalogue for northeastern British Columbia and western Alberta, 2014-2016. Geological Survey of Canada.
Walker, R.T., Andalibi, M.J., Gheitanchi, M.R., Jackson, J.A., Karegar, S. and Priestley, K., 2005. Seismological and field observations from the 1990 November 6 Furg (Hormozgan) earthquake: a rare case of surface rupture in the Zagros mountains of Iran, Geophysical Journal International, pp. 567-579.
Walpersdorf, A., Hatzfeld, D., Nankali, H., Tavakoli, F., Nilforoushan, F., Tatar, M., Vernant, P., Chéry, J. and Masson, F., 2006. Difference in the GPS deformation pattern of North and Central Zagros (Iran). Geophysical Journal International, 167(3): 1077-1088.
Walsh III, F.R. and Zoback, M.D., 2016. Probabilistic assessment of potential fault slip related to injection-induced earthquakes: Application to north-central Oklahoma, USA. Geology, 44(12): 991-994.
Wang, B., Harrington, R.M., Liu, Y., Kao, H. and Yu, H., 2019. Remote dynamic triggering of earthquakes in three unconventional Canadian hydrocarbon regions based on a Multiple-Station matched-filter ApproachRemote dynamic triggering of earthquakes in three unconventional Canadian hydrocarbon regions. Bulletin of the Seismological Society of America, 109(1): 372-386.
Wang, B., Harrington, R.M., Liu, Y., Yu, H., Carey, A. and van der Elst, N.J., 2015. Isolated cases of remote dynamic triggering in Canada detected using cataloged earthquakes combined with a matched-filter approach. Geophysical Research Letters, 42(13): 5187-5196.
Wang, Y., Cao, Z. and Au, S.-K., 2010. Efficient Monte Carlo simulation of parameter sensitivity in probabilistic slope stability analysis. Computers and Geotechnics, 37(7-8): 1015-1022.
Ward, C.D. and Andreassen, E., 1997. Pressure while drilling data improves reservoir drilling performance. SPE 37588 In: SPE/IADC Drilling Conference, Amsterdam.
Weides, S.N., Moeck, I.S., Schmitt, D.R. and Majorowicz, J.A., 2014. An integrative geothermal resource assessment study for the siliciclastic Granite Wash Unit, northwestern Alberta (Canada). Environmental Earth Sciences, 72(10): 4141-4154.
Weingarten, M., Ge, S., Godt, J.W., Bekins, B.A. and Rubinstein, J.L., 2015. High-rate injection is associated with the increase in US mid-continent seismicity. Science, 348(6241): 1336-1340.
Wozniakowska, P. and Eaton, D.W., 2020. Machine Learning-Based Analysis of Geological Susceptibility to Induced Seismicity in the Montney Formation, Canada. Geophysical Research Letters, 47(22): e2020GL089651.
Yaghoubi, A., 2019. Hydraulic fracturing modeling using a discrete fracture network in the Barnett Shale. International Journal of Rock Mechanics and Mining Sciences, 119: 98-108.
Yaghoubi, A., 2020. List of the earthquake recorded by IRSC since 2010 in the Dezful Embayment. Harvard Dataverse.
Yaghoubi, A., Dusseault, M. and Leonenko, Y., 2022. Injection-induced fault slip assessment in Montney Formation in Western Canada. Scientific reports, 12(1): 1-12.
Yaghoubi, A., Dusseault, M., Mahbaz, S. and Leonenko, Y., 2020. Probabilistic Injection-Induced Fault Slip Assessment in Fox Creek Alberta. 54th US Rock Mechanics/Geomechanics Symposium.
Yaghoubi, A., Mahbaz, S., Dusseault, M.B. and Leonenko, Y., 2021. Seismicity and the State of Stress in the Dezful Embayment, Zagros Fold and Thrust Belt. Geosciences, 11(6): 254.

Yaghoubi, A. and Zeinali, M., 2009. Determination of magnitude and orientation of the in-situ stress from borehole breakout and effect of pore pressure on borehole stability—Case study in Cheshmeh Khush oil field of Iran. Journal of Petroleum Science and Engineering, 67(3-4): 116-126.

Yale, D.P., Rodriguez, J., Mercer, T.B. and Blaisdell, D.W., 1994. In-situ stress orientation and the effects of local structure-Scott Field, North Sea, Rock Mechanics in Petroleum Engineering. Society of Petroleum Engineers.

Yamini-Fard, F., Hatzfeld, D., Tatar, M. and Mokhtari, M., 2006. Microearthquake seismicity at the intersection between the Kazerun fault and the Main Recent Fault (Zagros, Iran). Geophysical Journal International, 166(1): 186-196.

Yang, W. and Hauksson, E., 2013. The tectonic crustal stress field and style of faulting along the Pacific North America Plate boundary in Southern California. Geophysical Journal International, 194(1): 100-117.

Yu, H., Harrington, R., Liu, Y. and Wang, B., 2019. Induced seismicity driven by fluid diffusion revealed by a near-field hydraulic stimulation monitoring array in the Montney Basin, British Columbia. Journal of Geophysical Research: Solid Earth, 124(5): 4694-4709.

Yu, H., Harrington, R.M., Kao, H., Liu, Y. and Wang, B., 2021a. Fluid-injection-induced earthquakes characterized by hybrid-frequency waveforms manifest the transition from aseismic to seismic slip. Nature communications, 12(1): 1-11.

Yu, H., Kao, H., Visser, R. and Wang, B., 2021b. From Seismic Quiescence to Surged Activity After Decades of Wastewater Disposal: A Case Study in Central-West Alberta, Canada. Geophysical Research Letters, 48(22): e2021GL095074.

Zang, A., Oye, V., Jousset, P., Deichmann, N., Gritto, R., McGarr, A., Majer, E. and Bruhn, D., 2014. Analysis of induced seismicity in geothermal reservoirs–An overview. Geothermics, 52: 6-21.

Zhai, G., Shirzaei, M. and Manga, M., 2021. Widespread deep seismicity in the Delaware Basin, Texas, is mainly driven by shallow wastewater injection. Proceedings of the National Academy of Sciences, 118(20).

Zhang, H., Eaton, D.W., Rodriguez, G. and Jia, S.Q., 2019. Source-mechanism analysis and stress inversion for hydraulic-fracturing-induced event sequences near Fox Creek, Alberta. Bulletin of the Seismological Society of America, 109(2): 636-651.

Zoback, M., 2007. Reservoir Geomechanics. cambridge university press.

Zoback, M.D. and Harjes, H.P., 1997. Injection-induced earthquakes and crustal stress at 9 km depth at the KTB deep drilling site, Germany. Journal of Geophysical Research: Solid Earth, 102(B8): 18477-18491.

Zoback, M.L., 1992. First and Second Order Patterns of Tectonic Stress: the World Stress Map Project. J Geophys Res, 97: 11703–28.

Zoback, M.L. and Richardson, R.M., 1996. Stress perturbation associated with the Amazonas and other ancient continental rifts. Journal of Geophysical Research: Solid Earth, 101(B3): 5459-5475.

Appendices

Appendix A

Seismicity and the State of Stress in the Dezful Embayment in the Zagros Fold and Thrust Belt

Introduction

Five supplementary figures and three tables are presented here as supporting information. Figure A1 illustrates the stratigraphy column of the Dezful Embayment, and Figure A2 shows the mud weight and direct pore pressures data vs the depth of several wells drilled in the Dezful Embayment. The figure also shows that the Gachsaran Formation is a major pressure step when sedimentary formations in the Dezful Embayment are drilled. It is worth pointing out that Figure A2 shows a typical and general pore pressure variation with depth in the sedimentary cover. Figure A3 provides one example of the depths, and orientations of borehole breakouts plus their frequency in CK-9 and LL-29. Figures A4 and A5 show the result of stress inversion for 108 focal mechanisms using the MATLAB™ code developed by Martines-Garzon et al. (2014). Table A-2 includes earthquake source parameters used for stress determination and the tectonic regime in the Dezful Embayment of the ZFTB. The table presents seismically maximum horizontal stress (S_{Hmax}) orientations, stress regimes (A_{φ}) calculated using Simpson's (1997) approach, as well as two nodal planes and other source parameters of the earthquakes. The preferred nodal plane for each earthquake focal mechanism is highlighted in each row.

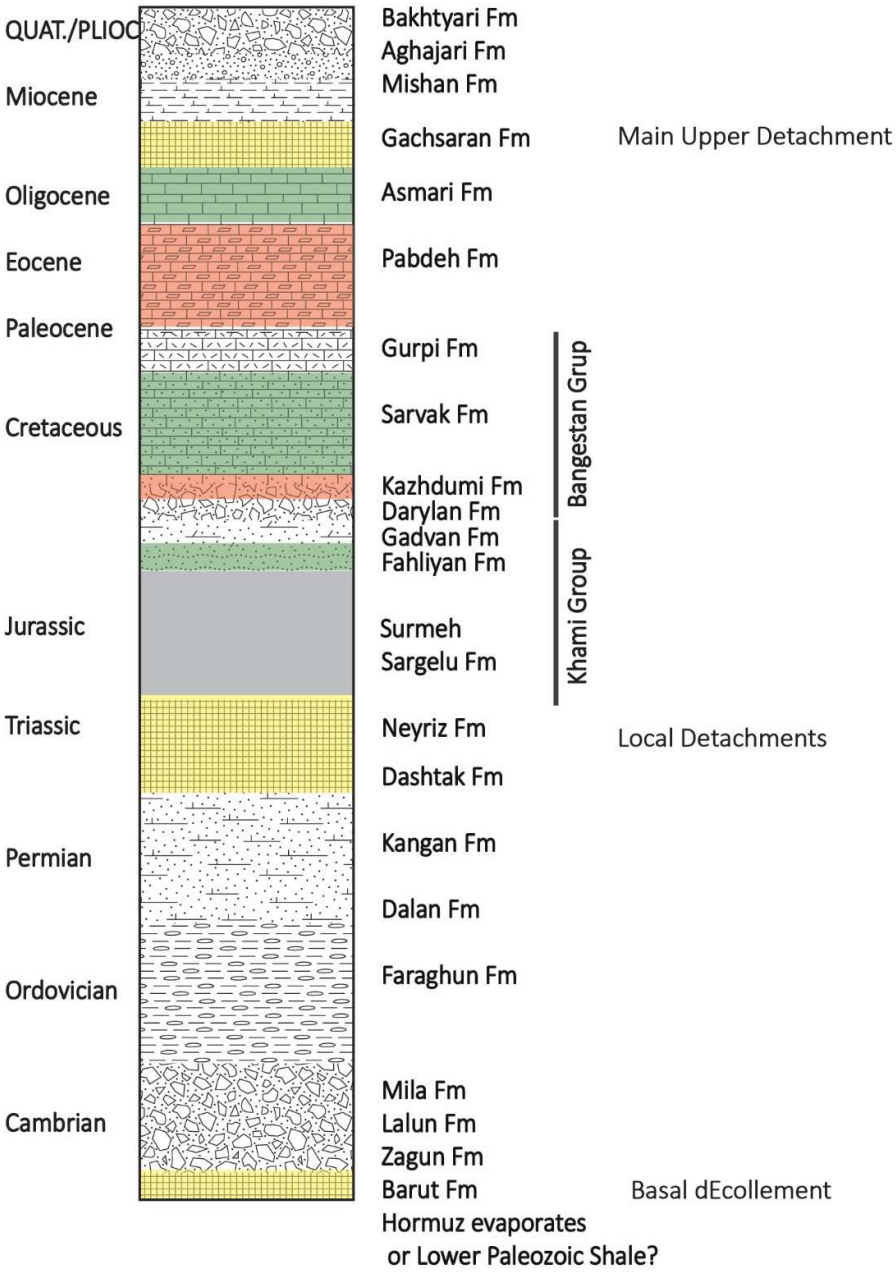

Figure A1: Stratigraphy column, source rocks, and reservoir formations for the Dezful Embayment. The main detachment rocks are indicated in yellow, reservoir rocks in green, and main source rocks in red (modified from Sherkati and Letouzey (2004))

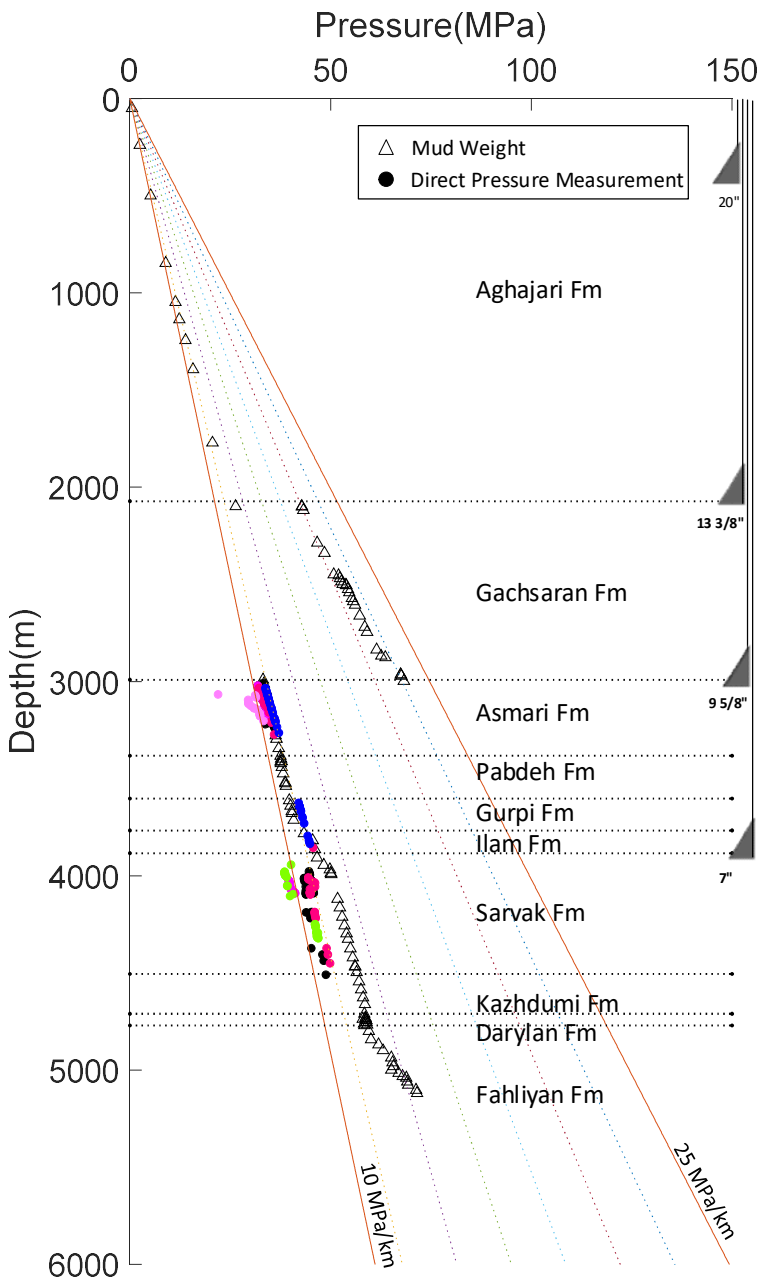

Figure A2: A typical mud weight profile from several wells drilled in the Dezful Embayment. Extremely high pore pressures are observed in the Gachsaran (Fars) Formation, whereas in the formations below and above, there is slightly higher than hydrostatic pressure. The colored dots represent direct pore pressure measurements at different oil fields in the Dezful Embayment.

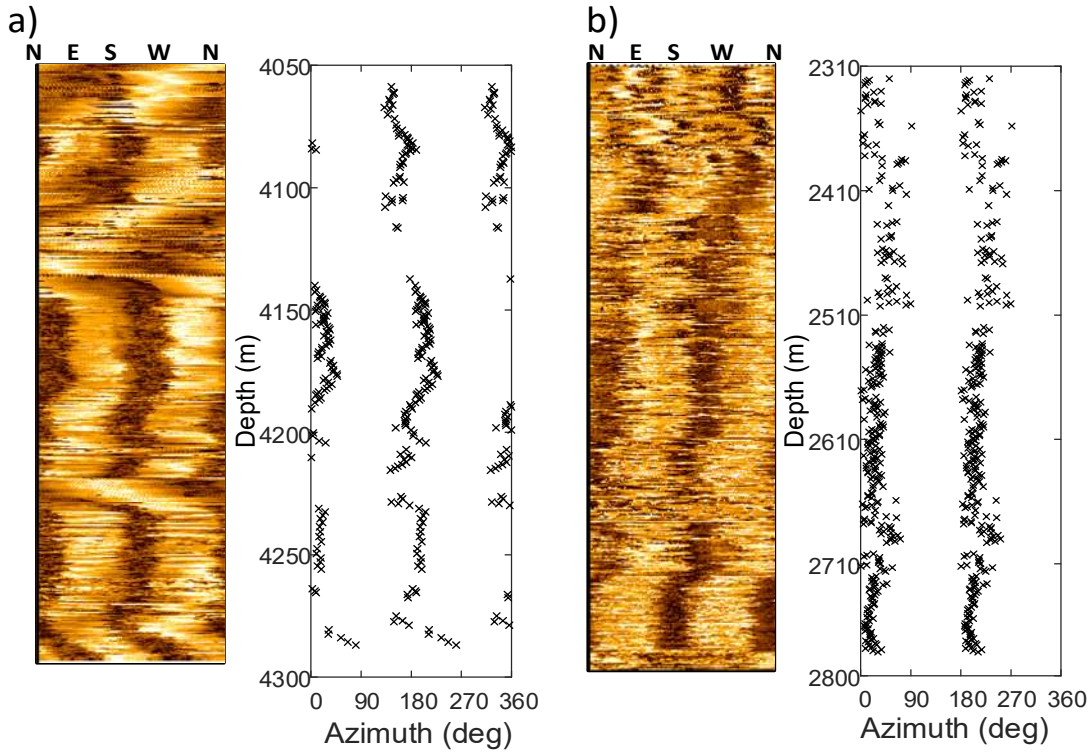

Figure A3: Ultrasonic image logs of a) CK-9 and b) LL-29 along with depth juxtaposed with observations of breakout orientations (minimum principal stress). Breakout orientations terminated abruptly, and then gradually rotated at 4110 m, 4221 m 4242 m, and 4272 m in CK-9. The same pattern occurred in LL-29, with anomalies in breakout orientation observed at 2510 m and 2695 m.

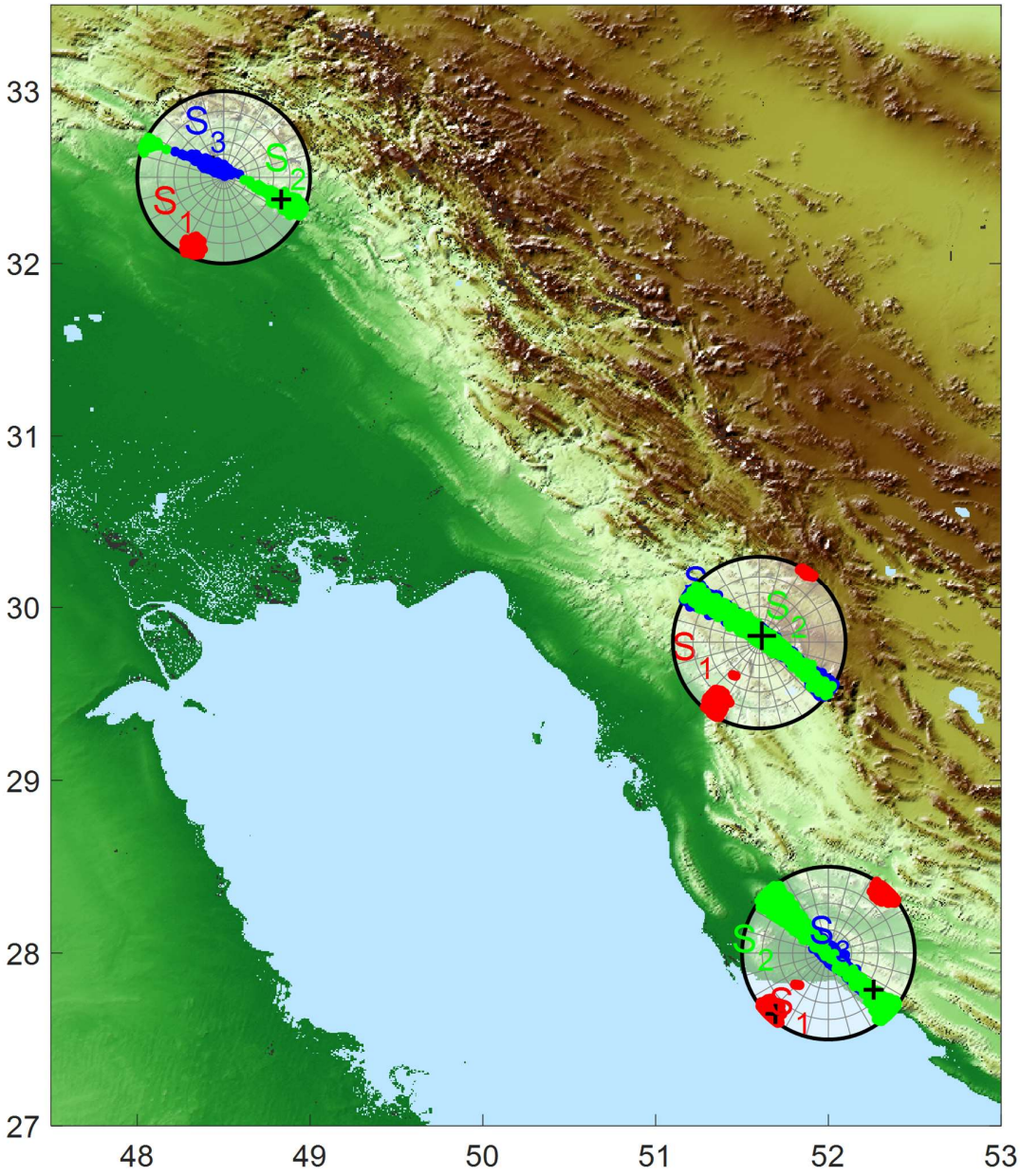

Figure A4: The result of stress inversion of focal mechanisms using the approach developed by Martines-Garzon et al. (2014) in the northern, southern, and around Kazrun fault system (middle) in the Dezful Embayment. Lower-hemisphere stereonets show the distributions of the principal stress orientations (S1-red, S2-green, S3-blue). The "+" symbol presents the best fit of principal stress orientations and colored dots are the 95% confidence of each orientation.

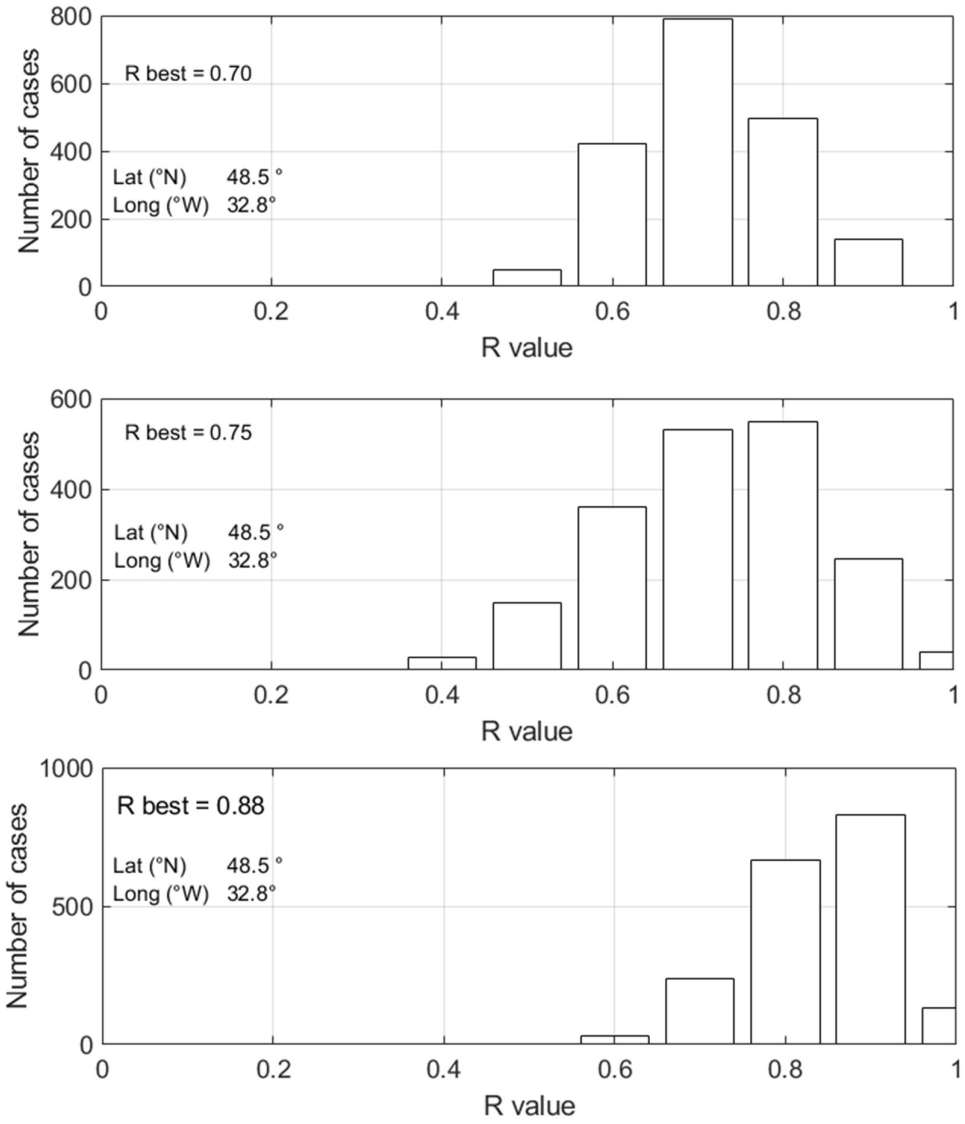

Figure A5: Histogram of R-value (1-ϕ) from the inversion of focal mechanism within the 95% confidence region in the northern (top), southern (middle), and around Kazerun fault system (bottom). Latitude and longitude in each subplot represent the centroid of the corresponding earthquake group.

Table A-1: Detailed information on sidetracks of well P-7.

ITEM	SD-1	SD-2
KOP	3928 m	3899 m
Azimuth	2050	2920
Final Inclination	900	900
Duration (Day)	20 Days	15 Days
Mud Weight	70 pcf	63 pcf
Drilled Meter	212 m	711m
Mud Type	OBM	OBM
MD	4140 m	4610 m
TVD	4025 m	4018m
Hole Size	6 1/8"	6 1/8"
Formation	Sarvak	Sarvak

Table A2. Earthquake source parameters used for stress determination and the tectonic regime in the ZFTB of the Dezful Embayment. The columns are: year, month, day, origin time (hr: min), latitude, longitude, depth, strike, dip, rake (nodal plane 1), strike, dip, rake (nodal plane 2), Paxis and Taxis and the result of calculated A_{φ}.

Date			Lat.	Lon.	Strike	Dip	Rake	Depth	M_w	Regime	S_{Hmax}	A_{φ}	Reference
1968	6	23	29.74	51.25	136 **319**	45 **45**	88 **92**	9	5.5	TF	47	2.25	Baker *et al.* (1993)
1971	4	6	29.79	51.89	62 **332**	79 **88**	2 **169**	6	5.2	SS	16	1.57	Baker *et al.* (1993)
1972	6	12	33.04	46.27	114 **306**	56 **35**	83 **100**	11	5	TF	29	2.23	Ni and Barazangi (1986)
1972	6	14	33.03	46.13	198 **65**	40 **60**	51 **118**	10	5.3	TF	135	2.24	Jackson and McKenzie (1984)
1972	7	2	30.06	50.85	132 **312**	64 **26**	90 **90**	9	5.3	TF	42	3.00	Ni and Barazangi (1986)
1976	4	22	28.68	52.12	312 **148**	52 **39**	80 **103**	7	5.7	TF	49	2.12	Ni and Barazangi

Date			Lat.	Lon.	Strike	Dip	Rake	Depth	M_w	Regime	S_{Hmax}	A_φ	Reference
													(1986)
1976	11	7	33.19	47.93	138 **269**	58 **43**	121 **51**	10	4.8	TF	26	2.19	Jackson and McKenzie (1984)
1977	4	6	31.96	50.65	112 **228**	64 **48**	132 **36**	6	5.9	TF	173	2.24	Baker *et al.* (1993)
1977	4	26	32.64	48.91	293 **110**	29 **61**	93 **88**	20	5.5	TF	21	2.29	Maggi *et al.* (2000)
1977	6	5	32.62	48.09	293 **112**	34 **56**	91 **89**	12	6.1	TF	22	2.31	Jackson and Fitch (1981)
1980	10	19	32.70	48.57	327 **116**	19 **74**	120 **80**	17	5.6	TF	33	2.61	Maggi *et al.* (2000)
1983	5	28	32.59	48.58	314 **106**	38 **55**	113 **73**	8	5.5	TF	28	2.18	Ni and Barazangi (1986)
1986	7	12	29.91	51.56	4 **268**	73 **70**	-159 **-18**	4±3	5.5	SS	45	1.06	Baker *et al.* (1993)
1986	12	20	29.90	51.58	344 **81**	65 **75**	163 **26**	8±3	5.3	SS	31	1.82	Baker *et al.* (1993)
1988	8	11	29.88	51.66	350 **258**	82 **76**	-166 **-8**	9±3	5.8	SS	33	1.20	Baker *et al.* (1993)
1988	8	11	29.94	51.58	3 **271**	69 **85**	-175 **-21**	7±3	5.5	SS	49	1.35	Baker *et al.* (1993)
1988	8	30	29.95	51.72	242 **337**	57 **82**	12 **-147**	16	5.1	SS	15	1.31	Maggi *et al.* (2000)
1988	12	6	29.89	51.63	357 **262**	74 **73**	198 **-17**	10	5.6	SS	39	1.02	Baker *et al.* (1993)
1991	11	4	30.69	50.25	135 **6**	80 **16**	78 **140**	5	5.8	TF	55	2.78	Talebian and Jackson (2004)
1993	6	22	30.18	50.83	301 **154**	44 **51**	65 **112**	5	5.2	TF	48	2.10	Maggi *et al.* (2000)

Date			Lat.	Lon.	Strike	Dip	Rake	Depth	M_w	Regime	S_{Hmax}	A_{φ}	Reference
1994	3	29	29.20	51.36	334 **136**	40 **51**	104 **79**	7	5.1	TF	54	2.09	Talebian and Jackson (2004)
1994	7	31	32.68	48.42	288 **108**	17 **73**	90 **90**	14	5.5	TF	18	3.00	Priestley *et al.* (1994)
1995	4	22	30.97	49.93	121 **297**	61 **29**	92 **86**	14	5.1	TF	30	2.06	Talebian and Jackson (2004)
1998	6	15	31.60	50.84	78 **294**	68 **26**	75 **123**	5	5	TF	179	2.48	Talebian and Jackson (2004)
1998	10	4	33.30	47.22	111 **288**	37 **53**	92 **88**	9	5.2	TF	20	2.46	Talebian and Jackson (2004)
1998	10	5	33.28	47.26	290 **119**	51 **39**	84 **97**	7	5.3	TF	24	2.11	Talebian and Jackson (2004)
1999	5	6	29.52	51.91	49 **142**	77 **78**	-12 **-167**	7	6.1	SS	5	1.03	Talebian and Jackson (2004)
1999	10	31	29.37	51.85	117 **324**	34 **59**	67 **105**	5	5.2	TF	43	2.30	Adams *et al.* (2009)
2000	5	3	29.56	50.81	292 **152**	26 **70**	53 **106**	5	5.1	TF	49	2.55	Talebian and Jackson (2004)
2001	3	23	32.98	46.64	337 **121**	10 **82**	126 **84**	7	5.2	TF	36	2.84	Nissen *et al.* (2011)
2001	4	3	32.55	48.02	110 **281**	38 **52**	97 **85**	9	4.9	TF	15	2.15	Nissen *et al.* (2011)
2002	2	17	28.08	51.79	288	68	83	6	5.3	TF	23	2.48	Adams *et*

Date			Lat.	Lon.	Strike	Dip	Rake	Depth	M_w	Regime	S_{Hmax}	A_φ	Reference
					126	**23**	**107**						*al.* (2009)
2002	9	25	32.06	49.32	142 **310**	47 **44**	98 **82**	8	5.3	TF	46	2.05	Nissen *et al.* (2011)
2008	8	27	32.31	47.35	338 **248**	88 **78**	-168 **-2**	10	5.6	SS	22	1.40	Nissen *et al.* (2011)
2010	9	27	29.67	51.66	280 **119**	13 **78**	71 **94**	16	5.6	TF	26	2.71	Nissen *et al.* (2011)
2012	5	3	32.74	47.61	299 **97**	44 **48**	106 **75**	10	5.3	TF	18	2.07	IRCS[1]
2012	7	1	31.81	51.02	89 **250**	38 **53**	105 **79**	6.3	5	TF	168	2.12	IRCS
2012	7	24	31.84	51.02	86 **253**	34 **57**	101 **83**	10	4.9	TF	168	2.21	IRCS
2012	10	10	29.33	52.49	311 **98**	60 **35**	108 **62**	8.8	4.7	TF	28	2.28	IRCS
2013	1	12	31.90	51.09	77 **300**	26 **71**	50 **107**	5	4.9	TF	17	2.55	IRCS
2013	4	9	28.47	51.57	151 **317**	39 **52**	101 **81**	11.3	6.3	TF	53	2.10	IRCS
2013	4	9	28.46	51.56	147 **330**	45 **45**	88 **92**	11.1	5.3	TF	58	2.25	IRCS
2013	4	9	28.49	51.58	163 **313**	55 **39**	109 **65**	20	4.5	TF	60	2.17	IRCS
2013	4	9	28.42	51.67	160 **329**	53 **37**	96 **82**	20	4.6	TF	66	2.01	IRCS
2013	4	10	28.34	51.64	332 **63**	84 **77**	167 **6**	20	4.6	SS	17	1.72	IRCS
2013	4	10	28.40	51.64	145 **304**	38 **54**	107 **77**	20	5.5	TF	43	2.16	IRCS
2013	4	10	28.26	51.69	311 **109**	58 **34**	102 **72**	10	5.2	TF	32	2.28	IRCS
2013	4	10	28.41	51.65	161	53	106	20	5.2	TF	60	2.09	IRCS

[1] Iranian Seismological Center (www.irsc.ut.ac.ir)

Date			Lat.	Lon.	Strike	Dip	Rake	Depth	M_w	Regime	S_{Hmax}	A_{φ}	Reference
					315	**40**	**69**						
2013	4	10	28.42	51.64	338 **69**	85 **74**	164 **5**	13.7	4.5	SS	23	1.64	IRCS
2013	4	10	28.24	51.79	317 **114**	57 **35**	103 **71**	16.6	4.4	TF	38	2.21	IRCS
2013	4	11	28.44	51.55	151 **326**	47 **43**	93 **87**	20	4.9	TF	59	2.11	IRCS
2013	4	19	32.78	51.81	94	62	49	10	4	TF	32	2.20	IRCS
2013	4	24	28.44	51.55	138 **331**	42 **49**	80 **99**	13.7	4.5	TF	55	2.05	IRCS
2013	5	1	28.32	51.71	309 **110**	54 **37**	101 **75**	20	4.9	TF	31	2.16	IRCS
2013	5	2	28.25	51.76	319 **107**	51 **43**	111 **66**	16	4.7	TF	34	2.08	IRCS
2013	5	6	28.52	51.67	153 **305**	57 **36**	107 **66**	20	4.9	TF	51	2.26	IRCS
2013	5	12	29.55	52.70	274 **113**	36 **56**	74 **101**	10	4.3	TF	15	2.22	IRCS
2013	5	13	28.41	51.69	281 **180**	53 **76**	18 **141**	10	4.6	SS	55	1.75	IRCS
2013	8	10	28.42	51.69	183 **284**	67 **66**	154 **25**	17.2	4.5	SS	54	1.99	IRCS
2013	8	10	28.40	51.69	176 **321**	55 **41**	112 **62**	14.2	4.6	TF	71	2.12	IRCS
2013	8	14	30.83	50.47	307 **128**	24 **66**	89 **90**	7.1	4.2	TF	38	2.17	IRCS
2013	11	19	28.57	51.55	155 **266**	60 **58**	143 **37**	10	4.2	TF	31	2.03	IRCS
2013	11	28	29.32	51.31	118 **357**	70 **36**	60 **144**	7.8	5.6	TF	50	2.47	IRCS
2013	11	28	29.29	51.32	31 **122**	88 **73**	163 **2**	10	4.2	SS	75	1.53	IRCS
2014	1	28	32.53	50.01	197	63	-7	6	4.6	SS	151	1.34	IRCS

Date			Lat.	Lon.	Strike	Dip	Rake	Depth	M_w	Regime	S_{Hmax}	A_φ	Reference
					291	**84**	**-153**						
2014	4	16	28.55	51.61	191 **282**	86 **83**	173 **4**	14.9	4.8	SS	56	1.78	IRCS
2014	5	21	29.60	50.86	126 **306**	57 **33**	90 **90**	19	5.2	TF	36	2.34	IRCS
2014	5	21	29.63	50.86	125 **315**	64 **27**	86 **99**	15	4.9	TF	38	2.34	IRCS
2014	6	20	29.88	50.89	100 **338**	50 **58**	44 **131**	11	4.5	TF	41	2.09	IRCS
2014	8	15	28.49	51.68	276 **7**	87 **69**	-21 **-177**	10	4.6	SS	53	1.41	IRCS
2014	8	17	32.72	47.70	114 **302**	73 **17**	88 **98**	7.5	4.5	TF	26	2.66	IRCS
2014	8	17	32.74	47.64	115 **299**	72 **18**	89 **94**	9	4.6	TF	26	2.62	IRCS
2014	8	18	32.71	47.64	104 **320**	63 **32**	72 **121**	10	6.2	TF	27	2.34	IRCS
2014	8	18	32.76	47.51	113 **297**	70 **20**	89 **94**	12	4.7	TF	24	2.53	IRCS
2014	8	18	32.72	47.69	98 **332**	59 **45**	55 **134**	12	5.7	TF	32	2.17	IRCS
2014	8	18	32.76	47.60	313 **111**	49 **43**	105 **74**	10	4.7	TF	32	2.10	IRCS
2014	8	18	32.64	47.63	102 **323**	38 **59**	56 **113**	8	4.6	TF	36	2.24	IRCS
2014	8	18	32.73	47.60	293 **97**	47 **44**	101 **78**	15	5.1	TF	15	2.05	IRCS
2014	8	18	32.73	47.53	75 **325**	42 **73**	25 **129**	7.4	5.4	TF	28	2.48	IRCS
2014	8	18	32.58	47.61	305 **97**	52 **42**	109 **68**	17.2	5.9	TF	22	2.11	IRCS
2014	8	18	32.71	47.60	283 **124**	41 **51**	74 **104**	12.2	4.6	TF	24	2.13	IRCS

Date			Lat.	Lon.	Strike	Dip	Rake	Depth	M_w	Regime	S_{Hmax}	A_{φ}	Reference
2014	8	18	32.71	47.56	126 **333**	30 **63**	65 **103**	8.9	4.6	TF	54	2.33	IRCS
2014	8	19	32.74	47.53	105 **307**	46 **46**	74 **105**	7.8	5.2	TF	26	2.00	IRCS
2014	8	20	32.64	47.74	115 **305**	77 **13**	88 **99**	17.7	5.6	TF	27	2.75	IRCS
2014	8	22	32.73	47.62	133 **271**	74 **22**	104 **50**	16	4.6	TF	32	2.62	IRCS
2014	8	23	32.72	47.77	105 **344**	61 **47**	51 **139**	20	5.3	TF	42	2.20	IRCS
2014	8	24	32.68	47.79	146 **55**	88 **68**	-158 **-2**	19.4	4.9	SS	8	1.41	IRCS
2014	8	25	32.74	47.71	124 **292**	75 **15**	93 **78**	12	4.7	TF	32	2.60	IRCS
2014	10	15	32.58	47.79	95 **273**	32 **58**	92 **89**	10	5.8	TF	4	2.44	IRCS
2014	10	15	32.51	47.92	78 **313**	66 **38**	59 **139**	12.2	4.4	TF	10	2.38	IRCS
2014	10	16	32.78	47.81	123 **306**	52 **38**	88 **92**	13.7	4.1	TF	34	2.07	IRCS
2014	12	12	30.47	50.48	314 **132**	19 **71**	92 **89**	17.7	4.9	TF	42	2.11	IRCS
2014	12	30	28.73	51.89	205 **340**	26 **71**	132 **72**	11	5	TF	84	2.56	IRCS
2015	1	1	28.73	51.85	235 **6**	18 **78**	137 **77**	10.1	4.5	TF	108	2.76	IRCS
2015	1	10	28.75	51.84	215 **125**	90 **74**	-164 **0**	10	4.6	SS	79	1.48	IRCS
2015	1	14	32.84	46.93	300 **121**	18 **72**	90 **90**	15	4.3	TF	30	2.90	IRCS
2015	2	15	32.78	46.84	125 **276**	71 **21**	100 **63**	8	4.9	TF	27	2.59	IRCS
2015	4	10	28.35	51.83	59	87	-21	8.5	4.6	SS	16	1.41	IRCS

Date			Lat.	Lon.	Strike	Dip	Rake	Depth	M_w	Regime	S_{Hmax}	A_φ	Reference
					150	**69**	**-176**						
2015	5	21	33.44	48.39	72 **318**	64 **51**	45 **146**	8	4.3	TF	12	2.19	IRCS
2015	9	25	32.85	46.53	132 **321**	63 **27**	86 **98**	17	5.1	TF	45	2.38	IRCS
2015	11	25	31.89	49.54	312 **130**	3 **85**	92 **90**	12	5.2	TF	0	3.00	IRCS
2015	12	4	28.91	52.02	118 **338**	83 **9**	84 **130**	22	4.7	TF	0	2.96	IRCS
2016	3	31	31.93	50.82	333 **66**	69 **81**	170 **21**	8	5	SS	18	1.73	IRCS
2016	9	23	30.60	50.38	141 **336**	74 **17**	86 **104**	18	4.5	TF	54	2.60	IRCS
2016	9	30	32.45	48.95	98 **283**	61 **29**	88 **94**	15	4	TF	9	2.04	IRCS
2016	10	14	31.09	50.07	120 **2**	77 **26**	67 **150**	10	4.5	TF	48	2.69	IRCS
2017	1	17	29.66	51.50	166 **75**	76 **86**	-176 **-14**	9	4.6	SS	31	1.35	IRCS
2017	9	3	29.06	51.66	144 **305**	41 **51**	104 **78**	9	4.9	TF	44.00	2.13	IRCS

Appendix B

Injection-Induced Fault Slip Assessment in Montney Formation in Western Canada

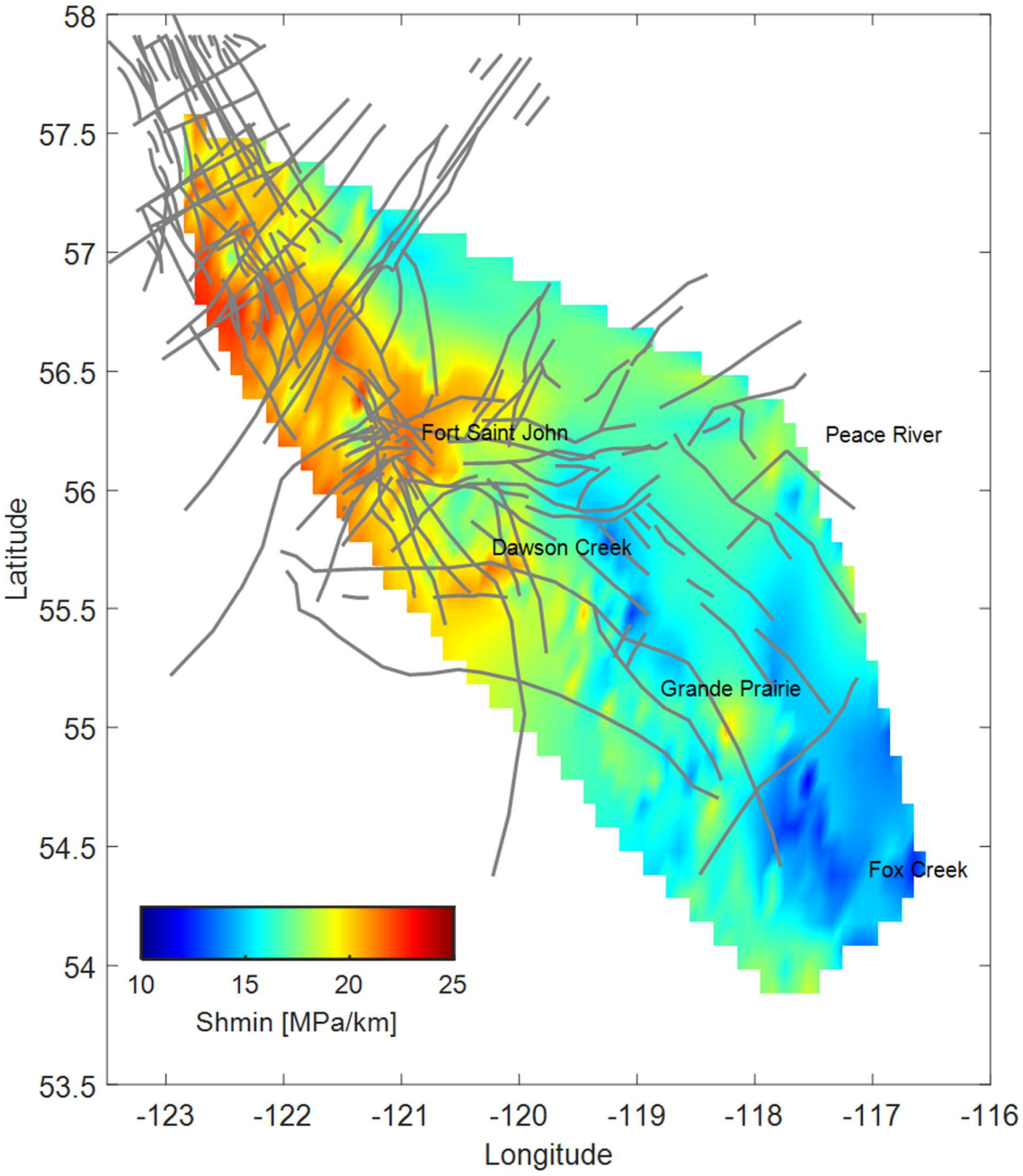

Figure B1: Minimum horizontal stress gradient values in the Montney Formation, derived from the source dataset presented in Figure 4-3.

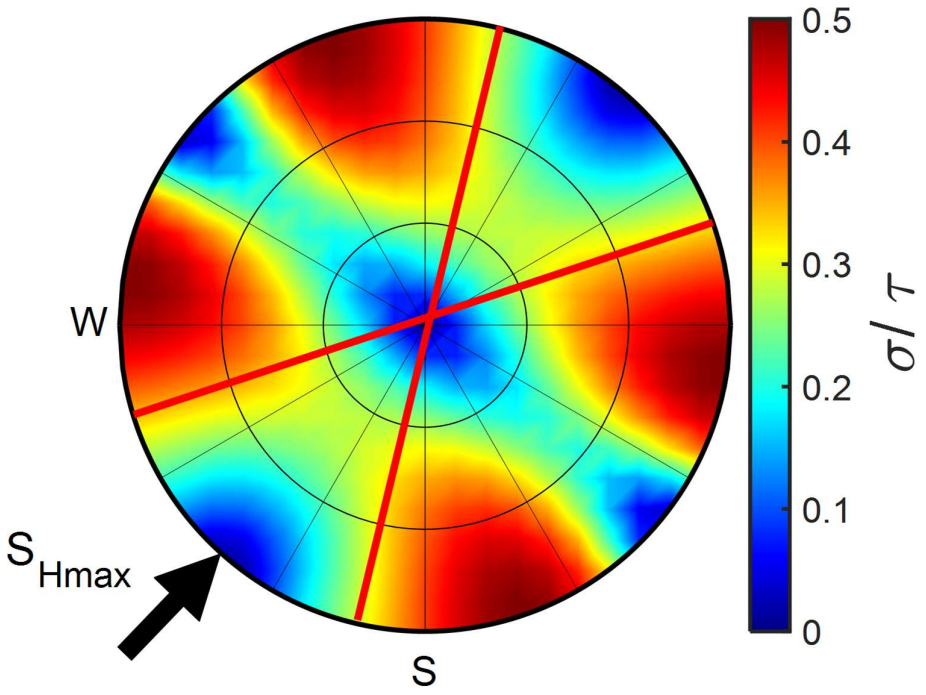

Figure B2: Stereonet plot illustrates the slip-tendency (ratio of resolved shear to normal stress) for the strike-slip faulting regime ($A_\varphi \approx 1.7$) in stress area 4. The red lines indicate the direction of the critically stressed faults in the Kiskatinaw area.

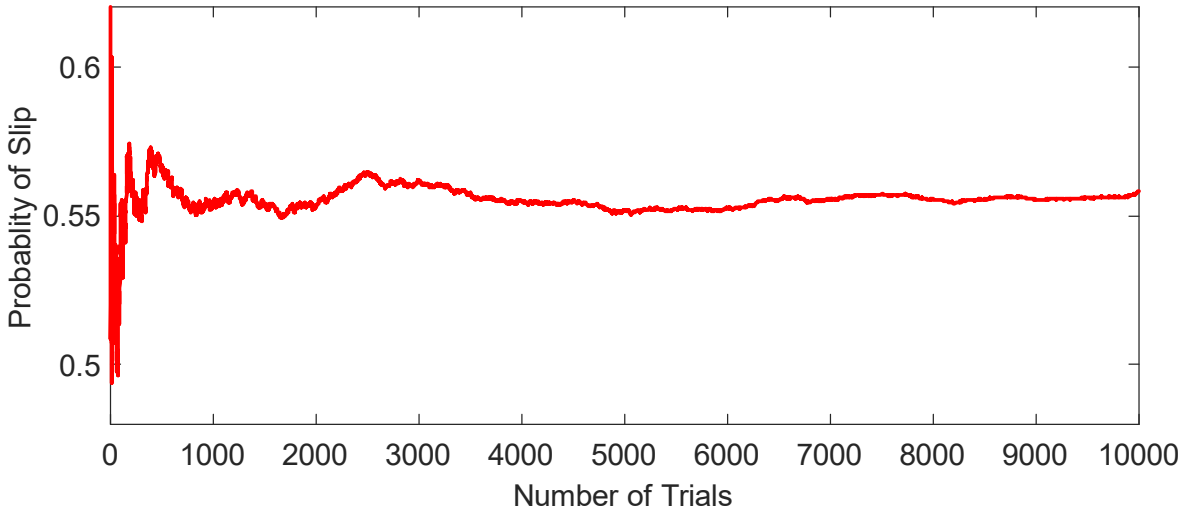

Figure B3: Probability of slip in a fault located in stress area 4 versus Monte Carlo simulations. 5000 represents an appropriate sample size (with two-digit precision) for Monte Carlo simulation for this study.

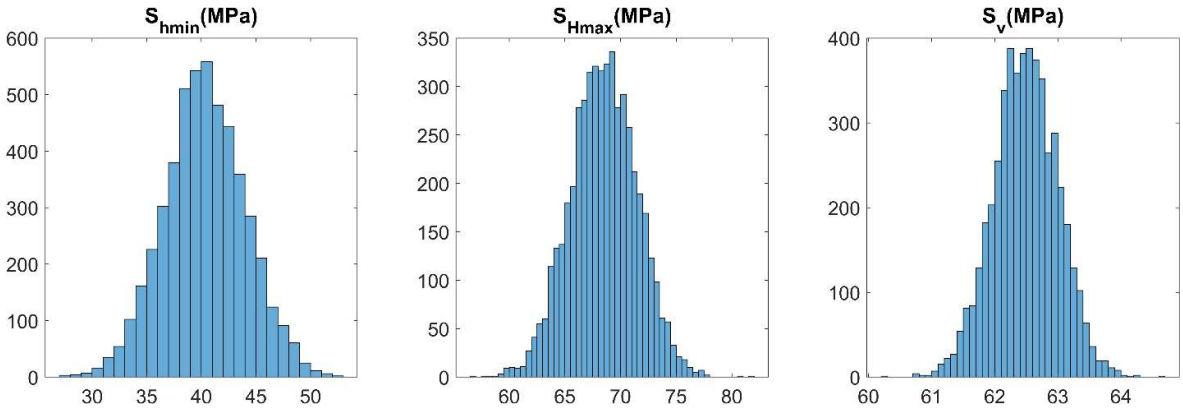

Figure B4: Variables used in Monte Carlo simulations for stress area 1.

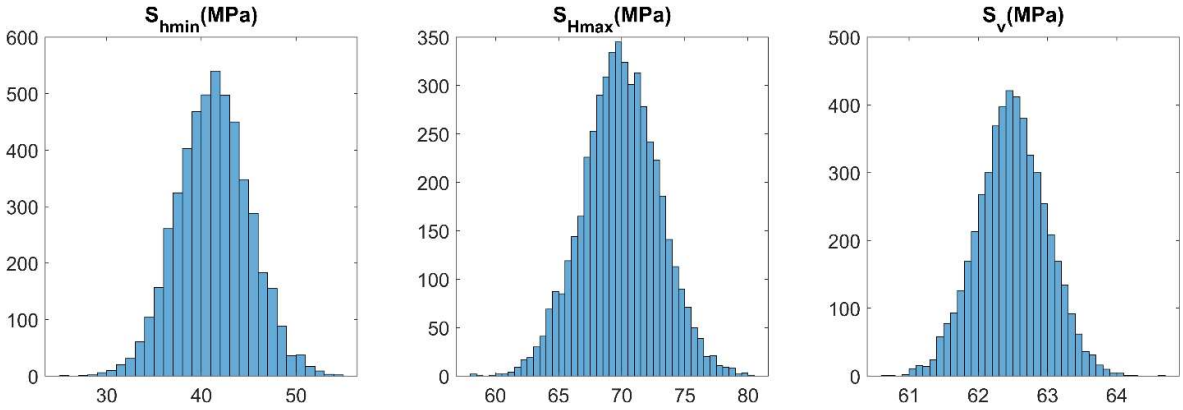

Figure B5: Variables used in Monte Carlo simulations for stress area 2.

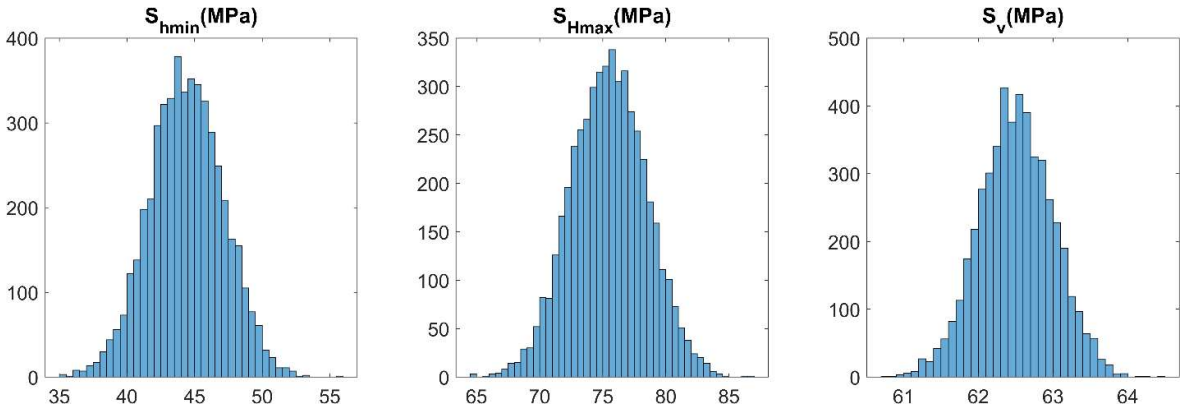

Figure B6: Variables used in Monte Carlo simulations for stress area 3.

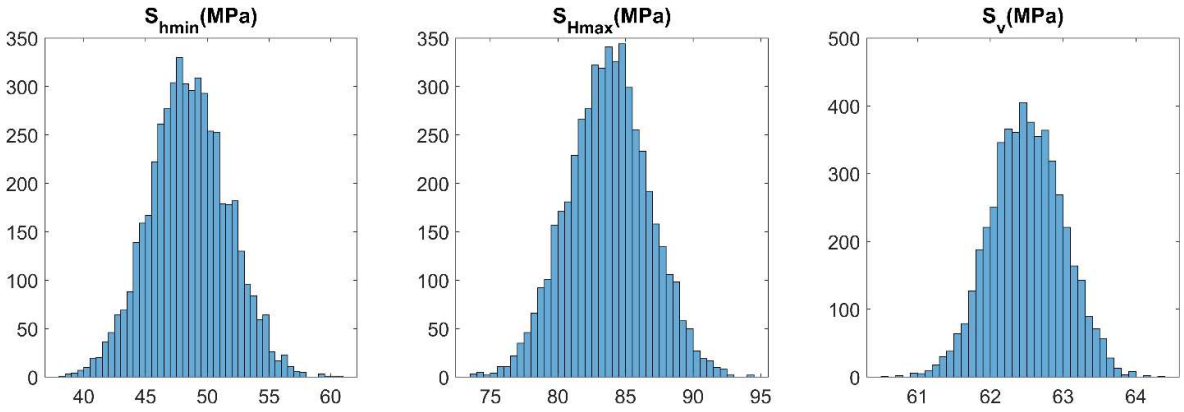

Figure B7: Variables used in Monte Carlo simulations for stress area 4.

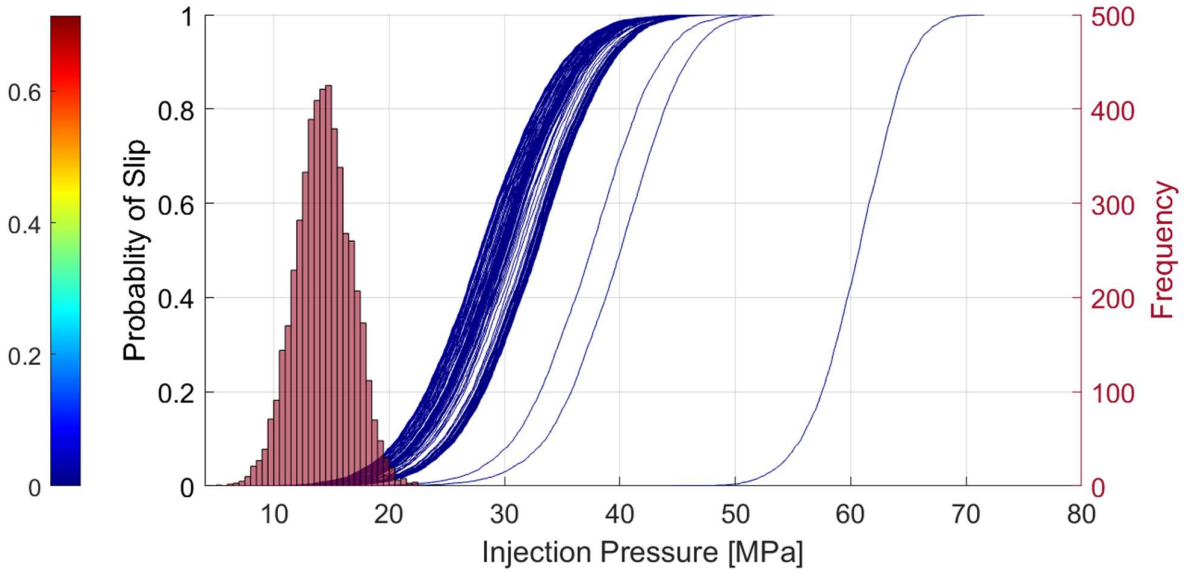

Figure B8: The cumulative probability function of the injection pressure required to cause a slip on faults located in stress area 1. A histogram illustrating the distribution of pore pressure in an area of stress 1. Each curve represents the cumulative probability function of slip for each fault segment at different injection pressure.

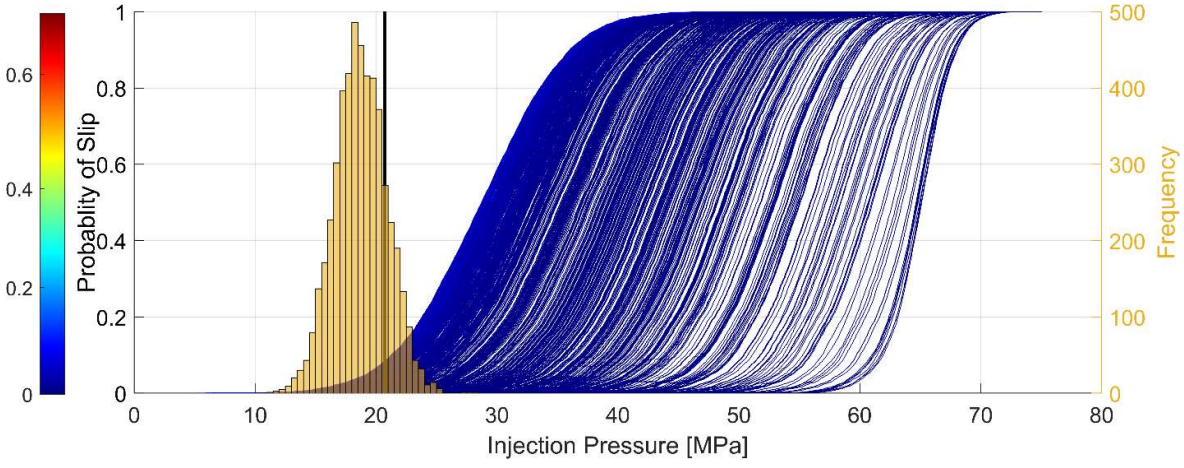

Figure B9: The cumulative probability function of the injection pressure required to cause a slip on faults located in stress area 2. The histogram illustrating the distribution of pore pressure in an area of stress 2.

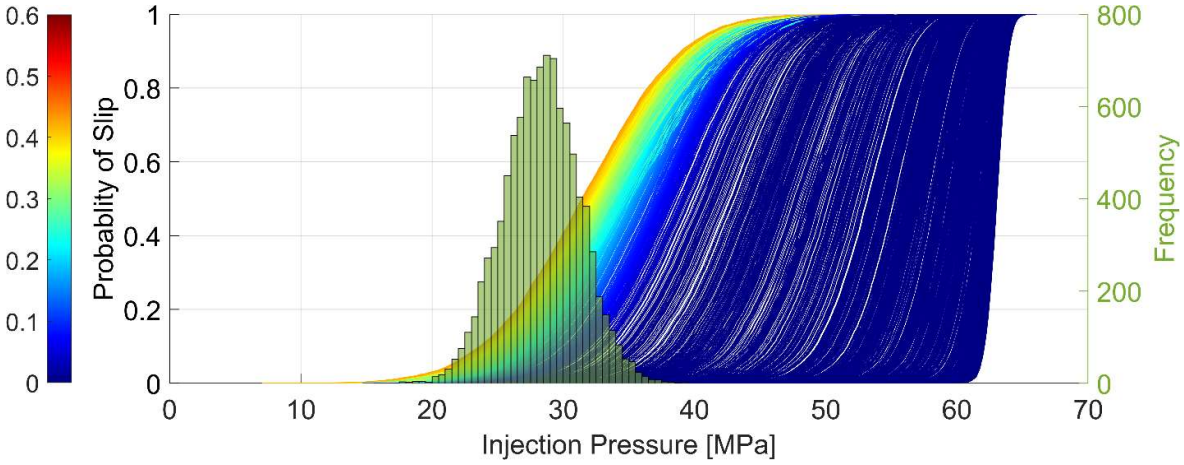

Figure B10: The cumulative probability function of the injection pressure required to cause a slip on faults located in stress area 3. The histogram illustrating the distribution of pore pressure in an area of stress 3.

Table B1. Earthquake source parameters used for determining stress and tectonic regime (A_φ)in the Montney Formation. The possible/actual nodal planes (Strike, Dip, and Rake) are indicated in bold.

Lat	Lon	Strike	Dip	Rake	Strike	Dip	Rake	A_φ
54.53	-118.51	**182.50**	**61.40**	**-147.10**	75.29	61.52	-33.00	1.02
54.53	-118.51	**179.80**	**69.20**	**-158.80**	81.96	70.24	-22.17	1.04
54.53	-118.51	**182.40**	**66.90**	**-157.80**	83.30	69.66	-24.73	1.12
54.53	-118.51	**179.50**	**65.20**	**-152.40**	77.13	65.13	-27.54	1.04
54.57	-118.52	**174.50**	**73.00**	**-172.30**	82.24	82.64	-17.15	1.26
54.56	-118.53	185.00	69.70	-170.20	**91.57**	**80.81**	**-20.58**	1.44
54.57	-118.53	**170.00**	**68.30**	**-161.60**	72.99	72.95	-22.75	1.05
54.56	-118.54	**181.20**	**62.80**	**-147.20**	74.79	61.20	-31.44	1.08
54.53	-118.51	185.40	56.10	-157.30	**82.27**	**71.32**	**-36.07**	1.33
54.56	-118.54	**177.60**	**69.00**	**-166.30**	82.61	77.23	-21.56	1.21
54.53	-118.50	**175.40**	**72.10**	**-162.80**	79.97	73.66	-18.68	1.00
54.53	-118.51	**172.50**	**48.50**	**-158.10**	67.58	73.78	-43.64	1.15
54.53	-118.44	**174.60**	**69.60**	**-146.00**	71.37	58.39	-24.16	1.35
54.53	-118.42	**191.80**	**56.00**	**-127.40**	65.62	48.81	-48.00	0.84
54.51	-118.47	190.40	49.20	-159.00	**86.32**	**74.26**	**-42.76**	1.50
54.51	-118.46	**176.80**	**50.10**	**-157.30**	71.78	72.78	-42.19	1.21
54.51	-118.46	**177.80**	**47.10**	**-157.40**	71.98	73.65	-45.19	1.24
54.51	-118.47	**180.20**	**55.50**	**-151.30**	72.97	66.69	-38.08	1.11
54.51	-118.46	**189.00**	**50.70**	**-158.50**	84.99	73.52	-41.34	1.46
54.50	-118.48	**174.00**	**74.90**	**-165.10**	80.03	75.63	-15.60	1.03
54.51	-118.48	**176.30**	**59.80**	**-154.10**	72.57	67.82	-32.90	1.04
54.51	-118.49	**177.20**	**67.90**	**-165.60**	81.68	76.68	-22.74	1.20
54.51	-118.48	185.30	53.60	-167.20	**87.62**	**79.73**	**-37.09**	1.50
54.51	-118.46	**348.50**	**80.40**	**170.60**	80.08	80.73	9.73	1.87
54.50	-118.46	**172.00**	**65.20**	**-158.90**	72.81	70.93	-26.35	1.02
54.50	-118.48	**169.40**	**68.50**	**-164.00**	73.40	75.14	-22.28	1.02
54.56	-118.53	**170.00**	**88.10**	**-177.80**	79.93	87.80	-1.90	1.16
54.51	-118.48	**177.60**	**61.70**	**-163.40**	79.56	75.43	-29.33	1.23
54.51	-118.48	**165.90**	**72.30**	**-156.30**	68.30	67.49	-19.22	1.40
54.51	-118.48	**165.40**	**73.40**	**-157.60**	68.68	68.58	-17.87	1.40

Lat	Lon	Strike	Dip	Rake	Strike	Dip	Rake	A_{φ}
54.51	-118.48	**170.30**	**68.40**	**-162.40**	73.64	73.67	-22.56	1.01
54.51	-118.48	**177.30**	**59.50**	**-159.90**	76.78	72.78	-32.10	1.18
54.52	-118.46	**173.60**	**64.10**	**-169.30**	78.88	80.39	-26.30	1.26
54.52	-118.46	2.30	63.30	160.20	**101.49**	**72.39**	**28.13**	1.97
54.51	-118.48	**178.90**	**70.10**	**-161.00**	82.22	72.17	-20.95	1.07
54.53	-118.49	**160.70**	**84.20**	**-154.00**	67.88	64.14	-6.45	1.67
54.50	-118.48	**176.40**	**73.60**	**-173.90**	84.67	84.15	-16.49	1.34
54.51	-118.48	**177.70**	**63.10**	**-161.10**	78.89	73.21	-28.20	1.17
54.51	-118.48	**186.60**	**60.40**	**-152.30**	82.06	66.16	-32.68	1.21
55.99	-120.62	**68.73**	**85.31**	**1.72**	338.59	88.29	175.31	1.79
55.99	-120.71	**72.92**	**56.84**	**158.70**	174.95	72.30	35.04	1.18
56.00	-120.66	**255.32**	**79.34**	**29.16**	159.43	61.39	167.83	1.62
55.98	-120.29	**251.26**	**86.39**	**1.78**	161.14	88.23	176.39	1.81
55.99	-120.70	**240.96**	**72.28**	**-6.66**	332.99	83.66	-162.17	1.57
55.97	-120.69	**241.68**	**74.73**	**-5.07**	333.02	85.11	-164.67	1.57
55.90	-120.37	**67.02**	**86.47**	**-1.08**	157.09	88.93	-176.47	1.49
55.97	-120.48	**72.61**	**58.30**	**27.16**	327.52	67.15	145.23	2.03
55.95	-120.56	**58.08**	**76.58**	**0.67**	327.93	89.35	166.58	1.80
55.93	-120.50	**73.39**	**49.76**	**33.19**	320.49	65.30	134.68	2.03
55.95	-120.63	**258.53**	**81.68**	**4.06**	167.94	85.98	171.66	1.68
55.93	-120.26	**245.73**	**84.78**	**167.39**	336.90	77.44	5.34	1.15
55.95	-120.64	**63.10**	**88.47**	**-1.17**	153.13	88.83	-178.47	1.35
55.91	-120.26	**249.89**	**87.20**	**18.36**	158.96	71.66	177.05	1.48
55.94	-120.31	**245.30**	**75.47**	**2.47**	154.68	87.60	165.46	1.75
56.01	-120.71	**243.96**	**86.84**	**-12.65**	334.67	77.37	-176.76	1.20
55.90	-120.18	**274.72**	**64.08**	**57.55**	150.21	40.63	137.83	2.36
56.04	-120.45	**303.10**	**74.21**	**163.49**	37.71	74.13	16.43	1.06
56.04	-120.45	**78.08**	**47.60**	**44.75**	314.32	58.68	127.87	2.15
55.91	-120.37	**245.31**	**89.90**	**5.07**	155.30	84.93	179.90	1.34
55.89	-120.54	**59.27**	**85.24**	**-12.59**	150.33	77.45	-175.12	1.08
55.91	-120.56	**63.25**	**88.91**	**3.93**	333.17	86.07	178.90	1.43

Lat	Lon	Strike	Dip	Rake	Strike	Dip	Rake	A_{φ}
56.05	-120.95	101.05	69.31	1.44	**10.55**	**88.66**	**159.30**	1.13
56.04	-120.58	**243.98**	**86.50**	**12.76**	153.18	77.26	176.41	1.43
55.93	-120.56	**62.07**	**88.77**	**0.38**	332.06	89.62	178.77	1.86
56.04	-120.68	**253.92**	**71.87**	**10.55**	160.60	79.98	161.58	1.82
55.93	-120.31	**69.46**	**82.95**	**-11.14**	160.84	78.94	-172.82	1.10
55.84	-120.55	**64.86**	**78.16**	**-7.66**	156.44	82.50	-168.06	1.37
55.91	-120.44	**64.45**	**75.64**	**2.04**	333.95	88.02	165.63	1.75
56.00	-120.38	**72.38**	**70.64**	**-4.73**	163.95	85.54	-160.58	1.42
55.99	-120.61	**64.62**	**82.61**	**8.31**	333.54	81.76	172.54	1.73
55.93	-120.36	**247.02**	**89.28**	**-3.66**	337.06	86.34	-179.27	1.27
56.00	-120.70	**68.03**	**83.60**	**12.76**	336.58	77.32	173.44	1.61
55.99	-120.70	**242.83**	**87.76**	**-0.61**	332.86	89.39	-177.76	1.58
56.05	-120.70	**261.08**	**57.65**	**32.74**	152.10	62.82	143.02	2.02
56.04	-120.70	**252.24**	**66.34**	**33.93**	147.13	59.25	152.17	2.28
56.04	-120.69	**271.08**	**68.54**	**54.64**	153.81	40.63	145.81	2.46
56.04	-120.69	125.73	66.51	107.83	**266.83**	**29.19**	**54.84**	2.04
55.91	-120.39	**68.58**	**79.93**	**9.30**	336.94	80.84	169.80	1.90
55.89	-120.38	**66.39**	**78.75**	**-2.45**	156.87	87.60	-168.74	1.54
56.04	-120.72	119.80	51.98	110.13	**269.05**	**42.30**	**66.24**	2.38
56.01	-120.51	**63.39**	**81.24**	**8.47**	332.09	81.63	171.15	1.76
56.00	-120.60	**246.05**	**76.04**	**-3.54**	336.91	86.56	-166.02	1.53
55.99	-120.62	**244.58**	**62.60**	**25.09**	142.42	67.88	150.22	1.68
55.98	-120.46	**66.73**	**71.61**	**2.19**	336.04	87.92	161.60	1.70
56.07	-120.94	**280.42**	**75.12**	**30.09**	181.95	61.02	162.92	1.82
55.90	-120.36	**249.69**	**82.37**	**5.08**	159.01	84.96	172.34	1.92
55.93	-120.55	**65.78**	**75.50**	**-2.71**	156.46	87.38	-165.48	1.57
55.97	-120.68	**72.75**	**86.84**	**-8.11**	163.20	81.90	-176.81	1.27
56.04	-120.65	68.60	83.16	14.67	**336.81**	**75.44**	**172.93**	1.60
55.99	-120.65	**91.99**	**88.47**	**-6.99**	182.18	83.02	-178.46	1.69
55.91	-120.30	**250.63**	**88.51**	**0.57**	160.61	89.43	178.51	1.76
56.01	-120.63	**315.63**	**71.33**	**88.18**	141.29	18.76	95.37	2.75

Lat	Lon	Strike	Dip	Rake	Strike	Dip	Rake	A_{φ}
55.89	-120.65	**68.46**	**88.33**	**-6.51**	158.65	83.49	-178.32	1.26
55.93	-120.27	**67.38**	**87.81**	**-9.13**	157.73	80.87	-177.79	1.26
55.89	-120.39	**67.43**	**84.82**	**10.12**	336.51	79.92	174.74	1.61
55.94	-120.54	**62.25**	**85.98**	**13.08**	331.32	76.95	175.87	1.41
55.99	-120.65	**270.39**	**79.66**	**14.91**	177.65	75.33	169.31	1.88
55.90	-120.22	**251.44**	**86.71**	**19.88**	160.25	70.15	176.50	1.51
55.95	-120.38	**64.29**	**89.00**	**10.05**	334.12	79.95	178.98	1.36
55.98	-120.27	**248.56**	**82.93**	**13.65**	156.85	76.45	172.72	1.62
55.99	-120.59	**250.98**	**88.67**	**-2.36**	341.03	87.64	-178.67	1.15
55.94	-120.66	**71.50**	**79.60**	**-11.65**	163.63	78.54	-169.39	1.01
56.00	-120.47	**70.92**	**83.06**	**12.14**	339.43	77.95	172.91	1.70